Tests of lepton universality in the rates of inclusive semileptonic B-meson decays at Belle II

Dissertation
zur
Erlangung des Doktorgrades (Dr. rer. nat.)
der
Mathematisch-Naturwissenschaftlichen Fakultät
der
Rheinischen Friedrich-Wilhelms-Universität Bonn

vorgelegt von
Henrik Alexander Junkerkalefeld
aus
Münster

Bonn, Februar 2024

Angefertigt mit Genehmigung der Mathematisch-Naturwissenschaftlichen Fakultät der Rheinischen Friedrich-Wilhelms-Universität Bonn

Gutachter und Betreuer:	Prof. Dr. Jochen Dingfelder
Gutachter:	Prof. Dr. Klaus Desch
Tag der Promotion:	28.06.2024
Erscheinungsjahr:	2024

Abstract

This thesis presents two precision tests of lepton universality: the first measurement of the ratio of light-lepton branching fractions of inclusive semileptonic B-meson decays, $R(X_{e/\mu}) = \mathcal{B}(B \to Xe\nu)/\mathcal{B}(B \to X\mu\nu)$, and the first successful measurement of inclusive $B \to X\tau\nu$ decays, measured in a ratio relative to $B \to X\ell\nu$ decays ($\ell = e, \mu$), $R(X_{\tau/\ell}) = \mathcal{B}(B \to X\tau\nu)/\mathcal{B}(B \to X\ell\nu)$.

Experimental data from electron-positron collisions at the $\Upsilon(4S)$ resonance collected with the Belle II detector is used, that corresponds to an integrated luminosity of 189 fb^{-1}. Continuum $e^+e^- \to q\overline{q}$ events are constrained using 18 fb^{-1} of off-resonance data, collected 60 MeV below the $\Upsilon(4S)$ resonance. One B meson from the $\Upsilon(4S) \to B\overline{B}$ decay is fully reconstructed in a hadronic decay mode. In the signal or normalization decay of the second B meson, $B \to X[\tau \to \ell\nu\nu]\nu$ or $B \to X\ell\nu$, a charged lepton candidate is required. The hadronic system X is left unconstrained, rendering this analysis sensitive to all possible hadronic final states.

The light-lepton ratio $R(X_{e/\mu})$ is extracted in a binned maximum-likelihood fit to the lepton-momentum spectra above 1.3 GeV. The fit is performed simultaneously for both lepton flavors, resulting in a substantial cancellation of correlated systematic uncertainties. The yields from $B\overline{B}$ backgrounds are constrained in a fit to control-sample data defined by the presence of two B-meson candidates with the same flavor. The value of

$$R(X_{e/\mu}) = 1.007 \pm 0.009\ (\text{stat.}) \pm 0.019\ (\text{syst.})$$

is obtained, which aligns with the Standard-Model expectation. This is the most precise branching fraction-based test of lepton universality in semileptonic B-meson decays to date.

For the measurement of $R(X_{\tau/\ell})$, significant discrepancies between experimental data and simulation, mostly attributed to the modeling of D-meson decays within the hadronic system X, are revealed. A new data-driven method to identify, quantify, and correct these modeling inaccuracies is developed, which simultaneously ameliorates the modeling of several observables that are associated with the hadronic system. This technique enables the extraction of $R(X_{\tau/\ell})$ in a two-dimensional binned maximum-likelihood fit to the lepton-momentum spectra and the squared missing mass in the event. The resulting $R(X_{\tau/\ell})$ values for electrons and muons are $R(X_{\tau/e}) = 0.232 \pm 0.020\ (\text{stat.}) \pm 0.037\ (\text{syst.})$, and $R(X_{\tau/\mu}) = 0.222 \pm 0.027\ (\text{stat.}) \pm 0.050\ (\text{syst.})$, respectively. The combination of lepton flavors in a weighted average of correlated values yields

$$R(X_{\tau/\ell}) = 0.228 \pm 0.016\ (\text{stat.}) \pm 0.036\ (\text{syst.}).$$

The results are in agreement with the Standard-Model predictions and represent a complementary test of the longstanding flavor anomaly observed in the exclusive ratios $R(D^{(*)})$.

Contents

1 Introduction 1

2 Theoretical overview 3
- 2.1 Standard Model of particle physics . . . 3
  - 2.1.1 Particles and forces . . . 3
  - 2.1.2 Quantum field framework of the Standard Model . . . 5
  - 2.1.3 Electroweak symmetry breaking . . . 9
  - 2.1.4 Shortcomings of the Standard Model . . . 12
- 2.2 Semileptonic B-meson decays . . . 14
  - 2.2.1 Fundamental characteristics . . . 14
  - 2.2.2 Decay kinematics and parameterization . . . 16
- 2.3 Lepton universality . . . 18
  - 2.3.1 The $R(D^{(*)})$ anomaly . . . 19
  - 2.3.2 Inclusive $b \to X\tau\nu$ measurements . . . 21
  - 2.3.3 Tests of light-lepton universality with B mesons . . . 23

3 Experimental setup 25
- 3.1 SuperKEKB accelerator . . . 25
- 3.2 Belle II detector . . . 27
  - 3.2.1 Vertexing and tracking system . . . 28
  - 3.2.2 Particle-identification system . . . 29
  - 3.2.3 Outer detector systems . . . 31
- 3.3 Particle reconstruction and identification . . . 32
  - 3.3.1 Cluster reconstruction . . . 32
  - 3.3.2 Track reconstruction . . . 32
  - 3.3.3 Particle identification . . . 34
- 3.4 Experimental data and simulated samples . . . 34
  - 3.4.1 Experimental data sample . . . 35
  - 3.4.2 Monte Carlo simulation . . . 36
  - 3.4.3 Modeling of semileptonic B-meson decays . . . 36
  - 3.4.4 Lepton-identification corrections . . . 42

4 Event reconstruction and selection 43
- 4.1 Hadronic B-meson tagging . . . 44
- 4.2 Continuum suppression . . . 48

4.3 Signal-lepton selection in the $R(X_{e/\mu})$ measurement . . . 52
4.4 Reconstruction of the hadronic system X . . . 54
4.4.1 Photon selection . . . 55
4.4.2 Charged-particle selection and X-system properties . . . 57
4.5 Event categorization . . . 58

5 Signal-extraction fit setup 61
5.1 $R(X_{e/\mu})$ and $R(X_{\tau/\ell})$ determination . . . 61
5.2 Fit model . . . 62
5.3 Systematic uncertainties . . . 64
5.3.1 Simulation-sample size . . . 64
5.3.2 Branching-fraction uncertainties . . . 65
5.3.3 Uncertainties of form-factor parameters . . . 65
5.3.4 Uncertainties of the track-reconstruction efficiency . . . 66
5.3.5 Lepton-identification uncertainties . . . 67
5.4 Independence of the B_{tag}-selection efficiency . . . 70
5.4.1 Signal vs. normalization decays . . . 70
5.4.2 Electron vs. muon normalization decays . . . 74

6 Measurement of the light-lepton ratio $R(X_{e/\mu})$ 79
6.1 $R(X_{e/\mu})$-extraction strategy and quantification of uncertainties . . . 79
6.1.1 Fit setup and background calibration . . . 80
6.1.2 Estimation of uncertainties . . . 82
6.1.3 Effects of modified D-meson decay distributions . . . 84
6.1.4 Validation of the fit setup . . . 86
6.2 Measurement and validation studies . . . 87
6.2.1 Measurement of $R(X_{e/\mu})$ . . . 87
6.2.2 Fiducial $R(X_{e/\mu})$ measurement . . . 90
6.2.3 Dependence on the lepton-momentum threshold . . . 91
6.2.4 Additional validations and crosschecks . . . 93

7 Towards a measurement of $R(X_{\tau/\ell})$: understanding the hadronic system X 99
7.1 Signal-lepton selection in the $R(X_{\tau/\ell})$ measurement and $B\bar{B}$-background suppression 99
7.1.1 Suppression of conversion photons and $\pi^0 \to e^+e^-(\gamma)$ decays . . . 101
7.1.2 Suppression of $K^-/\pi^- \to \mu^-\bar{\nu}_\mu$ decays . . . 104
7.1.3 Suppression of $J/\psi \to \ell^+\ell^-$ decays . . . 105
7.1.4 Lepton-momentum based background suppression . . . 106
7.1.5 Resonance-based muon-fake rejection . . . 107
7.2 Modeling of signal-extraction quantities in control samples . . . 109
7.2.1 Definition of control samples . . . 109
7.2.2 Discrepancies in simulation and experimental data . . . 110
7.2.3 D-meson decay mismodeling . . . 114
7.3 Data-driven simulation reweighting . . . 117
7.3.1 Yield calibration . . . 118
7.3.2 Reweighting of signal and normalization decays . . . 119

7.3.3 Extrapolation towards the low lepton-momentum region . . . 122
7.3.4 Reweighting of $B\bar{B}$-background events . . . 125

8 Measurement of the tau-to-light-lepton ratio $R(X_{\tau/\ell})$ 129
8.1 $R(X_{\tau/\ell})$-extraction strategy and quantification of uncertainties . . . 129
8.1.1 Fit setup . . . 129
8.1.2 Estimation of uncertainties . . . 130
8.1.3 Effects of modified D-meson decay distributions . . . 135
8.1.4 Dependence on the lepton-momentum threshold . . . 138
8.1.5 First box opening . . . 139
8.2 Measurement and validation studies . . . 141
8.2.1 Measurement of $R(X_{\tau/\ell})$ . . . 141
8.2.2 Result stability and crosschecks . . . 144
8.2.3 Implications of $R(X_{\tau/\ell})$ on the $b \to c\tau\nu$ anomaly . . . 148

9 Conclusion and outlook 153

A Additional studies 159
A.1 Suppression of bad B_{tag} candidates . . . 159
A.2 Optimization of bremsstrahlung corrections . . . 161
A.3 Validation of uncertainties on $R(X_{e/\mu})$ with toy data samples . . . 162
A.4 Validation of the fit setup and uncertainties to extract $R(X_{\tau/\ell})$ . . . 165

B Additional tables and figures 167
B.1 Lepton-identification correction tables . . . 167
B.2 Reconstructed B-meson decay modes by the FEI algorithm . . . 172
B.3 Impact of modified D-meson decay distributions on M_X and p_ℓ^B . . . 174
B.4 Additional information on the resonance-based muon-fake rejection . . . 180
B.5 Validation of the simulation reweighting in various control samples . . . 185
B.6 Impact of modified D-meson decay distributions on signal decays . . . 192
B.7 Correction weights introduced in the reweighting . . . 194
B.8 D-meson decay distributions to validate uncertainties on $R(X_{\tau/\ell})$ . . . 198
B.9 Pre-fit distributions of p_ℓ^B and M_{miss}^2 in various subsets of data . . . 200

Bibliography 203

List of Figures 219

List of Tables 223

List of Abbreviations 225

Acknowledgements 227

CHAPTER 1

Introduction

Particle physics aims to understand the fundamental building blocks of matter and the underlying forces that govern their interactions in the universe. The current state of knowledge is summarized in three fundamental symmetries within the Standard Model of particle physics (SM). This model successfully describes a wide range of phenomena and particle-physics processes across various scales, as elaborated on in Chapter 2. Despite its significant achievements, the SM cannot serve as a final theory due to inherent limitations. Hence, the aspiration of contemporary particle physicists is to extend the SM, aiming for a more comprehensive theory that addresses its shortcomings.

In particle-collider experiments, these topics are investigated on the microscopic scale by generating highly energetic interactions within a controlled environment. Advancements in our understanding are pursued using two distinct strategies. In the *high-energy* approach, the center-of-mass energies are maximally enhanced, allowing for the potential direct production of particles that are too massive to have been observed previously. On the other hand, the *high-precision* approach seeks to indirectly unveil new physical phenomena by measuring the properties of known particles within a precisely controlled setting.

An example of the latter approach is the Belle II experiment, where electrons and their antiparticles collide at a precisely controlled energy, amplifying the reaction $e^+e^- \to \Upsilon(4S) \to B\overline{B}$. Chapter 3 provides an overview of the experimental setup and introduces the techniques employed to interpret and validate the responses of the detector. The controlled production of heavy B-mesons enables to precisely measure their decay chains and to deepen the understanding of the underlying processes. Potential deviations from theoretically expected properties could indicate the presence of undiscovered heavy particles before their direct production.

Semileptonic B-meson decays $B \to Xl\nu$ into a hadronic final state X, a charged lepton ($l = e, \mu, \tau$), and an undetectable neutrino, provide both high experimental and theoretical precision, consequently serving as excellent probes of the SM. Over the past decade, results from various experiments focusing on *exclusive* semileptonic decays, where a specific decay mode is reconstructed ($X = D^{(*)}$), have started to suggest intriguing trends that challenge the concept of *lepton universality*. This principle, a fundamental property of the SM, postulates the three charged leptons to only differ by their masses.

In this thesis, lepton universality in semileptonic B-meson decays is investigated in an *inclusive* manner, where all decays involving the quark-level transitions $b \to cl\nu$ and, rarely, $b \to ul\nu$ are considered. This approach enhances statistical precision and sensitivity to all hadronic finals states X. However, this choice presents a substantial challenge in effectively controlling the various

background sources, and there is an increased sensitivity to inaccuracies in the modeling. The inclusive event selection resulting in such a generalized data set is presented in Chapter 4. In Chapter 5, the identification and quantification of potential sources of uncertainty, along with the overall signal-extraction fit setup, are detailed.

Based on these techniques, this thesis presents the first measurement of the ratio of branching fractions of inclusive semileptonic B-meson decays into light leptons, $R(X_{e/\mu}) = \mathcal{B}(B \to Xe\nu)/\mathcal{B}(B \to X\mu\nu)$, as outlined in Chapter 6 and published in Reference [1]. Due to the distinctive signatures of light leptons of both flavors within the Belle II detector, this marks the most precise branching-fraction based test of lepton universality with B-mesons to date.

Particular attention has been drawn to decays involving the $b \to c\tau\nu$ quark transition in recent measurements. The high mass of the τ lepton enhances the sensitivity of semitauonic B-meson decays to yet unobserved physical phenomena. However, the reconstruction of τ leptons solely relies on their decay products, leading to a substantially increased number and variety of background processes. This poses a significant difficulty in ensuring the reliable control and modeling of all participating processes, a challenge that has not been adequately addressed before.

In Chapter 7 of this thesis, experimental techniques are developed to investigate and correct inaccuracies in the modeling of physical processes, as well as to quantify remaining uncertainties. This advancement enables the first successful measurement of inclusive semitauonic B-meson decays, measured in the ratio $R(X_{\tau/\ell}) = \mathcal{B}(B \to X\tau\nu)/\mathcal{B}(B \to X\ell\nu)$ ($\ell = e, \mu$) and published in Reference [2]. This is presented and discussed in Chapter 8. In Chapter 9, the findings of this thesis are contextualized and an outlook on potential future improvements is provided.

Initially, this work started as a collaborative effort with the University of Melbourne. Unless explicitly stated otherwise, all the developments, techniques, and results presented in this thesis reflect the author's individual contributions to the research. Natural units, namely $\hbar = c = 1$, are used throughout, and charge conjugation is implied in all physical processes. The symbol l is used to denote all three charged leptons, $l = \{e, \mu, \tau\}$, whereas ℓ is specifically reserved for light leptons, $\ell = \{e, \mu\}$.

CHAPTER 2

Theoretical overview

The theoretical framework that summarizes the current knowledge of the universe at its smallest scales is referred to as the Standard Model of particle physics (SM), which is introduced in Section 2.1. This work is based on the analysis of semileptonic B-meson decays, with their distinctive characteristics detailed in Section 2.2. In this context, several intriguing measurements serve as motivation for conducting further precise tests to explore these decays for signs of phenomena beyond the SM, as elaborated on in Section 2.3.

2.1 Standard Model of particle physics

The SM includes the fundamental building blocks of matter, the elementary particles (see Sec. 2.1.1). Additionally, it describes the forces that govern the particle interactions in a relativistic quantum field theory (QFT) [3], namely the electromagnetic and weak nuclear forces [4–7], and the strong nuclear force [8] (see Secs. 2.1.2 and 2.1.3). The SM has been remarkably successful in explaining and predicting the behavior of particles, making it a cornerstone of modern theoretical physics. Nevertheless, the SM is known to be incomplete for several reasons that are outlined in Section 2.1.4.

2.1.1 Particles and forces

The SM was developed in the 1960s and consists of 17 different fundamental particles that are summarized in Figure 2.1. It successfully describes particle properties and interactions to very high precision [9–11] and predicted the existence of several particles like gluons, the charm and the top quark as well as the W and Z boson before their discovery [12]. In 2012, the SM was completed by the discovery of the Higgs boson [13–15].

In the SM, particles are characterized based on their spin, mass and charge. Apart of the gravitational force, which is negligibly weak on microscopic scale, the SM contains three of the four known interactions of the universe that are mediated by vector gauge bosons with integer spin $S = 1$. The characteristics of each interaction is encoded in each gauge boson's properties.

The electromagnetic force is mediated by the photon, denoted γ, which couples to the electric charge. Since the photon is massless, the range of the electromagnetic interaction is essentially boundless, rendering it relevant and observable even on macroscopic scales. Furthermore, this force facilitates

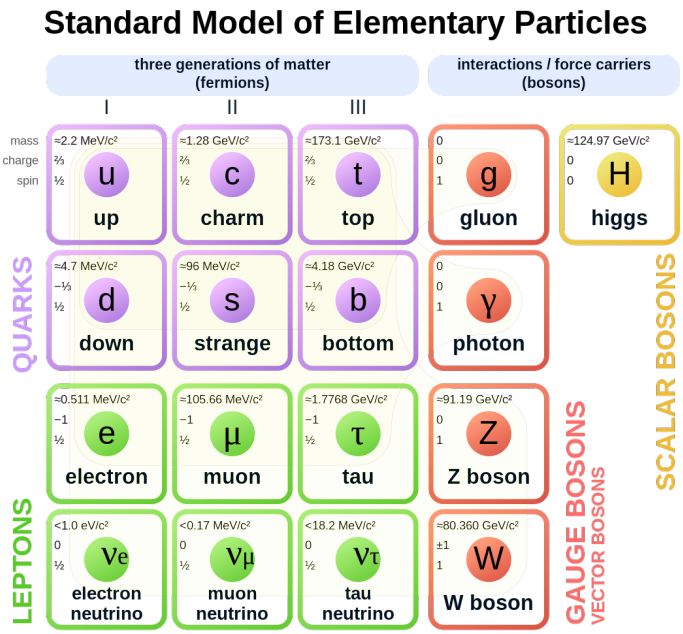

Figure 2.1: The elementary particles of the SM are illustrated. Different colors indicate different particle properties as outlined in more detail in the text. Figure from Reference [16].

the creation of bound states like atoms and molecules, consequently, manifesting prominently in our everyday experiences.

The strong nuclear interaction is mediated by gluons, denoted g. Unlike electric charge, which exists in two polarities (positive and negative), there are three distinct strong charges (as well as their corresponding anti-charges) that combine to strong-charge neutrality.These strong charges are commonly referred to as *color* charges. Gluons carry color and anticolor charge themselves, so that they interact with one another. This distinctive feature explains the short-range character of the strong force despite the gluon's masslessness.

The massive $W^{\pm}$ bosons and the Z^0 boson serve as the mediators of the weak nuclear force, which was initially observed in radioactive decays. Due to the substantial mass of these mediator bosons, the range of the weak force is constrained to approximately $O(1\,\mathrm{fm})$ and its effective strength is comparably weak. Consequently, it stands as the sole force that does not lead to the formation of bound states.

The consistency of the SM necessitates the existence of a scalar particle with a spin of zero, known as the Higgs boson. This particle arises from the Higgs mechanism, which generates the particle's masses and is explained in more detail in Section 2.1.3.

Fermions, that are defined to carry half-integer spin, are categorized into two types of particles, leptons and quarks, and into three generations of four particles each that only differ from the other generations by the particle's masses. Each fermion generation consists of two leptons organized in a weak isospin doublet. One of these leptons is the electrically neutral neutrino (ν_e, ν_μ, or ν_τ), that exclusively interacts via the weak force. The other member of the doublet is the charged lepton (electron, muon, or τ lepton), which additionally interacts electromagnetically. Furthermore, within

each fermion generation, there is a quark doublet. The up-type quark (up, charm, or top quark) in this doublet carries an electric charge of $q = +\frac{2}{3}$, while the down-type quark (down, strange, or bottom quark) possesses a charge of $q = -\frac{1}{3}$. Additionally, all quarks carry a color charge, making them subject to interactions via the strong force, as well as via the weak and the electromagnetic force.

For each fermion, there exists a corresponding anti-fermion with an identical mass but opposite quantum numbers (such as electric charge). In the SM, matter and antimatter particles are exclusively created in pairs and mutually annihilate, producing highly energetic radiation. Based on missing observations of sufficient amounts of such characteristic radiation in the universe, it is widely assumed that the existing universe is predominantly composed of matter rather than antimatter, as elaborated on in Section 2.1.4.

The particle's masses are distributed over several orders of magnitude ranging from the electron mass of 511 keV to the top-quark mass of 173 GeV [17]. The neutrinos are assumed to be massless in the SM. Due to the energetic preference for heavy particles to decay into lighter ones, only fermions belonging to the first generation (and neutrinos) are stable. Consequently, in today's cooled-down universe the vast majority of existing matter is composed of first-generation fermions. Particles of the second and third generation can be generated in high-energy processes but are relatively short-lived.

In the following sections, the theoretical foundation of the different forces and the SM in general are briefly presented.

2.1.2 Quantum field framework of the Standard Model

The SM is formulated as a local, gauge-invariant quantum field theory (QFT). This means that its mathematical framework ensures that its Lagrangian and equations of motion are invariant under certain gauge transformations associated with the fundamental symmetry group that describes the SM:

$$\mathrm{SU(3)_C} \times \mathrm{SU(2)_L} \times \mathrm{U(1)_Y} \tag{2.1}$$

In this context, $\mathrm{SU(3)_C}$ represents the symmetry group associated with the strong force. $\mathrm{SU(2)_L}$ represents the weak isospin symmetry group and $\mathrm{U(1)_Y}$ represents the group associated with hyptercharge which together form the theory of electroweak interaction. The Higgs mechanism eventually breaks the latter two symmetries $\mathrm{SU(2)_L} \times \mathrm{U(1)_Y} \rightarrow \mathrm{U(1)_{em}}$ as outlined in more detail in Section 2.1.3.

Quantum field theories provide a framework that combines the principles of quantum mechanics and special relativity and serves as the foundation for describing the behavior of particles and their interactions. By imposing the conditions of Lorentz invariance and local SU(N) gauge invariance, the Yang-Mills Lagrangian [18] of a any SU(N) gauge theory can be constructed as follows:

$$\mathcal{L}_{\mathrm{YM}} = \underbrace{\overline{\Psi}_f \left(i\gamma^\mu \partial_\mu - m_f\right)\Psi_f}_{\text{free fermion field}} - \underbrace{\frac{1}{4} F^{\mathrm{a}}_{\mu\nu} F_{\mathrm{a}}^{\mu\nu}}_{\text{vector boson field}} - \underbrace{g \overline{\Psi}_f \gamma^\mu T_{\mathrm{a}} \Psi_f A^{\mathrm{a}}_\mu}_{\text{fermion-boson coupling}} \tag{2.2}$$

Within this equation, $\overline{\Psi}_f$ and Ψ_f represent fermion fields, A^a_μ stands as the gauge boson field, T_{a} is identified as the generator of the SU(N) group, g represents the coupling strength and $F_{\mathrm{a}}^{\mu\nu}$ is the gauge-invariant bosonic field-strength tensor defined as:

$$F_{\mathrm{a}}^{\mu\nu} = \partial^\mu A^\nu_{\mathrm{a}} - \partial^\nu A^\mu_{\mathrm{a}} - g f_{\mathrm{abc}} A^\mu_{\mathrm{b}} A^\nu_{\mathrm{c}} \tag{2.3}$$

Here, f_{abc} represents the completely antisymmetric structure constant of the corresponding symmetry group, with its definition grounded in the commutator of the group's generators: $[T_{\mathrm{a}}, T_{\mathrm{b}}] = i f_{\mathrm{abc}} T_{\mathrm{c}}$.

The physical differential equations of motion for any field Φ_i such as Ψ_f or A^a_μ can be obtained by employing the principle of least action, resulting in the Euler-Lagrange equation:

$$\partial_\mu \left(\frac{\partial \mathcal{L}}{\partial(\partial_\mu \Phi_i)} \right) - \frac{\partial \mathcal{L}}{\partial \Phi_i} = 0 \tag{2.4}$$

Applying Equation (2.4) to (2.2), the first term yields the famous Dirac equation and describes a freely propagating fermion field Ψ_f (e.g. electrons or muons) with mass m_f. The subsequent terms are more gauge-group dependent and are discussed in the following.

The theory governing the electromagnetic interaction is **Quantum Electrodynamics (QED)** [19], a local $\mathrm{U(1)_{em}}$ gauge theory. Due to its abelian nature, the structure constant f_{abc} reduces to zero and the group generator T_{a} becomes trivial. Consequently, Equation (2.3) simplifies to $F^{\mu\nu} = \partial^\mu A^\nu - \partial^\nu A^\mu$. Within QED, A^μ can be identified as a free, massless vector field, commonly referred to as the photon.

In Equation (2.2), the third term accounts for the coupling between gauge bosons and fermions, with the interaction strength being the fermion's electric charge, $g = q_f$, in the context of QED. Remarkably, the addition of the coupling term is necessary to satisfy local SU(N) gauge invariance, thereby establishing boson-fermion interactions a direct consequence of this fundamental symmetry [20, 21].

The coupling "constant" $\alpha_{\mathrm{em}} = \frac{e^2}{4\pi}$, where e is the elementary electric charge, quantifies the effective coupling strength of the electromagnetic force. Despite its name, it is not a constant value but depends on the momentum transfer q^μ of a given process. Using the Callen-Symanzik equation of the renormalisation group [22, 23], the running coupling of QED can be calculated as follows:

$$\alpha_{\mathrm{em}}(q^2) = \frac{\alpha_{\mathrm{em}}(\mu^2)}{1 - \alpha_{\mathrm{em}}(\mu^2)\frac{1}{3\pi}\ln(q^2/\mu^2)} \tag{2.5}$$

Here, μ^2 represents the renormalization scale, usually chosen on the order of the external momentum scale q^2. The electromagnetic coupling strength α_{em} increases with higher energies, i.e., higher q^2 values or shorter distances, from approximately $\frac{1}{137}$ at atomic energy scales ($\mathcal{O}(10\,\mathrm{eV})$) to $\frac{1}{129}$ at the energy scale corresponding to the mass of the Z^0 boson (91.19 GeV).

Quantum Chromodynamics (QCD) [8], provides the theoretical framework for understanding the strong nuclear force and can be constructed analogously to QED. In the context of QCD, the gauge transformation corresponds to the non-abelian $\mathrm{SU(3)_C}$ gauge group.

Within the QCD Lagrangian (derived from Eq. (2.2)), the coupling strength of the strong force is denoted $g \equiv g_{\mathrm{s}}$. In this context, the vector gauge boson fields $A^{\mathrm{a}}_\mu \equiv G$ represent the eight massless gluon fields, each associated with a different color-anticolor combination. The fermions upon which this force acts are the quark fields Ψ_q. The distinctive phenomenological behaviors of the strong and the electromagnetic interactions can be attributed to the non-abelian nature of the SU(3) group. Consequently, the structure constant f_{abc} does not vanish and induces self interacting vertices of the

gluons. In a simplified representation, the QCD Lagrangian yields

$$\mathcal{L}_{\mathrm{QCD}} = \overline{\Psi}_q \Psi_q - GG - g_\mathrm{s} GGG - g_\mathrm{s}^2 GGGG - g_\mathrm{s} \overline{\Psi}_q \Psi_q G. \tag{2.6}$$

This formulation not only encompasses gluon-quark couplings similar to the photon-fermion couplings in QED, but also results in vertices involving three or four gluons (see Fig. 2.2).

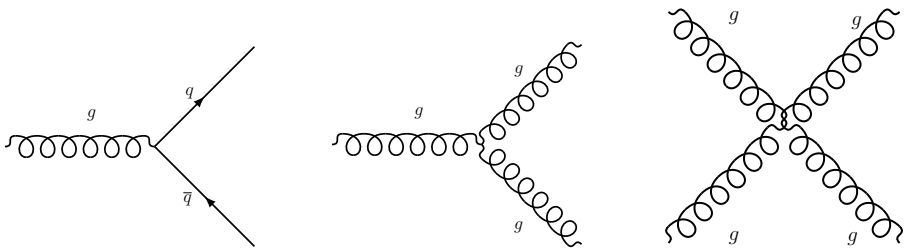

(a) $g_\mathrm{s} \overline{\Psi}_q \Psi_q G$ (b) $g_\mathrm{s} GGG$ (c) $g_\mathrm{s}^2 GGGG$

Figure 2.2: The QCD interaction vertices, as depicted in Feynman diagrams, are illustrated and associated with their corresponding terms in the Lagrangian.

One direct consequence of these self-interacting vertices in QCD is a modification in the running behavior of the strong coupling. Specifically, the three-gluon vertex introduces a change in the sign of the beta function in the Callen-Symanzik equation, leading to the running of the QCD coupling $\alpha_\mathrm{s} = \frac{g_s}{4\pi}$ being described as follows:

$$\alpha_\mathrm{s}(q^2) = \frac{\alpha_\mathrm{s}(\mu^2)}{1 + \alpha_\mathrm{s}(\mu^2) \frac{11 N_\mathrm{C} - 2 N_f}{12\pi} \ln(q^2/\mu^2)} \equiv \frac{12\pi}{(11 N_\mathrm{C} - 2 N_f) \ln(q^2/\Lambda_\mathrm{QCD}^2)} \tag{2.7}$$

In this equation, N_C represents the number of colors and N_f is the effective number of strongly interacting fermions (quarks in the SM). Due to this altered coupling behavior, α_s decreases as the momentum scale increases or as length scales shorten as illustrated in Figure 2.3. This phenomenon is known as the *asymptotic freedom* of quarks at high energies.

In contrast, at low momenta or larger distances, the strength of the coupling increases significantly. The energy scale at which QCD becomes too strong to be predictable with perturbation theory is characterized by Λ_QCD, with an approximate value ranging from 200 to 300 MeV [17]. When two color-charged quarks are separated, the strong coupling generates an increasingly powerful force field between them. This binding energy eventually surpasses the threshold for producing additional quark-antiquark pairs, which then combine to form color-neutral bound states (hadrons) in a process referred to as hadronization. Consequently, colored particles cannot be observed freely in nature, a concept known as *confinement*. Moreover, the range of the strong interaction is limited to short distances of approximately $1/\Lambda_\mathrm{QCD} \approx 1$ fm [20, 24].

These color-neutral hadrons can be categorized into two groups based on their constituents. Firstly, there are mesons, which consist of a color-charged quark and an anti-quark with corresponding anti-color. Secondly, a color-neutral state can be achieved by combining three quarks with distinct color charges. Such three-quark objects are referred to as baryons. Furthermore, it is theoretically possible to form color-neutral objects by binding higher numbers of quarks and antiquarks together. In fact, evidence for tetraquarks, composed of two quarks and two antiquarks, as well as for pentaquarks,

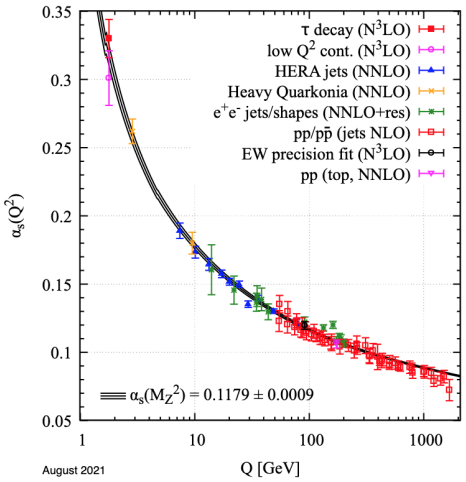

Figure 2.3: Measurements of the strong coupling strength α_s at different energies Q reveal its variation from high values at low energies (confinement) to relatively lower values at high energies (asymptotic freedom). Figure from Reference [17].

has been reported in recent experiments [25–28]. However, distinguishing these states from complex molecule-like baryon-meson structures can be challenging.

The third fundamental interaction within the SM is the weak nuclear force. In the 1960s, Glashow, Weinberg, and Salam demonstrated independently how it could be unified with the electromagnetic force to create the **electroweak interaction** [5–7]. This electroweak unification is governed by the symmetry group represented as $\mathrm{SU(2)_L} \times \mathrm{U(1)_Y}$ in which three vector bosons W_1^μ, W_2^μ, and W_3^μ and the interaction strength g_w are associated with the $\mathrm{SU(2)_L}$ symmetry group. The electroweak theory describes both charged and neutral currents of the electromagnetic and the weak interaction. The weak charged currents are mediated by the $W^\pm$ bosons, that are expressed as linear combinations of W_1^μ and W_2^μ:

$$W^{\mu,\pm} = \frac{1}{\sqrt{2}} \left(W_1^\mu \mp i W_2^\mu \right) \tag{2.8}$$

They exclusively interact with left-chiral particles (or right-chiral antiparticles), as indicated by the symmetry group's subscript. Mathematically, this is represented by the projection operator $P_\mathrm{L} = \frac{1}{2}(1 - \gamma^5)$, which is applied to each $W^\pm$-fermion interaction. This characteristics sets the weak interaction apart as the only force which is maximally parity violating, as experimentally shown in References [29, 30]. Consequently, all left-chiral particles are organized into weak isospin doublets $(u_\mathrm{L}, d_\mathrm{L})$ or $(\nu_\mathrm{L}, l_\mathrm{L})$ and carry a weak isospin $T_\mathrm{w} = \frac{1}{2}$. In contrast, right-chiral particles like e_R are singlets under $\mathrm{SU(2)_L}$ transformations with $T_\mathrm{w} = 0$. Additionally, every particle possesses a hypercharge Y due to the local $\mathrm{U(1)_Y}$ symmetry which governs the coupling to the corresponding vector boson B^μ with interaction strength g'. In this framework, the electric charge q follows from $q = T_3 + \frac{Y}{2}$, where T_3 signifies the third component of the weak isospin [20, 24].

The observed neutral gauge bosons, γ and Z^0, are mixtures of both B^μ and the W_3^μ through the

weak mixing angle θ_w:

$$\begin{pmatrix} A^\mu \\ Z^\mu \end{pmatrix} = \begin{pmatrix} \cos\theta_w & \sin\theta_w \\ -\sin\theta_w & \cos\theta_w \end{pmatrix} \cdot \begin{pmatrix} B^\mu \\ W_3^\mu \end{pmatrix} \tag{2.9}$$

Utilizing the relationship between the elementary electric charge and the weak mixing angle, expressed as $e = g_w \sin\theta_w = g' \cos\theta_w$, the coupling of the Z^0 boson to fermions, denoted as $g_Z = g_w T_3 \cos\theta_w - g' \frac{Y}{2} \sin\theta_w$, can be written as follows:

$$g_Z = \frac{g_w}{\cos\theta_w}(T_3 - q \sin^2\theta_w), \tag{2.10}$$

effectively resulting in different coupling strengths to the left-chiral and right-chiral components of a particle.

The name-giving weakness of the interaction is a direct consequence of the substantial masses of the gauge bosons, $W^\pm$ and Z^0, as the effective coupling scales with $g_w^2/m_{W/Z}^2$. The weak coupling constant $\alpha_w = \frac{g_w^2}{4\pi}$ itself amounts to roughly $\frac{1}{29.5}$ at low energies and hence would be larger than the electromagnetic coupling [20, 24].

The discovery of massive gauge bosons poses a challenge to the essential requirement of gauge invariance within the Yang-Mills theory. For instance, a term like $\frac{1}{2} m_A^2 A_\mu A^\mu$ is evidently not invariant under the local U(1) gauge transformation $A_\mu \rightarrow A'_\mu = A_\mu - \partial_\mu \chi$. Furthermore, the fermion mass term $-m_\Psi \overline{\Psi}\Psi$ (see Eq. (2.2)) can also be expressed as $-m_\Psi(\overline{\Psi}_R \Psi_L + \overline{\Psi}_L \Psi_R)$. This term couples left-chiral and right-chiral particle states, even though they respond differently to local $SU(2)_L$ gauge transformations. Consequently, this term violates the necessary gauge invariance, as demonstrated by t'Hooft [3, 31, 32], and renders the electroweak theory non-renormalisable.

To address this challenge, the Higgs mechanism was developed. It introduces a mechanism that breaks local gauge invariance, which will be discussed in the following section.

2.1.3 Electroweak symmetry breaking

In the SM, both the massive gauge bosons and the charged fermions acquire their mass due to the Higgs mechanism, independently proposed by Englert and Brout, as well as by Higgs in 1964 [33, 34]. Within this context, the corresponding mass terms in the Lagrangian emerge from the interaction between the particles and the Higgs field after spontaneous symmetry breaking of $SU(2)_L \times U(1)_Y \rightarrow U(1)_{em}$.

The minimal choice to enable the generation of three massive gauge bosons is to introduce a pair of complex scalar fields organized as a weak isospin doublet, the Higgs doublet:

$$\Phi = \begin{pmatrix} \phi^+ \\ \phi^0 \end{pmatrix} = \frac{1}{\sqrt{2}} \begin{pmatrix} \phi_1 + i\phi_2 \\ \phi_3 + i\phi_4 \end{pmatrix} \tag{2.11}$$

The possible additional terms arising in the Lagrangian for the scalar fields, maintaining invariance under both $SU(2)_L$ and $U(1)_Y$ gauge transformations, can be expressed as follows:

$$\mathcal{L}_{\text{Higgs}} \supset \underbrace{(D_\mu \Phi)^\dagger (D^\mu \Phi)}_{\text{free Higgs and Higgs-}W/Z^0\text{ interaction}} - \underbrace{y_f \left(\bar{L}\Phi R + \bar{R}\Phi^\dagger L\right)}_{\text{Higgs-fermion interactions}} - \underbrace{\left(\mu^2 \Phi^\dagger \Phi + \lambda(\Phi^\dagger \Phi)^2\right)}_{\text{Higgs potential } V_{\text{Higgs}}(\Phi)} \tag{2.12}$$

In this equation, the covariant derivative D_μ is given by $D_\mu = \partial_\mu + i\frac{g_w}{2}\vec{\sigma}\cdot\vec{W}_\mu + i\frac{g'}{2}Y_\Phi B_\mu$ with the hypercharge of the Higgs doublet of $Y_\Phi = 1$. The symbol L represents a left-handed lepton or quark doublet $L = (f_L^u, f_L^d)^\dagger$, R denotes the corresponding right-handed singlets, and y_f is the fermion-dependent strength of the Yukawa coupling to the Higgs [20, 24].

The Higgs potential (see Eq. (2.12)) obtains a non-trivial minimum when the μ^2 term adopts a negative value. Under this condition, the field Φ settles into a vacuum state in a process known as **spontaneous symmetry breaking**. This new state is characterized by

$$|\Phi| = \sqrt{-\frac{\mu^2}{2\lambda}} := \frac{v}{\sqrt{2}}. \tag{2.13}$$

Here, v is referred to as the vacuum expectation value of the Higgs field, which can be obtained from experimental measurements of m_W, m_Z, and g_w and is determined to be $v = 246\,\text{GeV}$. Excitations of the field around the new minimum define a particle state that corresponds to the SM Higgs boson. Without loss of generality, the *unitary gauge* can be chosen, expressing the Higgs doublet as

$$\Phi = \frac{1}{\sqrt{2}}\begin{pmatrix} 0 \\ v + h \end{pmatrix}. \tag{2.14}$$

In this equation, the Higgs boson is represented by h [20, 24]. Subsequently, the Higgs potential reads

$$V_{\text{Higgs}}(\Phi) = \lambda v^2 h^2 + \lambda v h^3 + \frac{1}{4}\lambda h^4 - \frac{1}{4}\lambda v^4. \tag{2.15}$$

The first term induces the **Higgs boson mass**, measured to be $m_h \approx 125\,\text{GeV}$ [35, 36]. Additionally, so far unmeasured Higgs self-couplings are predicted that are experimentally very challenging but interesting to probe [37–39].

After symmetry breaking, the first term of the Higgs Lagrangian yields:

$$(D_\mu\Phi)^\dagger(D^\mu\Phi) = \frac{1}{2}(\partial_\mu h)(\partial^\mu h) + \frac{1}{4}g_w^2 W_\mu^- W^{\mu,+}(v+h)^2 \tag{2.16}$$

$$+ \frac{1}{8}\begin{pmatrix} B_\mu & W_{\mu,3} \end{pmatrix}\begin{pmatrix} g'^2 & -g_w g' \\ -g_w g' & g_w^2 \end{pmatrix}\begin{pmatrix} B^\mu \\ W_3^\mu \end{pmatrix}(v+h)^2. \tag{2.17}$$

The components scaled by only the vacuum-expectation value result in the generation of the **gauge boson masses**. By acquiring mass, vector bosons obtain an additional degree of freedom, the longitudinal polarization, compared to their previous massless state. This additional degree of freedom can be attributed to the Goldstone modes of the Higgs field, that are absorbed by the weak gauge bosons.

Following the diagonalization of the term in Equation (2.17), along with the definition of the weak mixing angle $\theta_w = \tan\theta_w = \frac{g'}{g_w}$ and Equation (2.9), the mass matrix of the neutral gauge bosons can be formulated as

$$\frac{1}{8}v^2\begin{pmatrix} A_\mu & Z_\mu \end{pmatrix}\begin{pmatrix} 0 & 0 \\ 0 & g_w^2 + g'^2 \end{pmatrix}\begin{pmatrix} A^\mu \\ Z^\mu \end{pmatrix}. \tag{2.18}$$

The presence of a massless photon is deduced and the Z^0 boson mass can be derived [20, 24].

The second term of Equation (2.12) becomes responsible for generating **fermion masses** by coupling the left- and right-chiral fermion fields. As an illustrative example, for the first quark doublet, this term can be expressed as:

$$\mathcal{L} \supset -\frac{y_d}{\sqrt{2}}(\bar{d}_\mathrm{L} d_\mathrm{R} + \bar{d}_\mathrm{R} d_\mathrm{L})(v + h). \tag{2.19}$$

This term leads to the derivation of the down quark mass of $m_d = y_d \frac{v}{\sqrt{2}}$. The Hermitian conjugate of the Lagrangian provides masses to up-type quarks [20, 24].

Generally, the weak eigenstates that define the $\mathrm{SU(2)_L}$ doublets and singlets do not need to correspond to the physical mass eigenstates that are relevant for the free-particle propagation. Indeed, when explicitly extending the Higgs-fermion interaction term from Equation (2.12) to encompass multiple fermion generations, non-diagonal mass matrices for quarks emerge after symmetry breaking. The mass eigenstates of quarks can be derived through the diagonalization of these mass matrices, involving distinct transformations in flavor space for both left- and right-chiral fields. From these transformations, the **Cabibbo-Kobayashi-Maskawa (CKM) matrix** [40, 41] is obtained, which serves as a linkage between the weak eigenstates, from here on explicitly denoted with a prime, and the mass eigenstates:

$$\begin{pmatrix} d' \\ s' \\ b' \end{pmatrix} = \underbrace{\begin{pmatrix} V_{ud} & V_{us} & V_{ub} \\ V_{cd} & V_{cs} & V_{cb} \\ V_{td} & V_{ts} & V_{tb} \end{pmatrix}}_{V_\mathrm{CKM}} \begin{pmatrix} d \\ s \\ b \end{pmatrix} \tag{2.20}$$

When expressed in terms of mass eigenstates, the quark coupling to the W bosons becomes proportional to the CKM-matrix elements. Thus, the probability of a flavor transition from the i-th generation up-type quark to the j-th generation down-type quark is determined by $|V_{ij}|^2$ and flavor-changing charged currents do occur at tree level. The field of particle physics concerned with precise measurements of quark-flavor transitions is commonly referred to as **flavor physics**.

The CKM-matrix elements are fundamental parameters of the SM and must be measured experimentally. Their magnitudes are determined to be [17]:

$$|V_\mathrm{CKM}| = \begin{pmatrix} 0.97373 \pm 0.00031 & 0.2243 \pm 0.0008 & 0.00382 \pm 0.00020 \\ 0.221 \pm 0.004 & 0.975 \pm 0.006 & 0.0408 \pm 0.0014 \\ 0.0086 \pm 0.0002 & 0.0415 \pm 0.0009 & 1.014 \pm 0.029 \end{pmatrix} \tag{2.21}$$

This configuration reveals a clear hierarchy, resulting in what is known as CKM suppression of flavor transitions between different quark generations. The CKM matrix is required to be unitary in the absence of any unknown particles fields, making it a stringent test of the SM's consistency. One of the off-diagonal unitary conditions, referred to as the **unitary triangle** is particularly suitable for these tests due to similar orders of magnitude in its different terms:

$$V_{ud}V_{ub}^* + V_{td}V_{tb}^* + V_{cd}V_{cb}^* = 0 \tag{2.22}$$

It can be visualized as a triangle in the complex plane, typically represented after normalization by $V_{cd}V_{cb}^*$, so that its vertices are located at $(0, 0)$, $(0, 1)$, and $(\bar{\rho}, \bar{\eta})$. Here, $\bar{\rho}, \bar{\eta}$ are parameters from the Wolfenstein parameterization [42]). Testing the closure of this triangle is achieved through various approaches that combine available experimental data, as outlined in more detail in References [43, 44].

This results in one of the most iconic plots in the field of flavor physics, as illustrated in Figure 2.4.

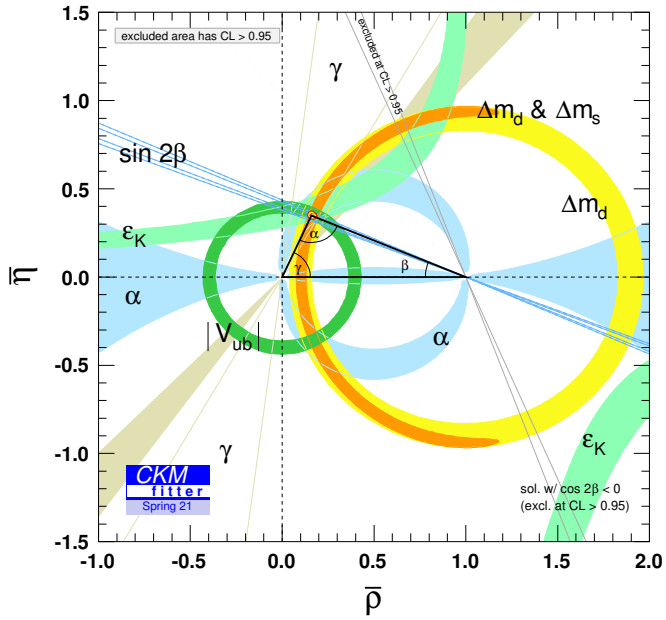

Figure 2.4: Experimental constraints on the unitary triangle are shown, as provided by the CKMfitter group [45]. Numerous different experimental measurements serve as input and are tested for consistency.

Sections 2.2 and 2.3 introduce additional powerful methods for scrutinizing the SM, leading to a similarly iconic plot (see Sec. 2.3.1). To provide context, Section 2.1.4 first presents reasons why these tests are imperative.

2.1.4 Shortcomings of the Standard Model

Despite the Standard Model's outstanding success in accurately describing microscopic processes with remarkable precision, it is evident that the SM must be incomplete.

This incompleteness becomes particularly obvious at cosmic scales, where gravity, the dominating force at these scales, is not accounted for within the SM framework at all. Instead, Einstein's theory of general relativity, formulated in 1915 [46], remains the most recent and successful theory of gravity, despite its incompatibility with the QFT framework of the SM [47]. While gravity has negligible effects at the energies that are currently explored in experimental particle physics, its significance becomes pronounced latest at the Planck scale of approximately 10^{19} GeV, necessitating the development of a coherent theory of quantum gravity.

In addition, astronomical observations have unveiled that only approximately 5% of the universe's energy is composed of baryonic matter [48], which is described by the SM. In contrast, about 26.5% is constituted by dark matter, which is observed solely through gravitational interaction. Potential dark matter candidates are as-yet-undiscovered particles that do not, or only extremely loosely, engage with the electromagnetic and strong force. The absence of observations of weakly interacting massive

particles (WIMPs) around their anticipated energy scale of $\mathcal{O}(1\,\text{TeV})$ [49, 50], which would account for the universe's dark matter abundance through thermal production with weak interaction cross-sections, has prompted expanded exploration of alternative dark matter candidates and solutions. These include scenarios like axions [51–54], sterile neutrinos [55–57], primordial black holes [58], or more exotic theories as modified Newtonian dynamics [59]. The remaining 68.5% of the universe's energy is attributed to dark energy with unknown origin, which is accountable for the observed accelerated expansion of the universe.

Furthermore, a significant matter-antimatter asymmetry characterizes our universe, substantiated not only by our existence but also through measurements of the relative abundance of light chemical elements in the early universe after nucleosynthesis [48, 60]. This contradicts the expected equal production of matter and antimatter after the Big Bang. Such an asymmetry can originate from scenarios that deviate from thermal equilibrium, such as potentially during the moment of electroweak symmetry breaking [61, 62] (see Sec. 2.1.3). Moreover, it necessitates baryon-number violating processes, like hypothetical sphalerons [63], and the violation of charge-parity ($\mathcal{CP}$) symmetry [64]. The CKM matrix, as discussed in Section 2.1.3, introduces a non-trivial complex phase due to its three-dimensionality, resulting in $\mathcal{CP}$ violation within the SM framework. Its size is directly related to the area of the unitary triangle depicted in Figure 2.4. However, it falls short by several orders of magnitude in explaining the observed asymmetry in the universe [65, 66]. Consequently, the existence of additional $\mathcal{CP}$-violating processes is indispensable.

In the SM, neutrinos are massless, as mentioned in Section 2.1.1. However, the observation of neutrino oscillations has established the existence of neutrino masses [67–69]. If these masses were acquired through the same Higgs mechanism as for other fermions (see Sec. 2.1.3), it would necessitate the existence of right-chiral neutrinos. These right-chiral neutrinos would be singlets under all of the SM's gauge transformations, implying that their properties are not protected by any intrinsic symmetry. This fact, along with the substantial difference in required Yukawa-coupling strengths of $y_\nu \lesssim \mathcal{O}(10^{-13})$ compared to $y_e = \mathcal{O}(10^{-6})$ or $y_t = \mathcal{O}(1)$ suggests alternative mechanisms for neutrino mass generation [70, 71]. The interplay of this issue with other unresolved questions in particle physics, as outlined above, is particularly intriguing.

In addition to the problems mentioned so far, several properties of the SM are unsatisfactory from a theoretical perspective.

Even without considering the neutrino sector, the SM involves 18 free parameters that are not predicted by theory. These include three force coupling constants, two parameters defining the Higgs mechanism, nine different Yukawa couplings determining the particle masses, three CKM angles, and the $\mathcal{CP}$-violating phase in V_{CKM}. Additionally, there is the possibility of a $\mathcal{CP}$-violating parameter in QCD, denoted as θ_{QCD}, which is experimentally measured to be indistinguishable from zero. It is desirable to seek more fundamental explanations for these parameters within more comprehensive theories.

Following the successful unification of the electromagnetic and weak forces, there is a compelling notion that all quantum field theories may arise from a more fundamental symmetry that is spontaneously broken. Such candidates for grand unified theories, like $\text{SO}(10) \rightarrow \cdots \rightarrow \text{SU}(3)_\text{C} \times \text{SU}(2)_\text{L} \times \text{U}(1)_\text{Y}$ [72], not only naturally require the existence of right-chiral neutrinos but also introduce leptoquarks, particles with quark and lepton properties. Leptoquarks will be further explored in Section 2.3. The existence of a connection between fundamental forces gains support from the

observation that quantum anomalies are avoided solely because of specific relationships between the electric charges of quarks and the number of different colors in the strong interaction, despite the theoretical independence of these parameters. These grand unified theories are typically situated at energy scales around 10^{16} GeV, which is inferred from the running of interaction coupling strengths. It is not unfounded to speculate that quantum gravity, expected to become significant latest at Planck scale of 10^{19} GeV, might also play a role in such a unification.

Lastly, the Higgs mass lacks protection from symmetries due to the scalar nature of the Higgs boson. This implies that quantum corrections would naturally drive its value up to the highest existing energy scales. In essence, the presence of any hypothetical new particles at energy scales such as 10^{16} GeV - 10^{19} GeV, that interact directly or indirectly with the Higgs, would render the relatively low Higgs mass highly unnatural [73, 74].

Several extensions of the SM have been proposed to address some of the presented caveats. Many of these extensions, including the extensively studied supersymmetry [75], predict an extended Higgs sector, such as a two-Higgs-doublet model (2HDM) [76]. These extended Higgs sectors not only provide possible additional $C\mathcal{P}$-violating mechanisms to address the matter-antimatter asymmetry, they also introduce charged Higgs bosons, which will be discussed in Section 2.3.

2.2 Semileptonic B-meson decays

The Standard Model can be rigorously examined in a relatively model-independent manner by comparing precise experimental measurements of SM processes to their theoretical prediction. Depending on the precision of both, experiment measurements and theoretical calculations, it is possible to derive constraints on potential unknown interactions. These constraints can often surpass the limits of direct search experiments by a significant margin [77].

Usually, electroweak interactions can be precisely calculated using perturbation theory, allowing for accurate theoretical predictions. However, for the strong interactions, perturbation theory is inadequate beyond hard scattering processes, making theory predictions involving hadronization processes challenging. Semileptonic B-meson decays encompass both, as elaborated in the following sections.

2.2.1 Fundamental characteristics

The B meson is an intriguing particle for investigation. It consists of a third-generation bottom quark and a first-generation up or down quark, featuring a clear mass hierarchy between them. Additionally, the b-quark mass $m_b \approx 4.2\,\text{GeV}$ [17] is significantly larger than the QCD scale of $\Lambda_{\text{QCD}} \approx 200$ - 300 MeV, resulting in the b quark's velocity being minimally influenced by QCD dynamics. These properties allow for calculations within the framework of heavy quark effective theories (HQETs). HQETs reorganize the effective Lagrangian using an approach similar to perturbation theory, expressing it in inverse powers of m_Q, where Q represents a heavy quark, either b or c. In the heavy quark limit $m_Q \to \infty$, the effective Lagrangian becomes independent of the heavy quark's mass, flavor, or spin, essentially treating it as a static source of the color field. Consequently, the dynamics of the meson primarily involve interactions between the light quark and this stationary potential. Corrections to these simplifications are suppressed by $O(1/m_Q)$.

This work is centered around the study of semileptonic B-meson decays, $B \to Xl\nu$. They are initiated by the underlying parton decay $b \to c$ or, rarely, $b \to u$. In these processes, the B meson decays into either a charged electron, muon, or τ lepton, along with a neutrino ν and a hadronic component denoted as X. As illustrated in Figure 2.5, these decays occur at tree-level, making them relatively frequent. Furthermore, leptons generate distinct signatures in particle detectors (see Chap. 3), increasing experimental sensitivity. Additionally, semileptonic B-meson decays are theoretically better understood than purely hadronic decays for reasons elaborated below, which renders them highly effective for probing the SM and for measuring the fundamental CKM-matrix elements V_{qb}.

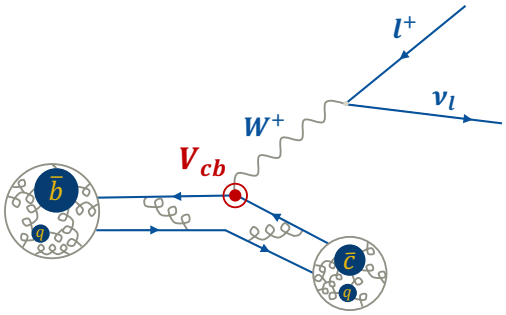

Figure 2.5: A tree-level $B \to X_c l\nu$ decay is illustrated as described in the SM.

In semileptonic $B \to Xl\nu$ decays, the four-momentum transfer to the leptonic system is significantly smaller than the mass of the W boson. Consequently, the dynamics of the W boson is negligible, leading to the effective Hamiltonian:

$$H_{\text{eff}} = V_{qb} \left(\overline{q}\gamma^{\mu}(1-\gamma^5)b\right) \frac{4G_{\text{F}}}{\sqrt{2}} \left(\bar{l}\gamma_{\mu}(1-\gamma^5)\nu\right) + \text{h.c.}, \quad \text{with} \quad q = \{u, c\}. \tag{2.23}$$

Here, the Fermi constant $\frac{G_{\text{F}}}{\sqrt{2}} = \frac{g_{\text{w}}^2}{8m_W^2}$ represents the effective coupling strength of weak decays in the low-energy limit. As leptons do not participate in the strong interaction, the equation can be factorized into a leptonic and a hadronic current. The leptonic part is governed by the weak interaction, making it straightforward to calculate via perturbation theory. In constrast, the hadronic current involves non-perturbative strong interactions resulting from the heavy quark interacting with the light degrees of freedom inside the hadrons.

Both theoretically and experimentally, two complementary approaches are employed to study these decays. In the exclusive approach, a specific decay mode like $B \to Dl\nu$ or $B \to D^* l\nu$ is selected, and different theoretical considerations are applied depending on the hadron's properties. This is briefly discussed in the following section.

In constrast, the inclusive approach does not specify the hadronic system, encompassing all of the exclusive decays. Inclusive theory calculations take advantage of the fact that the total decay rate can be expressed as an expansion involving a manageable number of non-perturbative terms, referred to as the heavy quark expansion (HQE) [78].

2.2.2 Decay kinematics and parameterization

Since $V_{cb} \gg V_{ub}$, the large majority of $B \to X l\nu$ decays ($l = e, \mu, \tau$) are governed by the $b \to c$ quark transition, resulting in a hadronic final state containing a c quark, denoted as X_c. The complexity of the decay kinematics varies depending on the properties of the X_c meson involved.

For the most prevalent $B \to D^{(*)} l\nu$ decays, the decay amplitude is proportional to the following matrix element, which is derived from Equation (2.23):

$$\mathcal{M}(B \to D^{(*)} l\nu) = -V_{cb}\langle D^{(*)}|\bar{c}\gamma^{\mu}(1-\gamma^5)b|B\rangle \frac{iG_{\mathrm{F}}}{\sqrt{2}}\left(\bar{l}\gamma_{\mu}(1-\gamma^5)\nu\right) \tag{2.24}$$

The description of non-perturbative hadron transitions relies on form factors. They are functions dependent on the squared transferred four-momentum q^2, with $q^{\mu} = P_l^{\mu} + P_{\nu}^{\mu} = P_B^{\mu} - P_{X_c}^{\mu}$, which correlates with the mass of the virtual W boson.[1] Various approaches exist for parameterizing these form-factor functions, which are discussed in the following.

In the context of the decay involving the pseudoscalar B meson transitioning to a pseudoscalar D meson, the hadronic current can be characterized in terms of the vector $f_+(q^2)$ and scalar $f_0(q^2)$ form factors, yielding the decay rate:

$$\frac{\mathrm{d}\Gamma}{\mathrm{d}q^2} = \frac{G_{\mathrm{F}}^2|V_{cb}|^2}{24\pi^3}|\vec{p}_D|^3\left(1-\frac{m_l^2}{q^2}\right)\left[f_+^2(q^2)\left(1+\frac{m_l^2}{2q^2}\right)+\frac{3}{2}\frac{m_l^2}{q^2}\left(\frac{m_B^2-m_D^2}{2m_B|\vec{p}_D|}\right)f_0^2(q^2)\right]. \tag{2.25}$$

For decays involving electrons or muons (denoted as $\ell = e, \mu$), the approximation $m_\ell \approx 0\,\mathrm{GeV}$ is suitable, leading to the differential rate of $B \to D\ell\nu$ becoming independent of $f_0(q^2)$.

For $B \to D^* l\nu$, which involves the vector meson D^*, the description is more complex, leading to four form-factor functions instead of two. The increased complexity of the decay kinematics is fully characterized by four independent kinematic variables, which also take into account the D^* meson's daughter particles ($D^* \to D\pi/\to D\gamma$). These variables include the momentum transfer q^2 or the related recoil parameter $w = (m_B^2 + m_{D^*}^2 - q^2)/(2m_B m_{D^*})$, along with three angular variables: the angle between lepton and virtual W boson θ_l, the angle between D and D^* meson θ_V, and the angle between the decay planes of the W boson and D^* meson χ.

The Caprini-Lellouch-Neubert (CLN) parameterization [79], leverages the spin-flavor symmetry of HQET to reduce the number of free parameters in the form factors. In this parameterization, the form factors are expressed as expansions in the complex variable z, which is derived from the momentum transfer q^2. Additionally, constraints from unitarity are applied. For $B \to D\ell\nu$ decays with $m_\ell \approx 0\,\mathrm{GeV}$, this results in two free parameters: the form factor at zero recoil, $\mathcal{G}(w(q^2_{\mathrm{max}}) = 1)$, and the linear slope parameter ρ^2. The latter parameter is determined experimentally from the differential q^2 spectrum, while regardless of the chosen form-factor parameterization and decay, input from lattice QCD theory predictions [80–82] is indispensable in order to derive the form-factor normalization (here $\mathcal{G}(1)$) to determine CKM-matrix elements. In the case of $B \to D^*\ell\nu$ and $m_\ell \approx 0\,\mathrm{GeV}$, four form-factor parameters are derived from the differential spectrum of the four characteristic decay variables described above. For decays involving τ leptons, the lepton mass becomes non-negligible,

[1] In this thesis, four-momenta are represented by uppercase letters, P, to differentiate them from the absolute values of three-momenta, denoted as lowercase $p \equiv |\vec{p}|$. However, for the squared transferred four-momentum q^2, the lowercase letter is employed in alignment with common literature.

introducing an additional parameter for both $B \to D\tau\nu$ and $B \to D^*\tau\nu$.

A more general parameterization is the Boyd-Grinstein-Lebed (BGL) parameterization [83]. This approach relies solely on QCD dispersion relations. The form factors in the BGL parameterization are expressed as a power series in z and are proportional to Blaschke factors, containing the B_c or B_c^* poles. The truncation order of the power series, and thus the number of independent parameters, can, for example, be determined on data using the nested hypothesis test [84]. Like in other parameterizations, these parameters must be determined through fits to experimental data, with additional input from lattice QCD at zero recoil.

More recently, the Bernlochner-Ligeti-Papucci-Robinson-Xiong-Prim (BLPRXP) parameterization [85] was proposed. This parameterization adopts a supplemental power counting scheme for HQET, which is based on counting insertions of the transverse residual momentum within HQET correlators, referred to as the residual expansion. What sets this approach apart is the independence from model-dependent calculations like QCD sum rules or light-cone sum rules. The authors argue that higher-order terms within this power counting may be naturally suppressed, and that adopting this parameterization can result in significant simplifications of the second-order power corrections in HQET. Furthermore, in Reference [85], all the form-factor parameters required for characterizing $B \to D^{(*)}\ell\nu$ and $B \to D^{(*)}\tau\nu$ decays are extracted simultaneously, ensuring a coherent treatment of semileptonic decays into light leptons and τ leptons.

An additional significant contribution of the inclusive $B \to X_c l\nu$ decays arises from orbital excitations of the X_c mesons, specifically the four $1P$ states with orbital angular momentum $L = 1$ in the non-relativistic quark model. The D_1 and D_2^* state, with subscripts indicating their total spin J, exhibit relatively narrow widths of approximately 30 MeV. Additionally, there are two broader resonances with widths of a few hundred MeV, known as the D_0^* and the D_1'. Collectively, these four states are summarized as D^{**}.

The decay kinematics of these states were initially studied by Leibovich, Ligeti, Stewart, and Wise (LLSW) [86, 87] within the HQET framework. In this model, the differential decay widths are expressed as functions of the recoil parameter and the angle between the lepton and charmed meson. A key observation is that certain $\Lambda_{\mathrm{QCD}}/m_{c,b}$ corrections to form factors at zero recoil are determined by the mass splittings of the (D, D^*), (D_0^*, D_1'), and (D_1, D_2^*) meson doublets. To reduce the number of free parameters, a linear shape is assumed for the unknown leading-order term[2] in the form-factor parameterization, and the form factors of the broad states are deduced from the narrow states' form-factor slope and normalization using quark-model predictions.

More recent investigations by Bernlochner, Ligeti, and Robinson (BLR) [88, 89] have aimed to mitigate model dependencies and assumptions in this parameterization, resulting in a more data-driven description of the decay kinematics. In this approach, the form-factor parameters for both narrow and broad D^{**} states are obtained through fits to experimental data independently, and several parameter-assumptions are generalized.

In comparison to the $1S$ states D and D^*, the experimental data for the D^{**} states remains relatively limited. This data limitation results in larger uncertainties in branching fraction and decay kinematics, particularly for the broad D^{**} states. A detailed discussion of these uncertainties is presented in Sections 3.4.3, 5.3.2, 5.3.3 and 8.1.2.

The $B \to X_u l\nu$ decays present a distinct and interesting topic within the field of semileptonic

[2] The leading-order Isgur-Wise function

B-meson decays, accompanied by both experimental and theoretical challenges. Unlike $B \to X_c l\nu$ decays, these events involve light hadronic final states and are theoretically described by various frameworks for inclusive decays [90–94]. Similarly to the description of $B \to D^{(*)} l\nu$ decays, exclusive B meson decays into light resonances, such as π, ρ, and ω mesons, are described using form-factor parameterizations as introduced, e.g., in References [95, 96]. Non-resonant decays into multiple hadronic final states play a more significant role, and their composition among existing light resonances is typically considered in hybrid models [97]. However, $B \to X_u l\nu$ decays experience strong CKM-suppression, resulting in significantly lower branching fractions compared to $B \to X_c l\nu$ decays, making their relevance limited in the context of this thesis.

2.3 Lepton universality

The coupling terms of charged leptons in the SM Lagrangian are given as:

$$\mathcal{L} \supset -\sum_{l=e,\mu,\tau} \overline{\Psi}_l \gamma^\mu \left[q A^{\mathrm{a}}_\mu + \frac{g_w}{2\sqrt{2}} \left(1-\gamma^5\right) W^\pm_\mu + \frac{g_{\mathrm{w}}}{2\cos\theta_{\mathrm{w}}} \left(T_3 - 2q\sin^2\theta_{\mathrm{w}} - \gamma^5 T_3\right) Z^0_\mu + \frac{y_l}{\sqrt{2}} h \right] \Psi_l \tag{2.26}$$

The electroweak gauge interactions are lepton-flavor independent, a symmetry referred to as *lepton universality*.[3] This symmetry has been experimentally validated to a high degree of precision ($O(1\,‰)$ to $O(1\%)$) in decays of $W^\pm$ and Z^0 bosons [98–110]. The coupling to the Higgs already violates global lepton universality, resulting in the different masses of the leptons. Therefore, lepton-universality tests primarily aim to examine the experimental agreement with theory predictions within the SM framework.

Numerous theoretical frameworks predict processes that introduce lepton-flavor dependent couplings, extending beyong the SM. One notable example is an extended Higgs sector featuring two Higgs doublets, a necessity in various beyond-the-SM scenarios. In this context, charged Higgs bosons $H^\pm$ emerge and directly establish charged currents with coupling strengths proportional to the distinct lepton masses at tree level [111]. These deviations from lepton universality would be particularly pronounced in B-meson decays involving τ leptons, making them a sensitive probe for such extensions.

Another intriguing theoretical avenue involves theories that unify QCD and electroweak interactions, introducing particles known as leptoquarks. Leptoquarks facilitate interactions between quarks and leptons and can give rise to lepton-specific couplings to the b quark. Such interactions could manifest as deviations in $B \to X l\nu$ decays [112], again increasing the sensitivity of these decays to new physical phenomena. Both of these processes are depicted in Figure 2.6. The magnitude of observed deviations from the SM-only predictions depends on the mass and coupling properties of these hypothetical intermediate particles.

Both in experimental measurements and theoretical calculations, precision is further enhanced when quantities are expressed as (branching-fraction) ratios of lepton flavors, as utilized in the two

[3] In the literature, the term *lepton-flavor universality* is also commonly used. However, some recent publications have favored a clearer distinction between measurements that probe the universality of the coupling (i.e., by looking for lepton universality violation (LUV)) and measurements that probe direct lepton-flavor violation (LFV) such as in decays like $Z^0 \to e\mu$. Therefore, this work follows the notation of lepton universality.

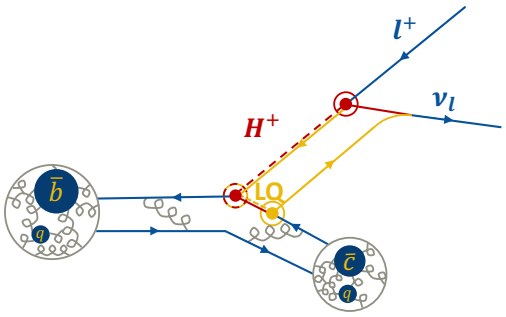

Figure 2.6: Lepton-universality violating processes are illustrated, that may alter the tree-level $B \to X_c l\nu$ decay. In the depicted scenario, a charged Higgs boson serves as the mediator particle, highlighted in red, while an alternative scenario involving an intermediate leptoquark (LQ) is represented in gold.

analyses presented in this thesis:

$$R(X_{e/\mu}) = \frac{\mathcal{B}(B \to Xe\nu)}{\mathcal{B}(B \to X\mu\nu)} \quad \text{and} \quad R(X_{\tau/\ell}) = \frac{\mathcal{B}(B \to X\tau\nu)}{\mathcal{B}(B \to X\ell\nu)} \quad \text{with} \quad \ell = \{e, \mu\}. \tag{2.27}$$

This enables the cancellation of experimental and theoretical uncertainties on common factors, such as those related to specific event-selection efficiencies (see Sec. 5.4) or the magnitude of $|V_{cb}|$.

In the past decade, several measurements investigating exclusive semileptonic B-meson decays have reported evidence of lepton-universality violation. Section 2.3.1 introduces various measurements indicating an enhanced $B \to D^{(*)}\tau\nu$ branching fraction. In Section 2.3.2, the experimental status of related inclusive measurements with b quarks is summarized, and the measurement of $R(X_{\tau/\ell})$ is motivated. Section 2.3.3 provides an overview of observations challenging light-lepton universality, motivating the measurement of $R(X_{e/\mu})$.

2.3.1 The $R(D^{(*)})$ anomaly

In a manner similar to Equation (2.27), exclusive branching-fraction ratios serve as a precise tool for investigating lepton universality:

$$R(D^{(*)}) = \frac{\mathcal{B}(B \to D^{(*)}\tau\nu)}{\mathcal{B}(B \to D^{(*)}\ell\nu)}. \tag{2.28}$$

These ratios have been quantified by various experiments at B factories (see Sec. 3.1), including *BABAR* [113, 114], Belle [115–118] and Belle II [119], as well as by LHCb [120, 121].

The *BABAR*, Belle and Belle II experiments use a relatively pure $B\bar{B}$ sample produced in $e^+e^- \to \Upsilon(4S) \to B\bar{B}$ decays [122]. One of the B mesons is reconstructed using specific tagging methods to determine its flavor. In References [113–117, 119], hadronic B-meson decay modes are employed (see Sec. 4.1), providing excellent kinematic information for the B mesons but resulting in very low efficiencies of $O(0.1\%)$. Semileptonic tagging, as used in Reference [118], reconstructs one B meson in semileptonic decays, yielding higher efficiencies of $O(1\%)$ but at the expense of less precise kinematic information due to the missing neutrino on the tag-side. Most analyses have measured leptonic signal τ-lepton decays into electrons and muons, $\tau \to \ell\nu\nu$. However, in the case of the

analysis summarized in References [116, 117], a different approach is taken by investigating hadronic final states $\tau \to \pi\nu$ and $\tau \to \rho\nu$, which provides the ability to probe polarization properties.

The LHCb experiment, operating in the forward direction of high-energy proton-proton collisions, operates within a significantly distinct experimental environment compared to the B factories. It is particularly well suited for the measurement of charged particle tracks. In Reference [120], a simultaneous determination of $R(D)$ and $R(D^*)$ is carried out by considering muonic τ-lepton decays, while Reference [121] extracted the ratio $\mathcal{B}(B^0 \to D^{*-}[\tau^+ \to \pi^+\pi^-\pi^+(\pi^0)\overline{\nu}_\tau]\nu_\tau)/\mathcal{B}(B^0 \to D^{*-}\pi^+\pi^-\pi^+)$, from which $R(D^*)$ can be derived.

The experimental findings are combined and compared to the SM predictions by the HFLAV collaboration [123] as illustrated in Figure 2.7.

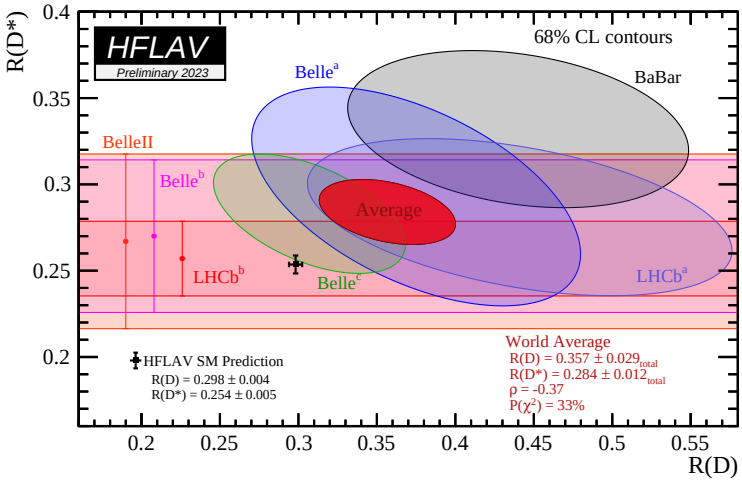

Figure 2.7: The experimental input from *BABAR* [113, 114], Belle a [115], b [116, 117], c [118], LHCb a [120], b [121] and Belle II [119] is combined by the HFLAV collaboration [123] and compared to the SM prediction. The experimental combination deviates from the SM prediction by $3.3\,\sigma$. Figure from Reference [123].

Despite the diverse experimental environments and analysis strategies, the different results exhibit a reasonable level of consistency with each other ($p(\chi^2) = 33\%$). When combined into an experimental world average, they reveal a significant deviation from the SM prediction by $3.3\,\sigma$ – commonly referred to as the $R(D^{(*)})$ anomaly.

The semileptonic branching fractions into light leptons are measured precisely and align with their SM expectation. Therefore, the observed excess in $R(D)$ and $R(D^*)$ indicates an elevated branching fraction of B mesons decaying into τ leptons.

Notably, the CMS collaboration recently reported excesses, each with a local significance of approximately three standard deviations, in two distinct analyses involving τ leptons [124, 125]. Both analyses possess sensitivity to leptoquarks with masses of $m_{\mathrm{LQ}} \gtrapprox \mathcal{O}(1\,\mathrm{TeV})$, which could enhance the coupling between b quarks and τ lepton. The concordance between these findings and their consistency with the $R(D^{(*)})$ anomaly is yet to be investigated.

2.3.2 Inclusive $b \to X\tau\nu$ measurements

Unlike exclusive measurements, which specifically select well-controlled D and D^* decay modes, inclusive measurements do not impose constraints on the particle composition of the decay's hadronic system. Therefore, the measurement of the inclusive ratio

$$R(X_{\tau/\ell}) = \frac{\mathcal{B}(B \to X\tau\nu)}{\mathcal{B}(B \to X\ell\nu)} \tag{2.29}$$

not only encompasses an unexplored fraction of 14 – 20 % of semitauonic B-meson decays (including D^{**}, non-resonant X_c, and X_u final states), but also includes a significant fraction of $B \to D^{(*)}\tau\nu$ and $B \to D^{(*)}\ell\nu$ decays that are excluded in $R(D^{(*)})$ analyses, as illustrated in Figure 2.8 for $B \to X\ell\nu$ decays.

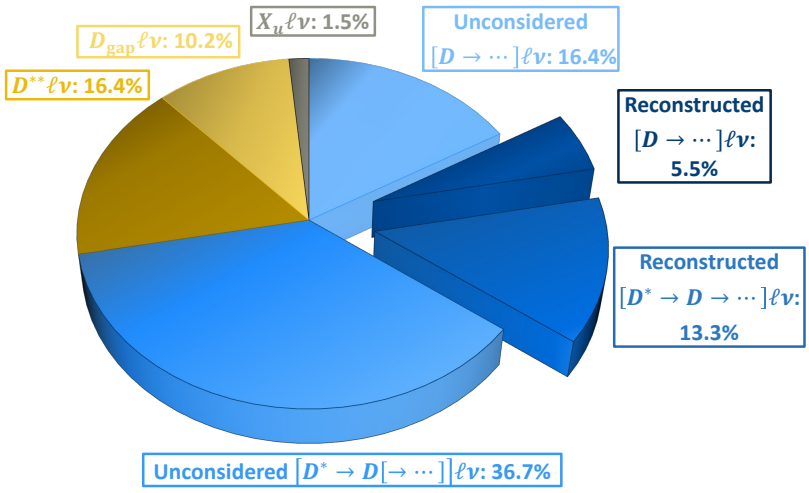

Figure 2.8: The composition of $B \to X\ell\nu$ decays ($\ell = e, \mu$) is depicted, highlighting the fraction of decays targeted in exclusive $R(D^{(*)})$ analyses. These modes, averaged from References [113–119], are represented by the dark blue displaced segments. Approximately a quarter of the $B \to D^{(*)}\ell\nu$ decays are intended for reconstruction in exclusive analyses, while the remaining $B \to D^{(*)}\ell\nu$ decays in lighter blue are not considered, primarily due to disregarded D-meson decay modes. The D^{**}, non-resonant D^{**}_{gap}, and X_u decays contribute only to an inclusive analysis, depicted in golden and gray.

The total statistical overlap of exclusive and inclusive analyses further reduces to approximately $\mathcal{O}(0.5\%)$ due to experimental selection efficiencies (see Sec. 8.2.3). This renders the inclusive approach independent, both statistically and in its sensitivity to systematic uncertainties, to exclusive measurements, making it a powerful and complementary test of the anomaly reported in Section 2.3.1.

For the parameter $R(X_{\tau/\ell})$, Reference [126] predicts $R(X_{\tau/e}) = 0.220 \pm 0.004$ and $R(X_{\tau/\mu}) = 0.221 \pm 0.004$, effectively replacing a prior calculation within the same theoretical framework that yielded $R(X_c) = 0.212 \pm 0.003$. [127]. Another theoretical calculation utilizing an alternative approach suggests $R(X_c) = 0.223 \pm 0.004$ [128], and by partly the same authors, $R(X_u) = 1/2.97$ [129]. These values can be combined with averaged branching-fraction values from [130].

$$\mathcal{B}(B \to X_c\ell\nu) = (10.65 \pm 0.16)\% \quad \text{and} \quad \mathcal{B}(B \to X_u\ell\nu) = (0.191 \pm 0.027)\% \tag{2.30}$$

to derive $R(X_{\tau/\ell}) = 0.225 \pm 0.006$. Taking the arithmetic average of the two $R(X_{\tau/\ell})$ predictions and their associated uncertainties yields

$$R(X_{\tau/\ell})_{\text{SM}} = 0.223 \pm 0.005 \tag{2.31}$$

and with $\mathcal{B}(B \to X\ell\nu) = (10.84 \pm 0.16)\%$ [130]

$$\mathcal{B}(B \to X\tau\nu)_{\text{SM}} = (2.41 \pm 0.06)\%. \tag{2.32}$$

Experimentally, inclusive B-meson decay measurements necessitate comprehensive angular coverage of the particle collisions and their decay products, as well as a precise understanding of the initial state conditions. Consequently, such measurements pose significant challenges for proton-proton collision experiments, making them widely recognized as uniquely suited to e^+e^- colliders.

The related decay branching fraction of an inclusive b-hadron admixture into τ leptons, $\mathcal{B}(\text{b-admix} \to X\tau\nu)$, has been measured using e^+e^- collisions at the Z^0 resonance at LEP by the L3 [131, 132], DELPHI [133], ALEPH [134], and OPAL [135] collaborations.

At LEP, b quarks are generated in pairs through the process $e^+e^- \to Z^0 \to b\bar{b}$. Subsequently, these b quarks undergo hadronization, resulting in a jet of particles each. This yields a distinct back-to-back event structure which is leveraged in the measurements to distinguish the daughters of the two b quarks. A multivariate tool is employed to identify a b-hadron signature within one of the jets allowing for the analysis of the other jet in terms of the signal signature. In this context, the selection process focuses exclusively on hadronically decaying τ leptons. The signal is extracted from the the missing energy distribution E_{miss}, which is calculated by subtracting the measured energy on the signal side from the beam energy. In these measurements, the primary sources of systematic uncertainties are related to the modeling of E_{miss} and the parameters associated with b-quark hadronization.

To facilitate a meaningful comparison of the LEP measurements with B-meson properties, for which both experimental and theoretical data are available, they must be corrected by the ratio of the B-meson lifetime and the average b-hadron lifetime at LEP $\tau_B/\tau_{b\text{-admix}} = 1.0075 \pm 0.0032$. In Figure 2.9, the corrected results are summarized, demonstrating alignment with the SM expectations for $\mathcal{B}(B \to X\tau\nu)$.

However, the experimental precision of the LEP results is insufficient to validate or falsify the findings outlined in the previous Section 2.3.1, as indicated in the same figure. Therefore, a dedicated measurement of $\mathcal{B}(B \to X\tau\nu)$ with B mesons, performed within the same experimental setup as the $R(D^{(*)})$ results, and considering the advancements made in B-meson physics over the last two decades, is desirable.

At Belle, such a measurement of $R(X_{\tau/\ell}) = \mathcal{B}(B \to X\tau\nu)/\mathcal{B}(B \to X\ell\nu)$ was accomplished as part of a PhD thesis [136]. In this study, the analysis utilized hadronic tagging, and the signal was extracted through a two-dimensional fit involving the lepton momentum in the B_{sig} frame, denoted p_ℓ^B, and the missing mass squared M^2_{miss}, which is a complex quantity discussed in more detail in Section 7.2.2. Notably, the M^2_{miss} distribution is exceptionally sensitive to a multitude of distinct detector-and-simulation based effects, all of which have the potential to be inaccurately modeled. Indeed, significant mismodeling of this quantity was observed in signal-depleted sidebands, and the issue could not be fully resolved within the scope of the thesis.

Consequently, the result was not approved by the Belle collaboration to be officially published in a peer-reviewed journal, and therefore, it should be considered with caution. Nonetheless, its suggested

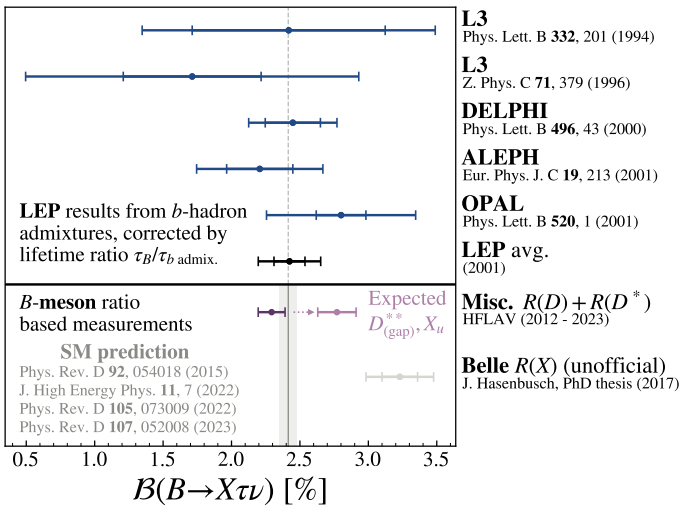

Figure 2.9: The individual lifetime-corrected LEP results of $\mathcal{B}(\text{b-admix} \to X\tau\nu)$ (blue, [131–135]) and their combination (black) are presented and compared to the sum of suggested $\mathcal{B}(B \to D^{(*)}\tau\nu)$ based on the exclusive $R(D^{(*)})$ findings (dark purple, [113–121, 123]). The latter already approaches saturation with the SM expectation of $\mathcal{B}(B \to X\tau\nu)$, leaving very little room for anticipated additional decays in $B \to X\tau\nu$. An extrapolation of this sum to account for remaining components of the full $X\tau\nu$ branching fraction is presented (light purple). Additionally, an unofficial $R(X_{\tau/\ell})$ measurement from a PhD thesis is included (light gray, [136]) and all these results are compared against the SM predictions of $\mathcal{B}(B \to X\tau\nu)$ (gray band, [126, 128–130]).

$\mathcal{B}(B \to X\tau\nu)$ value is presented in Figure 2.9. Similarly to the B-factory based $R(D^{(*)})$ results, it indicates a substantial increase in the production of τ leptons compared to their lighter counterparts.

The first successful, collaboration-approved B-meson-based measurement of $R(X_{\tau/\ell})$ is presented in this thesis and published in Reference [2].

2.3.3 Tests of light-lepton universality with B mesons

Beyond the intriguing results related to τ leptons that challenge lepton universality, evidence for lepton-universality violating processes has also been observed in measurements comparing electrons to muons in semileptonic B-meson decays.

An asymmetry in the angular distributions of electrons and muons originating from $B^0 \to D^{*-}\ell^+\nu$ decays has been reported in Reference [137], reaching a significance of four standard deviations ($4\,\sigma$). This finding is based on a reinterpretation of a measurement conducted by the Belle collaboration [138], which aimed to extract the CKM-matrix element V_{cb} by examining the distributions of w, θ_ℓ, θ_V, and χ (see Sec. 2.2.2). In the context of this reinterpretation, the aforementioned angles were compared between electrons and muons, revealing a notable deviation from SM expectations. This finding not only prompted more comprehensive investigations in the context of light-lepton universality in B-meson decays as presented in this thesis. A series of exclusive analyses by Belle and Belle II focused on the angular characteristics of $B \to D^*\ell\nu$ events. Their results, published shortly after the publication of this work's result related to electron-muon universality [1], do not find evidence for lepton-universality violation (LUV) in angular parameters within the limits of their precision [139–142]. Comprehensive investigations into the potential violation of light-lepton universality in $B \to X\ell\nu$

decays continue to be desirable.

Furthermore, in 2022, the LHCb collaboration reported a measurement of the ratio

$$R_{K^+}(1.1 < q^2 < 6.0\,\mathrm{GeV}^2) = \frac{\mathcal{B}(B^+ \to K^+ e^+ e^-)}{\mathcal{B}(B^+ \to K^+ \mu^+ \mu^-)} = 0.846^{+0.042+0.013}_{-0.039-0.012}. \tag{2.33}$$

This result deviates from the SM expectation of unity by 3.1 standard deviations [143]. The $b \to s\ell^+\ell^-$ transition, which is a loop process in the SM, is particularly sensitive to physics beyond the SM, such as leptoquarks which enable this transition already at tree-level. However, in an extended analysis that covered a wider q^2 range and included the related ratio $R_{K^0_S} = \mathcal{B}(B^0 \to K^0_S e^+ e^-)/\mathcal{B}(B^0 \to K^0_S \mu^+ \mu^-)$, LHCb updated their previous measurement with a new value that is consistent with the SM prediction [144, 145].[4]

Nevertheless, decays involving $b \to s\ell^+\ell^-$ transitions remain very interesting for probing LUV. Multiple analyses have measured the angular distributions for muons in such decays in several different hadronic modes [147–153], consistently revealing deviations from the anticipated SM distribution. Additionally, Belle II recently reported notable evidence of an elevated branching fraction in the related decay $B^+ \to K^+ \nu\bar{\nu}$, exhibiting a deviation from SM expectation at a level of 2.7 standard deviations [154].

In summary, the universality of electrons and muons has been questioned in various semileptonic B-meson decays, prompting a more comprehensive examination involving tree-level processes within the scope of this thesis. This analysis bridges an experimental gap by presenting the first measurement of the ratio of inclusive, semileptonic B meson decay rates, published in Reference [1]:

$$R(X_{e/\mu}) = \frac{\mathcal{B}(B \to X e \nu)}{\mathcal{B}(B \to X \mu \nu)}. \tag{2.34}$$

As documented in Reference [126], the SM calculation for $R(X_{e/\mu})$ results in the value

$$R(X_{e/\mu})_{\mathrm{SM}} = 1.006 \pm 0.001. \tag{2.35}$$

Prior to this work, the exclusive branching fraction ratio

$$R(D^{*-}_{e/\mu}) = \frac{B^0 \to D^{*-} e^+ \nu}{B^0 \to D^{*-} \mu^+ \nu} = 1.01 \pm 0.01 \pm 0.03 \tag{2.36}$$

represented the sole measurement of its kind [138]. This measurement was conducted within the same analysis that served as input for the angular reinterpretation discussed above. While for inclusive decays, comparisons of kinematic distribution shapes in $B \to X_c \ell \nu$ decays have been made for electrons and muons [155], an inclusive, branching fraction-based test of light-lepton universality has not yet been performed before.

[4] The updated measurement was published on the same day as the $R(X_{e/\mu})$ analysis presented in this thesis and was featured in the same synopsis within the Physics Magazine [146].

CHAPTER 3

Experimental setup

In the scope of this thesis, data collected at the Belle II experiment is analyzed, which is situated at KEK in Tsukuba, Japan, and started full data taking in 2019. It is operated by the Belle II collaboration, which consists of 1170 scientists from 27 different countries at the moment of writing.

The primary objectives of Belle II encompass precision measurements at the intensity frontier, especially with B mesons but also with charmed mesons, to refine the knowledge about the fundamental CKM parameters and to search for physical phenomena beyond the SM. Additionally, searches for light dark matter, hadron spectroscopy and precision measurements with τ leptons are part of Belle II's competitive program beyond flavor physics [156, 157].

The pioneers of precision measurements involving B mesons were the CLEO [158] and ARGUS [159] experiments, which operated at symmetric e^+e^- collision energies starting 1979 and 1982. Their work laid the foundation for subsequent experiments, particularly the asymmetric-energy B-physics experiments *BABAR* [160] and Belle [161], that mainly operated in the 2000s. Belle II, in turn, is the direct successor of Belle. Additionally, since its launch in 2010, the LHCb experiment [162], based at the Large Hadron Collider (LHC) at CERN in Switzerland, is also specialized in precise b-hadron measurements, albeit in the context of proton-proton collisions.

In Section 3.1, the SuperKEKB particle accelerator and collider [163] is introduced. Surrounding its interaction region, the Belle II detector [164] is located, which is presented briefly in Section 3.2. Section 3.3 provides a brief overview of the algorithms employed for final-state particle reconstruction at Belle II. Finally, Section 3.4 elaborates on the experimental and simulated data samples utilized in this thesis.

3.1 SuperKEKB accelerator

The SuperKEKB accelerator is an asymmetric electron-positron collider primarily operating at a center-of-mass (c. m.) energy corresponding to the $\Upsilon(4S)$ mass, $\sqrt{s} = m_{\Upsilon(4S)} = 10.58\,\text{GeV}$. It serves as the successor to the KEKB accelerator, which was located at the same site and operated at similar energies [165, 166].

Due to the resonant production of $\Upsilon(4S)$ mesons, an excited $b\bar{b}$ state that almost exclusively decays into B^+B^- or $B^0\overline{B}^0$ pairs, the relative production of B mesons via the process $e^+e^- \to \Upsilon(4S) \to B\overline{B}$ is enhanced by a factor of three to four compared to non-resonant production at higher energies.

Consequently, such experiments are commonly referred to as B factories. This section provides a brief introduction to the essentials of SuperKEKB, with more detailed information available in References [156, 163].

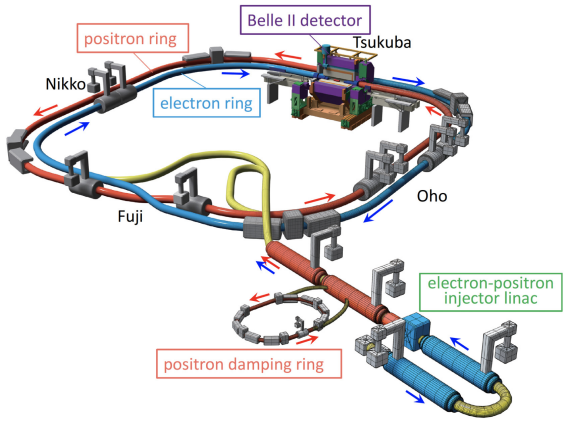

Figure 3.1: The SuperKEKB accelerator is illustrated schematically. Figure from Reference [163].

In Figure 3.1, a schematic view of SuperKEKB is provided. Initially, free electrons are generated using a photo-cathode high-current radio-frequency gun and are subsequently introduced into a linear accelerator. A collision of parts of the electron beam with a 14 mm thick tungsten target yields the production of positrons. These positrons are separated through a magnetic field and subsequently undergo controlled manipulation within the positron dumping ring to minimize their beam emittance. Following this, they are injected into the remaining section of the linear accelerator. In this linear accelerator segment, both electrons and positrons are accelerated to energies of 7 GeV and 4 GeV, respectively, before they are injected into the electron or positron ring. Ultimately, the electron and positron beams are brought into collision at the *interaction point* (IP), which is embedded by the Belle II detector.

The mass of the $\Upsilon(4S)$ meson is situated just above threshold for $B\bar{B}$ production, causing the B mesons to be generated nearly at rest in the c. m. system. Consequently, they would have a very limited flight length before undergoing decays, so that a separation between the IP and the B-meson decay vertices would experimentally become impossible. This challenge is overcome by the mentioned asymmetric electron and positron beam energies of 7 GeV and 4 GeV, respectively. This results in a Lorenz boost of $\beta\gamma = 0.28$ for the c. m. system relative to the laboratory frame, resulting in an average B-meson flight length of 130 µm. The ability to spatially separate the IP and the two B-meson decay vertices is particularly important for studies of $C\mathcal{P}$-violating events involving B mesons. These events were initially observed by the previous experiments Belle and *BABAR*, and the KEKB accelerator, the predecessor to SuperKEKB, operated at an even higher boost for this purpose.

The achievable instantaneous luminosity $\mathcal{L}$ is one of the key performance indicators of a particle accelerator. Luminosity refers to the number of interactions between beam particles per unit of time and area and is proportional to the number of particles per bunch, the number of bunches, and their collision frequency. Currently, the official target luminosity for SuperKEKB is set at $6 \times 10^{35}\ \mathrm{cm}^{-2}\mathrm{s}^{-1}$, representing a 30-fold increase compared to KEKB. This enhanced luminosity is expected to be achieved through the implementation of the *nano-beam* collision scheme, proposed in Reference [167]. This scheme focuses on squeezing the vertical beta function by minimizing the longitudinal size of the

beam overlap at the IP. This overlap is characterized by a relatively large crossing angle between the beams and an extremely small horizontal beam size. These design modifications are anticipated to reduce the vertical beta function by a factor of up to 15 – 20 when compared to KEKB. Furthermore, the beam currents are planned to be doubled. With this design, SuperKEKB has already surpassed the previous world record for instantaneous luminosity by more than twice its value, achieving $\mathcal{L} = 4.71 \times 10^{34}\,\mathrm{cm}^{-2}\mathrm{s}^{-1}$ [168].

3.2 Belle II detector

The Belle II detector, depicted in Figure 3.2, is a general-purpose detector and consists of several nested subsystems arranged in a closed cylinder structure around the IP. The cylindrical portion is referred to as the barrel, which is closed by the forward and backward endcaps. It is designed to provide necessary information to identify particles produced in the e^+e^- collision and to measure their energies and momenta over a broad range, spanning from tens of MeV to several GeV. The different subsystems, most of which are embedded in a uniform 1.5 T magnetic field generated by a superconducting solenoid, are introduced briefly in the following sections, while more extensive details are available in Reference [164].

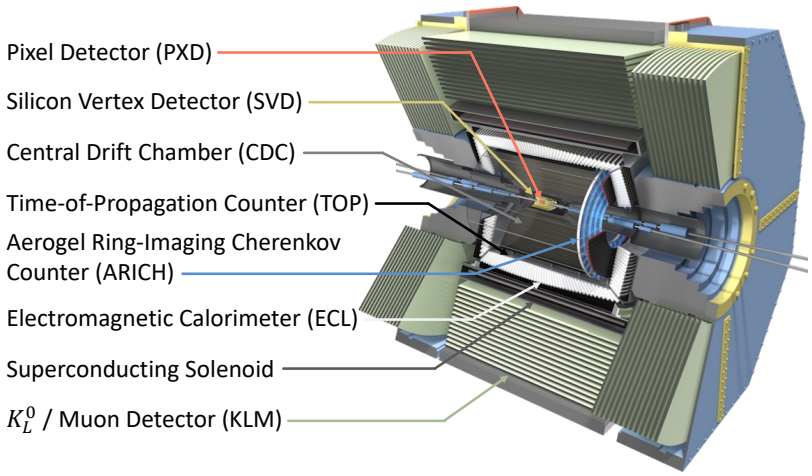

Figure 3.2: The Belle II detector is illustrated schematically. Figure adapted from Reference [169].

Belle II is equipped with several upgrades compared to its predecessor, the Belle detector [161]. These improvements allow the Belle II detector to maintain the same level of performance as Belle while operating in an environment characterized by considerably higher event rates and substantially increased radiation background levels.

The Belle II coordinate system is established as a right-handed system, originating at the IP. In this system, the z-axis extends in the direction of the electron beam, the y-axis points vertically upward, and the x-axis extends along the radial direction towards the outside of the accelerator ring. Considering the cylindrical structure of the detector, it is advantageous to employ cylindrical coordinates (r, ϕ, z), with $z = r\cos\theta$. Within this system, the polar angle θ quantifies the angle relative to to the z-axis and is directly related to various subdetector-acceptance regions. The radius r provides the distance to the IP within the x-y plane, and the detector's symmetry around the beam pipe renders it independent of

the azimuthal angle ϕ.

3.2.1 Vertexing and tracking system

The innermost detector systems have the primary task of measuring the charged particle trajectories, commonly referred to as tracks. Due to the uniform 1.5 T magnetic field, the charged particle trajectories are curved, enabling the determination of particle charges and momenta. Additionally, these tracks are extrapolated to identify the common point of origin of multiple particles, known as the decay vertex of their parent particle.

The precision achievable for primary particle vertices is limited by the distance between the IP and the first particle detection layers, as well as the resolution of the initial detector [170]. Consequently, the innermost detection layers are positioned as closely as feasible to the particle beams and their IP, which are enclosed by a double-walled beryllium beam pipe with an outer radius of 12 mm. This section introduces the three distinct subdetectors specializing in tracking and vertexing at Belle II.

Pixel Detector (PXD)

Compared to its predecessor, Belle II features a new innermost detector, the Pixel Detector (PXD) [171], which significantly improves the spatial resolution in the determination of particle vertex positions. The PXD is designed to incorporate two layers of silicon-pixel sensors positioned at radii of 14 mm and 22 mm, thereby covering an angular range of $\theta = 17°$ to $\theta = 150°$. The layers are composed of 8 and 12 ladders, respectively, with each ladder consisting two sensor modules with 768×250 pixel sensors each (see Fig. 3.3(a)). This arrangement results in a significantly larger number of channels when compared to silicon-strip detectors and comparably smaller occupancy levels. This is particularly advantageous when dealing with the substantial background rates near the beam pipe, as backgrounds increase inversely with the square of the radial distance. Due to a production delay, the configuration of the outer layer comprised only two ladders in the data-taking period relevant for this thesis. The complete installation of the PXD took place during the first long shutdown period from 2022 to 2023.

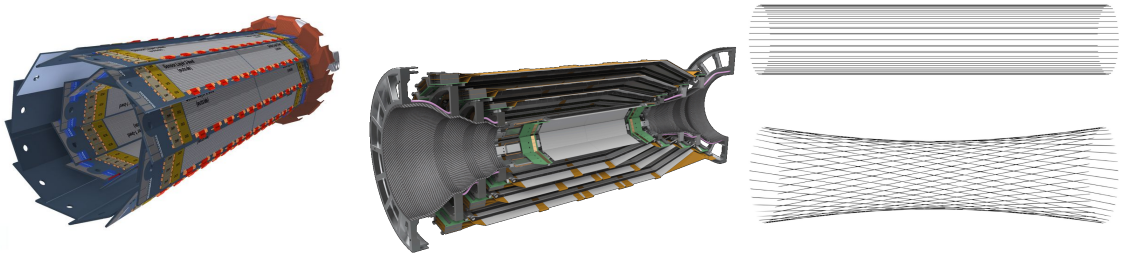

(a) (b) (c)

Figure 3.3: A schematic view of the PXD (a) and the SVD (b) are presented. Additionally, in (c) the axial (top) and stereo (bottom plot) wire structure of the CDC is illustrated. The relative size of the detectors with respect to each other is depicted in Figure 3.2. Figures from References [172–174].

As Belle II probes physics at much lower energies compared to the LHC experiments, the PXD utilizes DEPFET (DEpleted p-channel Field Effect Transistor) technology, which enables the use

of extremely thin sensors of only 75 µm, minimizing multiple scattering. The DEPFET technology provides the benefit of integrating signal detection and amplification within a single device. This technological advantage allows for the placement of the PXD's readout electronics outside the acceptance region, removing the requirement for active cooling within the detector. The modules are designed to withstand a 20 Mrad radiation dose and their hit-efficiency is measured to be 98%, while providing an average spatial resolution of 15 µm [171].

Silicon Vertex Detector (SVD)

The Silicon Vertex Detector (SVD) [175] comprises four layers of double-sided silicon-strip detectors, positioned at radii of 39 mm, 80 mm, 105 mm, and 135 mm, respectively. Similar to the PXD, the SVD provides an angular coverage of $\theta \in [17°, 150°]$. The SVD layers consist of 7 to 16 ladders, while each ladder contains 2 to 5 sensors, accumulating to a total of 224 000 strips (see Fig. 3.3(b)). In comparison to Belle, the SVD occupies a larger volume. Hence, the efficiency for reconstructing $K_S^0 \to \pi^+\pi^-$ decays is enhanced. Moreover, the readout chips are replaced to provide faster readout times.

The front and back-side readout strips are rotated by 90° relative to each other. This configuration allows for a two-dimensional reconstruction of charge deposition without the necessity for additional strip layers and thus minimizing the material budget per ladder. During its first year of data taking, the hit efficiency exceeded 99.5% and the spatial resolution ranged from 18 µm to 35 µm [176].

Central Drift Chamber (CDC)

The Belle II Central Drift Chamber (CDC) [177] is an upgrade of the Belle CDC and serves multiple essential functions. Its main purpose is the reconstruction of charged particle trajectories, enabling the determination of their charges and momenta. Additionally, the CDC plays a crucial role in particle identification, especially for low-momentum tracks that do not extend to the outer detectors specialized for this purpose. This is accomplished by assessing the energy loss of charged particles as they traverse the gas volume of the CDC.

The CDC is a multi-wire proportional drift chamber, filled with a gas mixture composed of equal parts helium (He) and ethane (C_2H_6). Its volume extends between an inner cylinder with a radius of 160 mm and an outer cylinder with a radius of 1 130 mm, encompassing more than 55 000 sense and field wires. These wires are organized in 56 radial layers, which are further subdivided into groups of alternating axial *superlayers*, aligned with the solenoidal magnetic field along to the z-axis, and stereo superlayers, slightly inclined relative to the axial layers (see Fig. 3.3(c)). This arrangement allows for three-dimensional track reconstruction.

The CDC maintains the same angular coverage as the previous subsystems, i.e., $\theta \in [17°, 150°]$, and delivers an average spatial resolution of 120 µm. In combination with the SVD and PXD, track finding efficiencies of more than 95% are achieved in most detector regions and relative p^{T} resolutions of less than 0.5% are attained for particles with momenta greater than 300 MeV [174].

3.2.2 Particle-identification system

In Belle II, two new dedicated particle-identification devices are introduced in both the barrel and the endcap regions. Compared to Belle, they significantly enhance the excellent π/K particle identification

also to the kinematic limits of low momenta. These devices are positioned outside the CDC and are briefly introduced in the following.

Time-of-Propagation counter (TOP)

The Time-of-Propagation counter (TOP) [178] is composed of 16 quartz radiator bars, each 2 cm thick, and encloses the CDC in the barrel region. Its bars are equipped with a mirror at one end and micro-channel-plate photomultiplier tube arrays at the other. Its operating principle is illustrated in Figure 3.4(a).

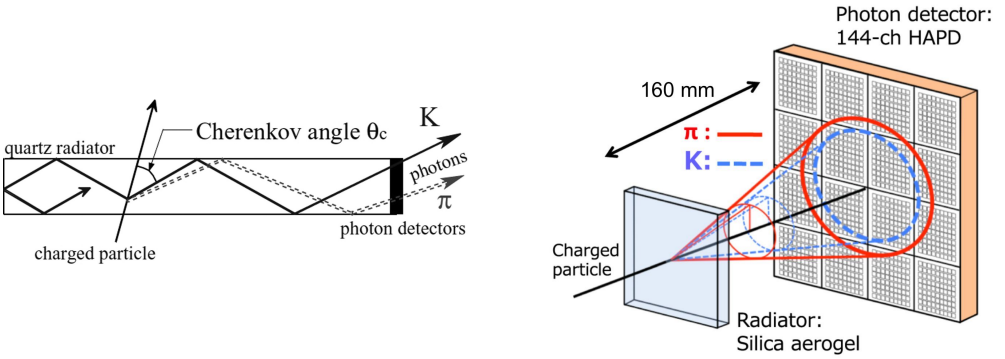

(a) TOP (b) ARICH

Figure 3.4: The operating principles of the TOP (a) and ARICH (b) detectors are illustrated. Figures from References [178, 179].

When charged particles traverse the quartz radiators, they emit Cherenkov photons in a cone characterized by an opening angle θ_C, which depends on the particle's velocity. Due to the high refractive index of quartz, the Cherenkov light is internally reflected, which enables the determination of θ_C based on the photon's propagation time from the emission point to the photomultipliers. Based on the time distribution of the photons, various charged particle hypotheses are evaluated and compared, although the TOP is tuned for an optimal π/K differentiation. The TOP achieves a 85% identification efficiency for charged kaons while maintaining a 10% pion-misidentification rate [180].

Aerogel Ring-Imaging Cherenkov counter (ARICH)

The Aerogel Ring-Imaging Cherenkov counter (ARICH) [181] completes the particle-identification system in the forward endcap region, which features a high particle occupancy due to the boost of the c. m. system. The ARICH detector consists of 20 mm thick silica aerogel tiles arranged in two layers, serving as the active material responsible for generating Cherenkov photons from traversing charged particles. These tiles are arranged in a ring-like structure with an inner radius of 420 mm and an outer radius of 1 145 mm. A photon detection system concludes the detector after 160 mm of expansion space, allowing the Cherenkov photons to produce a ring image whose radius depends on θ_C (see Fig. 3.4(b)).

This design enables ARICH to differentiate kaons from pions across most of their momentum spectrum, specifically $p \in [0.4, 4]$ GeV, and to provide discrimination power between electrons, muons,

and pions below 1 GeV. A kaon-identification efficiency of 94% is achieved at a pion-misidentification rate of 11% [179].

3.2.3 Outer detector systems

The subsystems located outside the particle-identification detectors are briefly summarized in this section.

Electromagnetic Calorimeter (ECL)

The Electromagnetic Calorimeter (ECL) [182] is designed to measure the energies of electromagnetically interacting particles. Hence, it is the central subsystem for the detection of photons and additionally contributes to the electron identification. Furthermore, it provides information for the K_L^0 detection, luminosity measurements, and for the trigger system.

It is composed of 8 736 thallium-doped caesium iodide CsI(Tl) crystals, which are reused from Belle's ECL. They are arranged within a 3 m long barrel structure with an inner radius of 1.25 m and forward and backward endcaps. The ECL provides an angular coverage of $\theta \in [12.4°, 155.1°]$ except for two gaps of roughly 1° between the barrel and endcap regions.

The interaction of traversing electromagnetically interacting particles and the dense CsI(Tl) crystal material yields electromagnetic showers, i.e., cascades of newly generated particles, that are proportional to the initial particle's energy. The crystals are designed to have a length of 30 cm, roughly corresponding to 16 radiation lengths, so that photons and electrons deposit their entire energy in the ECL. Positioned at the end of each crystal, photodiodes detect the scintillation light generated by the electromagnetic showers. This enables the measurement of photon energies spanning from 20 MeV to 4 GeV. Newly introduced readout electronic have been implemented in the ECL that help to mitigate the issue of noise pile-up, which is particularly important for missing-energy studies. The relative energy resolution achieved by the ECL varies from 2.5% for photon energies of $E_\gamma = 100$ MeV to 1.7% at $E_\gamma = 5$ GeV [182].

Superconducting solenoid

The barrel structure of the ECL is enclosed by a cylindrical solenoid measuring 3.4 m in diameter and 4.4 m in length. Its coil is constructed from a superconducting niobium-titanium-copper (NiTi/Cu) alloy and cooled by a liquid helium cryogenic system. It is supplied with a 4 400 A current, generating a uniform 1.5 T magnetic field aligned parallel to the beam axis, so that charged particle trajectories are bent inside the tracking system. The magnetic flux return is facilitated by Belle II's outer iron support structure.

K_L^0 and Muon detector (KLM)

The outermost and largest structure of Belle II, depicted in green in Figure 3.2, is the K_L^0 and Muon detector (KLM) [183]. It is dedicated to the K_L^0-meson and muon identification and is constructed using alternating layers of up to 47 mm thick iron plates, that serve as absorber material, and active detector elements. In the barrel region of the KLM, resistive plate chambers are used, while scintillator strips and silicon photomultipliers are employed in the end-cap regions and in the two innermost active barrel layers. The KLM provides an angular coverage of $\theta \in [20°, 155°]$.

Muons, being minimally ionizing particles, deposit only small amounts of energy in the preceding subsystems. Consequently, muons with sufficient momenta of $p_\mu > 0.6\,\text{GeV}$ traverse the KLM and leave unique particle-identification information.

Neutral K_L^0 mesons, which are undetected by the inner subsystems, interact either with the ECL, that accounts for 0.8 interactions lengths for orthogonally traversing hadrons, or the KLM (equivalent to 3.9 interaction lengths), resulting in the creation of hadronic showers. These showers can be utilized to determine the direction of the K_L^0 meson. However, due to persistent challenges in accurately simulating K_L^0 interactions with the KLM, any attempts at K_L^0 reconstruction are refrained from in this thesis. Instead, the KLM is exclusively utilized for the identification of muons.

3.3 Particle reconstruction and identification

To convert raw detector data into more manageable, higher-level information for analysis purposes, reconstruction algorithms are indispensable. These algorithms convert raw detector objects into clusters (see Sec. 3.3.1), collections of PXD, SVD, and CDC clusters and hits into particle tracks (see Sec. 3.3.2), and provide particle-identification (PID) variables (see Sec. 3.3.3).

Ultimately, the objective is to accurately identify all the final-state particles produced during the initial collision. Short-lived particles decay before interacting with the detector and must be reconstructed from their long-lived daughter particles, that are photons, K_L^0-mesons, electrons, muons, protons, deuterons, and charged kaons and pions. Neutrinos exit the detector without detection. Other particles may also exit the detector with minimal or no interaction, particularly beyond its acceptance regions. Moreover, each detector introduces intrinsic noise that can mimic detector responses.

3.3.1 Cluster reconstruction

Clustering involves the basic idea of combining spatially neighboring detector responses into merged clusters, which facilitates the measurement of their characteristic properties such as position and energy. This clustering process represents an initial stage in the reconstruction procedure and is employed by various detectors within Belle II. PXD and SVD clusters serve as input in the track reconstruction as discussed in the subsequent section.

ECL clusters are essential for the reconstruction of photons, since photons are electrically neutral and remain undetected by the tracking system. These clusters are formed by merging neighboring ECL crystals with an energy deposition above a certain threshold. Using local maxima in energy deposition, the regions of interest are iteratively divided into clusters. The final cluster energy is then corrected to account for potential fractions of the electromagnetic shower that passed through the entire ECL and other detector effects.

3.3.2 Track reconstruction

In a uniform magnetic field, charged particle trajectories follow a helical path and can be characterized by five parameters. These parameters include the track's coordinates at the point of closest approach (POCA) to the measured interaction point in both the x-y plane ($\mathrm{d}r$) and the z direction ($\mathrm{d}z$).[1] Additionally, they encompass the angle between the transverse momentum at the POCA and the

[1] Alternatively, the POCA's distance to the origin of the coordinate system can be used, referred to as d_0 and z_0.

x-axis, ϕ_0, the curvature of the track signed in accordance with the particle's charge ω, and the angle between the track and the z-axis, which is correlated with the polar angle of the coordinate system $\lambda = \frac{\pi}{2} - \theta$ [170, 174]. The purpose of a track-reconstruction algorithm is not only to identify charged-particle trajectories but also to accurately measure these five parameters to determine particle momenta and vertices.

The track reconstruction workflow in Belle II is illustrated in Figure 3.5 and relies on input hits or clusters from the PXD, SVD, and CDC tracking system. The algorithm must correctly combine these inputs into track candidates, while large amounts of signals from machine-induced backgrounds and detector noise complicate this task.

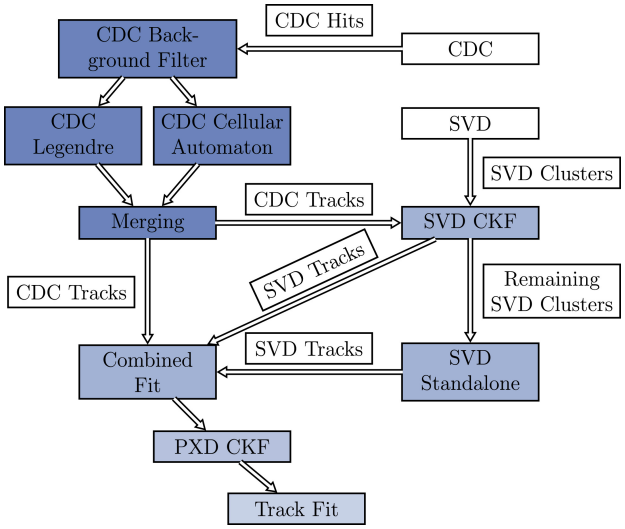

Figure 3.5: The track reconstruction workflow at Belle II is illustrated. Figure from Reference [174].

At the initial stage, filtered CDC hits serve as input for two distinct pattern-recognition algorithms: a global algorithm for track finding based on the Legendre algorithm [184], and a local cellular automaton algorithm [185]. The results obtained from these two algorithms are combined, and the CDC-only tracks are subsequently fitted using a deterministic annealing filter (DAF) [186].

A stochastic gradient-boosted decision tree (BDT) [187] is employed to combine various properties of CDC-track candidates, creating a quality indicator to distinguish between real particle tracks (*true* tracks), erroneous CDC hit combinations (*fake* tracks), and instances of multiple tracks originating from the same particle (*clone* tracks). These cases may arise due to factors such as low momentum particles traversing multiple turns of their helical trajectory or non-continuous track trajectories caused by particle-material interactions. The BDT builds upon prior work outlined in Reference [188]. As part of the Belle II author-list qualification task conducted by the author of this thesis, it underwent improvement, and was rigorously evaluated using real data. The input parameters for the quality indicator are selected based on their consistency between simulations and data. Among these parameters, the most important ones, in addition to kinematic properties, include the total number of hits, hits per layer, and the maximum distance without hits along the track.

The filtered CDC-track candidates are extrapolated to the SVD using a combinatorial Kalman filter (CKF) [189, 190] to merge appropriate SVD clusters with the track. The remaining SVD clusters are utilized by a dedicated standalone SVD track-finding algorithm [191], which is particularly useful

for low-momentum particles that do not generate enough hits in the CDC. The outcome from both processes are merged and refitted using the DAF.

As the PXD experiences excessive occupancies, it is not directly involved in the initial track-finding. Instead, the fitted CDC and SVD tracks are extrapolated to the PXD using another CKF. This step aims to identify matching PXD clusters, ultimately enhancing the impact parameter resolution. Subsequently, a track fit is performed with a DAF provided by the GENFIT2 package [186]. During this fit, all tracks are treated with the assumptions of pion, kaon, and proton mass hypotheses to accurately account for energy loss and material effects.

3.3.3 Particle identification

Final-state charged particles are differentiated from each other by exploiting their distinct interactions with various subdetectors. The information collected from each subdetector is independently analyzed to derive an individual subdetector-specific likelihood, $\mathcal{L}_i^{\text{subdet.}}$, for each charged-particle hypothesis, $i = e, \mu, \pi, K, p, d$. These subdetector-specific likelihoods are then multiplied to create a global likelihood for each particle hypothesis, $\mathcal{L}_i$. Subsequently, all information is combined into a global likelihood ratio, that is ultimately used for particle identification:

$$\mathcal{P}_i^{\mathcal{L}/\mathcal{L}} = \frac{\mathcal{L}_i}{\mathcal{L}_e + \mathcal{L}_\mu + \mathcal{L}_\pi + \mathcal{L}_K + \mathcal{L}_p + \mathcal{L}_d}. \tag{3.1}$$

Additionally, specific binary ratios are available, that are particularly interesting to distinguish charged pions and kaons:

$$\mathcal{P}_{(i|j)}^{\mathcal{L}/\mathcal{L}} = \frac{\mathcal{L}_i}{\mathcal{L}_i + \mathcal{L}_j}. \tag{3.2}$$

In the case of charged hadrons, the TOP and ARICH information is combined with specific ionization $\mathrm{d}E/\mathrm{d}x$ measurements from the CDC. The independent $\mathrm{d}E/\mathrm{d}x$ information provided by the SVD is currently not integrated into the official particle-identification procedure at Belle II. Muon identification primarily relies on data from the KLM for $p_\mu > 0.6\,\text{GeV}$, while electron identification utilizes data from the ECL. To maximize the utility of the ECL-cluster observables, a multiclass BDT classifier $\mathcal{P}_e$, presented in Reference [192], is used for electron identification. This classifier, which also incorporates the particle-identification likelihoods, outperforms $\mathcal{P}_e^{\mathcal{L}/\mathcal{L}}$ significantly. Lepton identification is particularly relevant for this analysis. Its performance is carefully investigated in experimental studies as outlined in more detail in Section 3.4.4.

In this thesis, neutral K_L^0 mesons are not considered, so that photons are the single neutral particles of interest. Their identification relies on the characteristics of ECL clusters. Clusters with a relatively symmetrical shape, typically produced by photons or electrons, can be differentiated from asymmetric clusters generated by hadrons. Photon candidates are identified by clusters that lack an associated charged particle track. Since hadron interactions often produce secondary *split-off* clusters, a distinction between these clusters and photons is essential and is outlined in Section 4.4.1.

3.4 Experimental data and simulated samples

This section provides an overview of the data samples used in this thesis. In Section 3.4.1, the experimental collision-data sample is presented, while Section 3.4.2 introduces the simulated data

sample. The modeling of semileptonic B-meson decays is particularly important for this work so that their simulation is revisited in Section 3.4.3. Additional adjustments applied to the simulation regarding lepton-identification efficiencies are discussed in Section 3.4.4.

Both, experimental and simulated data are analyzed using the Belle II analysis software framework (`basf2`) [193, 194], primarily written in C++ and Python.

3.4.1 Experimental data sample

In its initial four years of operation, spanning from 2019 to 2022, the Belle II detector recorded a total time-integrated luminosity, a measure for the data sample size, of $\int \mathcal{L} \mathrm{d}t = 424\ \mathrm{fb}^{-1}$ [195]. Out of this accumulated data set, 363 fb^{-1} were collected at the $\Upsilon(4S)$, with an additional 42 fb^{-1} gathered 60 MeV below the resonance. Additionally, 19 fb^{-1} of data were collected at slightly higher energies to facilitate studies concerned around quarkonium physics.

The analyses presented in this thesis, however, are restricted to data collected until the end of 2021. This data sample corresponds to an integrated luminosity of 189 fb^{-1} at the $\Upsilon(4S)$ resonance, equivalent to approximately 198×10^6 $B\overline{B}$ pairs. Additionally, an off-resonance data sample is used that corresponds to an integrated luminosity of 18 fb^{-1}.

The off-resonance data sample profits from the fact that only continuum events, i.e., $e^+e^- \to q\overline{q}$, where $q = \{u, d, s, c\}$, are produced in the hadronic channels below the $\Upsilon(4S)$ energy. This feature makes the off-resonance data sample a clean, data-driven representation of these events at Belle II. To compensate for the $1/s$ dependence in the $e^+e^- \to q\overline{q}$ cross section, the yield of the off-resonance data sample is adjusted by a global correction factor $c_{\text{off-res}}$:

$$c_{\text{off-res}} = \left(\frac{\sqrt{s}_{\text{off-res}}}{\sqrt{s}_{\Upsilon(4S)}} \right)^2 \approx 0.989 \tag{3.3}$$

The energy and momentum of particles in this data set are also adjusted by a scaling factor of $1/\sqrt{c_{\text{off-res}}} = 1.006$ to account for the reduced c. m. energy available in comparison to collisions at the $\Upsilon(4S)$ resonance. While this correction has a minor impact on most applications, it is particularly important when calculating the beam-constrained mass M_{bc} and the energy difference ΔE between the reconstructed tag-side B-meson candidate B_{tag} and the expected collision energy $\sqrt{s}_{\Upsilon(4S)}$ as discussed in Section 4.1. For off-resonance data samples, these quantities must be calculated using

$$M_{\text{bc}}^{\text{corr}} = \sqrt{\left(\frac{\sqrt{s}_{\Upsilon(4S)}}{2} \right)^2 - \left(\frac{p^*_{B_{\text{tag}}}}{\sqrt{c_{\text{off-res}}}} \right)^2} \tag{3.4}$$

$$\Delta E^{\text{corr}} = \frac{E^*_{B_{\text{tag}}}}{\sqrt{c_{\text{off-res}}}} - \frac{\sqrt{s}_{\Upsilon(4S)}}{2}. \tag{3.5}$$

Here, $E^*_{B_{\text{tag}}}$ and $p^*_{B_{\text{tag}}}$ indicate the measured energy and the absolute value of the three-momentum of the tagged B-meson candidate in the c. m. system, respectively.

3.4.2 Monte Carlo simulation

Simulation plays a critical role in high-energy physics, serving as a vital tool for understanding the behavior of particle interactions and the response of detectors. Monte Carlo (MC) simulations are used to model and analyze both signal and background events.

The simulation of $e^+e^- \to \Upsilon(4S) \to B\overline{B}$ events is performed using the software package EvtGen [196]. This event generator relies on input information of the produced particles, encompassing their masses, spins, decay widths, lifetimes, and decay modes with their corresponding branching fractions and theoretical decay models. All known semileptonic and hadronic B-meson and D-meson decays based on Reference [17] are included. In addition, approximately 42% of the B-meson decays are modeled to decay fully hadronically using hadronization and fragmentation functions from PYTHIA [197]. The continuum events $e^+e^- \to q\overline{q}$ are simulated with KKMC [198] and PYTHIA. In most relevant parts of this analysis, however, they are substituted by the off-resonance data sample unless otherwise specified, as the modeling of quark fragmentation is very challenging and not always reliable. For final-state radiation of photons emitted from charged particles, Photos [199] is used. The detector geometry, its responses and material interaction is simulated with Geant4 [200]. Subsequently, specifically simulated beam-induced backgrounds are added to the events [201].

In addition to the quantities reconstructed based on the (simulated) detector response, MC simulations provide insights into the underlying generated physical processes. In this thesis, the former is denoted *reconstruction level*, while the latter is referred to as *generator-level* information. This facilitates the classification of reconstructed particle candidates into *true* and *fake* particles, depending on their underlying nature (see Sec. 3.4.4).

Additionally, simulations allow for the design of signal-extraction strategy in a *box closed* analysis,[2] i.e., without direct feedback of experimental data in the signal region. The efficiencies of selection criteria are assessed for both signal and backgrounds and MC-simulated templates serve as probability density functions in the signal-extraction fit input. For these purposes, it is crucial to confirm that the simulation accurately reproduces real-world data and validation of the simulations against experimental observations is a substantial component of this process.

The MC simulations are produced centrally by the collaboration. This analysis uses simulation samples corresponding to an integrated luminosity of 900 fb^{-1} for $\Upsilon(4S) \to B^0\overline{B}^0$ and $\Upsilon(4S) \to B^+B^-$ events. The important semileptonic $B \to Xl\nu$ decays are carefully revisited and updated to reflect the latest knowledge. This is presented in detail in the following section.

3.4.3 Modeling of semileptonic B-meson decays

As introduced in Section 2.2, inclusive semileptonic B-meson decays, $B \to Xl\nu$, are a miscellany of different exclusive decays. Their relative composition is determined by the individual branching fractions, which are introduced below. The kinematic characteristics of these decays are governed by form-factor parameterizations that are discussed subsequently. Finally, necessary adjustments of experimentally poorly constrained non-resonant gap-mode and $B \to D^{**}l\nu$ decays are outlined.

[2] This is also commonly known as a *blind* analysis, but this term is now sometimes considered ableist.

Branching fractions

Table 3.1 provides a summary of the branching fractions, that all semileptonic B-meson decays are updated to. Their relative composition is additionally illustrated in Figure 2.8.

Decay	$\mathcal{B}(B^+)$	$\mathcal{B}(B^0)$
$B \to X_u \ell\nu$	$(1.65 \pm 0.21) \cdot 10^{-3}$	$(1.51 \pm 0.19) \cdot 10^{-3}$
$B \to D\ell\nu$	$(2.41 \pm 0.07) \cdot 10^{-2}$	$(2.24 \pm 0.07) \cdot 10^{-2}$
$B \to D^*\ell\nu$	$(5.50 \pm 0.11) \cdot 10^{-2}$	$(5.11 \pm 0.11) \cdot 10^{-2}$
$B \to D_0^*\ell\nu$	$(4.20 \pm 0.75) \cdot 10^{-3}$	$(3.90 \pm 0.70) \cdot 10^{-3}$
$B \to D_1'\ell\nu$	$(4.20 \pm 0.90) \cdot 10^{-3}$	$(3.90 \pm 0.84) \cdot 10^{-3}$
$B \to D_1\ell\nu$	$(6.63 \pm 1.09) \cdot 10^{-3}$	$(6.16 \pm 1.01) \cdot 10^{-3}$
$B \to D_2^*\ell\nu$	$(2.93 \pm 0.32) \cdot 10^{-3}$	$(2.73 \pm 0.30) \cdot 10^{-3}$
$B \to D^{(*)}\pi\ell\nu$	-	-
$B \to D\pi\pi\ell\nu$	$(0.62 \pm 0.89) \cdot 10^{-3}$	$(0.58 \pm 0.82) \cdot 10^{-3}$
$B \to D^*\pi\pi\ell\nu$	$(2.16 \pm 1.02) \cdot 10^{-3}$	$(2.01 \pm 0.95) \cdot 10^{-3}$
$B \to D\eta\ell\nu$	$(3.77 \pm 3.77) \cdot 10^{-3}$	$(4.09 \pm 4.09) \cdot 10^{-3}$
$B \to D^*\eta\ell\nu$	$(3.77 \pm 3.77) \cdot 10^{-3}$	$(4.09 \pm 4.09) \cdot 10^{-3}$
$B \to D_s K\ell\nu$	$(0.30 \pm 0.14) \cdot 10^{-3}$	-
$B \to D_s^* K\ell\nu$	$(0.29 \pm 0.19) \cdot 10^{-3}$	-
$\sum B \to X_c\ell\nu$	$(10.8 \pm 0.6) \cdot 10^{-2}$	$(10.1 \pm 0.6) \cdot 10^{-2}$
$B \to X_u\tau\nu$	$(0.56 \pm 0.28) \cdot 10^{-3}$	$(0.51 \pm 0.25) \cdot 10^{-3}$
$B \to D\tau\nu$	$(7.21 \pm 0.22) \cdot 10^{-3}$	$(6.70 \pm 0.22) \cdot 10^{-3}$
$B \to D^*\tau\nu$	$(1.41 \pm 0.03) \cdot 10^{-2}$	$(1.31 \pm 0.03) \cdot 10^{-2}$
$B \to D_0^*\tau\nu$	$(0.34 \pm 0.14) \cdot 10^{-3}$	$(0.31 \pm 0.13) \cdot 10^{-3}$
$B \to D_1'\tau\nu$	$(0.25 \pm 0.10) \cdot 10^{-3}$	$(0.23 \pm 0.09) \cdot 10^{-3}$
$B \to D_1\tau\nu$	$(0.66 \pm 0.13) \cdot 10^{-3}$	$(0.62 \pm 0.12) \cdot 10^{-3}$
$B \to D_2^*\tau\nu$	$(0.21 \pm 0.04) \cdot 10^{-3}$	$(0.19 \pm 0.03) \cdot 10^{-3}$
$B \to D\pi\pi\tau\nu$	$(0.70 \pm 1.00) \cdot 10^{-4}$	$(0.66 \pm 0.94) \cdot 10^{-4}$
$B \to D^*\pi\pi\tau\nu$	$(0.25 \pm 0.12) \cdot 10^{-3}$	$(0.23 \pm 0.11) \cdot 10^{-3}$
$B \to D\eta\tau\nu$	$(0.43 \pm 0.43) \cdot 10^{-3}$	$(0.47 \pm 0.47) \cdot 10^{-3}$
$B \to D^*\eta\tau\nu$	$(0.43 \pm 0.43) \cdot 10^{-3}$	$(0.47 \pm 0.47) \cdot 10^{-3}$
$\sum B \to X_c\tau\nu$	$(2.40 \pm 0.08) \cdot 10^{-2}$	$(2.24 \pm 0.08) \cdot 10^{-2}$

Table 3.1: The presented branching fractions are used for simulated $B \to X\ell\nu$ and $B \to X\tau\nu$ decays for charged (left) and neutral (right) B-mesons.

The majority of semileptonic decays into light leptons are attributed to the resonant $B \to D\ell\nu$ and $B \to D^*\ell\nu$ decays. Their measured branching fractions are combined for neutral and charged B mesons

under the assumption of isospin symmetry, using the world-averaged values from Reference [130]. For the $B \to D^{**}\ell\nu$ decays ($D^{**} = D_0^*, D_1', D_1, D_2^*$), not all possible final states have been measured to date. To estimate their total branching fraction, an extrapolating from existing measurement to the unobserved D^{**} final-state decays is conducted while also assuming isospin symmetry. This extrapolation, along with the expected abundance of $D^{**} \to D^{(*)}\pi$ decays in comparison to the measured branching fraction of non-resonant $B \to D^{(*)}\pi\ell\nu$ decays, aligns with the assumption that all measured $B \to D^{(*)}\pi\ell\nu$ events originate from D^{**} decays. Consequently, the branching fraction of this specific non-resonant portion is set to zero.

The sum of all previously mentioned resonant decays is smaller than the measured total semileptonic decay width $B \to X_c\ell\nu$ [17]. This difference is filled with non-resonant *gap modes* $B \to D^{(*)}\pi\pi\ell\nu$ and $B \to D^{(*)}\eta\ell\nu$. Among these, only $\mathcal{B}(B \to D^{(*)}\pi^+\pi^-\ell\nu)$ has been experimentally measured [202]. This result is extrapolated to the other charge configurations to estimate their total branching fractions. The remaining gap is accounted for by $B \to D^{(*)}\eta\ell\nu$ decays and is assigned a branching-fraction uncertainty of 100%.

Both resonant and non-resonant CKM-suppressed $B \to X_u\ell\nu$ decays are simultaneously simulated using a hybrid model [97] which is adjusted in terms of its internal parameters based on Reference [17]. The overall $B \to X_u\ell\nu$ branching fraction is taken from the same reference.

The branching fractions of semitauonic B-meson decays are determined by combining the corresponding light-lepton branching fractions with the SM predictions for $R(D^{(*)})$ [203], $R(D^{**})$ [88], and $R(X_u)$ [129]. The remaining difference to the inclusive $\mathcal{B}(B \to X\tau\nu)$, based on the SM prediction of $R(X_{\tau/\ell})$ [126, 128–130] (see Eq. (2.32)), is accounted for by including semitauonic gap modes, with their relative fractions assumed to be equivalent to those of the corresponding light-lepton gap modes.

The branching fractions of leptonically decaying τ leptons are updated according to Reference [17]:

$$\mathcal{B}(\tau \to e\nu\nu) = (17.82 \pm 0.04)\% \tag{3.6}$$

$$\mathcal{B}(\tau \to \mu\nu\nu) = (17.39 \pm 0.04)\% \tag{3.7}$$

Form factor modeling

The kinematic distributions of $B \to Xl\nu$ decays are described using form-factor parameterizations as introduced in Section 2.2.2. For the $R(X_{e/\mu})$ measurement (see Chap. 6), the $B \to D^{(*)}\ell\nu$ decays are described using the BGL model [83] with parameters extracted from experimental data in References [204, 205]. For the measurement of $R(X_{\tau/\ell})$ (see Chap. 8), the consistent treatment of B-meson decays into τ leptons and into light leptons is essential. A consistent and recent extraction of all relevant parameters is presented in Reference [85], using the BLPRXP parameterization. This is adopted for all $B \to D^{(*)}\ell\nu$ and $B \to D^{(*)}\tau\nu$ decays.

The $B \to D^{**}\ell\nu$ and $B \to D^{**}\tau\nu$ decays, involving higher excitations of the charmed meson, are described using the BLR model [88, 89]. As elaborated in the following, the non-resonant gap modes are modeled using intermediate, broad D^{**} resonances within the BLR model.

Modeling of non-resonant $B \to X_c l\nu$ decays

Semileptonic B-meson decays into non-resonant final states, specifically $B \to D^{(*)}\pi\pi l\nu$ and $B \to D^{(*)}\eta l\nu$, represent a region of interest that is insufficiently constrained by existing measurements. These decays, introduced to bridge the gap between the sum of individual branching ratios for measured

exclusive decays $B \to D^{(*,**)} l\nu$ and the total semileptonic B-meson decay width, are referred to as gap modes.

As summarized in Table 3.2, dedicated simulated samples are generated to account for these gap modes, using intermediate broad D^{**} resonances, denoted D^{**}_{gap}, in the decay description with masses and widths identical to D_0^* and D_1':

$$B \to [D^{**}_{\text{gap}} \to D^{(*)}\pi\pi] l\nu \qquad B \to [D^{**}_{\text{gap}} \to D^{(*)}\eta] l\nu \tag{3.8}$$

As of now, there is no experimental evidence supporting the existence of an additional broad state in semileptonic transitions. Nonetheless, this model provides a more plausible representation of the kinematics in the three-body decay, $B \to D^{**}_{\text{gap}} l\nu$, than compared to a purely phase-space-based model in which all final-state particles are evenly distributed. A visual comparison of the kinematic distributions for the different models are shown in Figure 3.6.

Decay	**Simulated sample size** $B^0/\bar{B}^0$	B^+/B^-
$B \to [D_1' \to D\pi\pi]\ell\nu$	16.0 ab^{-1}	14.0 ab^{-1}
$B \to [D_0^* \to D\pi\pi]\ell\nu$	16.0 ab^{-1}	14.0 ab^{-1}
$B \to [D_1' \to D^*\pi\pi]\ell\nu$	3.2 ab^{-1}	2.8 ab^{-1}
$B \to [D_0^* \to D^*\pi\pi]\ell\nu$	3.2 ab^{-1}	2.8 ab^{-1}
$B \to [D_0^* \to D\eta]\ell\nu$	1.8 ab^{-1}	1.8 ab^{-1}
$B \to [D_1' \to D^*\eta]\ell\nu$	1.8 ab^{-1}	1.8 ab^{-1}
$B \to [D_1' \to D\pi\pi]\tau\nu$	44.2 ab^{-1}	40.8 ab^{-1}
$B \to [D_0^* \to D^*\pi\pi]\tau\nu$	12.8 ab^{-1}	11.1 ab^{-1}
$B \to [D_0^* \to D\eta]\tau\nu$	6.3 ab^{-1}	6.5 ab^{-1}
$B \to [D_1' \to D^*\eta]\tau\nu$	6.3 ab^{-1}	6.5 ab^{-1}

Table 3.2: The sample sizes in units of integrated luminosity are summarized for the simulated $B \to D^{**}_{\text{gap}} l\nu$ decays.

A phase-space based description would result in lower lepton momenta than what is expected from semileptonic B-meson decays. Consequently, both the transferred momentum q^2 and the invariant mass of the hadronic system M_X would be affected, with q^2 being smaller and M_X being larger than compared to the D^{**}-meson based model.[3]

Broad D^{**} modeling

Table 3.3 summarizes the masses and widths of the four orbitally excited D^{**} mesons.

Two of the four D^{**} mesons, specifically the D_0^* and the D_1', which are also used in the gap-mode modeling, feature a significant width of hundreds of MeV. This poses a substantial challenge when

[3] In this thesis, the lowercase symbol m is used to denote particle masses, such as $m_{\Upsilon(4S)}$, $m_{D^{(*,**)}}$, and m_ℓ. For composite quantities like M_X, M_{bc}, and M^2_{miss}, that rely on the reconstruction and combination of multiple particles, the uppercase symbol M is used.

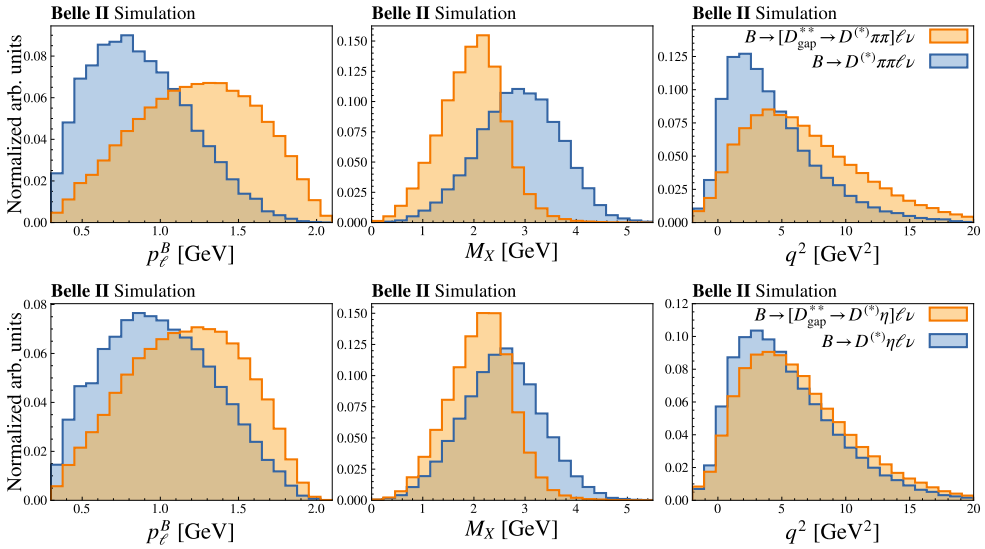

Figure 3.6: The introduced $B \to D^{**}_{\text{gap}}\ell\nu$ decay model for non-resonant B-meson decays into light leptons (orange) is compared to kinematic distributions as prediction by pure phase-space considerations (blue).

Particle	D_0^*	D_1'	D_1	D_2^*
Mass	2 343 MeV	2 412 MeV	2 422 MeV	2 461 MeV
Width	229 MeV	314 MeV	31.3 MeV	47.3 MeV

Table 3.3: The central mass values and widths of the D^{**} mesons, according to Reference [17], are presented.

modeling their lineshapes. Within the used simulations, a notable contribution of $B \to D^{**}\ell\nu$ decays is observed with implausibly high values of the mass of the D^{**} meson, reaching up to 5 GeV, as illustrated in Figure 3.7. In $B \to D^{**}\tau\nu$ decays, the substantial τ-lepton mass prevents such scenarios.

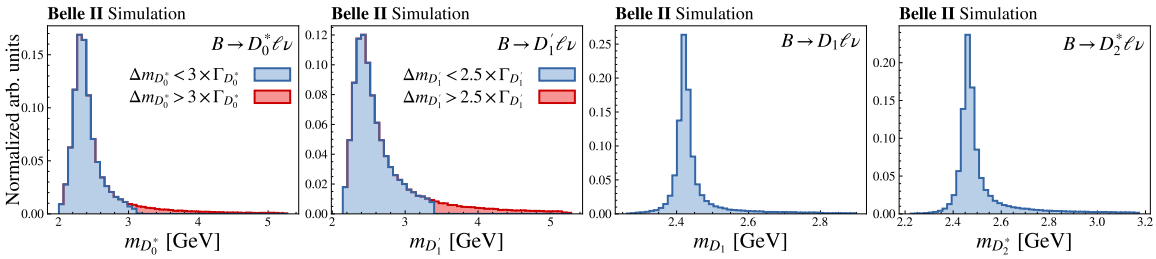

Figure 3.7: The generator-level mass distributions of the different D^{**} mesons, originating from $B \to D^{**}\ell\nu$ decays ($\ell = e, \mu$), are illustrated.

While these instances are not explicitly forbidden from a physical perspective, it is expected that their occurrence is significantly suppressed due to the limited phase space available. Consequently, a simplistic Breit-Wigner assumption might be inadequate for describing the broad D^{**} lineshape. This is particularly evident in the kinematic distributions of the momentum transfer q^2, the recoil

parameter $w = (m_B^2 + m_{D^{**}}^2 - q^2)/(2m_B m_{D^{**}})$, and the lepton momentum in the B-meson rest frame, p_ℓ^B, as presented in Figure 3.8. Especially the w distribution exhibits a conspicuous peak at its minimal value of $w = 1$, which is expected to be unrealistic. Similarly, events around $q^2 \approx 0\,\text{GeV}^2$ are overrepresented.

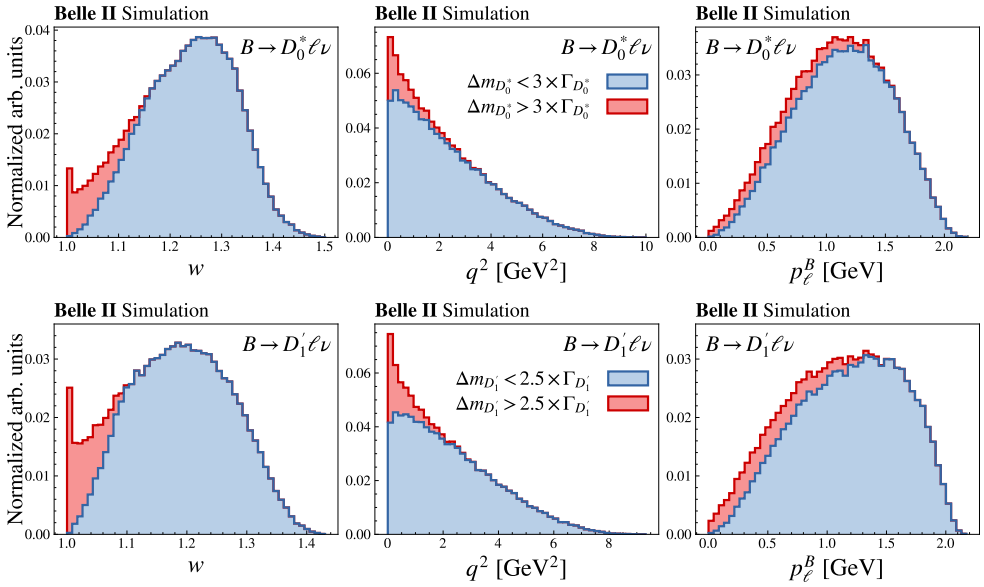

Figure 3.8: The generator-level w, q^2 and p_ℓ^B distributions for $B \to D_0^* \ell\nu$ and $B \to D_1' \ell\nu$ decays are illustrated. Simulated events featuring a very high D^{**} mass are highlighted in red.

At the moment, the kinematic characteristics of the $B \to D^{**} l\nu$ decays are modeled using the BLR model, which relies on the narrow-width approximation, a feature shared with any other existing form-factor model of semileptonic B-meson decays. Various theoretical uncertainties concerning the D^{**} mesons, such as the possibility of the D_0^* being an exotic quark state (see Ref. [17]) and the potential for interferences with other $D\pi$ final states, currently prevent the precise prediction of kinematics that takes into account the substantial D^{**} widths. Consequently, the BLR model remains the most reliable choice for describing $B \to D^{**} l\nu$ decays. Since its parameters are obtained from a fit to data in Reference [89], the model effectively reproduces the experimentally confirmed decay kinematics as long as D^{**} masses do not significantly deviate from their central values.

Hence, to address the occurrence of physically implausible events, this analysis incorporates upper thresholds on the D^{**} masses. For the D_0^* meson, all events are rejected in which the generator-level mass deviates from its central value by more than 3 times the width (approximately 700 MeV). In the case of the D_1' meson, events with mass deviations exceeding 2.5 times the width (approximately 1 GeV) are excluded. The impact of these threshold implementations can be observed in Figure 3.8, where the blue distributions, after excluding events with excessively high D^{**} masses, yield considerably more physically realistic shapes for the kinematic variables w and q^2.

To account for the rejected events, the remaining events are scaled up to maintain a constant total number of events. Additional shape and efficiency uncertainties resulting from this procedure are discussed in Section 8.1.2.

3.4.4 Lepton-identification corrections

The classification of charged tracks and neutral clusters into particle types relies on the specific detector responses that can be difficult to model correctly. Hence, discrepancies in particle-identification efficiencies and misidentification probabilities between the simulated MC samples and collision data are expected to a certain extend. To account for these inaccuracies, the particle-identification performance is calibrated in dedicated control samples, consisting of well-measurable decays. In the presented analyses, the lepton identification (LID) is particularly important, so that its calibration is outlined below.

Using generator-level information, a reconstructed lepton candidate is classified as a *true* lepton if it can be associated with a generated MC lepton, denoted $\ell^\pm \xrightarrow{\text{ID}} \ell^\pm$. If the reconstructed object arises from another particle type, typically a charged pion or kaon, or if the underlying track cannot be linked to any generated particle, it is labeled a *fake* lepton.

Efficiencies for the identification of true leptons are studied in $J/\psi \to \ell^+\ell^-$ as well as $e^+e^- \to \ell^+\ell^-(\gamma)$ and $e^+e^- \to (e^+e^-)\ell^+\ell^-$ decays using a tag and probe method. Probabilities for charged pions to be misidentified as leptons, also referred to as fake rates, are obtained in $K^0_S \to \pi^+\pi^-$ and $e^+e^- \to \tau^\pm(\text{1-prong})\tau^\mp(\text{3-prong})$ decays. For charged-kaon fake rates, $D^{*+} \to [D^0 \to K^-\pi^+]\pi^+$ events are used.

Correction weights, w^{LID}, for simulated efficiencies and fake rates are determined in discrete intervals of lab-frame momentum p_ℓ, polar angle θ_ℓ, and lepton charge q via $w^{\text{LID}}(p_\ell, \theta_\ell, q) = \epsilon_{\text{data}}(p_\ell, \theta_\ell, q)/\epsilon_{\text{MC}}(p_\ell, \theta_\ell, q)$. They are provided by the Belle II Particle Identification group for different lepton-selection working points based on the identification classifier $\mathcal{P}_\ell^{\mathcal{L}/\mathcal{L}}$ or $\mathcal{P}_\ell$ introduced in Section 3.3.3. The LID-classifier thresholds are either set to fixed values or optimized in a three-dimensional grid of p_ℓ, θ_ℓ, and q to achieve a uniform lepton-identification efficiency throughout the entire phase space.

The correction weights, uncertainties, and their kinematic coverage are illustrated in the appendix in Section B.1, specifically Figures B.2 to B.5. An overview of the average correction weights applied to electron and muon candidates is provided in Table 3.4. The kinematic coverage and the treatment of uncertainties are discussed in Section 5.3.5.

Particle Identification	**Electron**		**Muon**	
	$\mathcal{P}_e : \epsilon_e = 80\%$	$\mathcal{P}_e > 0.99$	$\mathcal{P}_\mu^{\mathcal{L}/\mathcal{L}} > 0.95$	$\mathcal{P}_\mu^{\mathcal{L}/\mathcal{L}} > 0.99$
	$p_e^B > 1.3\,\text{GeV}$	$p_e > 0.5\,\text{GeV}$	$p_\mu^B > 1.3\,\text{GeV}$	$p_\mu > 0.7\,\text{GeV}$
$\ell^\pm \xrightarrow{\text{ID}} \ell^\pm$	0.971 ± 0.012	0.976 ± 0.013	0.935 ± 0.023	0.931 ± 0.009
$\pi^\pm \xrightarrow{\text{ID}} \ell^\pm$	2.2 ± 0.8	2.1 ± 0.5	0.81 ± 0.03	0.85 ± 0.03
$K^\pm \xrightarrow{\text{ID}} \ell^\pm$	1.2 ± 0.5	1.5 ± 0.9	1.29 ± 0.13	1.15 ± 0.24

Table 3.4: The average correction weights and uncertainties for lepton efficiencies and hadron-to-lepton misidentification probabilities are summarized for the two different lepton-selection strategies that are used in this work (see Secs. 4.3 and 7.1).

CHAPTER 4

Event reconstruction and selection

As motivated in Section 2.3, the primary objective of this thesis is to measure two inclusive branching-fraction ratios: the light-lepton ratio $R(X_{e/\mu})$ and the tau-to-light-lepton ratio $R(X_{\tau/\ell})$:

$$R(X_{e/\mu}) = \frac{\mathcal{B}(B \to Xe\nu)}{\mathcal{B}(B \to X\mu\nu)} \quad \text{and} \quad R(X_{\tau/\ell}) = \frac{\mathcal{B}(B \to X\tau\nu)}{\mathcal{B}(B \to X\ell\nu)} \quad \text{with} \quad \ell = \{e, \mu\}. \tag{4.1}$$

To achieve this goal, the event selection is specifically tailored to reconstruct $B \to X\ell\nu$ (referred to as *normalization*) and $B \to X\tau\nu$ (denoted *signal*) decays in $e^+e^- \to \Upsilon(4S) \to B\bar{B}$ events. Here, X represents an inclusive sample encompassing all possible hadronic states, as described in Section 2.3.2. The τ lepton in signal events is reconstructed using leptonic $\tau \to \ell\nu\nu$ decays. While this constraint limits the selection to 35% of all τ-lepton decays (see Eq. (3.6)), it enables the effective suppression of substantial levels of hadronic backgrounds, streamlines the event-selection process, and mitigates several experimental uncertainties. An illustrative representation of such an event is presented in Figure 4.1.

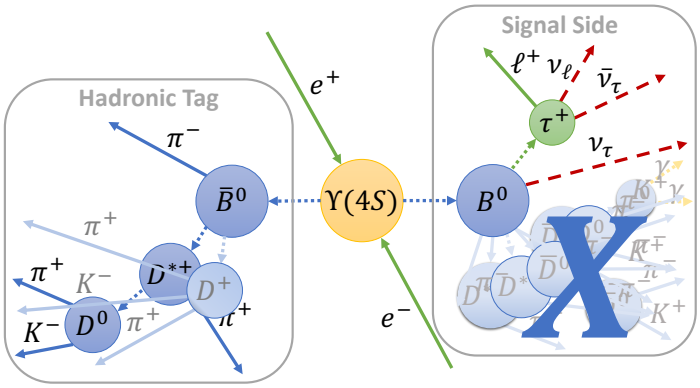

Figure 4.1: A schematic view of an $\Upsilon(4S) \to [B_{\text{tag}} \to \text{had.}][B_{\text{sig}} \to X[\tau \to \ell\nu\nu]\nu]$ event is shown.

One B meson, referred to as the tagged B meson (B_{tag}), is reconstructed to decay fully hadronically as outlined in more detail in Section 4.1. The remaining final-state particles in the event are associated with the accompanying B meson, referred to as the signal B meson (B_{sig}). To enhance the purity

of events originating from $e^+e^- \to \Upsilon(4S) \to B\bar{B}$, a dedicated algorithm is developed to suppress continuum events resulting from $e^+e^- \to q\bar{q}$, as introduced in Section 4.2.

From the particles assigned to the signal B meson, either an electron or a muon is required, referred to as the *electron* or *muon channel*, respectively. Section 4.3 details the selection criteria for the signal lepton in the $R(X_{e/\mu})$ measurement, while Section 7.1 motivates the signal-lepton selection used for the $R(X_{\tau/\ell})$ measurement. The reconstruction of the hadronic system X follows an inclusive approach in both measurements, involving the combination of all remaining charged-particle tracks and ECL clusters not associated with the B_{tag} candidate or the signal lepton. To maintain the purity of the selected sample and suppress particles originating from sources other than the B_{sig} decay, such as beam-induced backgrounds, quality criteria are imposed as outlined in Section 4.4.

One of the key challenges in both analyses is to ensure that all relevant components are accurately modeled. Therefore, the event selection is meticulously designed to prevent any bias between simulated and experimental data, as elaborated in the subsequent sections.

4.1 Hadronic B-meson tagging

At B factories like Belle II, the controlled collision of electrons and positrons at the $\Upsilon(4S)$ energy serves a dual purpose. It not only increases the relative abundance of B mesons but also provides a coherent production of $B^0\overline{B}^0$ and B^+B^- pairs in the $\Upsilon(4S)$ decays. A common strategy is the reconstruction of the kinematics and flavor of one of the two B mesons, a process known as tagging, with the identified B meson denoted as B_{tag}. Due to the coherent $B\bar{B}$ production, this allows for direct inferences regarding the kinematics and flavor of the accompanying signal B meson, B_{sig}. Furthermore, each final-state particle can be uniquely associated with one of the two B mesons within the event.

Several tagging strategies are possible ranging from high-efficiency approaches with limited kinematic control and signal purity in inclusive tagging, to strategies with lower efficiencies of $O(1\%)$ providing good flavor information but limited kinematic knowledge in semileptonic tagging, and finally, full kinematic and flavor control with high purity at the cost of very low efficiencies of $O(0.1\%)$ in the case of hadronic tagging.

This analysis is characterized by an inclusive signal decay $B_{\text{sig}} \to Xl\nu$. Any imposition of requirements on the X system itself restricts its inclusiveness, which makes the task of background rejection particularly challenging. To address this issue, stringent kinematic constraints from the B_{tag} candidate are desirable. Hence, this analysis adopts the hadronic tagging approach. For this purpose, the Full Event Interpretation (FEI) algorithm [206] is utilized, which is integrated into the `basf2` framework.

The Full Event Interpretation algorithm

Figure 4.2 provides a schematic overview of the working principles of the FEI algorithm. It processes objects identified within `basf2`, including charged tracks, displaced vertices, and neutral clusters. In a hierarchical six-stage approach, these objects are reconstructed as final-state particles ($e^\pm, \mu^\pm, K^\pm, \pi^\pm, p, K_L^0, \gamma$). Subsequently, they are combined to form intermediate particles ($\pi^0, K_S^0, J/\psi, D^{(*)}, D_s^{(*)}, \Lambda, \Lambda_c, \Sigma$), and ultimately, a combination of intermediate and final-state particles results in the identification of the tagged B meson. At each stage of this process, a BDT evaluates the likelihood that the (combined) particle is reconstructed accurately. The BDT uses various

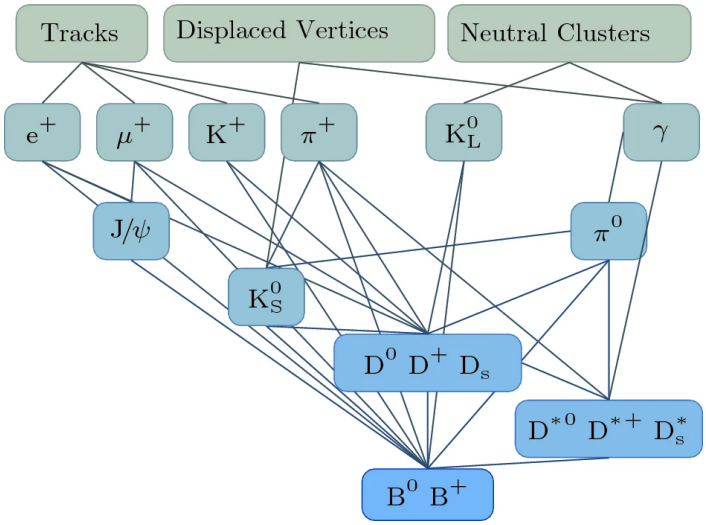

Figure 4.2: A schematic overview of the FEI algorithm is presented, to be read from top to bottom. Figure from Reference [206].

input features to generate a numerical output-classifier score for each particle. These features comprise the particle's kinematic information, vertex position, and, where applicable, properties of its daughter particles, such as their relative angle or their respective output-classifier scores. In total, $O(10\,000)$ distinct decay chains are reconstructed by the FEI algorithm, resulting in 36 different exclusive B^+ decay modes and 32 B^0 decay modes, as summarized in Tables B.1 and B.2 in the appendix. The reconstruction quality of the B_{tag} meson is assessed using the final output score, denoted as $\mathcal{P}_{\text{FEI}}$.

In this thesis, centrally produced subsets of experimental and simulated data are used that are skimmed based on the successful application of the FEI algorithm. A general event-level preselection is applied to these samples, designed to reduce events that deviate substantially from a $B\overline{B}$ event where one B meson undergoes a purely hadronic decay:

$$\begin{aligned}
&\text{Cleaned track:} && |d_0| < 0.5, \quad |z_0| < 2.0, \quad p^{\text{T}} > 0.1\,\text{GeV} \\
&\text{Cleaned cluster:} && \theta \in [17°, 150°], \quad E > 0.1\,\text{GeV} \\
&\text{Event requirements:} && N_{\text{cleaned track}} \geq 3 \\
& && N_{\text{cleaned cluster}} \geq 3 \\
& && E^*_{\text{tot.}} > 4\,\text{GeV}
\end{aligned} \tag{4.2}$$

A minimal number of tracks and clusters, subject to specific quality criteria, is required to suppress low-multiplicity events like $e^+e^- \to \ell^+\ell^-(\gamma)$. Additionally, the total c. m. energy $E^*_{\text{tot.}}$ is required to exceed 4 GeV. In a previous selection approach, an additional constraint was placed on the total energy deposited in the ECL by the cleaned tracks and clusters: $E_{\text{ECL}} \in (2, 7)$ GeV. However, in the scope of this thesis, it was recognized that this criterion introduces an electron-momentum-dependent bias in the comparison between experimental and simulated data, as elaborated in Section 8.1.5. Consequently, this requirement was removed at a later stage of the analysis, and new skimmed samples were generated for the entire collaboration, forming the basis for the presented results.

Efficiency calibration

The modeling of the reconstruction efficiency of the FEI relies not only on a precise simulation of the individual detector responses to the final-state particles (see Sec. 3.4.4), but also on the accurate representation of all hadronic B and charm-meson decays. As mentioned in Section 3.4.2, however, around half of the hadronic B decays are modeled using a general approach with PYTHIA, which may not always be entirely reliable. Similarly, approximately 40% of the kinematic D-decay descriptions are based on phase-space assumptions due to a lack of more precise knowledge. Consequently, significant differences between simulated and experimental tagging efficiencies are expected.

As demonstrated in Section 5.4, the data-to-MC discrepancies in the B_{tag}-reconstruction efficiencies cancel in the measured ratios $R(X_{e/\mu})$ and $R(X_{\tau/\ell})$, rendering the absolute correction factor irrelevant for these measurements. Nevertheless, preliminary correction factors for B_{tag}-reconstruction efficiencies, derived in a FEI-calibration study using $B \to X\ell\nu$ events as in Reference [207], are applied to align the absolute count of experimental and simulated events. These calibration factors, dependent on the reconstructed B_{tag} and signal-lepton flavors, are summarized in Table 4.1.

$B^+_{\text{tag}}e^-$	$B^+_{\text{tag}}\mu^-$	$B^0_{\text{tag}}e^-$	$B^0_{\text{tag}}\mu^-$
0.65 ± 0.03	0.64 ± 0.03	0.72 ± 0.04	0.72 ± 0.04

Table 4.1: The FEI-calibration factors for $\mathcal{P}_{\text{FEI}} > 0.1$ in dependence of the reconstructed B_{tag} and signal-lepton flavor are summarized. They are applied as a baseline correction to the simulations.

They are provided for various $\mathcal{P}_{\text{FEI}}$ thresholds corresponding to different B_{tag} selection efficiencies and purities. As precise modeling of the diverse participating decay modes is a pivotal challenge in inclusive analyses, any added complexity arising from misidentified B_{tag} candidates is minimized by selecting the most stringent threshold, for which calibration factors are provided, namely, $\mathcal{P}_{\text{FEI}} > 0.1$. In Section 7.3.1, the calibration is revisited and the calibration factors are updated.

Selection refinements

A single event may yield multiple B_{tag} candidates reconstructed within the same or different decay channels. In such instances, the B_{tag} candidate with highest $\mathcal{P}_{\text{FEI}}$ is chosen. The independence of the best-candidate selection from particle selections associated with the B_{sig} minimizes tag-side dependencies for signal events as discussed, for example, in Reference [208] and validated in Section 5.4.

To further enhance the purity of the B_{tag} candidates, requirements on the beam-constrained mass M_{bc} and the energy difference ΔE are imposed, that are motivated in the following: [1]

$$M_{\text{bc}} = \sqrt{\left(\frac{\sqrt{s}}{2}\right)^2 - \left(p^*_{B_{\text{tag}}}\right)^2} \in [5.2725, 5.285]\ \text{GeV} \tag{4.3}$$

$$\Delta E = E^*_{B_{\text{tag}}} - \frac{\sqrt{s}}{2} \in [-0.15, 0.1]\ \text{GeV}. \tag{4.4}$$

[1] For off-resonance data, these quantities are corrected as presented in Equations (3.4) and (3.5).

These quantities leverage the understanding that the $\Upsilon(4S) \to B\bar{B}$ decay is a two-body decay into two B-mesons with same mass. Consequently, in the c. m. frame, each B-meson's energy equals the particle beam energy, or correspondingly, half of the c. m. energy $\sqrt{s}$. For correctly reconstructed B_{tag} candidates, M_{bc} should align with the nominal B-meson mass, either $m_{B^+} = 5\,279.3\,\text{MeV}$ or $m_{B^0} = 5\,279.7\,\text{MeV}$ [17]. The energy difference ΔE should be close to zero within detector resolution effects. While ΔE strongly relies on the assigned particle hypotheses of the particles associated with the B_{tag}, the dependence of the beam-constrained mass M_{bc} on particle identification is comparably weak and only emerges in the boost into the c. m. system [122].

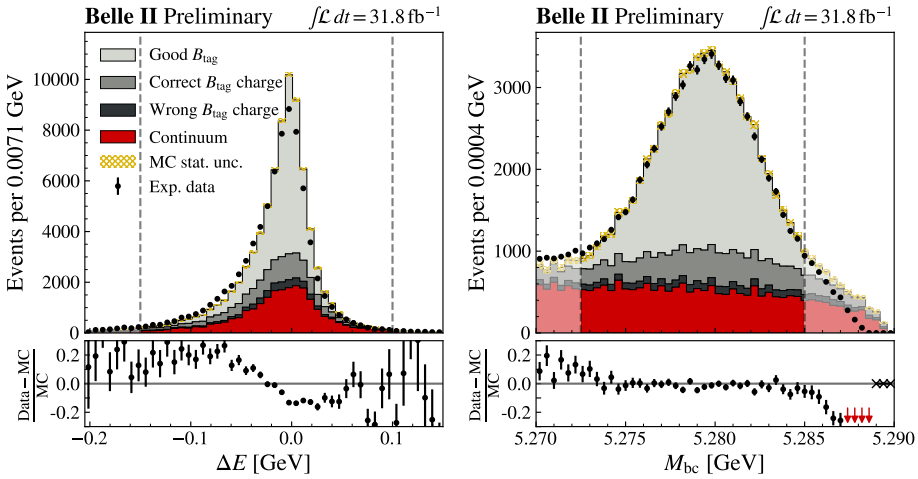

Figure 4.3: The energy difference ΔE and the beam-constrained mass M_{bc} are presented for experimental data (black points) and MC simulations (filled histograms). Dashed lines depict the event-selection requirements imposed on these quantities. Continuum events are determined by off-resonance data (red). Simulated $B\bar{B}$ events are categorized into good B_{tag} events, where all particles associated with the B_{tag} are correctly reconstructed. Candidates with inaccuracies in the reconstruction are then subdivided into correct and wrong-charge tags, based on the success in determining the B_{tag} charge.

In Figure 4.3, the modeling of M_{bc} and ΔE is examined by comparing experimental to simulated data.[2] For this purpose, the simulated $B\bar{B}$ sample is categorized into a set of *good* B_{tag} candidates, where all particles originating from the B_{tag} are correctly reconstructed and assigned. As expected, these tags exhibit a peak around $M_{\text{bc}} \approx m_B \approx 5.28\,\text{GeV}$. The remaining B_{tag} candidates are classified into *correct* and *wrong-charge* events, depending on the success of the B_{tag}-charge reconstruction. Similarly to continuum events, modeled via off-resonance data (see Sec. 3.4.1), events with inaccurately reconstructed B_{tag} candidates are expected to follow an empirical function introduced by the ARGUS collaboration [209]. While this holds for wrong-charge candidates, the correct-charge distribution features a small peaking structure around the B-meson mass, attributed to reconstructions with negligible shortcomings, such as the exchange of two pions in their relative position within the B_{tag} decay chain.

While a satisfactory agreement between data and MC is evident in the peaking structure of M_{bc}, a noticeable discrepancy becomes apparent at the kinematic endpoint of the spectrum. This disparity

[2] The figures presented are generated with additional signal-lepton requirements, as outlined in Section 4.3. Nonetheless, the influence of signal-side effects on these quantities is minimal.

is attributed to variations in the achieved c. m. energy, which determines the kinematic maximum of M_{bc}, towards lower values in experimental data, as depicted in Figure 4.4. In contrast, a constant value of $\sqrt{s} = 10.57956\,\text{GeV}$ is used in simulations and to correct off-resonance data.

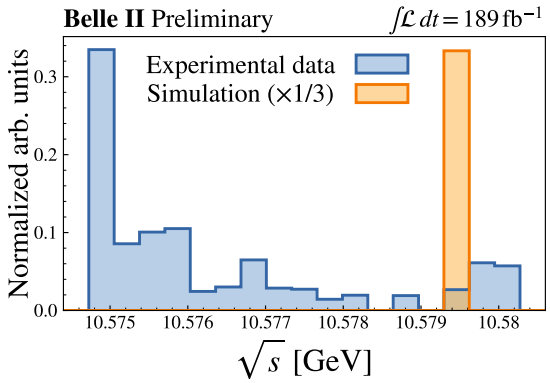

Figure 4.4: The achieved c. m. energies $\sqrt{s}$ in experimental data are depicted in blue. Unlike simulations, illustrated in orange, which consistently employ $\sqrt{s} = 10.57956\,\text{GeV}$, a substantial deviation of this value towards lower magnitudes is noticeable in the experimental collisions.

To eliminate poorly modeled regions, the M_{bc} requirement is tightened to $M_{\text{bc}} \in [5.2725, 5.285]$ GeV, effectively rejecting substantial portions of suboptimal B_{tag} candidates and continuum events while retaining the vast majority of good tags. Alternative strategies, such as a fixation of $\sqrt{s}$ in the M_{bc} calculations in data to the MC value, were tested but found to result in larger discrepancies.

Discrepancies between data and MC are also observed in the distributions of ΔE. However, the current requirement of $\Delta E \in [-0.15, 0.1]$ GeV, already present in the centrally produced skimmed data sets, has minimal impact on $B\overline{B}$ events and is thus considered to be negligible.

4.2 Continuum suppression

At the $\Upsilon(4S)$ resonance, the cross section for continuum events, $\sigma(e^+e^- \to q\overline{q}) = 3.69\,\text{nb}$, is more than three times higher than $\sigma(e^+e^- \to \Upsilon(4S)) = 1.11\,\text{nb}$ [156]. Despite the stringent constraints on the B_{tag} properties that effectively suppress the majority of continuum events, they still constitute a substantial background source for inclusive analyses. Event-shape quantities that leverage the unique characteristics of continuum and $B\overline{B}$ events provide an effective means of suppression. As B mesons are produced with c. m. momenta of approximately 330 MeV, i.e., nearly at rest in the c. m. system, their decay products distribute isotropically in the detector. In contrast, continuum events are produced with a significant boost of the much lighter initial particles, resulting in a back-to-back structure of the event. This distinction is visualized in Figure 4.5.

Various quantities were designed to quantify the different event topologies, with detailed explanations provided in Reference [122]. A brief summary is presented below.

- **Thrust axis and magnitude:** The thrust axis $\vec{T}$ defines the unit vector along which the total projection of a collection of momenta is maximized. For particles associated with the B_{tag} candidate, their momenta yield $\vec{T}_B$, while all *other* particles not associated with the B_{tag}

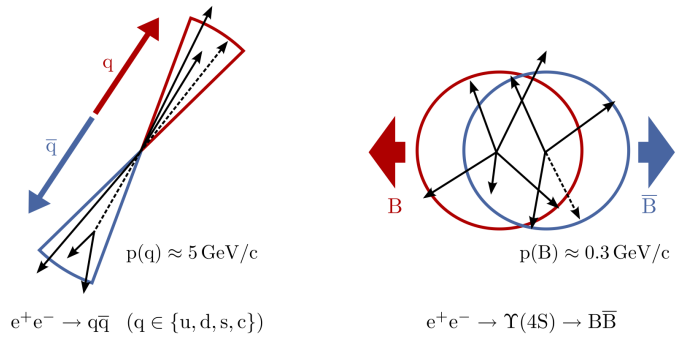

Figure 4.5: The characteristic event topology of $e^+e^- \to q\overline{q}$ events in the c. m. frame is visualized and compared to the $e^+e^- \to \Upsilon(4S) \to B\overline{B}$ topology. Due to different initial momenta, distinct features emerge that can be leveraged for effective separation. Figure from Reference [210].

contribute to $\vec{T}_o$.
The definition of thrust axes enables the measurement of quantities with high separation potential, such as the angle between the thrust of the B_{tag} candidate and the z-axis $\theta_{T_B,z}$, which is differently distributed for $\Upsilon(4S) \to B\overline{B}$ and continuum events due to the spins of the participating particles. Additionally, the cosine of the angle between B_{tag} candidate and the remaining particles' trust $\cos\theta_T$ peaks at high absolute values for continuum events with a back-to-back structure but is isotropically distributed for $B\overline{B}$ events (see Fig. 4.6(b)).
Furthermore, the thrust magnitude T, a scalar observable, is defined as:

$$T = \frac{\sum_i |\vec{T} \cdot \vec{p}_i|}{\sum_i |\vec{p}_i|}. \tag{4.5}$$

Jet-like structures result in values close to $T = 1$, while isotropic events are quantified with $T \approx 0.5$.

- **CLEO cones:** Originally introduced by the CLEO collaboration in Reference [211], CLEO cones denote a series of variables quantifying momentum flow. Starting at $\vec{T}_B$, the cones are defined along 10° intervals, and all magnitudes of particle momenta pointing into each interval are summed (CC_i). Alternatively, only particles not associated with the B_{tag} can be used (CC_i^o). In the context of jet-like continuum events, the particle momentum flow is expected to be concentrated within small opening angles, whereas $B\overline{B}$ events should exhibit a more evenly distributed flow.

- **Fox-Wolfram Moments:** Another valuable parameterization of phase-space distributions of momentum and energy flow in an event was originally introduced in Reference [212]. The normalized k-th order Fox-Wolfram moment $H_k^{oo/so}$ is defined for a collection of particles with momenta $\vec{p}_i$ as

$$H_k^{oo/so} = \frac{\sum_{i,j} |\vec{p}_i||\vec{p}_j| P_k(\cos\theta_{i,j})}{\sum_{i,j} |\vec{p}_i||\vec{p}_j|}, \tag{4.6}$$

where P_k represents the k-th order Legendre polynomial.
When the normalized Fox-Wolfram moment is calculated with i associated with the B_{tag}

candidate's particles (labeled s) and j from the other particles, it is denoted as H_k^{so}. When i and j both are from the other particles, H_k^{oo} is used. Ratios of the Fox-Wolfram moments can be defined, with the most effective continuum suppression quantity being R_2 (see Fig. 4.6(a)), representing the ratio of the second-order to zeroth-order Fox-Wolfram moment.

The quantities are derived using the B_{tag} candidate, as detailed in Section 4.1, which enables a clear categorization of particles with respect to B_{tag} and B_{sig}. The remaining particles are required to include at least one signal-lepton candidate, as described in Section 4.3, and to fulfill specific quality requirements, as outlined in Section 4.4. However, the particle selection associated with B_{sig} is expected to be of secondary importance for this section.

To optimize separation, the listed continuum-suppression quantities are combined into a multivariate classifier, $\mathcal{P}_{\text{CS}}$. For this purpose, a BDT [187] is trained using $B\overline{B}$ events featuring a good B_{tag} candidate (see Sec. 4.1) as signal and simulated continuum events as background. In Table 4.2, the different input quantities are presented in order of their relative importance for the separation power when training an *inclusive* classifier that utilizes all quantities as input.

The superordinate target of the presented continuum suppression is to avoid any data-MC bias in the remaining $B\overline{B}$ events. Since continuum backgrounds are subsequently determined by the limited off-resonance data set, characterized by significant statistical uncertainties, a maximized separation remains desirable.

Figure 4.6 displays two quantities with the highest separation power, R_2 and $\cos\theta_T$. While good agreement between data and simulation is evident for $\cos\theta_T$, a notable discrepancy is observed for R_2. Simulated $B\overline{B}$ events, in particular, exhibit substantially different distributions compared to experimental data, where the latter suggests a more continuum-like behavior for $B\overline{B}$. Consequently, if R_2 was used in the event selection, the simulation would overestimate the remaining number of $B\overline{B}$ events with similar event shapes as continuum, as demonstrated in Figure 4.6(c).

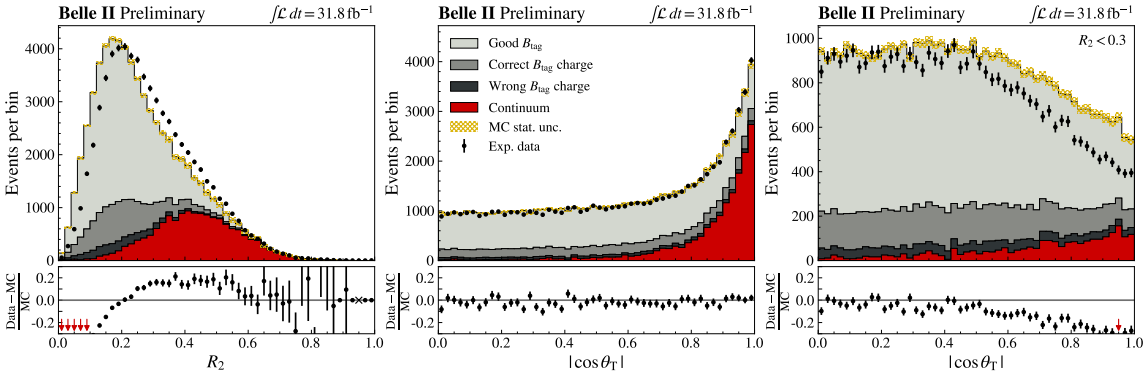

(a) (b) (c)

Figure 4.6: Experimental data is compared to MC simulation for quantities expected to exhibit the highest differences between continuum and $B\overline{B}$ events: the ratio of Fox-Wolfram moments, R_2 (a), and the cosine of the angle between $\vec{T}_B$ and $\vec{T}_o$, $\cos\theta_T$. The latter is presented without additional cuts (b) and with an additional cut of $R_2 < 0.3$ applied (c).

To prevent potential bias, any quantity that exceeds a threshold in a χ^2 comparison test between

CS quantities	Importance		CS quantities	Importance	
	Inclusive $\mathcal{P}_{\text{CS}}$	Selective $\mathcal{P}_{\text{CS}}$		Inclusive $\mathcal{P}_{\text{CS}}$	Selective $\mathcal{P}_{\text{CS}}$
R_2	100	–	H_1^{oo}	1	–
$\lvert\cos\theta_T\rvert$	53	100	CC_5^o	1	3
H_{20}^{so}	24	–	H_4^{oo}	1	4
H_{10}^{so}	17	–	H_{04}^{so}	1	4
T_o	12	–	CC_9^o	1	3
H_{12}^{so}	12	31	CC_3	1	–
$\lvert\cos\theta_{T_B,z}\rvert$	10	15	H_{03}^{so}	1	2
H_{22}^{so}	8	11	CC_7^o	0	2
T_B	7	–	H_{24}^{so}	0	3
CC_2^o	7	9	CC_8^o	0	2
H_0^{oo}	4	–	CC_9	0	–
χ	4	–	CC_6	0	–
H_{02}^{so}	4	19	H_{00}^{so}	0	–
H_{01}^{so}	4	7	H_3^{oo}	0	–
CC_3^o	3	6	CC_6^o	0	2
CC_1^o	2	4	CC_5	0	–
H_2^{oo}	2	–	CC_7	0	–
CC_2	2	–	CC_8	0	–
E_{T}	2	9	H_{14}^{so}	0	2
CC_1	2	–	CC_4	0	–
CC_4^o	1	4			

Table 4.2: The quantities considered in the training of two multivariate classifiers to suppress continuum, denoted as $\mathcal{P}_{\text{CS}}$, are listed. For the *inclusive* classifier, all variables are utilized, while the *selective* classifier only employs variables listed with a number in the corresponding column. These numbers represent the variable's importance for the multivariate classifier and are derived by quantifying the difference in the classifier's separation potential with and without the respective quantity. The importance values are normalized such that the most relevant quantity is assigned a value of 100.

experimental data and simulation[3] is excluded from the multivariate classifier, and a *selective* BDT is trained using only the well-modeled quantities. In Table 4.2, the relative importance of the remaining quantities is presented, while excluded quantities are indicated by not having a value.

In Figure 4.7, the output classifier values are compared between experimental data and simulation for both the inclusive and the selective BDT. Notably, the data-MC agreement improves when only well modeled quantities serve as input. Significance scans using $S/\sqrt{S+B}$ with $B\bar{B}$-event yields as signal S and continuum-event yields as background B demonstrate that the selective classifier,

[3] A relatively arbitrary threshold of $\chi^2/\text{dof.} < 3$ is chosen. In this study, only statistical uncertainties of the simulated distributions are considered, leading to an underestimation of the total uncertainties and artificially high resulting χ^2 values.

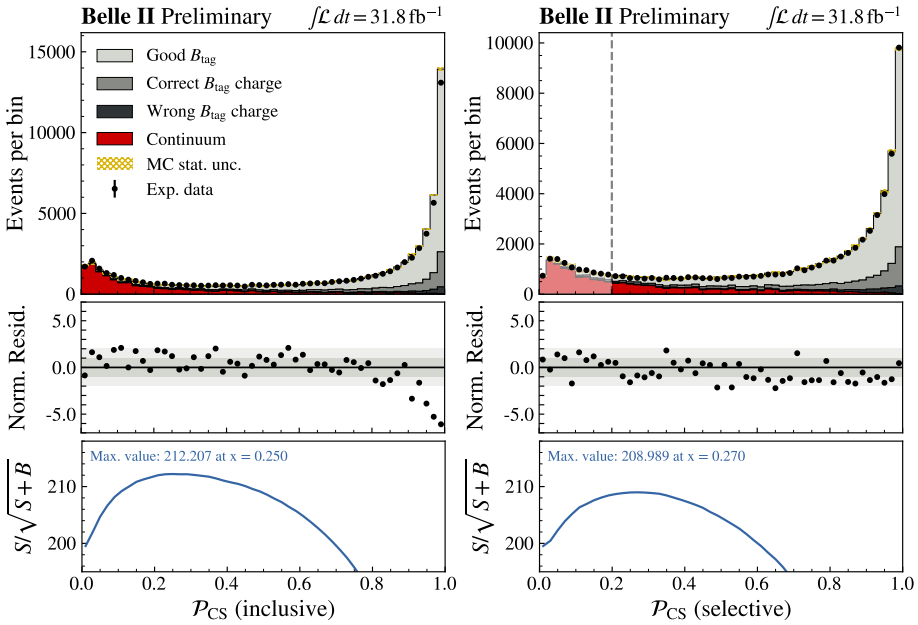

Figure 4.7: Experimental data is compared to MC simulations for both the *inclusive* classifier, utilizing all quantities listed in Table 4.2, and the *selective* classifier, relying solely on well-modeled ones (top row). Uncertainty-normalized residuals $(N_{\mathrm{Data}} - N_{\mathrm{MC}})/\sqrt{\sigma^2_{\mathrm{Data}} + \sigma^2_{\mathrm{MC}}}$ are shown below (central row). The separation potential of the classifiers is assessed through a significance scan, where the classifier threshold is incrementally raised along the x-axis, and the remaining number of signal $B\overline{B}$ events S is compared to the number of background continuum events B via $S/\sqrt{S+B}$ (bottom row). The event-selection requirement $\mathcal{P}_{\mathrm{CS}}$ (selective) > 0.2 is illustrated as a dashed line.

although not performing as well as an inclusive classifier, still provides substantial separation power. For the event selection, a conservative threshold value of $\mathcal{P}_{\mathrm{CS}} > 0.2$ is chosen based on the selective classifier, roughly rejecting 55% of the continuum events while retaining 96.5% of the $B\overline{B}$ events. The higher $S/\sqrt{S+B}$ values achievable by the inclusive classifier demonstrate that the continuum suppression can be optimized in future when the modeling of event-shape variables improves.

In theory, the separation of good and bad B_{tag} candidates could be similarly improved, as discussed in Section A.1 in the appendix. This refinement might enhance the good-B_{tag} purity sufficiently to enable a relaxation of the B_{tag}-selection criterion of $\mathcal{P}_{\mathrm{FEI}} > 0.1$, thereby resulting in substantially increased data sample sizes. However, given the existing inaccuracies in the modeling of c. m. energies, as depicted in Figure 4.4, no additional selections are implemented for now.

4.3 Signal-lepton selection in the $R(X_{e/\mu})$ measurement

The tracks and neutral ECL clusters not associated with the B_{tag} candidate constitute the B_{sig} side. Among the reconstructed tracks, either an electron or a muon candidate is required with a lepton charge corresponding to the inferred B_{sig} flavor.

Different signal-lepton requirements are applied for the measurements of $R(X_{e/\mu})$ and $R(X_{\tau/\ell})$. This section focuses on the criteria used in the measurement of $R(X_{e/\mu})$, as summarized in Table 4.3.

Section 7.1 motivates the updated lepton-selection requirements used for the measurement of $R(X_{\tau/\ell})$.

Signal lepton flavor	Requirements
ℓ	$p_\ell^B > 1.3\,\text{GeV}$, $\mathrm{d}r < 1\,\text{cm}$, $\lvert\mathrm{d}z\rvert < 3\,\text{cm}$, $\theta \in [17°, 150°]$
e	$\mathcal{P}_e : \epsilon_e = 80\%$, $p_e^{\mathrm{T}} > 0.3\,\text{GeV}$, $\mathcal{P}_p^{\mathcal{L}/\mathcal{L}} < 0.9$
μ	$\mathcal{P}_\mu^{\mathcal{L}/\mathcal{L}} > 0.95$, $p_\mu^{\mathrm{T}} > 0.4\,\text{GeV}$

Table 4.3: The requirements used to identify signal-lepton candidates in the $R(X_{e/\mu})$ measurement are presented. Common requirements for both lepton flavors are denoted by ℓ.

Prompt light leptons originating from $B \to X\ell\nu$ decays exhibit relatively higher momenta compared to leptons from $B \to X[\tau \to \ell\nu\nu]\nu$ decays. Moreover, as discussed in more detail in Section 7.1, various $B\bar{B}$-background events, semileptonic D-meson decays and hadrons mimicking leptons, yield lepton candidates with relatively low momenta. Consequently, in the measurement of $R(X_{e/\mu})$, a stringent requirement is imposed on the lepton momentum in the B_{sig} frame, specifically $p_\ell^B > 1.3\,\text{GeV}$ (see Fig. 4.12, presented in Sec. 4.5). This criterion is primarily chosen to ensure the independence of $R(X_{e/\mu})$ from potential beyond-SM contributions from $B \to X\tau\nu$ decays (see Sec 2.3.1), [4] but it also effectively suppresses the majority of background events.

The selection of electron candidates relies on $\mathcal{P}_e$ with classifier thresholds tuned in a three-dimensional grid of (p_ℓ, θ_ℓ, q) to achieve a uniform 80% identification efficiency (see Secs. 3.3.3, 3.4.4, Fig. B.1). The corresponding pion and kaon fake rates for $p_e > 1\,\text{GeV}$ are approximately 0.04% and less than 0.01%, respectively [213]. To suppress secondary electrons from other sources, their extrapolated trajectories are required to satisfy $\mathrm{d}r < 1\,\text{cm}$ and $\lvert\mathrm{d}z\rvert < 3\,\text{cm}$. Additionally, electron candidates are required to be within the CDC-acceptance region.

In contrast to the likelihood-ratio based classifier $\mathcal{P}_e^{\mathcal{L}/\mathcal{L}}$, high $\mathcal{P}_e$ values can coexist with high likelihoods for another particle type. Indeed, a notable fraction of fake electrons is attributed to antiprotons, which interestingly tend to be almost exclusively negatively charged. Fortunately, they are effectively suppressed by requiring $\mathcal{P}_p^{\mathcal{L}/\mathcal{L}} < 0.9$, rejecting 80% of the antiproton fakes while minimally affecting signal leptons ($\mathcal{O}(0.1\%)$).

Due to their small mass, bremsstrahlung radiation is common for electrons as they traverse the dense detector material. Therefore, their four-momenta are adjusted by incorporating photon candidates detected within a cone centered on the electron's direction. The opening angle of this cone is optimized in a dedicated study depending on the electron's momentum magnitude in the laboratory frame, as detailed in Section A.2 in the appendix. For $p_e > 1.0\,\text{GeV}$, the large majority of events in this measurement due to the stringent requirement on p_ℓ^B, photon clusters with $E_\gamma < 1.2\,\text{GeV}$ are added if their angle to the track falls within a 3.6° cone. For $p_e < 0.6\,\text{GeV}$ and $p_e \in [0.6, 1.0]\,\text{GeV}$, only relevant for electron candidates associated with the X system as outlined in Section 4.4, maximal photon energies of 90 MeV and 0.9 GeV are considered, respectively, and optimized cone opening angles of 7.8° and 4.2° are selected. The bremsstrahlung corrections are validated on experimental data in a study conducted by Paolo Rocchetti from Melbourne, which employs an inclusive sample of

[4] In fact, the measurement of $R(X_{e/\mu})$ was initially designed to serve as a cross-check in a high-p_ℓ^B control sample of the $R(X_{\tau/\ell})$ analysis. Additional minor requirements on the transverse lepton momenta p_ℓ^{T} (see Tab. 4.3) have been introduced in the same context.

$J/\psi \to e^+e^-$.

The bremsstrahlung correction method influences the distribution of electron momenta. However, as the measurements of $R(X_{e/\mu})$ and $R(X_{\tau/\ell})$ do not rely on electron momenta to reconstruct specific invariant masses of mother particles, the selection efficiencies are hardly affected. In general, there is good agreement between data and simulation in all pertinent bremsstrahlung properties, including the fraction of corrected electrons and the absolute and relative energy distributions of bremsstrahlung photons. Thus, both $R(X_{e/\mu})$ and $R(X_{\tau/\ell})$ are essentially unaffected by the specific bremsstrahlung-correction approach chosen, as demonstrated in Section 6.2.4.

Similar to electrons, muon candidates must be within the CDC-acceptance region and meet the criteria $\mathrm{d}r < 1\,\mathrm{cm}$ and $|\mathrm{d}z| < 3\,\mathrm{cm}$. Identification is based on $\mathcal{P}_\mu^{\mathcal{L}/\mathcal{L}}$, with a stringent requirement of $\mathcal{P}_\mu^{\mathcal{L}/\mathcal{L}} > 0.95$. For $p_\mu > 1\,\mathrm{GeV}$, the resulting muon selection efficiency averages to 90%, corresponding to pion and kaon fake rates of 3% and 1.2%, respectively [213].

If multiple signal-lepton candidates from the same event meet the criteria, the lepton with the highest likelihood-ratio classifier $\mathcal{P}_\ell^{\mathcal{L}/\mathcal{L}}$ is chosen.

4.4 Reconstruction of the hadronic system X

The hadronic system X is reconstructed using the remaining tracks and ECL clusters that are not associated with the B_{tag} or the signal-lepton candidate. They need to fulfill specific quality requirements outlined in Table 4.4, as motivated in the following.

Particle	Requirements
γ	$N_{\mathrm{crystal}} > 1.5$, $\lvert t_\gamma - t_0\rvert < 200\,\mathrm{ns}$, $\theta \in [17°, 150°]$, $E_\gamma^{\mathrm{forward}} > 40\,\mathrm{MeV}$, $E_\gamma^{\mathrm{barrel}} > 55\,\mathrm{MeV}$, $E_\gamma^{\mathrm{backward}} > 90\,\mathrm{MeV}$, $\Delta R_{\mathrm{cluster}}^{\mathrm{track}} > 30\,\mathrm{cm}$
Leptons	$\mathrm{d}r < 1\,\mathrm{cm}$, $\lvert\mathrm{d}z\rvert < 3\,\mathrm{cm}$, $\theta \in [17°, 150°]$
e	$\mathcal{P}_e : \epsilon_e = 80\%$, $p_e^{\mathrm{T}} > 0.3\,\mathrm{GeV}$, $\mathcal{P}_p^{\mathcal{L}/\mathcal{L}} < 0.9$
μ	$\mathcal{P}_\mu^{\mathcal{L}/\mathcal{L}} > 0.95$, $p_\mu^{\mathrm{T}} > 0.4\,\mathrm{GeV}$
Charged hadrons	$\mathrm{d}r < 2\,\mathrm{cm}$, $\lvert\mathrm{d}z\rvert < 4\,\mathrm{cm}$, $\theta \in [17°, 150°]$
K	$\mathcal{P}_K^{\mathcal{L}/\mathcal{L}} > 0.6$
p	$\mathcal{P}_p^{\mathcal{L}/\mathcal{L}} > 0.5$
π	all remaining tracks

Table 4.4: The requirements used to identify particle types within the X system are summarized. Lepton requirements are commonly applied to electron and muon candidates, while kaon, proton, and pion candidates need to satisfy the common requirements of charged hadrons.

4.4.1 Photon selection

The identification of photons faces the primary challenge of distinguishing them from ECL clusters generated by beam-induced backgrounds and from split-off clusters caused by charged hadrons (see Sec. 3.3.3).

In accordance with internal recommendations from the Belle II Neutral Particle Group, photon clusters are required to satisfy baseline-selection criteria outlined in Table 4.4. The number of ECL crystals included in the cluster, N_{crystal}, must exceed 1.5. Non-integer values arise when energies are split among neighboring clusters. Additionally, the fitted time of the recorded waveform of the highest-energy crystal, t_γ, in relation to the event time, t_0, is required to agree within 200 ns. Moreover, the angle θ must be within the CDC-acceptance region so that clusters caused by charged particles can be excluded based on their detected track.

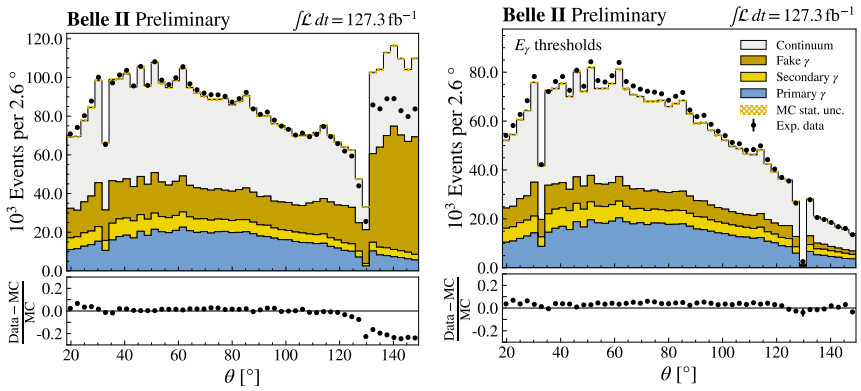

(a) Baseline-selection only

(b) Region-dependent E_γ requirements

Figure 4.8: The distribution of ECL clusters in the polar angle θ is illustrated for clusters meeting the baseline selection criteria (a) and those subjected to additional cluster-energy requirements (b). Simulated events are categorized into primary photons (light blue), generated at any stage within the $B\overline{B}$ decay chain; secondary photons (yellow), emerging in particle-detector interactions and encompassing split-off clusters caused by hadrons; and fake photons (gold), representing ECL clusters without MC particle origin, such as hadron split-offs (again) and clusters from beam-induced backgrounds. Additionally, continuum events, identified by off-resonance data without generator-level information, are summarized in one category (light gray).

In Figure 4.8(a), the distribution of ECL clusters with respect to the polar angle θ is presented. While experimental data agrees well with simulated distributions in most regions, it is apparent that the number of ECL clusters in the backward region ($\theta \in [130.7°, 155.1°]$) is overestimated by simulation. This region is expected to be highly polluted by beam-induced background events, that are particularly challenging to model. To investigate this further, the energy distributions of the reconstructed ECL clusters are studied, as shown in Figure 4.9 in the forward ($\theta \in [12.4°, 31.4°]$), barrel ($\theta \in [32.2°, 128.7°]$), and background regions, respectively.

A clear deficit in data compared to simulation is evident at low energies, where beam-induced background clusters are expected. This further supports the hypothesis that the data-MC discrepancies can be attributed to an overestimation of beam-induced backgrounds in the simulation. To address this, low-energy clusters are excluded by imposing minimal-energy requirements depending on the detector region. Specifically, ECL clusters are required to have energies greater than 40 MeV, 55 MeV, and

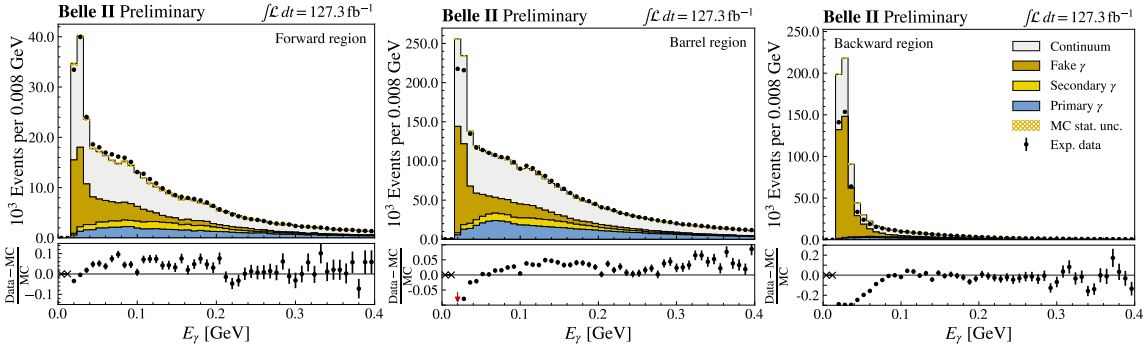

(a) Forward: $\theta \in [12.4°, 31.4°]$ (b) Barrel: $\theta \in [32.2°, 128.7°]$ (c) Backward: $\theta \in [130.7°, 155.1°]$

Figure 4.9: The energy distributions of ECL clusters are compared between experimental data and simulation in the forward (a), barrel (b) and backward (c) region. Simulated events are categorized as in Figure 4.8.

90 MeV in the forward, barrel, and backward region, respectively.

The variations in beam currents and collimator adjustments during different data-taking periods result in varying fractions of beam-induced backgrounds. Primary-photon clusters originating from $\Upsilon(4S) \rightarrow B\bar{B}$ events, however, are unaffected by changes in the beam current. Therefore, any dependencies in the ECL-cluster distribution on the data-taking period can be attributed to beam-induced backgrounds. Figure 4.10(a) illustrates the ECL-cluster distributions for different data-taking periods. Indeed, distinct patterns are observed when clusters are only required to meet the baseline-selection criteria. These discrepancies disappear when the minimal-energy requirements are applied, as demonstrated in Figure 4.10(b). This suggests that a sufficient beam-induced background suppression is achieved.

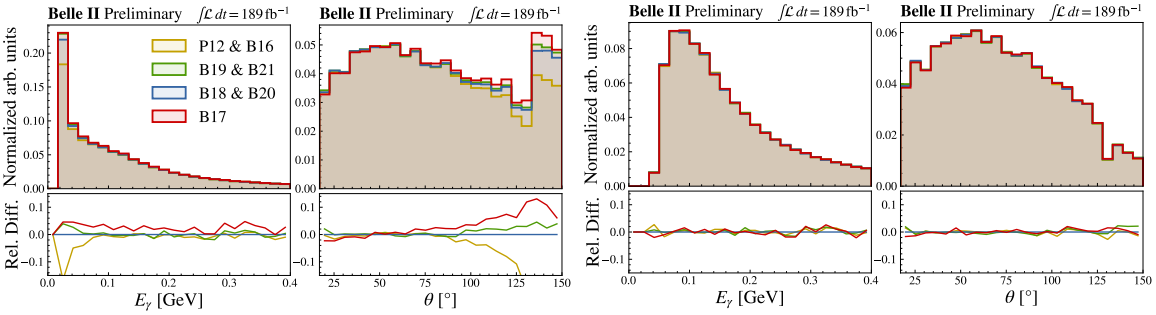

(a) Baseline selection only (b) Region-dependent E_γ requirements

Figure 4.10: The normalized energy and polar-angle distributions of ECL clusters are presented for different data-taking periods: "P12 & B16", recorded in 2020 with comparatively low beam currents (gold); and different data *buckets*, recorded early 2021 (green, blue, red). The clusters are selected using the baseline-selection only (a) or with additional region-dependent E_γ requirements (b). In the lower plots, the difference of each distribution compared to the blue "B18 & B20" is presented relative to the latter one.

Apart of beam-induced backgrounds, another significant source of backgrounds are split-off clusters caused by hadron interactions with the detector. Three quantities are studied to separate such clusters from physical photons. First, clusters caused by charged hadrons are expected to feature a small spatial

separation from the particle track. Therefore, the distance of the cluster to the closest track, $\Delta R^{\text{track}}_{\text{cluster}}$, is considered. Additionally, clusters caused by hadron interactions are expected to deviate in shape compared to photon clusters. This is utilized in the multivariate classifier $\mathcal{P}_{\text{Zernike}}$, which employs eleven Zernike moments [214]. Finally, a specific multivariate classifier was designed to suppress background clusters $\mathcal{P}_{\text{BKG}}$. Both, $\mathcal{P}_{\text{Zernike}}$ and $\Delta R^{\text{track}}_{\text{cluster}}$ serve as inputs together with more high-level cluster properties such as E_γ, θ_γ, and $|t_\gamma - t_0|$.

In Figure 4.11 all quantities are presented for experimental data and simulation. Moreover, their separation potential between physical photons originating from $B\overline{B}$ decays and background clusters is examined using the metric $S/\sqrt{S+B}$.

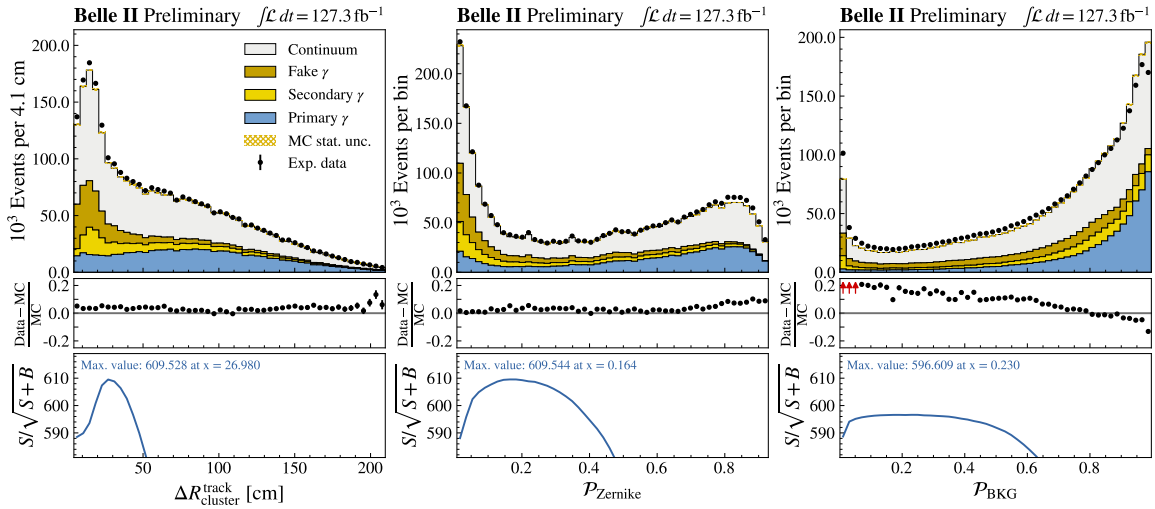

Figure 4.11: The most promising quantities for suppressing background clusters are compared between experimental data and simulation (top and center). Their separation potential, assessed through a significance scan with threshold values incrementally increasing with the x-axis, is illustrated in the bottom row. Simulated events are categorized as in Figure 4.8.

The multivariate classifier $\mathcal{P}_{\text{BKG}}$ exhibits a continuous drift in the ratio of experimental data to simulation, which cannot be attributed to mismodeling of background clusters. Consequently, this quantity is not considered further. The modeling of both $\Delta R^{\text{track}}_{\text{cluster}}$ and $\mathcal{P}_{\text{Zernike}}$ is satisfactory, and their separation potential is nearly identical. Hence, the simpler quantity $\Delta R^{\text{track}}_{\text{cluster}}$ is used and clusters are required to satisfy $\Delta R^{\text{track}}_{\text{cluster}} > 30\,\text{cm}$. All cluster requirements for photon identification are summarized in Table 4.4.

4.4.2 Charged-particle selection and X-system properties

Charged-particle tracks not associated with the B_{tag} or the signal-lepton candidate are assigned to the X system if they are consistent with originating from the interaction point. In comparison to lepton candidates, the IP requirements are slightly relaxed for hadron candidates to $\text{d}r < 2\,\text{cm}$ in radial direction and $|\text{d}z| < 4\,\text{cm}$ along the beam axis, allowing for the inclusion of tracks from $K^0_S \to \pi^+\pi^-$ decays. Mass hypotheses are assigned to the tracks in a sequential order. The mass of the first satisfied particle-identification criterion, listed in Table 4.4, is chosen in the order electron, muon, kaon, proton. Any remaining tracks that do not satisfy any of these criteria are assigned the pion mass.

In this context, electron candidates are chosen from reconstructed tracks with transverse momentum p_e^{T} exceeding 0.3 GeV. This criterion facilitates detection in the ECL, aiding the differentiation from charged hadrons. Muons are particularly challenging to distinguish from charged pions, especially at lower momenta, due to their similar masses. Therefore, the initial momentum threshold for muon candidates on the transverse momentum p_μ^{T} is set slightly tighter than for electrons, requiring $p_\mu^{\mathrm{T}} > 0.4\,\mathrm{GeV}$. Both times, the same LID-classifier working points are utilized as in the signal-lepton selection.

To maximize the inclusiveness of the analysis, no additional constraints are imposed. This approach minimizes potential data-MC bias by reducing the number of quantities on which the event selection relies. Furthermore, no efforts are made to combine particles within the X system into intermediate resonances like π^0, K_S^0, or Λ^0. Similarly, track curlers are not explicitly rejected, as investigations show discrepancies between experimental and simulated data for associated variables.

The four-momentum P_X of the X system is obtained by combining the four-momenta of all charged-particle and photon candidates associated with the X system. The invariant mass of the X system, denoted as M_X, is calculated via:

$$M_X = \sqrt{E_X^2 - |\vec{p}_X|^2}. \tag{4.7}$$

This quantity is crucial in the $R(X_{\tau/\ell})$ extraction, as detailed in Section 7.3. Additionally, the kinematic properties of the X system serve as input for the measurement of the momentum transfer (q^2) and the missing mass squared (M_{miss}^2):

$$q^2 = \left((\sqrt{s}, \vec{0}) - P_{B_{\mathrm{tag}}}^* - P_X^*\right)^2 \tag{4.8}$$

$$M_{\mathrm{miss}}^2 = \left((\sqrt{s}, \vec{0}) - P_{B_{\mathrm{tag}}}^* - P_X^* - P_\ell^*\right)^2. \tag{4.9}$$

Here, $P_{B_{\mathrm{tag}}}^*$ and P_ℓ^* represent the measured four-momenta of the B_{tag} and signal-lepton candidate in the c. m. system, respectively.

The criteria for selecting photons and charged particles are further investigated in relation to the ultimate precision on $R(X_{\tau/\ell})$. To achieve this, the $R(X_{\tau/\ell})$ signal-extraction fit, detailed in Chapters 5 and 8, is executed with varying degrees of stringency applied to the requirements for photon candidates or charged particles. Optimal signal significance is attained with the presented, relatively loose criteria, as imposing stricter requirements leads to an increased number of missed particles, consequently elevating M_{miss}^2 values. Given that high M_{miss}^2 values are a distinctive characteristic of $B \to X[\tau \to \ell\nu\nu]\nu$ signal decays, as elaborated in Section 8.1.1, overly stringent requirements diminish the potential for effective separation.

4.5 Event categorization

In Figure 4.12, the lepton momentum distributions in the B_{sig} rest frame, p_ℓ^B, are depicted for the electron and muon channels.

The simulated events are categorized based on the signal-lepton candidate's nature and origin, using generator-level information. The most frequently used event categories are introduced in the following.

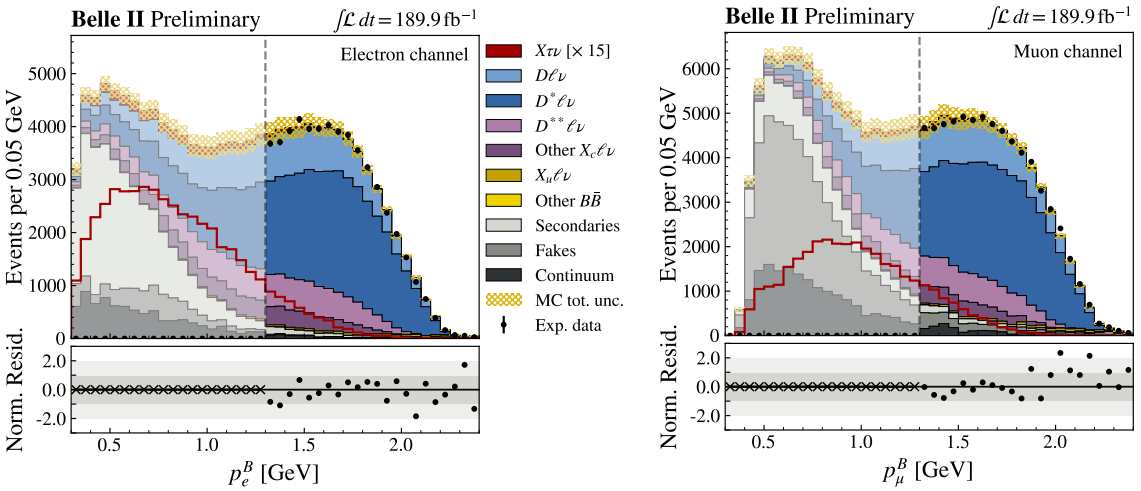

Figure 4.12: The lepton-momentum distributions in the B_{sig} rest frame, p_ℓ^B, are depicted for the electron (left) and muon (right) channels. The stringent requirement of $p_\ell^B > 1.3\,\mathrm{GeV}$, applied in the $R(X_{e/\mu})$ measurement, is represented by a dashed line. The $B \to X\tau\nu$ signal-decay distribution, enhanced by a factor of 15, is prominently displayed with a red line. Uncertainty-normalized residuals in box-opened regions $(N_{\mathrm{Data}} - N_{\mathrm{MC}})/\sqrt{\sigma^2_{\mathrm{Data}} + \sigma^2_{\mathrm{MC}}}$ are shown below.

- **$\mathbf{X\tau\nu}$:** Events are classified to be $B \to X\tau\nu$ signal decays when the lepton is correctly identified as an electron or muon, and the lepton's origin is a τ-lepton from a $B \to X\tau\nu$ decay. This category encompasses all possible hadronic states X. The specification of the leptonic decay mode ($\boldsymbol{X[\tau \to \ell\nu\nu]\nu}$) is used interchangeably, for instance, to highlight the light-lepton flavor.

- **$\mathbf{D^{(*)}\ell\nu}$:** Events with signal-lepton candidates correctly identified from a $B \to D\ell\nu$ decay are labeled accordingly, as are candidates from a $B \to D^*\ell\nu$ decay.

- **$\mathbf{D^{**}\ell\nu}$:** Events with signal-lepton candidates correctly identified from a $B \to D^{**}\ell\nu$ decay ($D^{**} = D_0^*, D_1', D_1, D_2^*$) are labeled accordingly. The D^{**} meson is restricted to decay into experimentally observed decay modes or their isospin-symmetric counterparts, in contrast to $B \to D^{**}_{\mathrm{gap}}\ell\nu$ decays, that are assigned to the next category.

- **Other $\mathbf{X_c\ell\nu}$:** This category includes signal-lepton candidates correctly identified from $B \to X_c\ell\nu$ decays that are not listed before. In this example, this encompasses the non-resonant D^{**}_{gap} modes $B \to D^{(*)}\pi\pi\ell\nu$ and $B \to D^{(*)}\eta\ell\nu$, which are simulated with an intermediate D_0^* or D_1' resonance (see Sec. 3.4.3), but also includes the rare $B \to D_s^{(*)}K\ell\nu$ decays.

- **$\mathbf{X_u\ell\nu}$:** This category comprises correctly identified signal-lepton candidates originating from resonant and non-resonant $B \to X_u\ell\nu$ decays, i.e., B-meson decays into light hadrons.

- **Other $\boldsymbol{B\bar{B}}$:** This category includes all $\Upsilon(4S) \to B\bar{B}$ processes that cannot be assigned to the other listed categories. In this example, only true signal-lepton candidates from $B \to X_s\ell\ell$ decays are included, which are extremely rare compared to the other events, with an order of $O(1)$ events.

- **Secondaries:** Events with signal-lepton candidates from $B\overline{B}$ events that are associated with a true lepton, originating neither from a B meson nor from a τ lepton in a $B \to X\tau\nu$ decay, are labeled as *secondaries*. This category mostly consists of electrons and muons from semileptonic D-meson decays but also includes events like $J/\psi \to \ell^+\ell^-$, $\gamma \to e^+e^-$, and $K^-/\pi^- \to \mu^-\overline{\nu}_\mu$.
- **Fakes:** Events with signal-lepton candidates from $B\overline{B}$ events not stemming from a true lepton are labeled *fakes*. This category is primarily composed of charged pions and kaons mimicking the signal lepton, and in the case of electrons, (anti)protons. Misreconstructed tracks lacking a generator-level particle origin also contribute.
- **Continuum:** Continuum events from $e^+e^- \to q\overline{q}$ decays are labeled accordingly. They are determined by off-resonance data (see Sec. 3.4.1).

In control samples enriched with specific processes, these categories are further divided or combined, such as into $B \to X\ell\nu$ ($\ell = e, \mu$) or $B \to Xl\nu$ ($l = e, \mu, \tau$) decays.

As illustrated in Figure 4.12, the high-momentum sample $p_\ell^B > 1.3\,\text{GeV}$ is predominantly populated by $B \to X\ell\nu$ decays, making it well-suited for the precise measurement of $R(X_{e/\mu})$ (see Chap. 6). The low-momentum sample is box-closed, i.e., no experimental data is used to probe $B \to X\tau\nu$ decays before their extraction in Section 8.2.1. Continuum backgrounds, as well as $B\overline{B}$ backgrounds (fakes and secondaries), are also most abundant at low-momenta. In the electron channel, backgrounds are predominantly composed of secondary events. In the muon channel, the total amount of backgrounds is higher, due to a notably larger occurrence of fake leptons.

CHAPTER 5

Signal-extraction fit setup

The determination of the inclusive branching-fraction ratios $R(X_{e/\mu})$ and $R(X_{\tau/\ell})$ relies on the measured yields N_k^{meas} for $B \to Xe\nu$, $B \to X\mu\nu$, and $B \to X[\tau \to \ell\nu\nu]\nu$ decays, along with their corresponding selection efficiencies ϵ_k, as outlined in Section 5.1. The yields are extracted in a maximum-likelihood fit to experimental data detailed in Section 5.2, while the selection efficiencies are obtained using MC simulation. The quantification of statistical and systematic uncertainties associated with N_k^{meas} and ϵ_k is fundamental to the presented measurements and is extensively discussed in Sections 5.3 and 5.4.

5.1 $R(X_{e/\mu})$ and $R(X_{\tau/\ell})$ determination

To compute $R(X_{e/\mu})$, the branching fraction for each light-lepton decay $B \to X\ell\nu$ is determined by dividing the extracted yield N_ℓ^{meas} by the corresponding selection efficiency $\epsilon_\ell = N_\ell^{\text{sel}}/N_\ell^{\text{gen}}$. This efficiency is calculated by comparing the number of events for the specific decay in simulation satisfying the event-selection requirements, N_ℓ^{sel}, to the total number of generated events for that decay, denoted as N_ℓ^{gen}. In each $\Upsilon(4S) \to B\bar{B}$ decay, two B mesons are produced. Therefore, N_ℓ^{gen} is given by $N_\ell^{\text{gen}} = 2 \cdot N_{B\bar{B}} \cdot \mathcal{B}(B \to X\ell\nu)$, using the corresponding branching fraction used in simulation (see Tab. 3.1). The quantity $N_{B\bar{B}}$ represents the generated number of $B\bar{B}$ pairs in simulation, which is $54 \cdot 10^6$ of B^+B^- events in addition to $51 \cdot 10^6$ of $B^0\bar{B}^0$ events in each 100 fb^{-1} of simulated data.

Consequently $R(X_{e/\mu})$ is determined as:

$$R(X_{e/\mu}) = \frac{\mathcal{B}(B \to Xe\nu)}{\mathcal{B}(B \to X\mu\nu)} = \frac{N_e^{\text{meas}}/\epsilon_e}{N_\mu^{\text{meas}}/\epsilon_\mu} = \frac{N_e^{\text{meas}}}{N_\mu^{\text{meas}}} \cdot \frac{N_\mu^{\text{sel}}}{N_e^{\text{sel}}} \cdot \frac{N_e^{\text{gen}}}{N_\mu^{\text{gen}}}. \tag{5.1}$$

The extracted yields N_ℓ^{meas} and the efficiencies ϵ_ℓ are treated as uncorrelated. However, due to shared systematic uncertainties, N_e^{meas} and N_μ^{meas}, as well as ϵ_e and ϵ_μ, exhibit correlations. Therefore, the

uncertainty on $R(X_{e/\mu})$, denoted as $\Delta R(X_{e/\mu})$, is expressed as follows:

$$\Delta R(X_{e/\mu})^2 = \left(\frac{R(X)\cdot\Delta N_e}{N_e}\right)^2 + \left(\frac{R(X)\cdot\Delta N_\mu}{N_\mu}\right)^2 + \left(\frac{R(X)\cdot\Delta\epsilon_e}{\epsilon_e}\right)^2 + \left(\frac{R(X)\cdot\Delta\epsilon_\mu}{\epsilon_\mu}\right)^2 + 2\cdot\left(\frac{R(X)}{N_e}\right)\cdot\left(-\frac{R(X)}{N_\mu}\right)\cdot C_{N_e,N_\mu} + 2\cdot\left(-\frac{R(X)}{\epsilon_e}\right)\cdot\left(\frac{R(X)}{\epsilon_\mu}\right)\cdot C_{\epsilon_e,\epsilon_\mu}. \tag{5.2}$$

In this equation, $R(X) \equiv R(X_{e/\mu})$ and $N_i \equiv N_i^{\text{meas}}$ are used for brevity. A leading Δ denotes the uncertainty associated with the respective variable, and $C_{i,j}$ denotes the covariance between two correlated values.

In the $R(X_{\tau/\ell})$ measurement, signal τ leptons are required to decay leptonically, $B \to X[\tau \to \ell\nu\nu]\nu$. Hence, the signal efficiency is computed as $\epsilon_{\tau\to\ell} = N^{\text{sel}}_{\tau\to\ell}/N^{\text{gen}}_{\tau\to\ell}$ with $N^{\text{gen}}_{\tau\to\ell} = N^{\text{gen}}_{\tau}\cdot\mathcal{B}(\tau\to\ell\nu\nu)$. The semitauonic B-meson branching fraction required for $R(X_{\tau/\ell})$ is obtained by $\mathcal{B}(B\to X\tau\nu) = \mathcal{B}(X[\tau\to\ell\nu\nu]\nu)/\mathcal{B}(\tau\to\ell\nu\nu)$, resulting in the cancellation of the dependence on $\mathcal{B}(\tau\to\ell\nu\nu)$ in a lepton-flavor specific extraction:

$$\begin{aligned} R(X_{\tau/\ell}) &= \frac{\mathcal{B}(B\to X\tau\nu)}{\mathcal{B}(B\to X\ell\nu)} = \frac{1}{\mathcal{B}(\tau\to\ell\nu\nu)}\cdot\frac{\mathcal{B}(X[\tau\to\ell\nu\nu]\nu)}{\mathcal{B}(B\to X\ell\nu)} = \frac{1}{\mathcal{B}(\tau\to\ell\nu\nu)}\cdot\frac{N^{\text{meas}}_{\tau\to\ell}/\epsilon_{\tau\to\ell}}{N^{\text{meas}}_{\ell}/\epsilon_{\ell}} \\ &= \frac{N^{\text{meas}}_{\tau\to\ell}}{N^{\text{meas}}_{\ell}}\cdot\frac{N^{\text{sel}}_{\ell}}{N^{\text{sel}}_{\tau\to\ell}}\cdot\frac{N^{\text{gen}}_{\tau\to\ell}/\mathcal{B}(\tau\to\ell\nu\nu)}{N^{\text{gen}}_{\ell}} = \frac{N^{\text{meas}}_{\tau\to\ell}}{N^{\text{meas}}_{\ell}}\cdot\frac{N^{\text{sel}}_{\ell}}{N^{\text{sel}}_{\tau\to\ell}}\cdot\frac{N^{\text{gen}}_{\tau}}{N^{\text{gen}}_{\ell}}, \quad \ell = \{e,\mu\}. \end{aligned} \tag{5.3}$$

The lepton-flavor specific ratios $R(X_{\tau/e})$ and $R(X_{\tau/\mu})$ are combined in a weighted average of correlated values $R(X_{\tau/\ell})$, following the methodology outlined in Reference [215], as expressed by

$$R(X_{\tau/\ell}) = \xi\cdot R(X_{\tau/e}) + (1-\xi)\cdot R(X_{\tau/\mu}) \quad \text{with} \quad \xi = \frac{\Delta_\mu^2 - C_{e,\mu}}{\Delta_e^2 + \Delta_\mu^2 - 2C_{e,\mu}}. \tag{5.4}$$

Here, Δ_ℓ represents the uncertainty of each lepton-flavor specific value of $R(X_{\tau/\ell})$, and $C_{e,\mu}$ denotes their correlation. The uncertainty on the combined average is determined, following the same reference and notation, as

$$\Delta R(X_{\tau/\ell})^2 = \frac{\Delta_e^2\Delta_\mu^2 - C_{e,\mu}}{\Delta_e^2 + \Delta_\mu^2 - 2C_{e,\mu}}. \tag{5.5}$$

5.2 Fit model

In the fitting procedure, the set of model parameters $(\vec{N}^{\text{meas}}, \vec{\theta})$ that provides the best agreement with experimental data is determined. Here, $\vec{N}^{\text{meas}} = (N_e^{\text{meas}}, N_\mu^{\text{meas}}, \dots)$ is a vector encompassing all extracted yields. For this purpose, a binned maximum-likelihood fit is performed that utilizes the shape differences of signal, normalization, and background events in one or two discriminating variables to extract their yields N_k^{meas}. The different event types are represented in the fit by normalized templates that are derived from MC simulation. The fraction of events of a specific event type k in bin

i is denoted f_{ik} and is directly obtained from the MC histogram h via

$$f_{ik} = \frac{h_{ik}}{\sum_j^{\text{bins}} h_{jk}}, \tag{5.6}$$

where h_{ik} is the number of reconstructed events of the event type k in histogram bin i. The total amount of expected events in each bin i is denoted by ν_i^{exp} and is obtained by summing over the expected fractions of each event type in this bin times their respective yields:

$$\nu_i^{\text{exp}}(\vec{N}^{\text{meas}}) = \sum_k^{\text{templates}} N_k^{\text{meas}} \cdot f_{ik}. \tag{5.7}$$

The probability of observing ν_i^{obs} events in bin i when ν_i^{exp} events are expected follows the Poisson distribution:

$$\mathcal{P}(\nu_i^{\text{obs}}|\nu_i^{\text{exp}}) = \frac{\left(\nu_i^{\text{exp}}\right)^{\nu_i^{\text{obs}}}}{\nu_i^{\text{obs}}!} \exp(-\nu_i^{\text{exp}}). \tag{5.8}$$

Therefore, the likelihood $\mathcal{L}$ of observing a specific distribution of events in experimental data is calculated as the product of independent Poisson probabilities for all bins:

$$\mathcal{L}(\vec{\nu}^{\,\text{obs}}|\vec{\nu}^{\,\text{exp}}(\vec{N}^{\text{meas}})) = \prod_i^{\text{bins}} \mathcal{P}(\nu_i^{\text{obs}}|\nu_i^{\text{exp}}). \tag{5.9}$$

Systematic template-shape uncertainties are directly integrated into the likelihood function through nuisance parameters θ_{ik} for each template k and bin i. This modifies Equation (5.6) to

$$f_{ik} = \frac{h_{ik} + \sigma_{ik}\theta_{ik}}{\sum_j^{\text{bins}} \left(h_{jk} + \sigma_{jk}\theta_{jk}\right)}, \tag{5.10}$$

where σ_{ik} denotes the uncertainty of the histogram entry h_{ik}. During the fitting procedure, the nuisance parameters are constrained by a multivariate Gaussian distribution $\mathcal{N}(\vec{\theta}|\,\vec{0}, \Sigma_\theta)$ with mean values $\vec{0}$ and the correlation matrix Σ_θ. This correlation matrix contains the bin-to-bin correlation within and among templates arising from systematic uncertainties. It is of size (bins · templates) × (bins · templates) and is derived from the total covariance matrix C_θ, discussed in Section 5.3.

Additionally, a template yield N_k^{meas} can be constrained to an external value with uncertainty $N_k^{\text{ext}} \pm \sigma_k^{\text{ext}}$ via $\mathcal{N}(N_k^{\text{meas}}|\,N_k^{\text{ext}}, \sigma_k^{\text{ext}})$. Consequently, the final likelihood function is given by

$$\mathcal{L}(\vec{\nu}^{\,\text{obs}}|\vec{\nu}^{\,\text{exp}}(\vec{N}^{\text{meas}}, \vec{\theta})) = \prod_i^{\text{bins}} \mathcal{P}(\nu_i^{\text{obs}}|\nu_i^{\text{exp}}) \cdot \mathcal{N}(\vec{\theta}|\vec{0}, \Sigma_\theta) \cdot \prod_k^{\text{constraints}} \mathcal{N}(N_k^{\text{meas}}|\,N_k^{\text{ext}}, \sigma_k^{\text{ext}}). \tag{5.11}$$

The set of model parameters $(\vec{N}^{\text{meas}}, \vec{\theta})$ that maximizes this function corresponds to the most suitable model to explain observed data. To enhance computational efficiency and avoid expensive products and exponential functions, the negative logarithm of the likelihood is minimized instead, utilizing an optimization procedure based on the MINUIT software package [216].

For the $R(X_{\tau/\ell})$ measurement presented in Chapter 8, four templates are defined for each lepton flavor: the signal template $X\tau\nu$, the normalization template $X\ell\nu$, the $B\bar{B}$-background template, and the template representing continuum events $e^+e^- \to q\bar{q}$. Both lepton flavors, $\ell = \{e, \mu\}$, are simultaneously fitted, resulting in a total of eight templates, to capture systematic correlations between lepton flavors. Off-resonance data is used to constrain the continuum-template yields $N^{\text{meas}}_{\text{cont.}}$ of each lepton flavor individually, based on the total observed number of lepton-flavor specific off-resonance data $N^{\text{obs}}_{\text{off-res}}$ via (see Sec. 3.4.1)

$$N^{\text{ext}}_{\text{cont.}} = N^{\text{obs}}_{\text{off-res}} \cdot c_{\text{off-res}} \cdot \frac{189\ \text{fb}^{-1}}{18\ \text{fb}^{-1}} \quad \text{and} \quad \sigma^{\text{ext}}_{\text{cont.}} = \sqrt{N^{\text{obs}}_{\text{off-res}}} \cdot c_{\text{off-res}} \cdot \frac{189\ \text{fb}^{-1}}{18\ \text{fb}^{-1}}. \tag{5.12}$$

For the $R(X_{e/\mu})$ measurement presented in Chapter 6, a similar setup is chosen. Since $B \to X\tau\nu$ decays are suppressed via a stringent p^B_ℓ threshold, any remaining $B \to X\tau\nu$ decays are merged into the $B\bar{B}$-background templates, which are constrained as outlined in Section 6.1.1.

The implementation of systematic uncertainties as nuisance parameters is discussed in the following.

5.3 Systematic uncertainties

Systematic effects introduce uncertainties to the input template shapes, and these uncertainties can be correlated between different templates and lepton flavors. They are quantified in a concatenated vector $\vec{\sigma}$ of size (bins · templates), where each entry represents the uncertainty of a template's histogram bin. This approach enables the quantification of correlations across different templates, which is particularly important for the achieved precision in the measurement of $R(X_{e/\mu})$. Similarly, all template-histogram entries are concatenated into the vector $\vec{h}$. A covariance matrix $C^{\text{syst.}}_\theta$ is constructed for each systematic uncertainty. The total covariance matrix C_θ, and subsequently, the correlation matrix Σ_θ used in the likelihood function (see Eq. (5.11)), is derived by summing all individual covariance matrices.

The total uncertainty of the selection efficiency ϵ_k of event type k is obtained by summing individual efficiency uncertainties in quadrature. Correlations across event types are tracked by the covariance matrix C_ϵ. It is convenient to define the vectors $\vec{\epsilon}$ and $\Delta\vec{\epsilon}$ of size k with event-type efficiencies and uncertainties as entries, respectively.

The quantification of the uncertainties is based on event weights w_{evt} and is outlined in the following. Here, the event weight $w_{\text{evt}} = w^{\mathcal{B}} \cdot w^{\text{LID}} \cdot \ldots$ is the product of all event-specific correction factors that are already applied to simulation, such as updates to the branching fractions (see Sec. 3.4.3) or calibrated lepton-identification efficiencies (see Sec. 3.4.4). If not stated differently, the running indices i and j always refer to the (bins · templates) entries of $\vec{h}$ or $\vec{\sigma}$ in this section.

5.3.1 Simulation-sample size

The limited number of simulated events introduces statistical uncertainties on the expected number of events per histogram bin h_i. For each bin i, these uncertainties are derived as

$$\sigma_i = \sqrt{\sum_{\text{evt}\in i} \left(w^2_{\text{evt}}\right)} \quad (i \in \text{bins, templates}). \tag{5.13}$$

The uncertainty on the selection efficiency $\Delta\epsilon_k$ for each event type k is calculated in a similar manner but by summing over all events of that type. The uncertainties associated with simulation-sample size are uncorrelated due to their statistical nature. Consequently, the covariance matrices are given by diagonal matrices $C_\theta^{\mathrm{MC}} = \mathrm{diag}(\vec{\sigma}^2)$ and $C_\epsilon^{\mathrm{MC}} = \mathrm{diag}(\Delta\vec{\epsilon})$.

5.3.2 Branching-fraction uncertainties

Branching-fraction uncertainties of exclusive decays like $B \to D^{(*,**)} l\nu$ alter the effective composition of inclusive $B \to Xl\nu$ decays. This causes a shape uncertainty in the $X\ell\nu$ and $X\tau\nu$ template histograms. The individual uncertainty on each histogram bin σ_i is quantified by replacing the event weight w_{evt} by $w_{\mathrm{evt}} \cdot \sigma^{\mathcal{B}}/w^{\mathcal{B}}$, where $w^{\mathcal{B}} \pm \sigma^{\mathcal{B}} = (\mathcal{B}_{\mathrm{new}} \pm \Delta\mathcal{B}_{\mathrm{new}})/\mathcal{B}_{\mathrm{MC}}$ for events of the specific probed branching fraction, and $w^{\mathcal{B}} \pm \sigma^{\mathcal{B}} = 1 \pm 0$ otherwise. Here, $\mathcal{B}_{\mathrm{MC}}$ is the branching fraction used in MC simulations, which is updated by the values $(\mathcal{B}_{\mathrm{new}} \pm \Delta\mathcal{B}_{\mathrm{new}})$ as summarized in Table 3.1.

The branching-fraction uncertainties for light leptons are assumed to be fully correlated between $B \to Xe\nu$ and $B \to X\mu\nu$ decays, resulting in the cancellation of most branching-fraction uncertainties for $R(X_{e/\mu})$. For simplicity, semitauonic branching-fraction uncertainties are assumed not to be correlated with those of light leptons, which is a conservative assumption.[1] Finally $\vec{\sigma}$ is obtained by the sum of replaced weights:

$$\sigma_i = \sum_{\mathrm{evt}\in i} \left(w_{\mathrm{evt}} \cdot \frac{\sigma^{\mathcal{B}}}{w^{\mathcal{B}}} \right) \quad (i \in \text{bins, templates}). \tag{5.14}$$

In the determination of the efficiency uncertainties, branching-fraction uncertainties simultaneously alter N^{sel} and N^{gen}, canceling most but not all of their impact on ϵ_k.

The branching-fraction uncertainties of one decay are fully correlated across all bins and templates that contain this decay. Therefore, the covariance matrices are constructed using the outer products $C_\theta^{\mathcal{B}} = \vec{\sigma} \otimes \vec{\sigma}$ and $C_\epsilon^{\mathcal{B}} = \Delta\vec{\epsilon} \otimes \Delta\vec{\epsilon}$.

5.3.3 Uncertainties of form-factor parameters

As described in Section 2.2.2, form-factor parameters govern the kinematic properties of the semileptonic B-meson decays. The number of parameters required to describe the decay varies depending on the decay mode and form-factor model. Experimental measurements of the parameters used in this thesis are provided in References [85, 89, 204, 205].

The uncertainties of the parameters are converted into histogram-shape uncertainties through event weights $w_{\mathrm{evt}}^{\mathrm{FF}}$. For this purpose, the software package HAMMER [217] is used. It provides weight factors for each event, quantifying the relative likelihood of this event to occur in one form-factor model with a specific set of parameters (FF_1) compared to another one (FF_2):

$$w_{\mathrm{evt}}^{\mathrm{FF}} = \frac{\mathrm{d}\Gamma_{\mathrm{evt}}^{\mathrm{FF}_1}}{\mathrm{d}\Gamma_{\mathrm{evt}}^{\mathrm{FF}_2}} \cdot \frac{\Gamma^{\mathrm{FF}_2}}{\Gamma^{\mathrm{FF}_1}}. \tag{5.15}$$

[1] In fact, as described in Section 3.4.3, the semitauonic branching fractions are directly proportional to the light-lepton ones, multiplied by predictions of the ratios $R(D^{(*,**)})$. The resulting positive correlation slightly reduces the uncertainty on $R(X_{\tau/\ell})$ associated with branching fractions. However, the uncertainties on $R(D^{(*,**)})$ are significantly larger than those on light-lepton branching fractions, making this effect negligible.

Here, the ratio of differential decay rates $\mathrm{d}\Gamma_{\mathrm{evt}}^{\mathrm{FF}_1}/\mathrm{d}\Gamma_{\mathrm{evt}}^{\mathrm{FF}_2}$ depends on the kinematic properties of the input event on generator level. Additionally, different form-factor models or parameter sets yield different total decay rates Γ^{FF}. Uncertainties on the total rate, however, are already considered in branching-fraction uncertainties (see Sec. 5.3.2). Therefore, the event weight is normalized by the ratio of total rates of the two compared models. Consequently, $w_{\mathrm{evt}}^{\mathrm{FF}}$ only reflects changes to the kinematic distributions.

This procedure is performed both to update MC simulations to more recent form-factor models as summarized in Section 3.4.3, and to quantify the effect of form-factor parameter uncertainties. For the latter, the measured parameter set, represented as the vector of nominal values $\vec{p}^{\,\mathrm{nom}}$, is orthogonally varied via

$$\vec{p}_m^{\,\pm} = \vec{p}^{\,\mathrm{nom}} \pm \sqrt{\lambda_m}\vec{e}_m \quad (m = 1, \ldots, N_{\mathrm{params}}). \tag{5.16}$$

Here, λ_m and $\vec{e}_m$ represent the m-th eigenvalue and eigenvector of the covariance matrix of the form-factor parameters.

Similar to the previous section, the impact on the template histograms is determined by replacing each event weight w_{evt} by $w_{\mathrm{evt}}^{\pm m} = w_{\mathrm{evt}} \cdot w_{\mathrm{evt}}^{\mathrm{FF}(\vec{p}_m^{\,\pm})}/w_{\mathrm{evt}}^{\mathrm{FF}(\vec{p}^{\,\mathrm{nom}})}$. This yields histograms that represent the up (+) and down (−) variations. The bin uncertainties are calculated for each eigendirection m through

$$\sigma_i^m = \frac{h_i^{+m} - h_i^{-m}}{2} \quad (i \in \text{bins, templates}), \tag{5.17}$$

and the covariance matrix, which includes correlated and anticorrelated bins, is given by

$$C_\theta^{\mathrm{FF}} = \sum_m^{N_{\mathrm{params}}} \vec{\sigma}^m \otimes \vec{\sigma}^m. \tag{5.18}$$

As the event selection relies on the lepton momentum, form-factor variations lead to an efficiency uncertainty despite their total-rate normalization. The efficiency uncertainty $\Delta\epsilon_k^{\mathrm{FF}}$ on event type k caused by each form-factor model is estimated by

$$\left(\Delta\epsilon_k^{\mathrm{FF}} \cdot N_k^{\mathrm{gen}}\right)^2 = \sum_m^{N_{\mathrm{params}}} \max\left(\left|\sum_{\mathrm{evt}\in k}\left(w_{\mathrm{evt}}^{+m}\right) - N_k^{\mathrm{sel}}\right|, \left|\sum_{\mathrm{evt}\in k}\left(w_{\mathrm{evt}}^{-m}\right) - N_k^{\mathrm{sel}}\right|\right)^2 \text{ with } N_k^{\mathrm{sel}} = \sum_{\mathrm{evt}\in k}\left(w_{\mathrm{evt}}\right). \tag{5.19}$$

The efficiency uncertainties associated with one form-factor model are assumed to be fully correlated across templates, i.e., $C_\epsilon^{\mathrm{FF}} = \Delta\vec{\epsilon}^{\,\mathrm{FF}} \otimes \Delta\vec{\epsilon}^{\,\mathrm{FF}}$.

More specific treatments of additional form-factor uncertainties are discussed in Section 8.1.2.

5.3.4 Uncertainties of the track-reconstruction efficiency

Uncertainties of the track-reconstruction efficiency are considered by assigning an uncertainty of 0.3% per track associated with B_{sig}. This number is based on recommendations from the Belle II Performance Group and is derived in studies using $e^+e^- \to \tau^+\tau^-$ events. Consequently, the relative event-specific uncertainty is given by

$$\sigma_{\mathrm{evt}}^{\text{track. eff.}} = (1.003)^{N_{\mathrm{tracks}}^{B_{\mathrm{sig}}}} - 1, \tag{5.20}$$

from which $\vec{\sigma}$ is calculated as in Equation (5.14) with $w^{\text{track. eff.}} = 1$. For $\Delta\epsilon_k$, the counterpart of Equation (5.14) is summed over all events of event type k and $C_{\epsilon}^{\text{track. eff.}} = \Delta\vec{\epsilon} \otimes \Delta\vec{\epsilon}$.

5.3.5 Lepton-identification uncertainties

As discussed in Section 3.4.4, uncertainties associated with the lepton identification are determined in a three-dimensional grid of lab-frame momentum p_ℓ, polar angle θ_ℓ, and lepton charge q for true and fake leptons of each lepton flavor. The extensive number of resulting weight factors and uncertainties makes an approach as used in the previous sections inconvenient. Instead, the LID-correction factor w_m^{LID} of each (p_ℓ, θ_ℓ, q) interval m is assigned a set of variations

$$\vec{w}_m^{\mathcal{G}} = w_m^{\text{LID}} + \vec{\mathcal{G}}\left(0, \sigma_m^{\text{stat.}}\right) + \vec{\mathcal{G}}_m\left(\vec{0}, C_w^{\text{syst.}}\right) \quad \left(m = 1, \ldots, N_{\text{intervals}}^{p_\ell, \theta_\ell, q} \text{ for } e, \mu, \pi \to e, \ldots\right). \tag{5.21}$$

Here, $\vec{\mathcal{G}}$ represents a set of $N_{\text{var}} = 300$ values generated from the corresponding Gaussian distribution. The statistical uncertainty of each correction factor $\sigma_m^{\text{stat.}}$ is assumed to be independent for each (p_ℓ, θ_ℓ, q) interval, while possible correlations of the systematic uncertainties between all correction factors are incorporated by using the m-th entry of a multivariate Gaussian distribution with covariance matrix $C_w^{\text{syst.}}$.

For the $R(X_{e/\mu})$ extraction, the systematic uncertainties are assumed to be fully correlated between all phase-space intervals of the same *lepton type* but uncorrelated between different types. In this context, lepton type refers to the lepton flavor, charge and origin. For example, efficiency-correction factors of positively charged electrons are not linked to fake-rate correction factors for negatively charged kaons mimicking muons. This approach leads to maximal efficiency uncertainties for $B \to Xe\nu$ and $B \to X\mu\nu$ decays.

In the high-momentum sample used for the $R(X_{e/\mu})$ extraction, the systematic uncertainties associated with the LID corrections used in this measurement are primarily influenced by discrepancies between the muon-efficiency calibration factors derived from the $J/\psi \to \mu^+\mu^-$ and the low-multiplicity $e^+e^- \to \mu^+\mu^-(\gamma)$ control channels. As recognized by the Belle II Particle Identification Group subsequently, these discrepancies are caused by an inaccurate treatment of the low-multiplicity trigger, resulting in a systematic shift of the correction factors across all intervals of (p_ℓ, θ_ℓ, q) for $e^+e^- \to \mu^+\mu^-(\gamma)$. Thus, the assumption of completely correlated systematic uncertainties is retroactively found to be valid.

The measurement of $R(X_{\tau/\ell})$ is particularly sensitive to the shapes of lepton-momentum distributions. Thus, for this measurement, the systematic uncertainties are assumed to be completely uncorrelated, resulting in maximal shape uncertainties, especially between the low-momentum and high-momentum regions.

Since the set of variations $\vec{w}_m^{\mathcal{G}}$ is assigned to each event in interval m, full correlation for uncertainties of the same factor are maintained across all templates, while factors from different (p_ℓ, θ_ℓ, q) intervals are either uncorrelated or only systematically correlated. A set of varied template histograms is generated by a set of replaced event weights for each bin i using

$$\vec{h}_i^{\mathcal{G}} = \sum_{\text{evt}\in i}\left(w_{\text{evt}} \cdot \frac{\vec{w}^{\mathcal{G}}}{w^{\text{LID}}}\right) \quad (i \in \text{bins, templates}). \tag{5.22}$$

Finally, the covariance matrix C_θ^{LID} is constructed as follows:

$$\left(C_\theta^{\mathrm{LID}}\right)_{ij} = \frac{1}{N_{\mathrm{var}} - 1} \sum_{n=1}^{N_{\mathrm{var}}} (h_{in}^{\mathcal{G}} - h_i)(h_{jn}^{\mathcal{G}} - h_j) \quad (i, j \in \text{bins, templates}). \tag{5.23}$$

The efficiency uncertainty for each event type k is estimated as the standard deviation, denoted std, of observed variations on N_k^{sel}:

$$\Delta\epsilon_k \cdot N_k^{\mathrm{gen}} = \mathrm{std}\left(\sum_{\mathrm{evt}\in k}\left(w_{\mathrm{evt}} \cdot \frac{\vec{w}^{\mathcal{G}}}{w^{\mathrm{LID}}}\right) - N_k^{\mathrm{sel}}\right) \quad (k \in \text{templates}). \tag{5.24}$$

The efficiency correlation between two event types k and l is determined by the Pearson correlation coefficients of the different variations on N_k^{sel} and N_l^{sel}.

As depicted in Figures B.2 to B.5, not all phase-space regions of all lepton types are covered by correction factors. In cases where correction factors are not available for certain lepton candidates, they are assigned a correction weight of $w^{\mathrm{LID}} = 1$. For uncovered regions, where correction weights are available for the lepton type in other phase-space regions, the weight uncertainty is determined by calculating the arithmetic average of the total (stat. & syst.) uncertainties, along with the deviations of the nominal weight factors from unity for this lepton type and charge:

$$\sigma^2_{\mathrm{uncovered}} = \left(N_{\mathrm{intervals}}^{p_\ell,\theta_\ell}\right)^{-1} \sum_{m}^{\mathrm{intervals}} \left[\sigma_m^2 + \left(w_m^{\mathrm{LID}} - 1\right)^2\right]. \tag{5.25}$$

For lepton types that lack coverage entirely, such as antiprotons mimicking electrons or lepton candidates based on a misreconstructed track without generator-level particle origin, a 100% uncertainty ($\sigma_{\mathrm{uncovered}} = 1$) is assigned. The weight variations for lepton candidates in uncovered phase-space regions or for uncovered lepton types are generated through

$$\vec{w}_m^{\mathcal{G}} = 1 + \vec{\mathcal{G}}\left(0, \sigma_{\mathrm{uncovered}}\right) (m \in \text{uncovered types}). \tag{5.26}$$

Distinct variations are generated independently for each uncovered lepton type and charge. Specifically, for electron candidates stemming from (anti)protons, separate variations are introduced for low- and high-momentum fake leptons ($p_e \lesseqgtr 1\,\mathrm{GeV}$). This distinction is motivated by differences in observed data-MC discrepancies in the proton-fake momentum distribution, as illustrated in Figure 5.1.

LID-efficiency corrections exhibit excellent coverage for all lepton flavor and charge configuration, ensuring complete coverage for all true leptons, including secondaries, in the measurements of $R(X_{e/\mu})$ and $R(X_{\tau/\ell})$. Likewise, correction weights are provided for nearly the entire phase space for pions falsely identified as leptons.

Table 5.1 provides a summary of the relative compositions of fake leptons per lepton flavor and charge in the $R(X_{e/\mu})$ and the $R(X_{\tau/\ell})$ measurements, respectively. The percentage of uncovered fake types relative to the total number of backgrounds in each lepton channel is presented, providing insights into their relative importance. Additionally, the relative uncertainty, derived by Equation (5.25), is displayed for uncovered lepton candidates.

In the $R(X_{e/\mu})$ analysis, 2.9% of the electron backgrounds, that are mostly composed of well-covered secondary leptons, are not covered by LID corrections (mostly antiproton fakes). In the muon channel,

Fake origin	Fake composition of this charge	Uncovered by LID tables	Rel. unc. of uncovered	Uncovered vs. tot. bkgs. of this lepton flavor
$R(X_{e/\mu})$: $[\mathcal{P}_e : \epsilon_e = 80\%, \mathcal{P}_\mu^{\mathcal{L}/\mathcal{L}} > 0.95, p_\ell^B > 1.3\,\text{GeV}]$				
$\pi^- \xrightarrow{\text{ID}} e^-$	30.7%	-	-	-
$K^- \xrightarrow{\text{ID}} e^-$	29.3%	0.7%	54%	0.01%
$\overline{p} \xrightarrow{\text{ID}} e^-$	38.7%	100%	100%	2.5%
Nan $\xrightarrow{\text{ID}} e^-$	1.6%	100%	100%	0.1%
$\pi^+ \xrightarrow{\text{ID}} e^+$	66.0%	-	-	-
$K^+ \xrightarrow{\text{ID}} e^+$	28.4%	0.7%	32%	0.01%
$p \xrightarrow{\text{ID}} e^+$	1.0%	100%	100%	0.05%
Nan $\xrightarrow{\text{ID}} e^+$	4.6%	100%	100%	0.2%
$\pi^- \xrightarrow{\text{ID}} \mu^-$	66.4%	-	-	-
$K^- \xrightarrow{\text{ID}} \mu^-$	24.1%	-	-	-
Nan $\xrightarrow{\text{ID}} \mu^-$	9.4%	100%	100%	3.1%
$\pi^+ \xrightarrow{\text{ID}} \mu^+$	65.4%	-	-	-
$K^+ \xrightarrow{\text{ID}} \mu^+$	25.5%	-	-	-
Nan $\xrightarrow{\text{ID}} \mu^-$	9.1%	100%	100%	3.0%
$R(X_{\tau/\ell})$: $[\mathcal{P}_e > 0.99, p_e > 0.5\,\text{GeV}, \mathcal{P}_\mu^{\mathcal{L}/\mathcal{L}} > 0.99, p_\mu > 0.7\,\text{GeV}]$				
$\pi^- \xrightarrow{\text{ID}} e^-$	12.2%	-	-	-
$K^- \xrightarrow{\text{ID}} e^-$	31.3%	2.3%	372%	0.05%
$\overline{p} \xrightarrow{\text{ID}} e^-$	54.0%	100%	100%	3.4%
Nan $\xrightarrow{\text{ID}} e^-$	2.5%	100%	100%	0.01%
$\pi^+ \xrightarrow{\text{ID}} e^+$	39.8%	1.0%	356%	0.01%
$K^+ \xrightarrow{\text{ID}} e^+$	57.0%	2.0%	1 052%	0.04%
$p \xrightarrow{\text{ID}} e^+$	1.5%	100%	100%	0.05%
Nan $\xrightarrow{\text{ID}} e^+$	1.7%	100%	100%	0.05%
$\pi^- \xrightarrow{\text{ID}} \mu^-$	73.7%	-	-	-
$K^- \xrightarrow{\text{ID}} \mu^-$	16.9%	25.4%	95%	1.3%
Nan $\xrightarrow{\text{ID}} \mu^-$	9.4%	100%	100%	2.9%
$\pi^+ \xrightarrow{\text{ID}} \mu^+$	74.6%	-	-	-
$K^+ \xrightarrow{\text{ID}} \mu^+$	16.3%	25.3%	43%	1.4%
Nan $\xrightarrow{\text{ID}} \mu^-$	9.1%	100%	100%	3.0%

Table 5.1: The relative composition of mis-identified leptons is summarized for both lepton flavors and charges in the $R(X_{e/\mu})$ (top) and the $R(X_{\tau/\ell})$ (bottom) measurements. Lepton-candidates caused by misreconstructed tracks are labeled *Nan*.The relative coverage of the LID correction tables is displayed for each fake type and, if applicable, their assigned relative uncertainty is presented. Additionally, their total relevance compared to the whole background composition per lepton channel (electron or muon, charges combined) is listed.

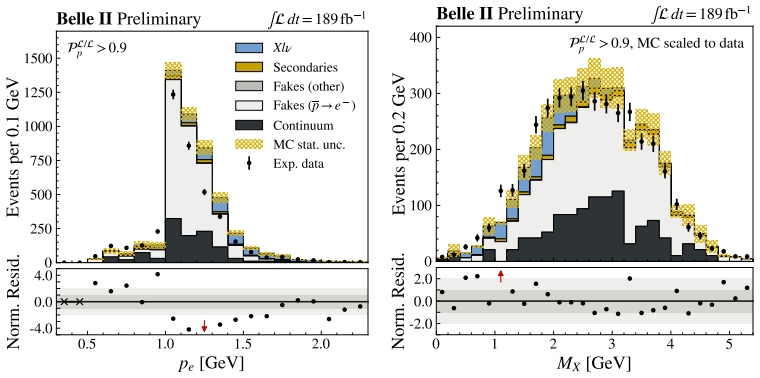

Figure 5.1: Simulation is compared to experimental data in the proton-fake enriched control sample defined by $\mathcal{P}_p^{\mathcal{L}/\mathcal{L}} > 0.9$ as introduced in Section 7.2.1. Below each plot, uncertainty-normalized residuals are shown, excluding the introduced 100% LID uncertainty. The left plot, illustrating the momentum distribution, justifies the introduction of uncorrelated sets of LID correction-weight uncertainties for proton fakes below and above $p_e = 1\,\text{GeV}$. In the right plot, depicting the distribution of proton fakes in M_X, the overall MC yield is adjusted to match the data, enhancing the comparability in shape rather than yield.

in total 6.1% of all backgrounds are not covered. In the $R(X_{\tau/\ell})$ analysis, the total uncovered fractions are 3.6% for the electron channel and 8.6% for the muon channel. In both analyses, the total background composition is carefully reinvestigated and calibrated in control samples as outlined in Sections 6.1.1 and 7.3.4.

5.4 Independence of the B_{tag}-selection efficiency

As discussed in Section 4.1, significant deviations between experimental and simulated data are observed for the B_{tag}-selection efficiency, caused by various effects.

To mitigate systematic uncertainties associated with the B_{tag}-selection efficiency in the measurements, the selection of B_{tag} candidates is conducted independently of any signal-side information. Moreover, the semileptonic B-meson decay rates are measured in ratios $R(X_{\tau/\ell})$ and $R(X_{e/\mu})$, where the tag-induced data-MC bias is expected to cancel. In this section, the validity of this assumption is demonstrated for the tau-to-light-lepton ratio $R(X_{\tau/\ell})$ (see Sec. 5.4.1) and for the electron-to-muon ratio $R(X_{e/\mu})$ (see Sec. 5.4.2).

5.4.1 Signal vs. normalization decays

In this study, the requirement specified in Table 4.3 of $p_\ell^B > 1.3\,\text{GeV}$ is omitted from the event selection, allowing for low-momentum signal-lepton candidates with $p_e^{\text{T}} > 0.3\,\text{GeV}$ and $p_\mu^{\text{T}} > 0.4\,\text{GeV}$. Figure 5.2 provides a comparison of key B_{tag} properties between signal ($B_{\text{sig}} \to X\tau\nu$) and normalization ($B_{\text{sig}} \to X\ell\nu$) decays **in simulation**.

The normalized distributions for the FEI output classifier $\mathcal{P}_{\text{FEI}}$, essential in the event selection, are presented. Moreover, the composition of FEI reconstruction modes, as summarized in Tables B.1 and B.2, is compared between signal and normalization decays. In each case, the $X\tau\nu$ and $X\ell\nu$ distributions are statistically consistent with the hypothesis that they are drawn from the same underlying

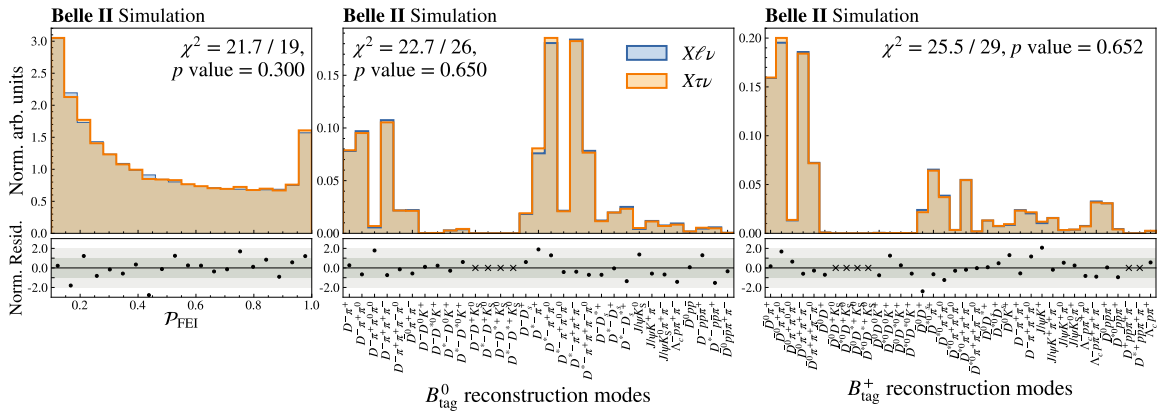

Figure 5.2: The normalized $\mathcal{P}_{\text{FEI}}$ and B_{tag} reconstruction-mode distributions are presented for $B \to X\tau\nu$ and $B \to X\ell\nu$ decays, along with the uncertainty-normalized residuals shown below. A χ^2 test is performed, not considering empty bins, to assess the hypothesis that signal and normalization distributions agree within statistical uncertainty. The corresponding p values are provided in each figure, with one degree of freedom subtracted from the count of filled bins to account for the normalization of the distributions.

distribution, as demonstrated in χ^2 tests. The unobserved reconstruction modes $B_{\text{tag}} \to \overline{D}^{(*)} D^{(*)+} K^0_S$, $B^+_{\text{tag}} \to D^{(*)+} p\bar{p}\pi^+\pi^-$, and $B^0_{\text{tag}} \to \overline{D}^{*0} p\bar{p}\pi^+\pi^-$ (not shown) are excluded from the χ^2 tests.

The absence of any observable discrepancies in the reconstruction-mode distribution between signal and normalization decays strongly supports the assumption that any mechanism introducing tag-side dependencies is not manifesting in a significant way. This finding underscores the independence of the ratio $R(X_{\tau/\ell})$ from B_{tag} properties.

Any interference between particles from the B_{sig} decay and the selected B_{tag} candidate, or vice versa, would lead to the classification of these events as bad B_{tag} candidates. Consequently, B_{tag} dependencies on the signal side would be evident in varied fractions of bad to good tags for different B_{sig} decay modes. As detailed in Section 4.1, the beam-constrained mass M_{bc} serves as an excellent discriminator between bad and good tags, providing a robust indication of whether the B_{tag} selection is differently affected by B_{sig}-meson decays into $X\tau\nu$ compared to $X\ell\nu$.

In Figure 5.3(a), the normalized M_{bc} distributions are displayed for various event types. Fake and secondary events feature a significantly lower fraction of events in the $M_{\text{bc}} \approx m_B$ peak compared to $X\ell\nu$ or $X\tau\nu$ decays, suggesting a reduced presence of good B_{tag} candidates. Analogously, their fraction of events with a bad B_{tag} candidate, contributing to the empirical ARGUS function, is higher. This observation may be attributed to the fact that most fake and secondary events emerge from hadronically decaying B_{sig} mesons, leading to higher multiplicities compared to semileptonic B_{sig} decays. As a result, the probability of falsely assigning one of the signal-side particles to the B_{tag} is enhanced.

Signal and normalization decays, however, feature the same final-state particles so that equal good-to-bad B_{tag} fractions are expected. A χ^2 test confirms the statistical consistency of their M_{bc} distributions within uncertainties. Moreover, the comparison of high- and low-momentum $B \to X\ell\nu$ decays in Figure 5.3(b) does not reveal evidence of a dependence of M_{bc} on the signal-lepton momentum. Given that the lepton momentum is the primary distinction between signal and normalization decays (in addition to the number of undetected neutrinos) this further substantiates the assumption of tag-side

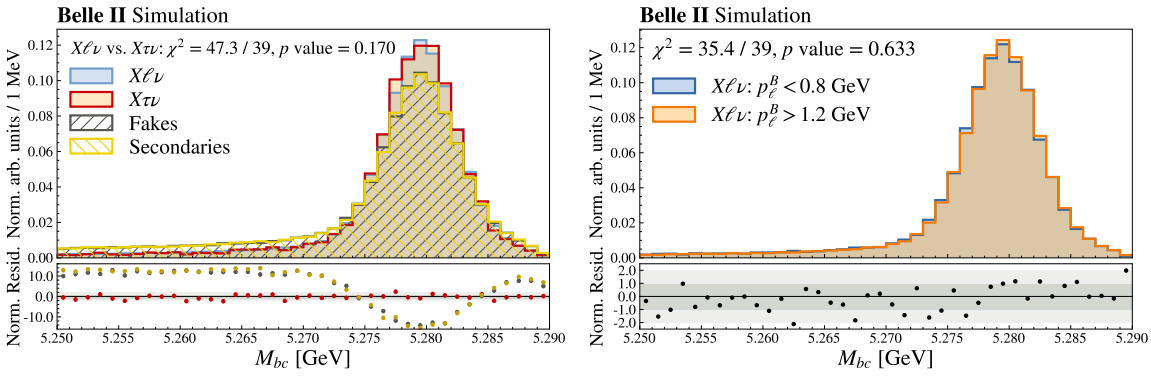

(a) (b)

Figure 5.3: In (a), the normalized M_{bc} distributions for fakes, secondaries, $X\tau\nu$, and $X\ell\nu$ events are presented, with uncertainty-normalized residuals compared to the $X\ell\nu$ distribution shown below. A χ^2 test is performed on the latter two distributions, supporting the assumption that they are indistinguishable within statistical uncertainties. In (b), the M_{bc} distributions for normalization decays are shown, categorized by high and low lepton momenta, and compared in a χ^2 test.

equality for $X\tau\nu$ and $X\ell\nu$.

In summary, no difference in the B_{tag} properties is observed in simulated signal and normalization modes within statistical precision. A repetition of the studies in a lepton-flavor specific manner, i.e., $X[\tau \to e\nu\nu]\nu$ vs. $Xe\nu$ and $X[\tau \to \mu\nu\nu]\nu$ vs. $X\mu\nu$, yields the same conclusion. This makes any efficiency difference between the two templates highly unlikely, as it would need to be caused by factors not adequately represented in simulation.

To further investigate and rule out such a scenario, the **B_{tag} properties** are also examined **in experimental data** in the following.

Two challenges complicate such a comparison: the absence of a kinematic region with high signal purity and the difficulty of conducting the test without box-opening. A signal-enriched data sample is defined by $p_\ell^B < 1.0\,\text{GeV}$ and $M_{\text{miss}}^2 > 5.0\,\text{GeV}$ (see Fig. 8.1), resulting in a composition of 45% $X\ell\nu$, 32% $B\overline{B}$ backgrounds, 12% continuum events and 11% $X\tau\nu$ decays in simulation. Any potential B_{tag} differences are expected to first manifest in distinct M_{bc} distributions. Therefore, this study focuses on M_{bc} to address the limited statistical precision of this sample. Unfortunately, the M_{bc} range is constrained to $M_{\text{bc}} \in [5.2725, 5.285]\,\text{GeV}$ (see Eq. (4.3)) in this study.

In the initial step, the non-signal event types are subtracted from experimental data to exclusively attribute remaining events to signal decays. The M_{bc} shape of continuum events can be directly inferred from off-resonance data, utilizing the entire off-resonance data set to increase statistical precision. The M_{bc} shapes of the normalization mode are determined in experimental data with a requirement of $p_\ell^B > 1.6\,\text{GeV}$ (see Figs. 4.12 and B.17), achieving a purity of over 95% for $X\ell\nu$ decays. Backgrounds from $B\overline{B}$ events, i.e., fakes and secondaries, are constrained in the control sample $M_X > 3.0\,\text{GeV}$, which is composed of 4% $X\ell\nu$ decays, 23% continuum, and 73% $B\overline{B}$-background events (see Fig. B.20).

As demonstrated in Figure 5.4, off-resonance data features a significantly different M_{bc} shape compared to on-resonance data, as expected due to the absence of any good-tag candidates. Meanwhile, the M_{bc} shapes of experimental data agree well with predictions from simulation in the $X\ell\nu$ enriched

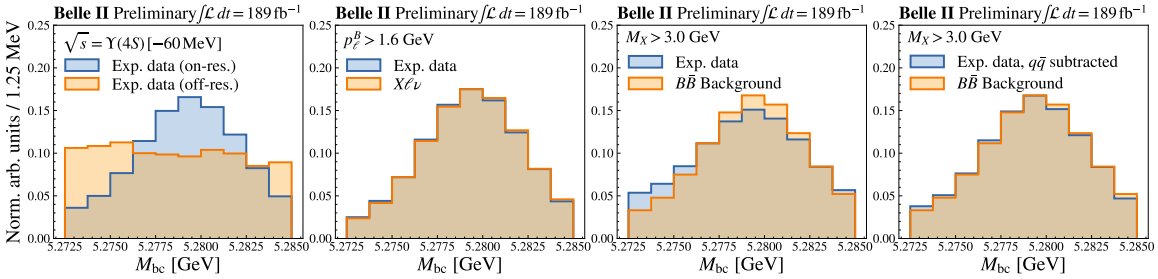

Figure 5.4: The normalized M_{bc} distributions in experimental data and simulation are presented for off-resonance data compared to on-resonance data (left), in a $X\ell\nu$-enriched control sample (center left), and a $B\bar{B}$ background-enriched sample (center right). After subtracting continuum components from data in the latter sample, experimental data shows improved agreement with the $B\bar{B}$-background shape predictions (right).

control sample. In the background-enriched high-M_X sample, the M_{bc} shapes in data do not match predictions from $B\bar{B}$ backgrounds alone. However, after subtracting the expected 23% continuum contribution, the remaining experimental data shape aligns well with the $B\bar{B}$ background-only M_{bc}-shape prediction.

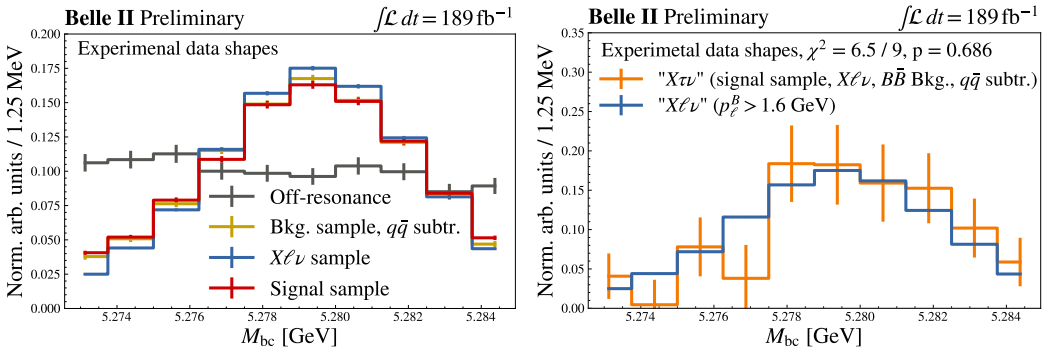

(a) (b)

Figure 5.5: In (a), the normalized M_{bc} distribution of experimental data in the signal-enriched sample is compared to experimental-data predictions of the three additional event types, as derived from Figure 5.4. The background-subtracted experimental data is then used to determine the M_{bc} shape for $X\tau\nu$, which is compared in a χ^2 test to the experimental observation of M_{bc} for $X\ell\nu$ (b).

In Figure 5.5(a), the M_{bc} shapes of the three extracted event types are compared to experimental data in the signal-enriched sample. To maintain a box-closed analysis, only normalized shapes of experimental data in the signal sample are considered. The expected M_{bc} shape of signal events in experimental data is determined by subtracting the M_{bc} shapes of the three other event types from the total M_{bc} shape in this sample. In this procedure, the absolute expected yield for each background component is derived from simulation. Assuming that their yield predictions are well-modeled, the remaining experimental data should exclusively arise from $X\tau\nu$ decays, regardless of any deviation in its yield from the simulated SM expectation. The subtracted data is then normalized to avoid revealing the actual signal-yield expectation and compared to the normalized M_{bc} shape of the $X\ell\nu$ control sample in a χ^2 test, as illustrated in Figure 5.5(b).

No evidence for an M_{bc}-shape difference in the signal and normalization mode is found in experimental data ($\chi^2 = 6.5/9$, corresponding to a p value of 0.686), although the statistical precision of the signal-shape prediction is very limited. The same procedure is repeated to test the B_{tag} reconstruction-mode distribution as presented in Figure 5.6. Again, no evidence for differences between signal and normalization is found within very high statistical uncertainties.

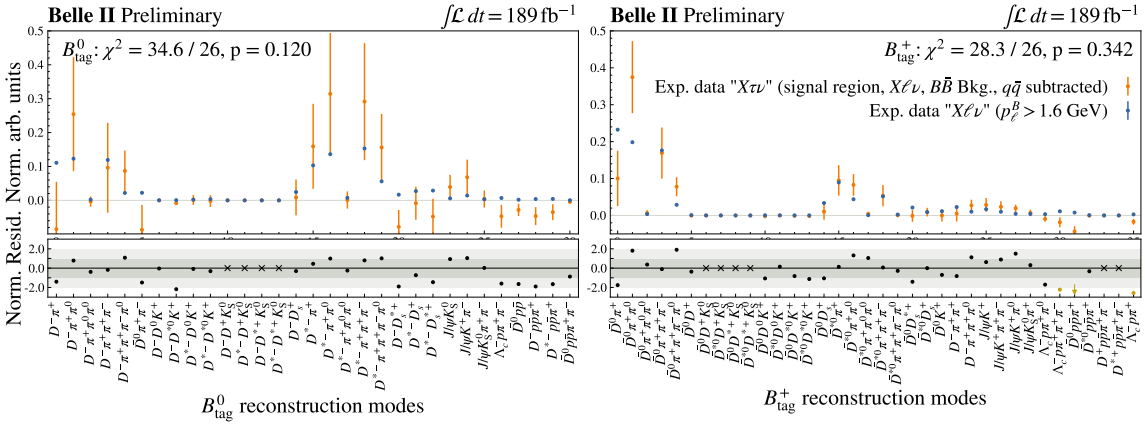

Figure 5.6: The B_{tag} reconstruction-mode distributions are compared between experimental data for background-subtracted $X\tau\nu$ and $X\ell\nu$. The agreement is quantified in χ^2 tests, excluding empty bins. Bins with significantly negative values are likely a result of background event overestimations, probably due to limited statistics especially in off-resonance data. These three bins in B^+, highlighted by yellow residuals, account for less than 1% of the normalization and signal decays, making their overall impact on $X\tau\nu$ and $X\ell\nu$ negligible. As a result, they are excluded from the χ^2 test.

The conclusions drawn from the aforementioned tests align with numerous similar analyses conducted within the Belle II collaboration. As a whole, there is no indication of a B_{tag} dependence on the signal side that is not adequately modeled. Consequently, this analysis operates under the assumption that the tagging efficiency completely cancels out in the measured ratio $R(X_{\tau/\ell})$ within the provided statistical precision, and no additional uncertainties are introduced.

5.4.2 Electron vs. muon normalization decays

In the $R(X_{e/\mu})$ measurement, the $B \to Xe\nu$ branching fraction is measured relative to $\mathcal{B}(B \to X\mu\nu)$, requiring $p^B_\ell > 1.3\,\mathrm{GeV}$ for both lepton flavors. This section investigates any potential data-MC bias in this ratio induced by the B_{tag} selection.

Figure 5.7 illustrates the normalized B_{tag} reconstruction-mode distributions in both experimental data and simulation for the electron and muon channels. In both cases, there is an observed disagreement in the relative fraction of certain reconstruction modes between $Xe\nu$ and $X\mu\nu$. For the muon channel, the fraction of selected B_{tag} candidates in $B_{\mathrm{tag}} \to \overline{D}^{(*)}\pi^+\pi^0$ reconstruction modes is enhanced compared to the electron channel. Similarly, B_{tag}-candidate decays into $B_{\mathrm{tag}} \to \overline{D}^{(*)}\pi^+\pi^+\pi^-(\pi^0)$ and $B_{\mathrm{tag}} \to \overline{D}D_s$ are relatively more frequent for B_{sig} decays into $Xe\nu$.

Speculatively, this phenomenon could be attributed to the increased difficulty in distinguishing muons from charged pions compared to electrons. Consequently, a signal muon might more frequently be misidentified as a pion associated with the B_{tag}, leading to a higher likelihood of the B_{tag}-candidate

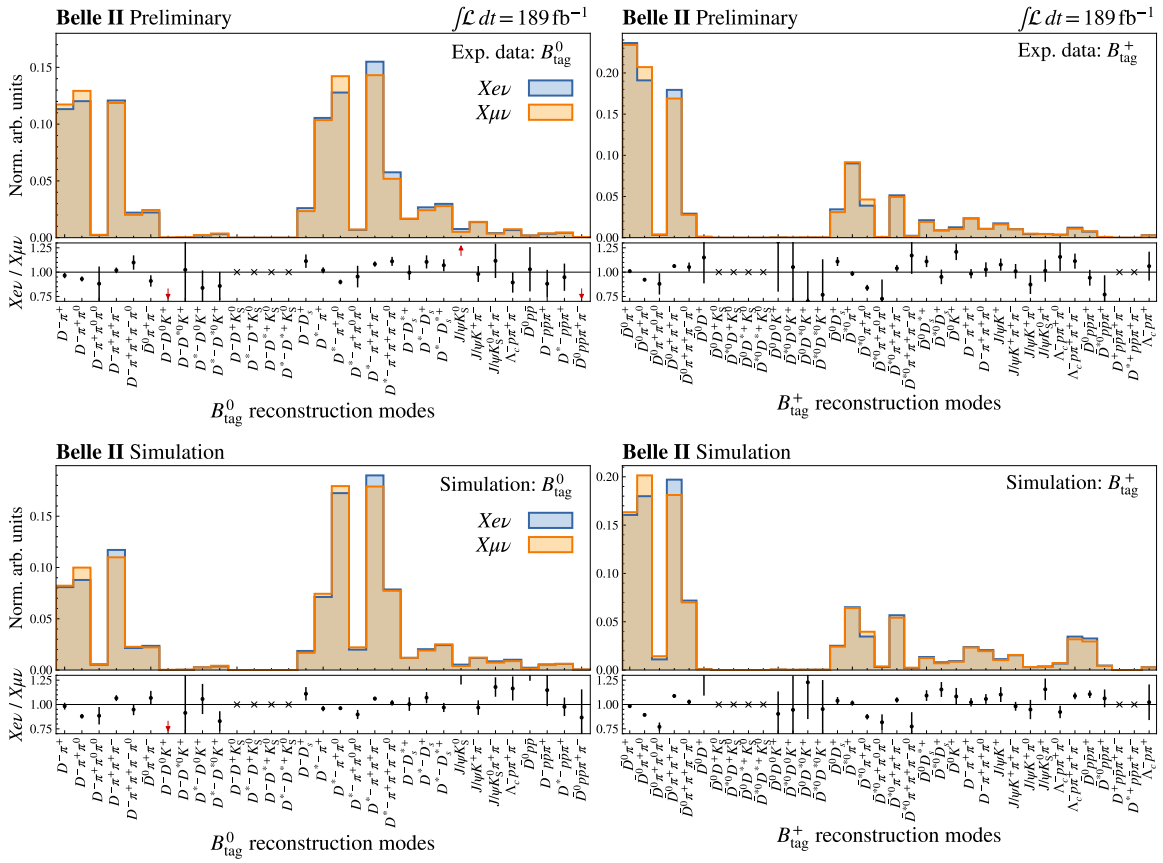

Figure 5.7: The normalized B_{tag} reconstruction-mode distributions for $B \to Xe\nu$ and $B \to X\mu\nu$ decays are displayed in experimental data (top) and simulation (bottom). The corresponding ratios of reconstruction-mode fractions are shown below.

to be rejected during the subsequent event selection based on $\mathcal{P}_{\text{FEI}}$ or M_{bc}. As a result, B_{tag} modes with a higher abundance of charged pions may experience a marginal depletion in the muon channel.

Differences in B_{tag} distributions for $Xe\nu$ and $X\mu\nu$ decays become relevant for $R(X_{e/\mu})$ only if these discrepancies are not accurately represented in the simulation. However, both experimental and simulated data show similar excesses. To quantify if these excesses are appropriately captured in the simulation, the relative ratio of normalized fractions for $Xe\nu$ and $X\mu\nu$ per reconstruction mode is compared between experimental data and simulation in Figure 5.8. The equivalence of the $Xe\nu/X\mu\nu$-ratio distributions in experimental data and simulation is tested in a χ^2 test. The resulting p values, 0.127 for B^0_{tag} candidates and 0.568 for B^+_{tag} candidates, provide no evidence of mismodeling of the electron-muon differences in the reconstruction-mode distributions.

The mismodeling of B_{tag}-selection efficiencies depends on the reconstruction mode as observed in the data-MC differences in Figure 5.9. This can be attributed in part to the inadequate modeling of D decays as discussed in more detail in Section 7.2.3, but various additional factors, such as mismodeled particle-identification probabilities and vertex-reconstruction efficiencies, may contribute. To ensure the absence of bias in the $R(X_{e/\mu})$ measurement, the mismodeling is required to be independent of the signal-lepton flavor. A comparison of the reconstruction-mode-dependent data-MC discrepancies

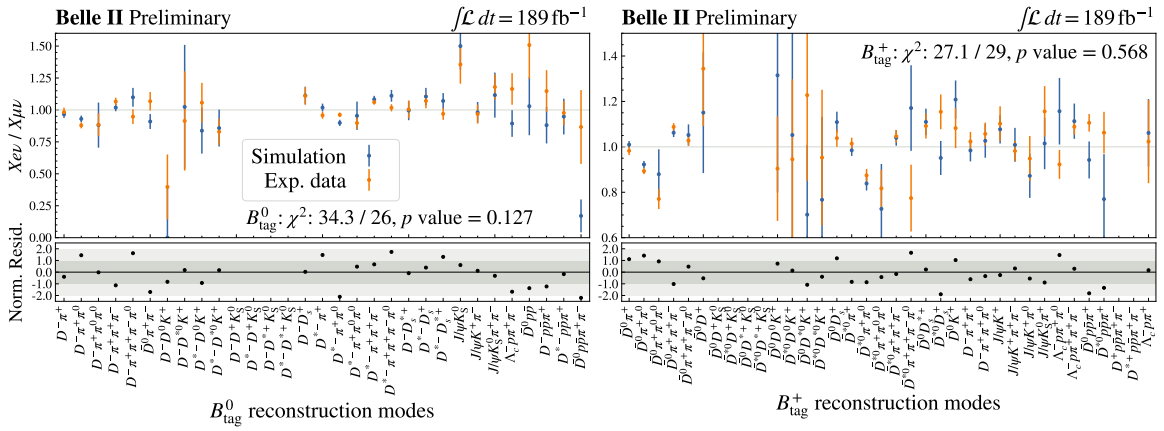

Figure 5.8: The correlation between the B_{tag}-reconstruction-mode selection and the signal-lepton flavor is examined in both experimental data and simulation, with normalized residuals shown below. The equality of distributions is tested using a χ^2 test, considering only statistical uncertainties, and the resulting p values are provided.

is performed for signal electrons and muons. Again, the hypothesis of equal distributions is tested in a χ^2 test, providing no evidence of discrepancies within statistical uncertainty (see Fig. 5.9).

In conclusion, there is no indication that reconstruction-mode-dependent effects between signal electrons and muons are inadequately modeled, within the limits of statistical precision. Consequently, to avoid double-counting statistical uncertainties, no additional uncertainties on the B_{tag}-selection process are introduced for $R(X_{e/\mu})$.

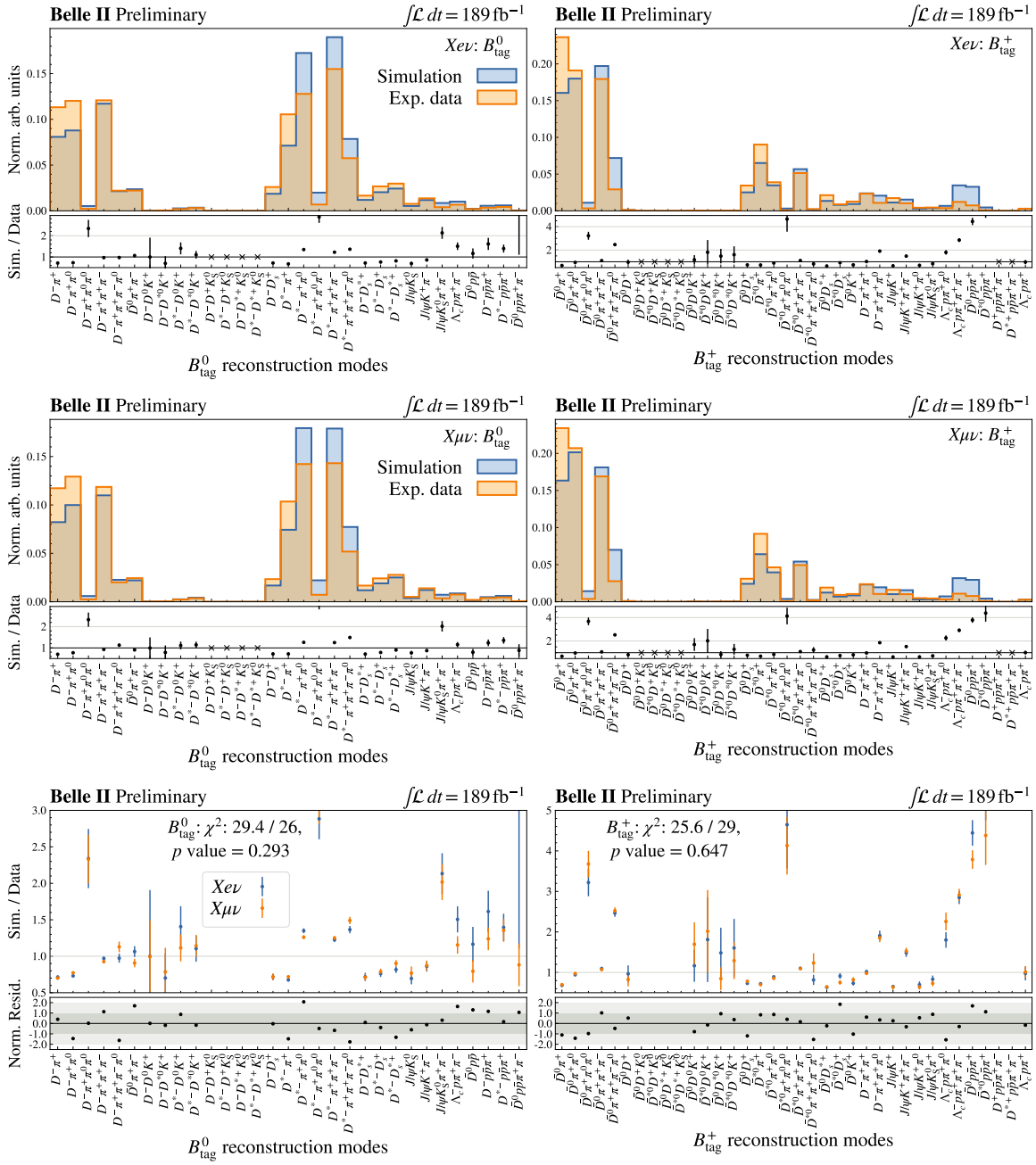

Figure 5.9: The reconstruction-mode-dependent data-MC discrepancies are presented for $Xe\nu$ (top) and $X\mu\nu$ (center). The corresponding ratios of reconstruction-mode fractions are shown below. These ratios are compared between electron and muon channel (bottom) and their equality of distributions is tested using a χ^2 test.

CHAPTER 6

Measurement of the light-lepton ratio $R(X_{e/\mu})$

In this chapter, the first measurement of the inclusive light-lepton branching-fraction ratio $R(X_{e/\mu}) = \mathcal{B}(B \to Xe\nu)/\mathcal{B}(B \to X\mu\nu)$ is presented. Initially anticipated as a cross-check for the $R(X_{\tau/\ell})$ measurement, the unique characteristics and competitive precision of the $R(X_{e/\mu})$ measurement inspired a dedicated effort to measure it independently, as motivated in Section 2.3.3. Some analysis choices, however, might have been different in an analysis specifically designed from the outset to measure $R(X_{e/\mu})$. The results are published in Reference [1].

In Section 6.1, the result-extraction strategy is outlined and tested. Statistical and systematic uncertainties of the $R(X_{e/\mu})$ measurement are quantified and validated. In Section 6.2, the measurement on experimental data is presented, discussed, and validated in its stability.

Initially, distinct simulation calibration factors were introduced for each lepton flavor to address mismodeled B_{tag}-selection efficiencies, as discussed in Sections 4.1 and 7.3.1. However, in Section 5.4.2, it is demonstrated that $R(X_{e/\mu})$ is not influenced by the B_{tag} selection, meaning that lepton-flavor dependent calibration factors directly correspond to distinct branching fractions for $\mathcal{B}(B \to Xe\nu)$ and $\mathcal{B}(B \to X\mu\nu)$. Consequently, the initial calibration need to be inverted to accurately extract non-trivial values of $R(X_{e/\mu})$. Although unintentional, this led to the analysis being effectively conducted in a box-closed manner, as the true electron-to-muon fraction remained obscured until shortly before their extraction in Section 6.2.

During the journal-review process of $R(X_{e/\mu})$ and the ongoing $R(X_{\tau/\ell})$ analysis, a selection criterion on the total ECL energy (E_{ECL}) applied at an early data-processing stage on centrally produced subsets was identified to introduce a notable bias in $R(X_{e/\mu})$, as discussed in Section 8.1.5. The measurement of $R(X_{e/\mu})$ was repeated with the selection removed while keeping all other analysis choices unchanged, and the results are presented in the following. Studies conducted prior to the removal of the E_{ECL} selection are appropriately identified.

6.1 $R(X_{e/\mu})$-extraction strategy and quantification of uncertainties

The $R(X_{e/\mu})$-extraction strategy, including the fit setup and the handling of background events, is discussed in Section 6.1.1. The quantification, validation, and discussion of the impact of various uncertainty sources are covered in Sections 6.1.2 and 6.1.3. Section 6.1.4 is dedicated to the validation of the fit setup, demonstrating its capability to extract various values of $R(X_{e/\mu})$.

6.1.1 Fit setup and background calibration

As detailed in Sections 4.3 and 5.2, the $R(X_{e/\mu})$ measurement is performed in the high-momentum data sample $p_\ell^B > 1.3\,\text{GeV}$ through a binned maximum-likelihood fit. This fit utilizes three templates – $X\ell\nu$, $B\bar{B}$-backgrounds, and continuum events – for each lepton flavor. The fitting process is carried out simultaneously in both the electron and muon channels, resulting in significant cancellation of systematic uncertainties. The yields of the continuum events are constrained using off-resonance data.

As extensively discussed in Section 7.2, notable discrepancies between experimental data and simulation are identified in various quantities correlated to the kinematic properties of the hadronic system X. As a consequence, the extraction of $R(X_{e/\mu})$ is conducted independently of any quantities dependent on X-system properties.[1] Instead, it is solely based on the lepton momentum in the B_{sig} frame, p_ℓ^B, which is demonstrated to be well-modeled, as illustrated in Figure 4.12. In detail, the momentum distribution is divided into ten intervals of 100 MeV each per lepton flavor, starting at the low-momentum threshold for the $R(X_{e/\mu})$ extraction of $p_\ell^B > 1.3\,\text{GeV}$. The uppermost bin edge is designated as an overflow bin to include all events with higher lepton momenta.

The number of unconstrained $B\bar{B}$ backgrounds per p_ℓ^B interval is tiny compared to $X\ell\nu$ decays in the utilized high-momentum region (see Fig. 4.12). In particular, the number of non-resonant D^{**}_{gap}-mode decays, assigned a 100% branching-fraction uncertainty, is similar in size in the muon channel and even larger in the electron case. Consequently, the capability of the extraction fit to distinguish the $B\bar{B}$-background templates from $X\ell\nu$ is limited. A two-dimensional fit incorporating additional quantities with enhanced separation power between the templates, such as M_X or q^2, would rely on the modeling of the X system, making it unfeasible without sophisticated simulation reweighting (see Sec. 7.3). Instead, a background-enriched control sample is employed to constrain the $B\bar{B}$-background template yields.

For this purpose, the same-flavor control sample is defined. In this data sample, the lepton-charge requirement is reversed compared to the nominal event selection, ensuring that only signal-lepton candidates are used that suggest a B_{sig} flavor equivalent to the B_{tag} candidate. As apparent in a comparison of Figures 6.1 and 6.5, this results in a significant enrichment of $B\bar{B}$ backgrounds, along with $X\ell\nu$ decays from $B^0/\bar{B}^0$-mixing events. Figure 6.2 illustrates substantial differences in the normalized shapes of $X\ell\nu$ and $B\bar{B}$-background templates, establishing the same-flavor control sample as effective for constraining backgrounds.

Analogous to the extraction in the opposite-flavor signal sample, the control-sample $B\bar{B}$-background yields are determined in a binned maximum-likelihood fit in ten intervals of p_ℓ^B using three templates per lepton flavor: continuum events constrained by off-resonance data, $B\bar{B}$ backgrounds, and $X\ell\nu$. The pre- and post-fit distributions are presented in Figure 6.1. In Table 6.1, the fit results of all template yields are summarized, while their correlations are presented in Table 6.2. The global χ^2 value, introduced in more detail in Equation 6.4, is $\chi^2_{\text{global}} = 14.7$, yielding a p value of 0.55 for 16 degrees of freedom.

The $B\bar{B}$-background and $X\ell\nu$ yields are strongly correlated. Nevertheless, the capability of the fit to accurately extract $B\bar{B}$-background calibration factors is demonstrated in Section 6.1.3. In this section, the impact of different D-meson decay distributions on $R(X_{e/\mu})$ is investigated. Since varying D-meson decay distributions lead to scaled high-p_ℓ^B $B\bar{B}$-background yields, this effectively serves as a $B\bar{B}$-background linearity test.

[1] In Section 6.1.3, the remaining effects of the mismodeling are demonstrated to cancel out for $R(X_{e/\mu})$.

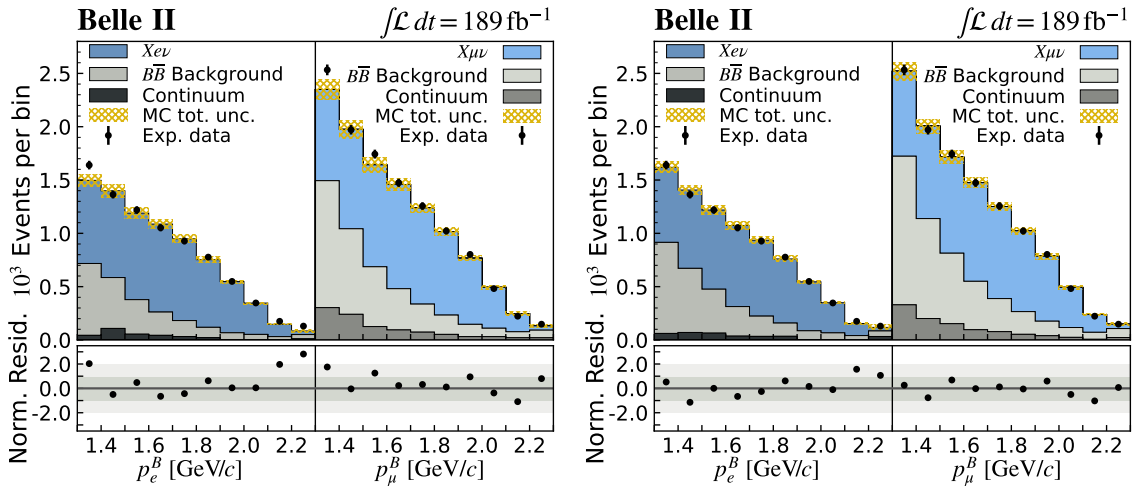

(a) (b)

Figure 6.1: The pre-fit (a) and post-fit (b) distributions of p_ℓ^B are presented for the fit templates and experimental data in the same-flavor control sample. The uncertainty-normalized residuals are displayed below. In the pre-fit case, uncertainties from both experimental data and simulation are combined for the residual normalization, while in the post-fit case, only statistical uncertainties from data are used.

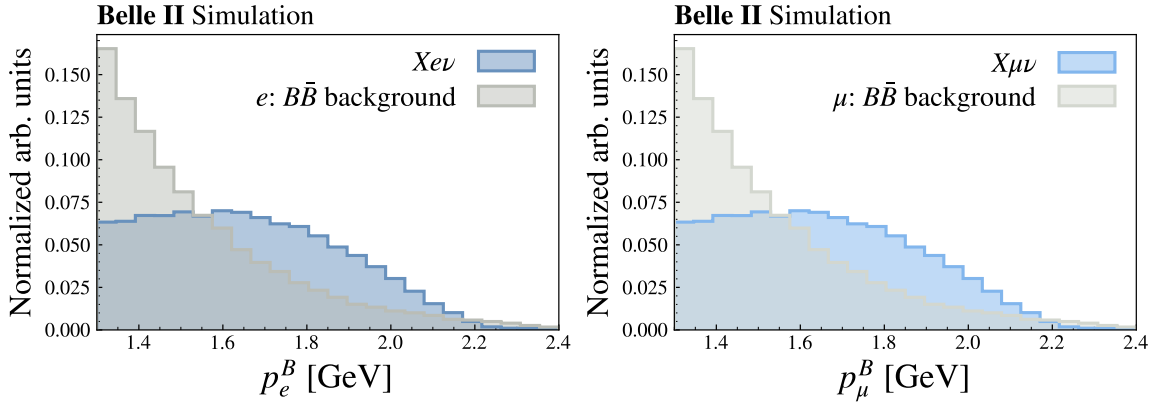

Figure 6.2: The normalized p_ℓ^B distributions of the $X\ell\nu$ and $B\bar{B}$-background templates in the same-flavor control sample for the electron (left) and muon (right) channel.

	Electron channel			Muon channel		
	N^{sel}	N^{meas}	$N^{\mathrm{meas}}/N^{\mathrm{sel}}$	N^{sel}	N^{meas}	$N^{\mathrm{meas}}/N^{\mathrm{sel}}$
$X\ell\nu$	5 555	5 142 ± 235	0.93 ± 0.05	6 617	6 303 ± 309	0.95 ± 0.05
$B\bar{B}$ background	2 131	2 705 ± 236	1.27 ± 0.11	3 707	4 346 ± 323	1.17 ± 0.09
Continuum	314	332 ± 53	1.05 ± 0.17	993	1 004 ± 102	1.01 ± 0.10

Table 6.1: The pre-fit (N^{sel}) and post-fit (N^{meas}) yields of the fit templates in the same-flavor control sample are summarized, along with their relative factor used to constrain $B\bar{B}$ backgrounds in the signal-sample fit.

	Electron channel			Muon channel		
	$Xe\nu$	$B\bar{B}$ Bkg. (e)	Cont. (e)	$X\mu\nu$	$B\bar{B}$ Bkg. (μ)	Cont. (μ)
$Xe\nu$	1.00	−0.89	0.00	0.27	−0.27	0.01
$B\bar{B}$ Bkg. (e)	−0.89	1.00	−0.31	−0.26	0.26	−0.01
Cont. (e)	0.00	−0.31	1.00	0.00	0.00	0.00
$X\mu\nu$	0.27	−0.26	0.00	1.00	−0.90	0.00
$B\bar{B}$ Bkg. (μ)	−0.27	0.26	0.00	−0.90	1.00	−0.22
Cont. (μ)	0.01	−0.01	0.00	0.00	−0.22	1.00

Table 6.2: The correlations of the extracted template yields in the same-flavor control sample are presented.

In both the electron and muon channel, the extracted $B\bar{B}$-background yields, N^{meas}, exceed their predictions by simulation, N^{sel}. The relative yield factors $N^{\text{meas}}/N^{\text{sel}}$ are used to correct and constrain the $B\bar{B}$-background yields $N^{\text{sel}}_{B\bar{B},\ell}$ in the signal-sample fit:

$$N^{\text{sel}}_{B\bar{B},e} = 1\,463 \xrightarrow{\cdot(1.27\pm0.11)} N^{\text{ext}}_{B\bar{B},e} = 1\,857 \pm 162 \tag{6.1}$$

$$N^{\text{sel}}_{B\bar{B},\mu} = 4\,463 \xrightarrow{\cdot(1.17\pm0.09)} N^{\text{ext}}_{B\bar{B},\mu} = 5\,233 \pm 389 \tag{6.2}$$

The $X\ell\nu$ yields experience a slight reduction in the fit. In Section 6.2.4, alternative fit setups to constrain the $B\bar{B}$-background yields are explored, demonstrating that they do not introduce deviations in the final result.

6.1.2 Estimation of uncertainties

To assess the magnitude of statistical and each systematic uncertainties on $R(X_{e/\mu})$, multiple fits are performed on the simulated spectrum using *Asimov* data. In this context, Asimov data refers to pseudo-data with bin yields precisely matching the simulated spectrum. Statistical uncertainties, stemming from the limited size of the experimental data sample, are determined in a fit where all nuisance parameters are fixed at zero. The impact of each systematic uncertainty (see Sec. 5.3) on the $R(X_{e/\mu})$ uncertainty is obtained by conducting a fit with all but one sources of uncertainty fixed, taking the quadrature difference on the resulting uncertainties between the two fit setups. These results are detailed in Table 6.3.

The total uncertainty is estimated through a fit incorporating all sources of systematic uncertainty. This outcome is then compared to the sum of squared individual uncertainties. Any discrepancies that persist are attributed to correlated effects between individual sources of uncertainty and are presented as *Total corr.*. In this context, negative values emerge when the summation of squared individual uncertainties produces a total uncertainty higher than what is observed in the fit. Likewise, the combined effect of all $X_c\ell\nu$ branching-fraction and form-factor uncertainties is compared to the sum of individual uncertainties in $\mathcal{B}(X_c\ell\nu)$ *corr.* and *FF* $X_c\ell\nu$ *corr.*, respectively.

At each step, the uncertainties on each yield N^{meas} are obtained from the output of MINUIT's HESSE function, which provides the Hessian matrix addressing correlations between parameters. Additionally, the results are cross-validated against the uncertainty prediction resulting from a profile-likelihood

Uncertainty source	Relative uncertainty [%]						$R(X_{e/\mu})$
	Electron channel			Muon channel			
	Cont.	$B\overline{B}$ Bkg.	$Xe\nu$	Cont.	$B\overline{B}$ Bkg.	$X\mu\nu$	
Total	11.6	8.6	0.6	7.8	6.5	0.7	2.1
Exp. sample size	9.4	8.2	0.5	7.7	5.3	0.6	0.8
Sim. sample size	6.4	1.3	0.1	0.8	2.4	0.2	0.3
Lepton ID	0.5	1.5	0.1	0.9	2.0	0.2	1.9
Track-reco. eff.	0.1	0.0	0.0	0.0	0.0	0.0	0.0
$\mathcal{B}(X\tau\nu)$ total	0.0	0.0	0.0	0.0	0.0	0.0	0.0
$\mathcal{B}(X\ell\nu)$ total	2.0	1.7	0.1	0.7	2.1	0.2	0.2
$\mathcal{B}(X_u\ell\nu)$	1.8	0.0	0.0	0.1	1.3	0.1	0.1
$\mathcal{B}(D\ell\nu)$	0.1	0.3	0.0	0.1	0.2	0.0	0.0
$\mathcal{B}(D^*\ell\nu)$	0.4	0.7	0.0	0.3	0.8	0.1	0.0
$\mathcal{B}(D^{**}\ell\nu)$	0.4	0.9	0.0	0.4	0.8	0.1	0.1
$\mathcal{B}(D^{(*)}\pi\pi\ell\nu)$	0.1	0.9	0.0	0.4	0.8	0.1	0.0
$\mathcal{B}(D^{(*)}\eta\ell\nu)$	0.5	1.7	0.1	0.7	1.5	0.2	0.1
$\mathcal{B}(D_s^{(*)}K\ell\nu)$	0.0	0.1	0.0	0.0	0.1	0.0	0.0
$\mathcal{B}(X_c\ell\nu)$ corr.	0.2	-1.5	-0.1	-0.6	-1.2	-0.1	-0.1
FF $X_c\ell\nu$ total	0.7	1.5	0.1	0.6	1.4	0.1	0.1
FF $D\ell\nu$	0.1	0.0	0.0	0.0	0.0	0.0	0.0
FF $D^*\ell\nu$	0.4	0.8	0.0	0.4	0.7	0.1	0.0
FF $D^{**}\ell\nu$	0.6	1.2	0.1	0.5	1.2	0.1	0.1
FF $D^{**}_{\text{gap}}\ell\nu$	0.4	1.3	0.1	0.6	1.2	0.1	0.1
FF $X_c\ell\nu$ corr.	-0.3	-1.3	-0.1	-0.6	-1.2	-0.1	-0.1
Total corr.	-0.4	-1.5	-0.1	-0.9	-1.5	-0.2	0.0

Table 6.3: A detailed breakdown of both relative statistical and systematic uncertainties is provided for each template yield N^{meas}. Uncertainties linked to form-factor parameters are denoted by the abbreviation "FF". The uncertainties on the ratio $R(X_{e/\mu})$, extracted from yields and efficiencies of the $X\ell\nu$ decays N_e^{meas}, N_μ^{meas}, ϵ_e, and ϵ_μ, are also provided.

scan, conducted using MINUIT's MINOS function.

In total, a combined uncertainty of 2.1% on $R(X_{e/\mu})$ is predicted. The uncertainties from branching fractions and form factors substantially cancel due to their correlation in $B \to Xe\nu$ and $B \to X\mu\nu$ decays. Residuals in the cancellation originate from interdependencies between $X\ell\nu$ yields and uncorrelated $B\overline{B}$ backgrounds. The largest individual source of uncertainty is associated with LID-efficiency and fake-rate uncertainties, accounting for a relative uncertainty on $R(X_{e/\mu})$ of 1.9%. This source of uncertainty is uncorrelated between lepton flavors and mostly affects $\Delta\epsilon_\ell$. Uncertainties associated with track-reconstruction efficiency or semitauonic branching fractions are negligible. Statistical uncertainties, resulting from the limited sizes of the experimental-data

and simulation samples, contribute to a total of 0.8% and 0.3%, respectively, making the $R(X_{e/\mu})$ extraction systematically limited.

In Section A.3 in the appendix, the predicted uncertainties are validated using ensembles of artificially generated data sets and are found to be robust.

6.1.3 Effects of modified D-meson decay distributions

As discussed in Section 7.2.2, properties that rely on information from the hadronic system X exhibit significant mismodeling. There is compelling evidence suggesting that this mismodeling is mainly attributed to inaccuracies in modeling D-meson decay distributions, particularly in the case of $D \to K_L^0$ (see Sec. 7.2.3). In this section, the expected independence of various D-meson decay distributions on $R(X_{e/\mu})$ is validated.

For this investigation, several simulation samples are generated by adjusting the D-meson decay distributions. The modifications involve varying the relative fraction of D-meson decays into specific kaon charges and excitations, as illustrated in Table 6.4. The presented distributions are designed to cover deviations from the nominal MC distribution for each individual branching fraction ($D \to K^0/K^\pm/K^*$) of several standard deviations in both directions.[2] By design, the resulting distribution may significantly differ from the experimental world averages reported in Reference [17] and Table 7.5 for other inclusive D-meson decay branching fractions.[3] Therefore, these distributions are not intended to serve as reliable scenarios. Instead, they are expected to represent edge cases within the vast hyperparameter space of physical and unphysical D-meson decay distributions, encompassing various kinematic properties of the decay products. Each distribution should be interpreted as a deviation from the SM values by several standard deviations.

In Figures B.6 to B.8 and B.9 to B.11 in the appendix, the resulting M_X and p_ℓ^B distributions for the investigated D-meson decay distributions are illustrated, respectively. While M_X is highly sensitive to the D-decay modeling, the lepton-momentum distribution for $X\ell\nu$ decays is almost unaffected. However, deviations in the lepton-momentum distribution are observed for $B\bar{B}$-background events. For the stringent threshold of $p_\ell^B > 1.3\,\text{GeV}$ used to measure $R(X_{e/\mu})$, these shape deviations primarily reduce to constant yield factors, making this study well-suited to probe the background calibration, as described in Section 6.1.1.

The reweighted samples are fitted against the nominal simulation in the opposite-flavor signal region. This involves executing the complete $R(X_{e/\mu})$-extraction pipeline, including the calibration of $B\bar{B}$-background yields in the same-flavor control sample through a fit against experimental data.

Table 6.5 presents the various $B\bar{B}$-background yields and the corresponding calibration factors extracted, compared to the nominal scenario of unchanged D-meson decay distributions.[4] The majority

[2] This is denoted as the *local* pull. In each distribution, the relevant deviation is measured against the nominal MC distribution (see Tab. 7.5). For example, the $D^0 \to K^0/\bar{K}^0$ branching fraction ranges from 23.6% (distribution 7), deviating by 16.3% or 4.1 times the branching-fraction uncertainty of 4% from Reference [17], to 53.8% (distribution 9), corresponding to a $3.5\,\sigma$ deviation in the opposite direction. For the local pull of each distribution, displayed in Figure 6.3, deviations in D^+ are additionally combined to these values. Variations of branching-fraction into charged kaons, normalized by their uncertainty, exhibit even stronger deviations.

[3] This is denoted as the *global* pull, where the deviations of all presented inclusive branching fractions from the nominal MC distribution are collectively combined in quadrature.

[4] This study is performed before the removal of the E_{ECL} requirement, resulting in background calibration factors of 1.22 and 1.07 in the default scenario. After removing the E_{ECL} selection, central calibration factors of 1.27 and 1.17 are extracted (see Tab. 6.1).

$D \to \ldots$	Distr. 1: $K^* \Uparrow$ [%]		Distr. 2: $K^* \Uparrow\Uparrow$ [%]		Distr. 3: $K^* \Downarrow\Downarrow$ [%]	
+ anything	$\mathcal{B}(D^0)$	$\mathcal{B}(D^+)$	$\mathcal{B}(D^0)$	$\mathcal{B}(D^+)$	$\mathcal{B}(D^0)$	$\mathcal{B}(D^+)$
K^-	55.1	34.6	52.9	41.7	57.6	26.6
K^+	3.5	6.5	3.2	5.7	3.9	7.4
$K^0/\,\overline{K}^0$	41.7	55.2	44.9	51.0	37.8	59.6
$K^{*+}/\,K^{*-}$	18.2	6.1	28.1	7.7	6.7	2.6
$K^{*0}/\,\overline{K}^{*0}$	12.7	28.3	17.8	44.9	4.9	9.1
$D \to \ldots$	Distr. 4: $K^0 \Downarrow\Downarrow$ [%]		Distr. 5: $K^0 \Uparrow\Uparrow$ [%]		Distr. 6: $K^\pm \Uparrow\Uparrow$ [%]	
+ anything	$\mathcal{B}(D^0)$	$\mathcal{B}(D^+)$	$\mathcal{B}(D^0)$	$\mathcal{B}(D^+)$	$\mathcal{B}(D^0)$	$\mathcal{B}(D^+)$
K^-	63.0	38.7	49.5	22.7	67.5	36.8
K^+	3.6	7.6	3.7	6.4	4.1	7.6
$K^0/\,\overline{K}^0$	31.9	45.9	47.8	68.9	30.5	52.5
$K^{*+}/\,K^{*-}$	11.6	4.1	13.8	5.0	11.6	4.5
$K^{*0}/\,\overline{K}^{*0}$	9.1	21.4	9.1	17.3	9.3	21.3
$D \to \ldots$	Distr. 7: $K^\pm \Uparrow\Uparrow\Uparrow$ [%]		Distr. 8: $K^\pm \Downarrow\Downarrow$ [%]		Distr. 9: $K^\pm \Downarrow\Downarrow\Downarrow$ [%]	
+ anything	$\mathcal{B}(D^0)$	$\mathcal{B}(D^+)$	$\mathcal{B}(D^0)$	$\mathcal{B}(D^+)$	$\mathcal{B}(D^0)$	$\mathcal{B}(D^+)$
K^-	76.0	41.4	47.8	26.1	39.4	21.5
K^+	4.5	8.0	3.3	6.5	3.0	6.1
$K^0/\,\overline{K}^0$	23.6	48.8	46.8	61.1	53.8	64.7
$K^{*+}/\,K^{*-}$	10.7	4.4	13.6	4.7	14.4	4.7
$K^{*0}/\,\overline{K}^{*0}$	9.4	22.7	9.0	17.9	8.9	16.4

Table 6.4: The nine investigated D-meson decay distributions used to probe $R(X_{e/\mu})$ stability are presented, created by adjusting the inclusive D-meson branching fractions to specific kaon flavors, as indicated in each title. The nominal D-meson decay distribution in simulation and the experimental world averages are provided in Table 7.5.

of the relative background calibration factors ("0" / i) align closely with the anticipated values based on the input $B\bar{B}$-background yield changes i / "0", deviating by no more than 1%. Deviations of up to 3% are observed only in the scenario with significantly enhanced K^* contributions (D-meson decay distribution number 2). The uncertainties of the extracted calibration factors, used as Gaussian constraints in the likelihood function, range from 10% to 20%.

Figure 6.3 illustrates the subsequently extracted $R(X_{e/\mu})$ values, which deviate from the expected unity by no more than 0.3%, recovering the 1% to 3% deviations observed in the background-calibration factors. Despite the extreme scenarios explored here (global pulls of up to 12 σ), the resulting effect on $R(X_{e/\mu})$ is an order of magnitude smaller than the leading systematic uncertainties associated with LID corrections. Consequently, the assumption of canceling D-meson branching-fraction uncertainties for $R(X_{e/\mu})$ is validated, and no additional uncertainties are introduced. Furthermore, the $B\bar{B}$-background calibration in the same-flavor control sample is demonstrated to be sensitive to small background-yield deviations.

Dist. number	"0"	1	2	3	4	5	6	7	8	9
e Bkg. yield	1 736	1 586	1 295	1 889	1 714	1 757	1 754	1 768	1 722	1 707
Extr. factor	1.219	1.354	1.703	1.104	1.226	1.211	1.197	1.179	1.235	1.253
Yield: i / "0"	1	0.914	0.746	1.088	0.988	1.013	1.011	1.019	0.992	0.984
Factor: "0" / i	1	0.900	0.716	1.104	0.994	1.006	1.018	1.033	0.987	0.973
μ Bkg. yield	3 567	3 320	2 855	3 824	3 567	3 565	3 613	3 649	3 532	3 498
Extr. factor	1.072	1.143	1.298	1.003	1.080	1.063	1.056	1.045	1.082	1.093
Yield: i / "0"	1	0.931	0.800	1.072	1.001	1.000	1.013	1.023	0.990	0.981
Factor: "0" / i	1	0.938	0.826	1.068	0.992	1.009	1.015	1.026	0.991	0.981

Table 6.5: The variations in $B\bar{B}$-background yields in the same-flavor control sample are presented for modified D-meson decay distributions (see Tab. 6.4) in the electron (top) and muon (bottom) channel. The corresponding extracted background-calibration factors from fits against experimental data are also presented. When compared to the nominal scenario "0", the ratio of calibration factors should align with the reverse ratio of yields in a perfect fit.

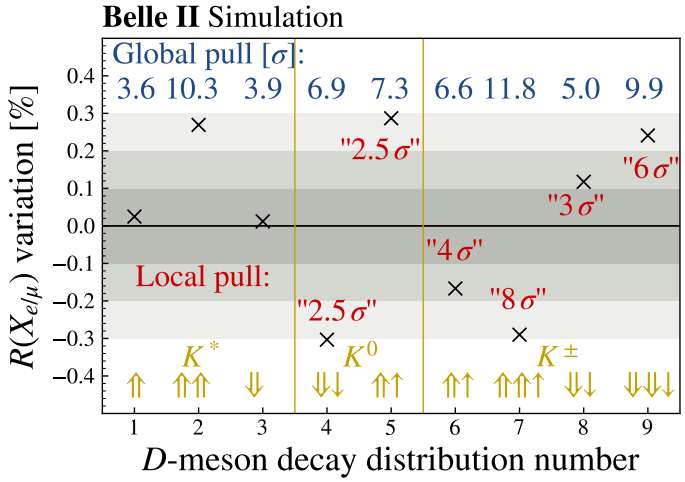

Figure 6.3: The extracted $R(X_{e/\mu})$ values, obtained by fitting templates with modified D-meson decay distributions (see Tab. 6.4) against the nominal simulation, are illustrated as black crosses. No deviation exceeds 0.3%. The approximate *local* pull on the specifically varied inclusive branching fractions (shown in gold) is highlighted in red, while the *global* pull, considering the deviation of all inclusive $D \to K$ branching fractions, is presented in blue on top of the plot.

6.1.4 Validation of the fit setup

The ability of the fit setup to extract different values of $R(X_{e/\mu})$ is tested in a linearity test. In this test, the value of $R(X_{e/\mu})$ in simulation is scaled by a certain factor in the target data set, achieved by multiplying the $Xe\nu$ yield accordingly. The probed factors and resulting values of $R(X_{e/\mu})$ are presented and visualized in Figure 6.4. Even for small scaling factors of a few percent, the extracted $R(X_{e/\mu})$ values deviate from expectations by not more than $3 \cdot 10^{-3}$%, i.e., at the fifth decimal place.

$Xe\nu$ factor	Extracted $R(X_{e/\mu})$
0.60	0.599999 ± 0.013433
0.75	0.749998 ± 0.016140
0.90	0.899999 ± 0.018998
0.96	0.959999 ± 0.020124
0.97	0.970016 ± 0.020211
0.98	0.980011 ± 0.020396
0.99	0.990028 ± 0.020341
1.01	1.010015 ± 0.021071
1.02	1.019984 ± 0.021160
1.03	1.029999 ± 0.021450
1.04	1.039999 ± 0.021639
1.10	1.100019 ± 0.022744
1.20	1.200010 ± 0.024687
1.35	1.350007 ± 0.027544
1.50	1.500009 ± 0.030300
2.00	2.000058 ± 0.039976

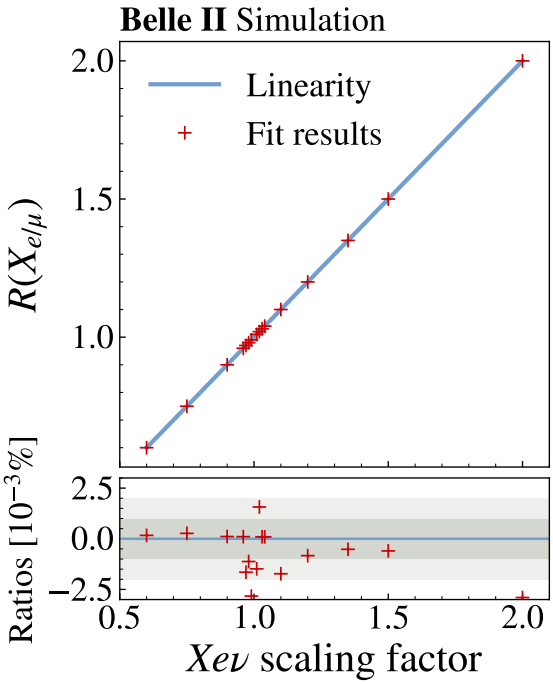

Figure 6.4: The tested $Xe\nu$ scaling factors are provided along with the corresponding extracted values of $R(X_{e/\mu})$. These values are visually represented on the right (red crosses), while a straight line representing perfect linearity is shown in blue. The uncertainty associated with $R(X_{e/\mu})$ (too small to be shown on the right) scales with the $Xe\nu$ yield, consequently increasing for larger scaling factors.

6.2 Measurement and validation studies

The measured value of $R(X_{e/\mu})$ is presented and discussed in Section 6.2.1. A fiducial result with reduced model-dependence is presented in Section 6.2.2. Section 6.2.3 explores a hypothetical dependence on the lepton-momentum threshold, $p_\ell^B > 1.3\,\text{GeV}$, and Section 6.2.4 demonstrates the stability of the result against various additional effects.

6.2.1 Measurement of $R(X_{e/\mu})$

Figure 6.5 presents a visual comparison between the $R(X_{e/\mu})$-extraction fit templates and experimental data both before and after the fitting process.

The extracted yields N^{meas} are provided in Table 6.6. The corresponding correlations are summarized in Table 6.7.

No significant deviations in pre-fit and post-fit yields are observed, suggesting that the constraints on $B\bar{B}$-background and continuum yields have only a minor impact on the overall likelihood. The electron efficiency is $\epsilon_e = (1.77 \pm 0.04) \cdot 10^{-3}$, and the muon efficiency is $\epsilon_\mu = (2.14 \pm 0.06) \cdot 10^{-3}$, with a correlation of 0.76 between the two efficiencies due to shared systematic uncertainties. Efficiency depletion resulting from the mismodeled B_{tag} selection, as demonstrated to cancel for $R(X_{e/\mu})$ in Section 5.4.2, is not taken into account in these values.

Utilizing Equations (5.1) and (5.2), $N_e^{\text{meas}} = 50956 \pm 287$, $N_\mu^{\text{meas}} = 61294 \pm 441$, and a correlation

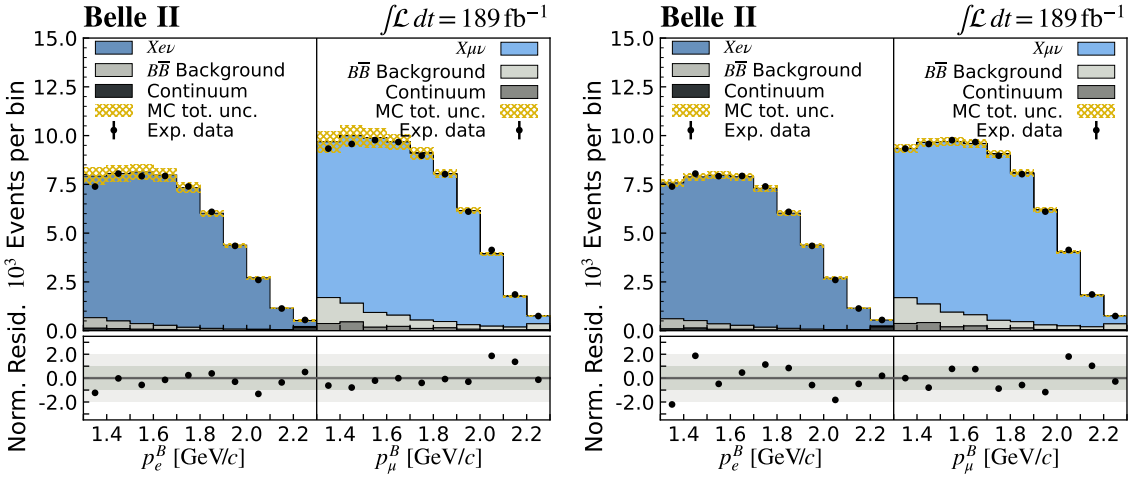

(a) (b)

Figure 6.5: The pre-fit (a) and post-fit (b) distributions of p_ℓ^B are presented for the fit templates and experimental data in the signal sample. The uncertainty-normalized residuals are displayed below. In the pre-fit case, uncertainties from both experimental data and simulation are combined for the residual normalization, while in the post-fit case, only statistical uncertainties from data are used.

	Electron channel		**Muon channel**	
	N^{sel}	N^{meas}	N^{sel}	N^{meas}
$X\ell\nu$	51 720 ± 289	50 956 ± 287	62 050 ± 440	61 294 ± 441
$B\bar{B}$ background	1 857 ± 159	1 794 ± 159	5 233 ± 340	5 211 ± 341
Continuum	648 ± 75	668 ± 74	1 684 ± 131	1 680 ± 132

Table 6.6: The pre-fit (N^{sel}) and post-fit (N^{meas}) yields of the fit templates in the $R(X_{e/\mu})$ signal sample are summarized. The uncertainties presented for N^{sel} are derived in fits to Asimov data as described in Section 6.1.2.

of 0.027, the extracted value of $R(X_{e/\mu})$ is

$$R(X_{e/\mu}) = 1.007 \pm 0.009\ (\text{stat.}) \pm 0.019\ (\text{syst.}). \tag{6.3}$$

This result is in agreement with the SM prediction of $R(X_{e/\mu}) = 1.006 \pm 0.001$ [126], as well as with previous [138] and subsequent [139, 141] exclusive measurements. It represents the first lepton-universality test based on inclusive B-meson branching fractions and stands as the most precise branching-fraction-based examination of lepton-universality in semileptonic B-meson decays to date.

In Figure 6.6, the pulls on the constrained nuisance parameters are depicted. Some deviations from zero are observed for the continuum template, likely stemming from statistical fluctuations due to the limited precision of the off-resonance data set. In the case of $Xe\nu$ and $X\mu\nu$, consistent pulls toward lower values are noted, particularly in the lower lepton-momentum region. This is attributed to the non-resonant D^{**}_{gap} components, which have a 100% uncertainty assigned and appear to be overestimated in the simulation. The observed evidence for overestimated gap-mode components is

	Electron channel			Muon channel		
	$Xe\nu$	$B\bar{B}$ Bkg. (e)	Cont. (e)	$X\mu\nu$	$B\bar{B}$ Bkg. (μ)	Cont. (μ)
$Xe\nu$	1.00	−0.75	−0.26	0.03	−0.02	−0.05
$B\bar{B}$ Bkg. (e)	−0.75	1.00	−0.05	−0.03	0.03	0.06
Cont. (e)	−0.26	−0.05	1.00	−0.01	0.01	0.01
$X\mu\nu$	0.03	−0.03	−0.01	1.00	−0.54	−0.23
$B\bar{B}$ Bkg. (μ)	−0.02	0.03	0.01	−0.54	1.00	−0.04
Cont. (μ)	−0.05	0.06	0.01	−0.23	−0.04	1.00

Table 6.7: The correlations of the extracted template yields in the signal-sample fit for $R(X_{e/\mu})$ are presented.

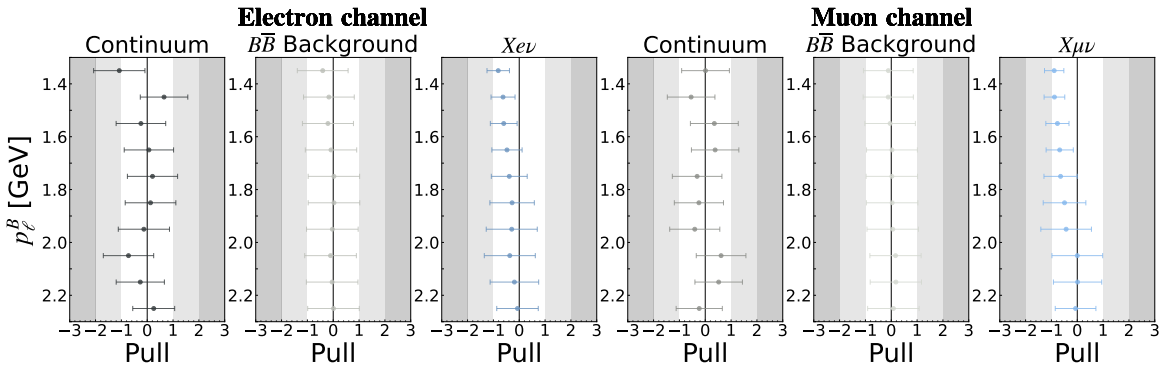

Figure 6.6: The pulls on the nuisance parameters for the electron and muon-channel templates are shown after the $R(X_{e/\mu})$-extraction fit.

consistent with similar findings in the $R(X_{\tau/\ell})$ analysis (see Sections 7.3.2 and 8.2.1), as well as with Belle II's measurements of hadronically [119] and semileptonically [218] tagged $R(D^{(*)})$ analyses.

Additionally, the post-fit uncertainties for these nuisance parameters are significantly smaller than one, indicating that the fit to experimental data successfully constrained them. As seen in Figure 4.12, the input gap-mode yields are notably larger than the statistical uncertainty of the data. Due to the distinct gap-mode shape, the fit is able to distinguish them from the remaining $X\ell\nu$ template, resulting in constrained nuisance parameters.

The overall agreement between the fit results and experimental data is evaluated through a global χ^2 value, computed by considering the remaining residuals between experimental data and post-fit templates, along with the pulls on nuisance parameters and the constraints on $B\bar{B}$-background and continuum yields:

$$\begin{aligned}\chi^2_{\text{global}} &= \chi^2_{\text{Data vs. MC}} + \chi^2_{\text{NP pulls}} + \chi^2_{\text{constraints}} \\ &= \sum_i^{\text{bins}} \left(\frac{N_i^{\text{data}} - N_i^{\text{MC}}}{\sigma_i^{\text{data}}} \right)^2 + \vec{\theta}^T C_\theta^{-1} \vec{\theta} + \sum_k^{\text{constraints}} \left(\frac{N_k^{\text{meas}} - N_k^{\text{ext}}}{\sigma_k^{\text{ext}}} \right)^2 \qquad (6.4) \\ &= 11.71 + 9.62 + 0.21 = 21.54. \qquad (6.5)\end{aligned}$$

The global χ^2 value is approximately evenly driven by post-fit data-MC residuals and nuisance parameter pulls. The corresponding p value for 18 degrees of freedom (dof.) is determined by

$$p \text{ value} \left(\chi^2_{\text{global}} = 21.54, \text{dof.} = N_{\text{bins}} - N^{\text{fitted}}_{\text{yields}} = 18\right) = 0.25. \tag{6.6}$$

This indicates reasonable agreement, with no evidence of concerning pulls in data, nuisance parameters, or constraints on continuum templates and $B\bar{B}$ backgrounds.

In Sections 6.2.3 and 6.2.4, the stability of the extracted $R(X_{e/\mu})$ result is thoroughly examined. No indications of instabilities are identified, affirming the reliability of the presented result.

6.2.2 Fiducial $R(X_{e/\mu})$ measurement

To mitigate model dependence, a fiducial measurement of $R(X_{e/\mu})$ is presented, where N^{gen}_{ℓ} (see Sec. 5.1) is recalculated in the restricted phase space defined by selecting events with a generated B_{sig}-frame lepton momentum satisfying $p^B_{\ell} > 1.3\,\text{GeV}$:

$$N^{\text{gen}}_{\ell} = 2 \cdot N_{B\bar{B}} \cdot \mathcal{B}(B \to X\ell\nu, p^B_{\ell} > 1.3\,\text{GeV}). \tag{6.7}$$

Here, $\mathcal{B}(B \to X\ell\nu, p^B_{\ell} > 1.3\,\text{GeV})$ denotes the branching fraction of B mesons decaying into $X\ell\nu$ with the respective p^B_{ℓ} requirements. Thereby, a model dependence is introduced for N^{gen}_{ℓ}, which aligns with the one for N^{sel}_{ℓ}. This results in a cancellation of both effects in the efficiency $\epsilon_{\ell} = N^{\text{sel}}_{\ell}/N^{\text{gen}}_{\ell}$ and, consequently, a reduced model dependence in the measurement of $R(X_{e/\mu})$.

For this purpose, $62 \cdot 10^6$ $B \to X\ell\nu$ events are generated with EvtGen (without detector simulation), aligning with the branching fractions and form-factor models as introduced in Section 3.4.3. The fraction of events, denoted as F_{ℓ}, exceeding $p^B_{\ell} = 1.3\,\text{GeV}$ is compared between electrons and muons, and their ratio is found to be

$$B^0 : F_e/F_{\mu} = 0.99750 \pm 0.00035\ (\text{stat.}) \pm 0.00020\ (\text{syst.}) \tag{6.8}$$

$$B^+ : F_e/F_{\mu} = 0.99772 \pm 0.00034\ (\text{stat.}) \pm 0.00021\ (\text{syst.}) \tag{6.9}$$

$$\text{Comb.} : F_e/F_{\mu} = 0.99761 \pm 0.00025\ (\text{stat.}) \pm 0.00021\ (\text{syst.}). \tag{6.10}$$

Systematic uncertainties are primarily induced by form-factor variations. The observed values are consistent for neutral and charged B mesons within statistical uncertainties. Hence, they are assumed to be equal, and their combined value is considered. The fiducial result, denoted as $R(X_{e/\mu} \mid p^B_{\ell} > 1.3\,\text{GeV})$, is obtained by multiplying F_e/F_{μ} with the nominal result from Equation (6.3):

$$R(X_{e/\mu} \mid p^B_{\ell} > 1.3\,\text{GeV}) = R(X_{e/\mu}) \cdot \frac{F_e}{F_{\mu}} = 1.005 \pm 0.009\ (\text{stat.}) \pm 0.019\ (\text{syst.}). \tag{6.11}$$

This result exhibits a reduced dependence on (form-factor) model predictions of the relative fraction of $B \to X\ell\nu$ decays with $p^B_{\ell} > 1.3\,\text{GeV}$.

6.2.3 Dependence on the lepton-momentum threshold

To assess the sensitivity of the result to the choice of the p_ℓ^B threshold, $R(X_{e/\mu})$ is remeasured while varying the threshold to 1.1, 1.2, and 1.4 GeV. Lower values would introduce non-negligible contributions from $B \to X\tau\nu$ decays, while higher values would necessitate a modified $B\bar{B}$-background calibration strategy due to the lower event counts. To maintain comparability, the same p_ℓ^B bin widths of 100 MeV each, up to 2.3 GeV, are retained, resulting in twelve, eleven, and nine bins for the three additionally investigated p_ℓ^B thresholds, respectively.

This study is performed before the removal of the E_{ECL} requirement. In this setting, the extracted value of $R(X_{e/\mu})$ with the nominal requirement of $p_\ell^B > 1.3\,\text{GeV}$ is

$$R(X_{e/\mu}) = 1.033 \pm 0.010\ (\text{stat.}) \pm 0.019\ (\text{syst.}). \tag{6.12}$$

The subsequent removal of the E_{ECL}-selection requirement is not expected to change the conclusions drawn in this section.

The $B\bar{B}$ backgrounds can be individually calibrated for each p_ℓ^B setup based on the same-flavor control sample, as outlined in Section 6.1.1. In Table 6.8, the different calibration factors $N^{\text{meas}}/N^{\text{sel}}$ for each p_ℓ^B threshold are summarized. Deviations between these factors may be attributed to a greater variety of backgrounds becoming relevant at lower momenta, including the controversial $X\tau\nu$ contribution. At higher momenta, the total number of backgrounds is reduced, making their calibration-factor extraction more challenging, as reflected by higher uncertainties. Both effects are beyond the scope of the probed effect in this section.

	$p_\ell^B > 1.1\,\text{GeV}$	$p_\ell^B > 1.2\,\text{GeV}$	$p_\ell^B > 1.3\,\text{GeV}$	$p_\ell^B > 1.4\,\text{GeV}$
e channel	1.24 ± 0.06	1.31 ± 0.09	1.22 ± 0.14	1.14 ± 0.21
μ channel	1.10 ± 0.04	1.19 ± 0.06	1.07 ± 0.10	0.94 ± 0.14

Table 6.8: The extracted background-calibration factors $N^{\text{meas}}/N^{\text{sel}}$ for each lepton flavor for different p_ℓ^B thresholds.

Subsequently, $R(X_{e/\mu})$ is extracted in the opposite-flavor signal sample, and the obtained values are illustrated in Figure 6.7(a).

As a substantial fraction of both experimental and simulated data is common across all results, these values exhibit strong correlations. To quantify the expected level of fluctuation among different p_ℓ^B threshold results, it is essential to determine the anticipated correlation.

Accurately capturing the correct correlations based on statistical and systematic uncertainties between the same-flavor control sample and the signal sample in toy data is a highly non-trivial task. Given this challenge, a simplified approach is adopted for the calibration of $B\bar{B}$-background yields, since the capability of the fit setup to correctly extract different $B\bar{B}$-background calibration factors is already demonstrated in Section 6.1.3. Consequently, in this section, background fluctuations are reduced by utilizing the $B\bar{B}$-background calibration factors corresponding to the nominal p_ℓ^B threshold of 1.3 GeV for the $R(X_{e/\mu})$ extractions with all investigated p_ℓ^B thresholds.

The corresponding $R(X_{e/\mu})$ results are visualized in Figure 6.7(b). Their deviations from the values extracted with individual $B\bar{B}$-background calibration factors (see Fig. 6.7(a)) align with the differences in $B\bar{B}$-background calibration factors outlined in Table 6.8. Moreover, any potentially

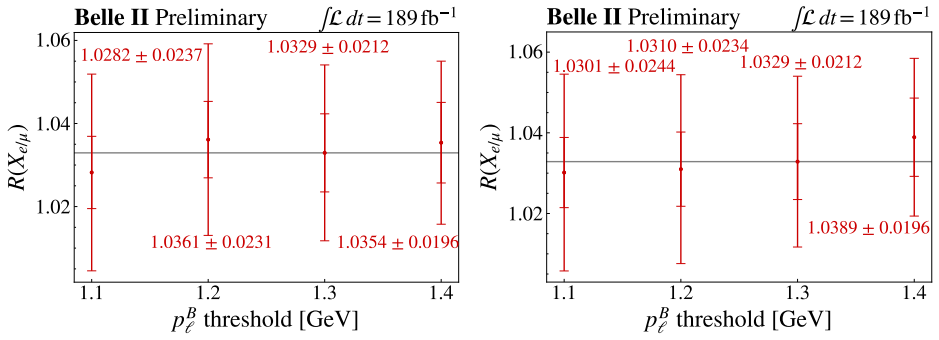

(a) (b)

Figure 6.7: The extracted $R(X_{e/\mu})$ values for different p_ℓ^B thresholds are presented in two scenarios: (a) when the background is calibrated separately for each threshold, and (b) when consistent calibration factors from the nominal threshold of 1.3 GeV are applied.

indicated systematic growth of $R(X_{e/\mu})$ with an increased p_ℓ^B threshold, as observed in Figure 6.7(b), is attributed to the limited $B\bar{B}$-background calibration method.

This approach enables the quantification of agreement among the individual $R(X_{e/\mu})$ measurements. To achieve this, 500 toy data samples are generated as target data (see Sec. A.3) for $p_\ell^B > 1.1$ GeV in the opposite-flavor signal region, capturing fluctuations from all systematic sources of uncertainty based on the total systematic covariance matrix C_θ. The choice of p_ℓ^B intervals allows the same set of toys to be employed for $R(X_{e/\mu})$ extractions with more stringent lepton-momentum thresholds. This is achieved by rejecting the first one, two, or three bins per lepton flavor. Consequently, four connected p_ℓ^B-threshold-dependent $R(X_{e/\mu})$ values are extracted for each toy sample, facilitating the quantification of their correlations.

The resulting two-dimensional scatter plots are illustrated in Figure 6.8(a). The correlation between each pair of $R(X_{e/\mu})$ values is given by Pearson correlation coefficients, resulting in a correlation matrix Σ_R of $R(X_{e/\mu})$ values of

$$\Sigma_R^{\text{syst.}} = \begin{pmatrix} 1.0000 & 0.9973 & 0.9942 & 0.9826 \\ 0.9973 & 1.0000 & 0.9984 & 0.9892 \\ 0.9942 & 0.9984 & 1.0000 & 0.9946 \\ 0.9826 & 0.9892 & 0.9946 & 1.0000 \end{pmatrix}. \tag{6.13}$$

The correlation among the four measurements, arising from their shared fraction of events in the experimental sample, is evaluated through 500 resamplings of the experimental data set with replacement – a technique referred to as *bootstrapping* [219]. The individual $R(X_{e/\mu})$ measurements, obtained by rejecting the first one, two, or three p_ℓ^B bins per lepton flavor, are illustrated in Figure 6.8(b). This leads to a correlation matrix of

$$\Sigma_R^{\text{stat.}} = \begin{pmatrix} 1.0000 & 0.9797 & 0.9615 & 0.9046 \\ 0.9797 & 1.0000 & 0.9912 & 0.9504 \\ 0.9615 & 0.9912 & 1.0000 & 0.9728 \\ 0.9046 & 0.9504 & 0.9728 & 1.0000 \end{pmatrix}. \tag{6.14}$$

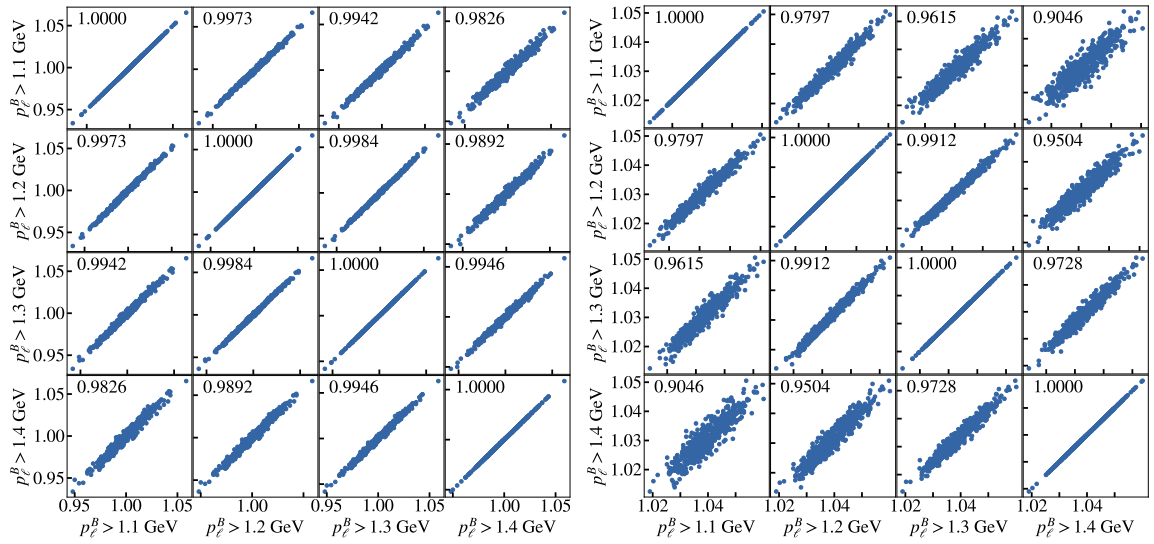

(a) (b)

Figure 6.8: Scatter plots, illustrating two of the four $R(X_{e/\mu})$ measurements per toy data sample each, are presented. In (a), variations due to systematic uncertainties are shown. Scatter plots resulting from bootstrapped experimental data, representing variations due to statistical uncertainties, are depicted in (b). In each upper right corner, the Pearson correlation coefficient is provided.

While systematic effects only induce a minimal decorrelation among different $R(X_{e/\mu})$ values (see Eq. (6.13)), statistical effects lead to greater fluctuations, reflected by smaller correlations among the various p_ℓ^B thresholds.

Finally, a χ^2 test is employed to assess the agreement among the four $R(X_{e/\mu})$ measurements from Figure 6.7(b):

$$\chi^2 = (\vec{R} - \bar{R})^{\mathrm{T}} \cdot C_R^{-1} \cdot (\vec{R} - \bar{R}) = 3.90. \tag{6.15}$$

Here, $\vec{R}$ represents each individual $R(X_{e/\mu})$ measurement, $\bar{R}$ is their weighted average, and C_R^{-1} is the inverted total covariance matrix, derived from the individual uncertainties and the total correlation matrix $\Sigma_R^{\text{stat.}} + \Sigma_R^{\text{syst.}}$. The p value, which quantifies the consistency of the four $R(X_{e/\mu})$ measurements, is given by

$$p \text{ value}\left(\chi^2 = 3.90, \text{dof.} = 3\right) = 0.27. \tag{6.16}$$

There is no significant evidence of deviations from consistency. Therefore, the $R(X_{e/\mu})$ measurement is expected to be stable against investigated variations of the p_ℓ^B threshold.

6.2.4 Additional validations and crosschecks

The robustness of the $R(X_{e/\mu})$ measurement against potentially underappreciated systematic effects is validated by re-evaluating it in various slightly modified fit setups or subsets of experimental data and simulation. The summarized results are presented in Table 6.9 and are discussed in the following.

Scenario	$R(X_{e/\mu})$	(rel. to nominal)
Nominal	1.007 ± 0.009 (stat.) ± 0.019 (syst.)	
No bremsstrahlung correction	1.006 ± 0.009 (stat.) ± 0.019 (syst.)	(−0.04%)
Simultaneous fit: OF + SF	1.006 ± 0.009 (stat.) ± 0.019 (syst.)	(−0.1%)
Simultaneous fit: OF + SF(B^+_{tag}) + SF(B^0_{tag})	1.007 ± 0.009 (stat.) ± 0.019 (syst.)	(+0.01%)
$N^X_\ell = 0$	1.011 ± 0.010 (stat.) ± 0.019 (syst.)	(+0.4%)
$N^X_\ell \geq 1$	0.985 ± 0.022 (stat.) ± 0.019 (syst.)	(−2.2%)

Table 6.9: Various $R(X_{e/\mu})$ values are presented for alternative fit setups or subsets of experimental data. Additional details for each configuration are outlined in the text.

Bremsstrahlung modeling

A potential bias arising from hypothetically mismodeled bremsstrahlung effects is assessed by refitting $R(X_{e/\mu})$ while using the uncorrected electron momenta. As detailed in Sections 4.3 and A.2, the accurate modeling of all relevant bremsstrahlung properties makes any bias caused by them unlikely. Indeed, the resulting extracted value deviates from the nominal value by only 0.04%, which is two orders of magnitude below leading uncertainties.

$B\bar{B}$-background calibration

In the background calibration presented in Section 6.1.1, the extracted $X\ell\nu$ yields experience a reduction of 7% (e) and 5% (μ), respectively, while their observed reduction in the signal-extraction fit only corresponds to 1.5% each (see Tab. 6.6). Due to the strong correlation with the $B\bar{B}$-background yields in the same-flavor sample (see Tab. 6.2), this directly influences the obtained background-calibration factors. To evaluate potential biasing effects resulting from a suboptimal background calibration, a simultaneous fit in the opposite-flavor signal sample (OF) and same-flavor control sample (SF) is performed, only allowing for consistent template-yield scaling.

In another test, the same-flavor control sample is additionally subdivided by B_{tag} charge, leveraging the fact that 90% of all $X\ell\nu$ events in the same-flavor sample populate the neutral-B_{tag} channel due to $B^0/\bar{B}^0$ mixing, while $B\bar{B}$ backgrounds are roughly evenly distributed by B_{tag} charge. In hindsight, such a setup generally appears superior compared to the artificial division of background calibration and signal extraction into two separate steps. However, due to the ongoing review process, the initial fit setup was not updated. Fortunately, the extracted $R(X_{e/\mu})$ values of all setups only deviate by 0.01% to 0.1% (see Tab. 6.9), demonstrating that the nominal scenario does not introduce biasing $B\bar{B}$-background calibrations.

Multiple lepton candidates

An $R(X_{e/\mu})$ extraction using only the 83% subset of events without a lepton candidate in the X system, denoted $N^X_\ell = 0$, yields $R(X_{e/\mu}) = 1.011 \pm 0.010$ (stat.) ± 0.019 (syst.), in contrast to $R(X_{e/\mu}) = 0.985 \pm 0.022$ (stat.) ± 0.019 (syst.) when using only events with one or more lepton candidates in addition to the signal lepton, $N^X_\ell \geq 1$. Since the majority of second-lepton candidates

exhibit the opposite charge compared to the signal lepton, this separation predominantly probes the impact of substantially different X-system properties for $R(X_{e/\mu})$. Additionally, potential biases from the selection of the best signal-lepton candidate are investigated, although with limited sensitivity.

The statistical correlations between the two subsets and the nominal data set are estimated using $\rho_{A,B} = N_{AB}/\sqrt{N_A N_B}$, where N_A, N_B, and N_{AB} represent the subset yield, the yield of the full data set, and the yield of the overlap (100% of the subset), respectively. For the single-lepton sample, a correlation of 0.91 is derived, while for the multiple-lepton data set, the correlation is 0.41. Considering these correlations, the resulting pulls between subset and nominal results are $0.97\,\sigma$ and $1.10\,\sigma$ for single and multiple lepton candidates, respectively. The two subsets, which are statistically independent of each other, are consistent with each other within $1.08\,\sigma$.

Thus, the probability of the $R(X_{e/\mu})$-deviations being solely caused by statistical fluctuation is approximately 16%, not even accounting for decorrelation of systematic uncertainties. Consequently, no significant evidence for a biasing effect is found.

Lepton charge, B_{tag} charge, and M_X

Several additional subsets of experimental data have been examined with the E_{ECL} requirement still in place. They are briefly summarized in the following.

In Table 6.10, the $R(X_{e/\mu})$ values extracted in subsets divided by signal-lepton and B_{tag} charge are summarized. The results split by signal-lepton charge show consistency within $0.14\,\sigma$. Similarly, values from the subsets split by B_{tag}-candidate charge agree within $0.8\,\sigma$, considering a 100% correlation of systematic uncertainties.

Scenario	$R(X_{e/\mu})$
Nominal	1.033 ± 0.010 (stat.) ± 0.019 (syst.)
ℓ^+	1.028 ± 0.014 (stat.) ± 0.028 (syst.)
ℓ^-	1.034 ± 0.014 (stat.) ± 0.027 (syst.)
B^+_{tag}	1.040 ± 0.017 (stat.) ± 0.019 (syst.)
B^0_{tag}	1.023 ± 0.013 (stat.) ± 0.019 (syst.)

Table 6.10: Extracted $R(X_{e/\mu})$ values are presented for various subsets of experimental data. In each test, the E_{ECL}-selection requirement is still present, causing a relative shift in all $R(X_{e/\mu})$ values compared to Table 6.9. Additional details for each configuration are outlined in the text.

The invariant mass of the hadronic system, denoted as M_X, is particularly sensitive to the mismodeling of D-meson decays (see Sec. 7.2.3). In addition to the study in Section 6.1.3, $R(X_{e/\mu})$ is extracted in two M_X samples: a low-M_X sample ($M_X < 1.6\,\text{GeV}$, or 1.7 GeV), enriched with D-meson decays that are underestimated by simulation (see Fig. 7.10), and a high-M_X sample ($M_X > 1.6\,\text{GeV}$, or 1.7 GeV), where the $X\ell\nu$ population is overestimated and most backgrounds are located. Two M_X thresholds are examined, chosen to approximately split either experimental or simulated data in half. Table 6.11 summarizes the relative deviations of the extracted $R(X_{e/\mu})$ values from the nominal value. All of these deviations are well below the statistical precision of 1%, providing further support for the assumption that mismodeling effects in the X system cancel out in $R(X_{e/\mu})$.

M_X threshold	Low M_X	High M_X
1.6 GeV	−0.1%	0.5%
1.7 GeV	0.65%	0.0%

Table 6.11: The relative deviations in the extracted $R(X_{e/\mu})$ values, based on subsets of M_X, compared to the nominal value from Table 6.10, are presented.

Data-taking periods

Subset label	$\int \mathcal{L}\,\mathrm{d}t$	$R(X_{e/\mu})$ value (rel. deviation)	$\frac{\epsilon_e^{\text{subset}}}{\epsilon_e^{\text{all}}}$	$\frac{\epsilon_\mu^{\text{subset}}}{\epsilon_\mu^{\text{all}}}$	$\left(\frac{\epsilon_\mu^{\text{subset}}}{\epsilon_\mu^{\text{all}}}\right) \cdot \left(\frac{\epsilon_e^{\text{subset}}}{\epsilon_e^{\text{all}}}\right)^{-1}$
P12	63.3 fb^{-1}	1.112 (+7.4%)	1.009	0.954	1.054 (+5.4%)
B16 - B21	64.1 fb^{-1}	1.034 (+0.1%)	0.997	1.023	0.974 (-2.6%)
B22 - B25	62.5 fb^{-1}	0.984 (-4.9%)	0.994	1.025	0.972 (-2.8%)

Table 6.12: The relative deviations of extracted $R(X_{e/\mu})$ values based on subsets of data-production periods, compared to the nominal value from Table 6.10, are presented. Additionally, the LID-efficiency differences of subset vs. the entire data set are provided. Since $R(X_{e/\mu})$ is proportional to ϵ_μ/ϵ_e, the expected effect of lepton-flavor combined efficiency differences is also provided.

Finally, a split into three different data-taking periods is conducted to test the run dependence of $R(X_{e/\mu})$. The details of this division and the corresponding results are outlined in Table 6.12.

Significant deviations from the nominal result from Table 6.10 are observed. As visible in Figure 6.9, these deviations arise from varying lepton-identification efficiencies across different data-taking periods. While run-independent MC simulations with constant efficiencies are used, the muon-identification efficiency is considerably lower in the early data-taking periods ("P12") compared to the values achieved in later periods. Unfortunately, specific LID-correction factors for each data period are not available. Instead, they are derived from the average difference between experimental data and simulation when considering the entire data set of 189 fb^{-1} . Consequently, the muon efficiencies are overestimated by simulation when $R(X_{e/\mu})$ is extracted only from P12-data, resulting in an enhanced value.

Similarly, averaged LID-correction factors underestimate the muon efficiency when only late run periods ("B22 - B25") are considered. The size of deviating efficiencies is estimated by comparing subset-specific LID efficiencies to the averaged values derived from the entire data set. These values are presented in Table 6.12 and align well with observed deviations in the extracted $R(X_{e/\mu})$ values.

Remaining discrepancies can be attributed to the fact that Figure 6.9, the sole information available at the time of this study, only presents efficiency results based on the $J/\psi \to \ell^+\ell^-$ calibration channel and LID working points of $\mathcal{P}_\ell^{\mathcal{L}/\mathcal{L}} > 0.9$. In contrast, this analysis employs a combination of all calibration channels, $\mathcal{P}_e : \epsilon_e = 80\%$ and $\mathcal{P}_\mu^{\mathcal{L}/\mathcal{L}} > 0.95$ (see Sec. 4.3). Furthermore, differences in fake-rate calibration factors are not considered in the presented considerations. Additionally, statistical fluctuations of the order of $1\% \cdot \sqrt{3} = 1.7\%$ are expected.

As a result, the observed deviations of $R(X_{e/\mu})$ values in different data-taking periods can be

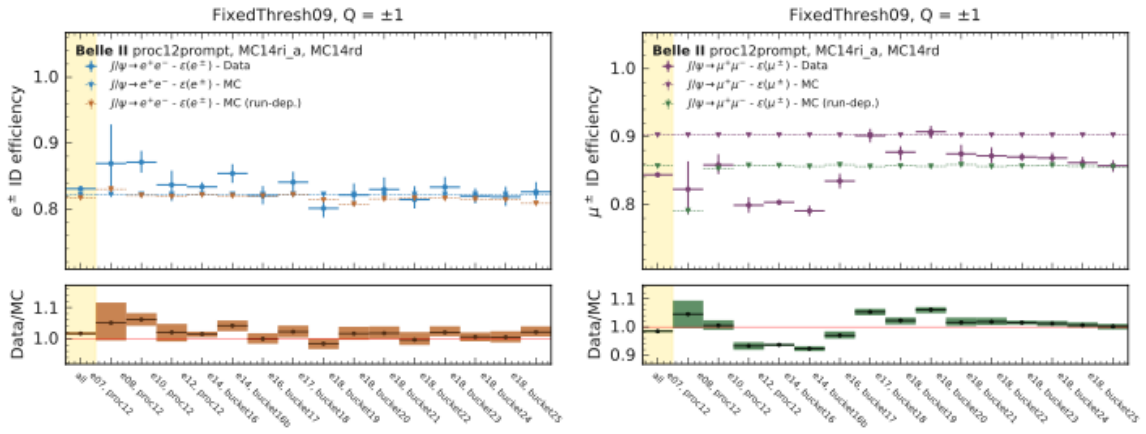

Figure 6.9: Lepton-identification efficiencies for electrons (left) and muons (right) in both experimental data and simulation are presented for different data-production periods. The efficiencies are based on the $J/\psi \to \ell^+\ell^-$ calibration channel and LID working points of $\mathcal{P}_\ell^{\mathcal{L}/\mathcal{L}} > 0.9$. LID correction factors are derived by comparing the efficiency of experimental data to the efficiency of run-independent MC (blue vs blue and purple vs purple). The x-axis displays different data-production periods, ranging from proc12 (referred to as P12 in the text), recorded up to summer 2020, to bucket 25 (B25), recorded in summer 2021. This figure, despite its limited pixel size, was generously provided by the Belle II Performance Group [213].

attributed to run-dependent LID efficiencies. The provided LID-correction factors are only valid for the entire data set, as used in the nominal result of $R(X_{e/\mu})$.

CHAPTER 7

Towards a measurement of $R(X_{\tau/\ell})$: understanding the hadronic system X

To enable the first successful measurement of the tau-to-light-lepton ratio $R(X_{\tau/\ell})$ (see Chap. 8), several adjustments to the event selection are necessary when compared to the extraction of the light-lepton ratio $R(X_{e/\mu})$ (see Chap 6). In particular, the lepton-momentum thresholds are significantly reduced to enhance the efficiency for $B \to X[\tau \to \ell\nu\nu]\nu$ signal decays. Low-momentum leptons, however, are more challenging to distinguish from hadrons, leading to a notable increase in the relative contribution of fakes. Similarly, lower momentum thresholds amplify the yield and diversity of true leptons from secondary decays. Consequently, additional criteria are implemented to mitigate background contributions, as elaborated in Section 7.1. Furthermore, incorporating additional kinematic properties becomes necessary to discriminate signal decays from backgrounds and the normalization decay $B \to X\ell\nu$. This renders a detailed understanding of the hadronic system X indispensable.

Due to the inclusiveness of this analysis, a large variety of different physical processes contribute, making a correct modeling of kinematic observables extremely challenging. In particular, the quantities M_X, q^2, and M^2_{miss} are powerful variables to separate signal, normalization, and backgrounds from each other. In Section 7.2, several control samples are introduced to validate the modeling of all relevant processes. A significant mismodeling is observed, which is thoroughly examined and understood within the same section. In Section 7.3, a data-driven reweighting strategy is introduced to correct the mismodeling. This reweighting is essential for this work, representing the key development that enables the first measurement of $R(X_{\tau/\ell})$.

7.1 Signal-lepton selection in the $R(X_{\tau/\ell})$ measurement and $B\overline{B}$-background suppression

In a first stage, the transverse momenta of electron candidates are required to satisfy $p_e^{\text{T}} > 0.3\,\text{GeV}$, while for muon candidates $p_\mu^{\text{T}} > 0.4\,\text{GeV}$ is demanded.

In order to mitigate fake-lepton backgrounds, the LID-classifier working points are updated compared to their selection for the $R(X_{e/\mu})$ extraction (cf. Sec. 4.3). For electrons, $\mathcal{P}_e > 0.99$ is used. Compared to the previous working point, tuned to a uniform efficiency of 80%, this results in lower efficiencies of 70% but stronger fake suppression for $p_e \in [0.5, 1.0]$ GeV and enhanced efficiencies of

95% for $p_e > 1\,\text{GeV}$. The average misidentification probabilities for pions are less than 0.1% and 0.1% for $p_e \in [0.5, 1.0]\,\text{GeV}$ and $p_e > 1\,\text{GeV}$, respectively. For kaons, the low- and and-momentum misidentification probabilities are 0.1% and 0.02%.

The muon-identification criterion is tightened to $\mathcal{P}_\mu^{\ell/\ell} > 0.99$, resulting in averaged efficiencies of 70% for $p_\mu \in [0.7, 1.0]\,\text{GeV}$ along with hadron misidentification probabilities of 4% for pions and 0.2% for kaons. In the high-momentum range $p_\mu > 1\,\text{GeV}$, the identification efficiency is 90% with fake rates of 2.5% and 1% for pions and kaons, respectively [220].

In contrast to Section 4.3, the criteria for conformity of the trajectories and the IP are relaxed to $\mathrm{d}r < 2\,\text{cm}$ and $|\mathrm{d}z| < 4\,\text{cm}$ in order to enhance specific $B\bar{B}$-background components for a more detailed investigation of their modeling. It is challenging to validate bremsstrahlung corrections for low-lepton momenta in data (see Sec. A.2), therefore the same approach is adopted as in the lepton-identification calibration studies. In these studies, electrons are corrected based on photons satisfying $E_\gamma < 1.0\,\text{GeV}$ if they lie within a cone of angle 2.9° around the electron track.

Various particle decays produce low-lepton momenta, denoted as secondaries (see Sec. 4.5), that satisfy the specified lepton-identification criteria. In Table 7.1, their composition is presented.

Lepton origin	e channel		μ channel	
	Abs. events	Rel. fraction	Abs. events	Rel. fraction
$\gamma \to e^+e^-$	9 273	32%	–	–
$\pi^0 \to e^+e^-(\gamma)$	1 357	5%	–	–
$\pi^- \to \mu^-\overline{\nu}_\mu$	–	–	1 948	15%
$K^- \to \mu^-\overline{\nu}_\mu$	–	–	1 305	10%
$D \to (X)\ell^-\overline{\nu}_\ell$	15 717	54%	8 390	64%
$J/\psi \to \ell^+\ell^-$	870	3%	715	5%
$\tau^- \to \ell^-\overline{\nu}_\ell\nu_\tau$	904	3%	620	5%
Others	834	3%	120	1%

Table 7.1: The composition of secondary events is presented, categorized by signal-lepton origin. The absolute event count and the relative fraction within the secondary category for each lepton flavor is provided. The entry labeled $D \to (X)\ell^-\overline{\nu}_\ell$ encompasses all events where the signal-lepton candidate originates from a $D^{+,0}$-meson or a D_s-meson decay. The $\tau^- \to \ell^-\overline{\nu}_\ell\nu_\tau$ category, where the signal lepton arises from a τ-lepton decay, excludes signal $B \to X[\tau \to \ell\nu\nu]\nu$ decays. The first four event types are referred to as *tertiaries*.

For convenience, in this section, the secondary-lepton category is further subdivided:

- **Tertiaries:** Events with signal-lepton candidates originating from the processes $\gamma \to e^+e^-$, $\pi^0 \to e^+e^-(\gamma)$, and $K^-/\pi^- \to \mu^-\bar{\nu}_\mu$ are classified as *tertiaries* because the lepton is generated later in the decay chain.

- **Secondaries:** Events with signal-lepton candidates from $B\bar{B}$ events that are associated with a true lepton, originating neither from a B meson nor from a τ lepton in a $B \to X\tau\nu$ decay, are labeled as *secondaries*, if they do not fall into the tertiary category. Apart from the largely dominating fraction of semileptonic D decays, this category includes decays such as $J/\psi \to \ell^+\ell^-$ and $D \to (X)[\tau \to \ell\nu\nu]\nu$.

In this section, additional criteria for the signal-lepton candidates are introduced to suppress $B\bar{B}$ backgrounds, which are summarized in Table 7.2 and are motivated in the following. In Table 7.3, the impact of each selection criterion on the different event types is presented. Compared to the initial composition, lepton-flavor exclusive tertiaries are suppressed by approximately 80% for both electrons and muons. The predominant portion of the remaining secondary events arises from semileptonic D-meson decays, which are largely consistent across lepton flavors. This allows for a unified treatment of such events in Section 7.3.4. Overall, the total number of background events is reduced by 55% for electrons and by 49% for muons.

Main rejection target	Electron channel	Muon channel
Baseline	$\mathcal{P}_e > 0.99$, $p_e^{\mathrm{T}} > 0.3\,\mathrm{GeV}$, $\theta \in [17°, 150°]$	$\mathcal{P}_\mu^{\ell/\mathrm{L}} > 0.99$, $p_\mu^{\mathrm{T}} > 0.4\,\mathrm{GeV}$, $\theta \in [17°, 150°]$
Tertiaries	$\lvert D_e\rvert < 1\,\mathrm{cm}$, $q^2 < 26\,\mathrm{GeV}^2$, For $p_e^B < 1\,\mathrm{GeV}$: $\ell \notin V^0$, $M_{e^+e^-} > 150\,\mathrm{MeV}$	$\lvert D_\mu\rvert < 0.15\,\mathrm{cm}$
$J/\psi \to \ell^+\ell^-$	$\Delta M_{J/\psi} \notin [-50, 30]\,\mathrm{MeV}$	$\lvert\Delta M_{J/\psi}\rvert > 30\,\mathrm{MeV}$
$B\bar{B}$ backgrounds	$p_e > 0.5\,\mathrm{GeV}$	$p_\mu > 0.7\,\mathrm{GeV}$
Muon fakes	–	$\lvert\Delta M_{\omega,K^*,D^0,D^+}\rvert > 15/20\,\mathrm{MeV}$ or $p(\chi^2_{\mathrm{vertex}})_{\omega,K^*,D^0,D^+} < 0.05/0.3/0.5$

Table 7.2: The criteria for selecting signal-lepton candidates in the $R(X_{\tau/\ell})$ measurement are outlined and organized based on the primary rejection target.

Tertiary and secondary rejection strategies are motivated in Sections 7.1.1, 7.1.2, and 7.1.3, while fake-lepton candidates are mitigated based on event selections introduced in Sections 7.1.4 and 7.1.5. Given that continuum background events, described with off-resonance data, are effectively caused by secondary and fake leptons as well, the introduced selections also lead to a significant reduction in their occurrence.

7.1.1 Suppression of conversion photons and $\pi^0 \to e^+e^-(\gamma)$ decays

As indicated in Table 7.1, a considerable amount of $B\bar{B}$-background events arises from electrons originating from $\gamma \to e^+e^-$ decays, i.e., from conversion photon events. These events are exclusive to the electron channel and result from interactions of particles with the detector material, which are challenging to simulate accurately. Additionally, electrons originating from $\pi^0 \to e^+e^-(\gamma)$ decays constitute a non-negligible source of backgrounds and share similar properties. Consequently, both types of events are collectively referred to as tertiaries.

The coherent production of oppositely charged electrons with a small invariant mass, typically with vertices distinct from the IP, presents a clean signature for their identification and suppression. To achieve this, the V^0 finder [221], a tool provided within `basf2`, is employed. This tool is designed to identify any displaced vertices resulting from the decay of neutral particles into oppositely charged

Event type	Baseline selection	Tertiary suppression	$\Delta M_{J/\psi}$ rejection	p_e, p_μ thresholds	$\Delta M_{\omega,K^*,D}$ rejection
			Electron channel		
Continuum	8 617	4 883 (57%)	4 863 (56%)	3 336 (39%)	
Fakes	2 992	2 684 (90%)	2 684 (90%)	1 381 (46%)	
Tertiaries	10 630	3 907 (37%)	3 907 (37%)	2 108 (20%)	
Secondaries	18 326	17 235 (94%)	16 799 (92%)	11 659 (64%)	
$Xe\nu$	100 926	100 071 (99%)	99 963 (99%)	97 910 (97%)	
$X[\tau \to e\nu\nu]\nu$	3 107	3 012 (97%)	3 012 (97%)	2 566 (83%)	
			Muon channel		
Continuum	13 040	11 461 (88%)	11 451 (88%)	7 247 (56%)	6 609 (51%)
Fakes	27 738	25 632 (92%)	25 625 (92%)	15 814 (57%)	14 429 (52%)
Tertiaries	3 253	1 284 (39%)	1 284 (39%)	839 (26%)	795 (24%)
Secondaries	9 846	9 782 (99%)	9 199 (93%)	6 441 (65%)	6 108 (62%)
$X\mu\nu$	93 902	93 768 (100%)	93 651 (100%)	91 865 (98%)	90 967 (97%)
$X[\tau \to \mu\nu\nu]\nu$	2 204	2 199 (100%)	2 198 (100%)	1 888 (86%)	1 857 (84%)

Table 7.3: The impacts of the $B\bar{B}$-background suppression requirements, as detailed in Table 7.2, are presented for each event type. The relative fraction remaining after each suppression requirement, compared to the initial amount, is presented in the brackets.

tracks, as anticipated in processes such as $\gamma \to e^+e^-$, $K^0_S \to \pi^+\pi^-$, and $\Lambda^0 \to p\pi^-$. No particle identification requirements are imposed, so that all reconstructed tracks are considered.

In Figure 7.1(a), the invariant mass of the V^0 candidate, denoted as M_{V^0}, is presented for cases where the signal-electron candidate is identified as part of a V^0 candidate. If multiple V^0 candidates are detected for the signal electron, the V^0 with an invariant mass closest to $m_\gamma = 0\,\text{GeV}$ is selected. As illustrated in the figure, almost exclusively tertiary events are selected. Consequently, all signal-electron candidates associated with a V^0 are rejected, regardless of the invariant mass of the V^0.

A considerable fraction of conversion photons generates at least one electron with very low momentum, $p_e \lesssim 0.2\,\text{GeV}$, resulting in a significant drop in track-reconstruction efficiency. Such events cannot be identified based on commonly shared vertices. Instead, the minimal three-dimensional distance from the electron candidate's track to the IP, denoted as $|D_e| = \sqrt{\mathrm{d}r^2 + \mathrm{d}z^2}$, is employed. As illustrated in Figure 7.1(b), $|D_e|$ can be sizable for conversion photon events, whereas other true leptons feature much smaller values. Hence, for signal-electron candidates, the requirement $|D_e| < 1\,\text{cm}$ is imposed. A more stringent threshold is avoided to prevent sensitivity to observed mismodeling around $|D_e| \approx 0.5\,\text{cm}$.

The V^0 finder exclusively identifies displaced vertices. To exclude signal-lepton candidates arising from conversion photons and $\pi^0 \to e^+e^-(\gamma)$ decays with vertices within the beam pipe, they are combined with oppositely charged tracks, not associated with the B_{tag} candidate and satisfying $\mathcal{P}_e^{\ell/\mathcal{L}} > 0.2$. The resulting invariant masses are shown in Figure 7.1(c). A substantial fraction of tertiary events is further rejected by imposing the requirement $M_{e^+e^-} > 150\,\text{MeV}$.

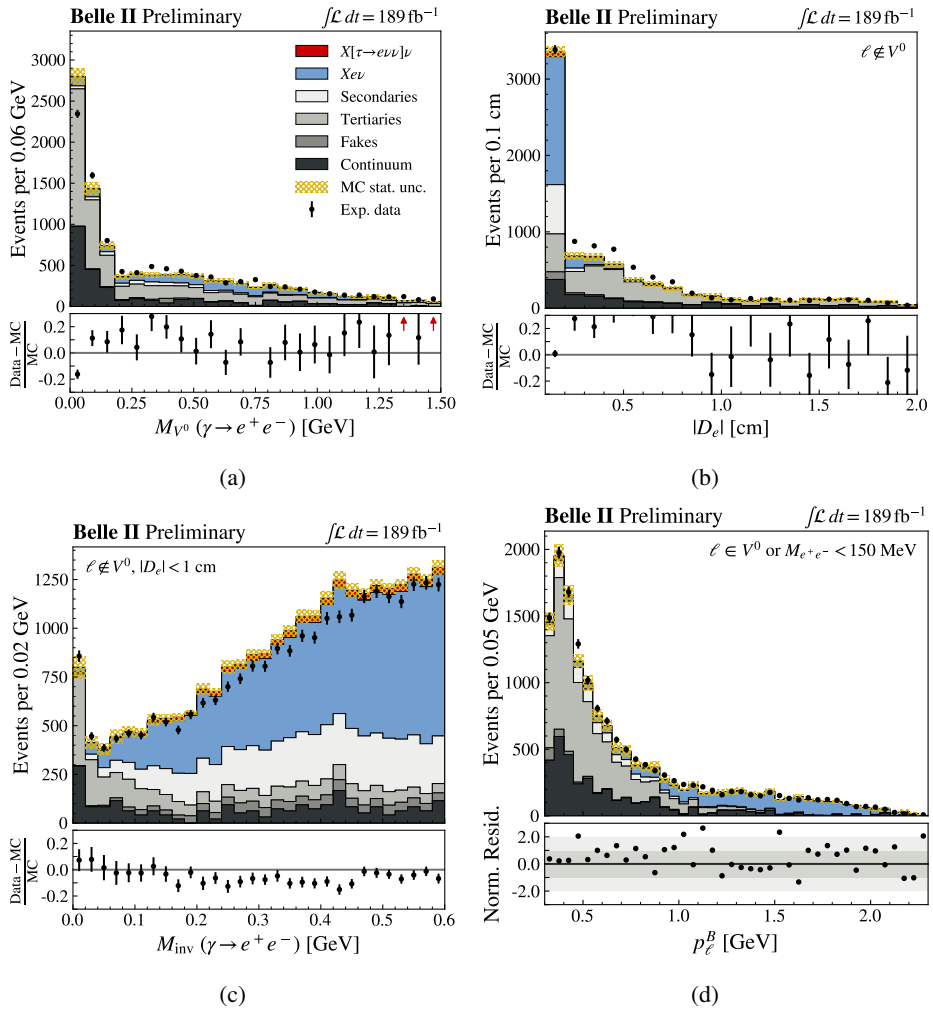

Figure 7.1: Various quantities employed to suppress electron tertiaries are visualized. In (a), the invariant mass of all V^0 candidates is displayed, where one of the two tracks is the signal-lepton candidate. In (b), the three-dimensional distance ($|D_e|$) of the extrapolated electron track to the IP is presented for values of $|D_e| > 0.1\,\text{cm}$, excluding the large peak of $O(10^5)$ events at $|D_e| \approx 0\,\text{cm}$. Events rejected based on the V^0 finder are not included. In (c), the invariant mass of the signal lepton and an oppositely charged track, satisfying $\mathcal{P}_e^{\mathcal{L}/\mathcal{L}} > 0.2$, is depicted for events not rejected by the V^0 finder and with $|D_e| < 1\,\text{cm}$. In (d), the p_e^B distribution of events that are rejected by the V^0 finder or $M_{\text{inv}}(\gamma \to e^+e^-) < 150\,\text{MeV}$ is presented.

Figure 7.1(d) displays the p_ℓ^B distribution for events rejected by the previously mentioned requirement on V^0 or $M_{e^+e^-}$, including a significant number of $B \to X\ell\nu$ normalization decays. Therefore, an additional condition is imposed, restricting these tertiary rejection criteria to signal-electron candidates with $p_e^B < 1\,\text{GeV}$. Furthermore, to mitigate a substantial number of continuum events, a constraint of $q^2 < 26\,\text{GeV}^2$ is imposed.

The p_ℓ^B, M_X, q^2, and M_{miss}^2 distributions for rejected events are presented in Figure 7.2. Experimental data aligns well with simulation, indicating that no bias is introduced by this selection. The impact of the introduced selection requirements is presented in Table 7.3. 63% of all tertiary events and 43% of

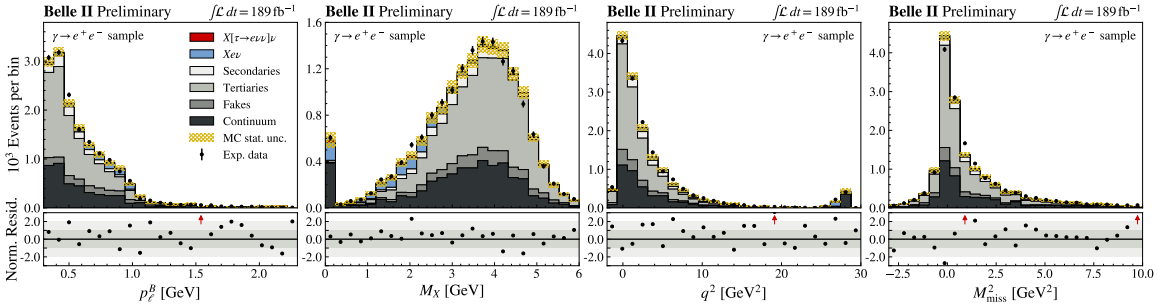

Figure 7.2: The p_ℓ^B, M_X, q^2, and M^2_{miss} distributions for events rejected by the electron-tertiary-suppression requirements are displayed. The presented events satisfy one of the following criteria: $\ell \in V^0$, or $M_{e^+e^-} < 150\,\text{MeV}$, for $p_\ell^B < 1\,\text{GeV}$, $|D_e| > 1\,\text{cm}$, or $q^2 > 26\,\text{GeV}^2$.

all continuum events are rejected, while signal and normalization yields remain almost unchanged.

7.1.2 Suppression of $K^-/\pi^- \to \mu^-\bar{\nu}_\mu$ decays

In the muon channel, a considerable amount of backgrounds arises from the decays of charged pions or kaons into muons (see Tab. 7.1), referred as tertiaries in this section. Due to the diverse range of decays leading to charged pions or kaons, muon tertiaries do not exhibit similarly distinct signatures as electron tertiaries. Nevertheless, Figure 7.3 illustrates that muon tertiaries often feature substantial deviations of the muon trajectory from the IP compared to other signal-lepton candidates due to the large lifetimes of charged pions and kaons.

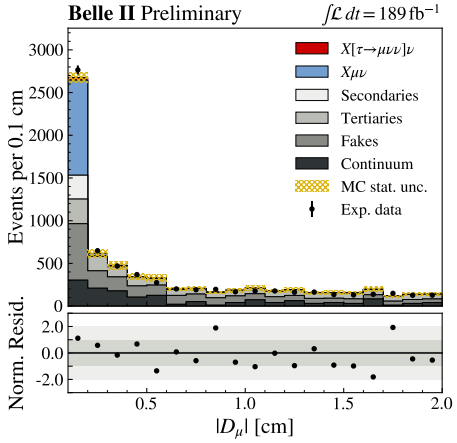

Figure 7.3: The three-dimensional distance of the extrapolated muon trajectory to the IP, denoted $|D_\mu|$, is displayed for $|D_\mu| > 0.1\,\text{cm}$, excluding the $O(10^5)$ events at $|D_\mu| \approx 0\,\text{cm}$.

Unlike in the electron channel (see Fig. 7.1(b)), there is no evidence of mismodeling for muons. Therefore, a stringent requirement of $|D_\mu| < 0.15\,\text{cm}$ is applied for signal-muon candidates. Figure 7.4 illustrates that the rejected events are well-modeled in the signal-extraction quantities.

This approach successfully rejects 61% of all muon-tertiary events, with no impact on the signal

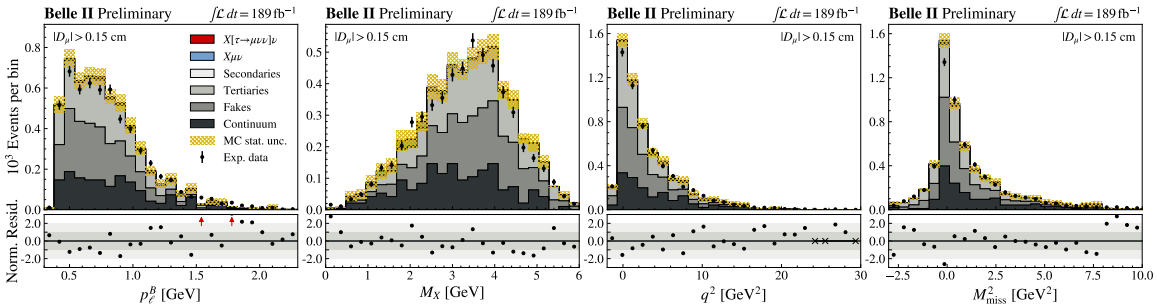

Figure 7.4: The p_ℓ^B, M_X, q^2, and M^2_{miss} distributions are presented for events that are rejected by the muon-tertiary-suppression requirement $|D_\mu| < 0.15\,\text{cm}$.

and normalization modes, as shown in Table 7.3.

7.1.3 Suppression of $J/\psi \to \ell^+\ell^-$ decays

A small yet non-negligible contribution to electron and muon backgrounds comes from $J/\psi \to \ell^+\ell^-$ decays, that are easily identifiable. For this purpose, the signal-lepton candidate is combined with any oppositely charged tracks that satisfies the loose requirement $\mathcal{P}_\ell^{\mathcal{L}/\mathcal{L}} > 0.2$. The resulting invariant masses, closest to $m_{J/\psi}$, are illustrated in Figure 7.5.

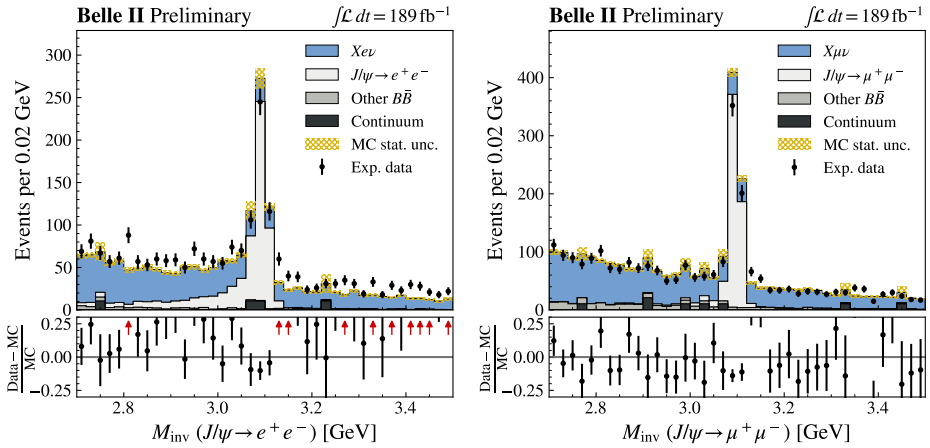

Figure 7.5: The distribution of invariant masses of signal-lepton candidates, combined with an oppositely charged track satisfying $\mathcal{P}_\ell^{\mathcal{L}/\mathcal{L}} > 0.2$, are presented around $m_{J/\psi} = 3.097\,\text{GeV}$ for the electron (left) and muon (right) channels.

In the muon channel, a distinct peak centered around $m_{J/\psi} = 3.097\,\text{GeV}$ is observed, which is almost exclusively composed of $J/\psi \to \mu^+\mu^-$ decays. To mitigate such events, muon candidates are required to satisfy $\left|\Delta M_{J/\psi}\right| \equiv \left|M_{\text{inv}} - m_{J/\psi}\right| > 30\,\text{MeV}$.[1] Since electrons are more susceptible to

[1] As introduced in Section 3.4.3, reconstructed invariant masses M are distinguished from particle-property masses m by using uppercase and lowercase letters.

bremsstrahlung, the $J/\psi \to e^+e^-$ mass peak features a broader structure towards lower values. This is accommodated by adjusting the rejection requirement to $(M_{\text{inv}} - m_{J/\psi}) \notin [-50, 30]$ MeV.

This approach rejects 430 events, approximately 50% of all $J/\psi \to e^+e^-$ decays, and 580 events (80%) of all $J/\psi \to \mu^+\mu^-$ backgrounds (see Tab. 7.3).

7.1.4 Lepton-momentum based background suppression

Secondary leptons arising from D-meson decays and misidentified fake leptons exhibit a broad range of characteristics, making them challenging to distinguish based on distinct features. Nonetheless, their prevalence notably rises as lepton momenta decrease. Therefore, the lepton momentum serves as a powerful quantity for background suppression, although signal $B \to X[\tau \to \ell\nu\nu]\nu$ decays also feature low lepton momenta.

To simultaneously optimize background rejection and signal efficiency, the significance, estimated using $S/\sqrt{S+B}$, is utilized. Here, S represents the number of signal events ($X\tau\nu$), and B summarizes background yields (fakes, secondaries, tertiaries, and continuum). Figure 7.6 illustrates the relative change of significance for increasing lab-frame (p_ℓ) and transverse (p_ℓ^{T}) lepton-momentum thresholds.

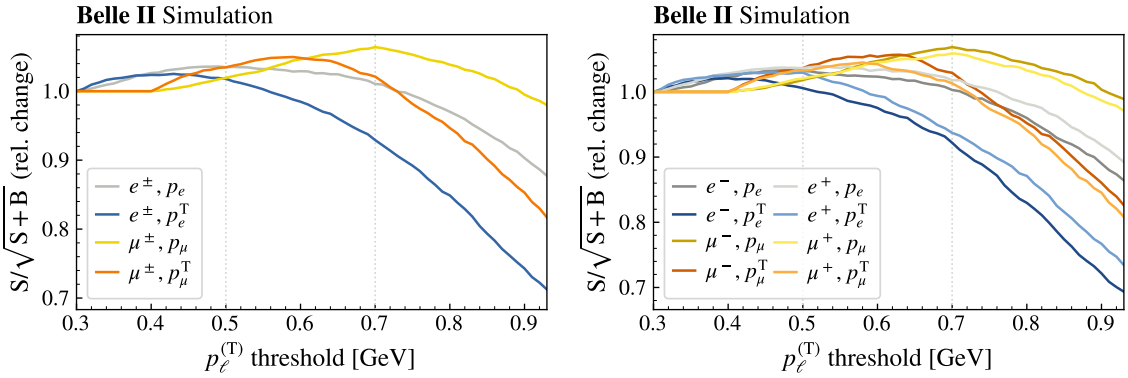

Figure 7.6: The significance $S/\sqrt{S+B}$, normalized to its initial value, is evaluated for increasing lepton-momentum thresholds in the laboratory frame (p_ℓ) and in the transverse plane (p_ℓ^{T}) for each lepton flavor. The study is performed for both lepton charges combined (left) and separately for each charge (right).

Based on these scans, the significance is optimized by imposing the requirements of $p_e > 0.5\,\text{GeV}$ and $p_\mu > 0.7\,\text{GeV}$ independently of the lepton charge. Lab-frame momenta provide a slight performance advantage compared to potential thresholds based on the transverse momentum p_ℓ^{T}.

In general, the significance-based approach presented here may not necessarily yield the optimal event selection, as signal and background events can be distinguished in the signal-extraction fit based on quantities orthogonal to lepton momentum. However, as detailed in Section 7.2, a substantial mismodeling of D-meson decays is observed, leading to significant systematic shape uncertainties for $B\bar{B}$ backgrounds. The quantification of uncertainties and correction of $B\bar{B}$-background shapes, as discussed in Section 7.3.4, necessitates a reduction of diversity in the $B\bar{B}$-background compositions, particularly for decays exclusive to one of the two lepton flavors.

Hence, the stringent background rejection, as motivated by the p_ℓ-based significance scan, is implemented. This results in a suppression of one-third to half of all remaining background sources, accompanied by a reduction in signal efficiency by 15% (see Tab. 7.3).

7.1.5 Resonance-based muon-fake rejection

The majority of hadrons misidentified as signal-lepton candidates are charged pions or kaons. A notable fraction of these hadrons are generated in hadronic decays of D mesons or intermediate resonances, such as ρ mesons or excited kaons. Given that no neutrino is produced in hadronic decays, all remaining decay products are, in principle, detectable if within the acceptance region and constitute part of the X system in cases with good B_{tag} candidates. Consequently, signal-lepton candidates are investigated to be compatible with forming a resonant state together with other particles from the X system.

In this procedure, either pion or kaon masses are assigned to the signal-lepton candidate and a loose identification requirement on the binary pion-kaon classifier (see Sec. 3.3.3) of $\mathcal{P}^{\ell/\mathcal{L}}_{(\pi|K)} \lesssim 0.1$ is imposed on X-system tracks to distinguish pion and kaon candidates. Additionally, following studies conducted in another Belle II analysis [119], neutral pion candidates are reconstructed from photons associated with the X system, satisfying

$$\left(\frac{\Delta R^{\text{track}}_{\text{cluster}}}{40}\right)^2 + \left(\frac{\mathcal{P}_{\text{Zernike}}}{0.4}\right)^2 > 1, \qquad M_{\pi^0} \in [120, 145]\,\text{MeV}. \tag{7.1}$$

In Table 7.4, all intermediate resonances are listed that are investigated for their potential in background rejection. Their invariant masses and p values of their vertex fit, denoted $p(\chi^2_{\text{vertex}})$, are compared in experimental data and simulation in Section B.4 in the appendix. In cases where a high purity of fakes is observed, selection criteria are imposed on $|\Delta M| \equiv |M_{\text{inv}} - m_i|$ and $p(\chi^2_{\text{vertex}})$, as summarized in Table 7.4. Due to Belle II's excellent electron identification and the stringent electron-classifier threshold, electron fakes are comparably rare. Therefore, the presented requirements are only applied to the muon channel.

Many candidates of uncharmed resonances (ρ, η', ω, K^0_S, K^*) feature a low purity of fakes. However, several of them are indirectly suppressed due to the preceding D-meson resonance. This is because there is no distinction in M_{inv} between, for example, $D^+ \to \pi^+\pi^+\pi^-\pi^0$ and $D^+ \to \pi^+[K^0_S \to \pi^+\pi^-]\pi^0$ decays (only in $p(\chi^2_{\text{vertex}})$). In total, approximately 10% of all remaining backgrounds are rejected in the muon channel, while the signal efficiency is reduced by 2% (see Tab. 7.3).

The events that are rejected based on the introduced criteria are compared between experimental data and simulation in Figure 7.7.

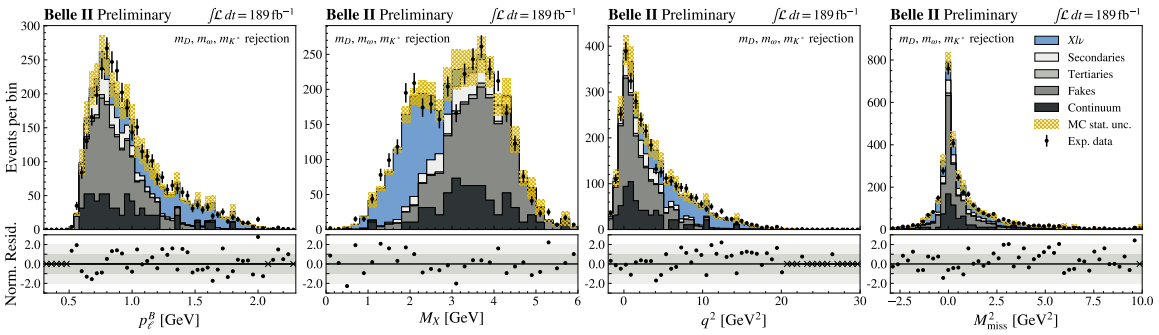

Figure 7.7: The p^B_ℓ, M_X, q^2, and M^2_{miss} distributions are presented for events that are rejected by the requirements based on intermediate resonances.

Decay	Suppression requirements $\lvert\Delta M\rvert$	$p(\chi^2_{\text{vertex}})$
$\rho^+ \to \pi^+_\ell \pi^0$	–	–
$\rho^0 \to \pi^+_\ell \pi^-$	–	–
$\eta' \to \pi^+_\ell \pi^- \gamma$	–	–
$\omega^0 \to \pi^+_\ell \pi^-$	–	–
$\omega^0 \to \pi^+_\ell \pi^- \pi^0$	20 MeV	0.3
$K^0_S \to \pi^+_\ell \pi^-$	–	–
$K^{*,0} \to \pi^-_\ell K^+$	20 MeV	0.05
$K^{*,0} \to K^+_\ell \pi^-$	–	–
$K^{*,+} \to K^+_\ell \pi^0$	–	–
$D^0 \to \pi^+_\ell K^-$	–	–
$D^0 \to K^-_\ell \pi^+$	–	–
$D^0 \to K^-_\ell \pi^+ \pi^0$	–	–
$D^0 \to \pi^+_\ell K^- \pi^0$	–	–
$D^0 \to \pi^+_\ell \pi^+ K^- \pi^-$	20 MeV	0.05
$D^0 \to \pi^-_\ell K^- \pi^+ \pi^+$	20 MeV	0.05
$D^0 \to K^-_\ell \pi^+ \pi^+ \pi^-$	20 MeV	0.05
$D^0 \to \pi^+_\ell K^- \pi^0 \pi^0$	–	–
$D^0 \to K^-_\ell \pi^+ \pi^0 \pi^0$	–	–
$D^0 \to K^-_\ell K^+$	–	–
$D^+ \to \pi^+_\ell [K^0_S \to \pi^+ \pi^-]$	–	–
$D^+ \to \pi^+_\ell [K^0_S \to \pi^+ \pi^-] \pi^0$	20 MeV	0.5
$D^+ \to \pi^+_\ell [K^0_S \to \pi^+ \pi^-] \pi^+ \pi^-$	20 MeV	0.05
$D^+ \to \pi^-_\ell [K^0_S \to \pi^+ \pi^-] \pi^+ \pi^+$	20 MeV	0.05
$D^+ \to \pi^+_\ell \pi^+ K^-$	15 MeV	0.05
$D^+ \to K^-_\ell \pi^+ \pi^+$	–	–
$D^+ \to \pi^+_\ell \pi^+ K^- \pi^0$	20 MeV	0.05
$D^+ \to K^-_\ell \pi^+ \pi^+ \pi^0$	20 MeV	0.05
$D^+ \to \pi^+_\ell \pi^+ \pi^+ K^- \pi^-$	–	–
$D^+ \to \pi^-_\ell K^- \pi^+ \pi^+ \pi^+$	–	–
$D^+ \to K^-_\ell \pi^+ \pi^+ \pi^+ \pi^-$	–	–

Table 7.4: All resonances that are investigated for their background-rejection potential are presented. Each decay is reconstructed from particles associated with the X system and the signal-lepton candidate, assigned the mass hypothesis of a pion (π_ℓ) or a kaon (K_ℓ). Intermediate K^0_S mesons are not explicitly reconstructed. Resonances are suppressed by imposing requirements on the invariant mass $|\Delta M| \equiv \left|M_{\text{inv}} - m_i\right|$ and $p(\chi^2_{\text{vertex}})$. If both requirements are met, the event is rejected. If no requirements are listed, the specified resonance is assessed insufficient to suppress fakes (see Sec. B.4). Charge conjugation is implied throughout.

7.2 Modeling of signal-extraction quantities in control samples

To measure $R(X_{\tau/\ell})$, signal decays have to be differentiated from normalization and background events based on their distinctive characteristics. Through simulation-based studies, the observables with the highest signal-extraction power are identified to be the lepton momentum in the B_{sig} frame, p_ℓ^B, and the missing mass squared M^2_{miss}. The lepton momentum proves particularly effective in separating normalization decays from signal and background events (see Sec. 4.3). For events featuring one (e.g., $B \to X\ell\nu$ decays or secondaries from semileptonic D decays) or zero neutrinos (fakes, secondaries created in pair production), the missing mass squared is anticipated to yield $M^2_{\text{miss}} \approx 0\,\text{GeV}^2$ under conditions of ideal reconstruction. In contrast, the signal decay $B \to X[\tau \to \ell\nu\nu]\nu$ involves three neutrinos, resulting in higher values of M^2_{miss}.

Given that several normalization and background events share signal-like properties, such as significant M^2_{miss} values arising from detector-resolution effects and particles beyond the detector acceptance, it is essential to validate their modeling in a signal-independent manner. Particularly, M^2_{miss} is a complex quantity dependent on the accurate modeling of the kinematics of the signal lepton, B_{tag} candidate, and the X system (see Eq. (4.9)), as well as the detector responses. Several of these effects also contribute to the determination of the quantities M_X and q^2, which, while correlated with M^2_{miss}, exhibit reduced complexity (see Eqs. (4.7) and (4.8)). Consequently, they serve as valuable observables to validate simulation with experimental data.

For this purpose, Section 7.2.1 introduces various signal-depleted control samples, each containing less than 0.5% signal decays, with the aim of scrutinizing the modeling of normalization and background events across diverse kinematic regions. Corresponding figures are provided in the appendix in Section B.5. These samples reveal substantial discrepancies between experimental data and simulation in the distributions of p_ℓ^B, M_X, q^2, and M^2_{miss}, discussed comprehensively in Section 7.2.2. As demonstrated in Section 7.2.3, the observed mismodeling is closely connected to inaccuracies in the modeling of D-meson decays.

7.2.1 Definition of control samples

As previously employed in the $R(X_{e/\mu})$ extraction in Chapter 6, one distinctive characteristic of normalization decays is the comparatively high momentum of the signal lepton, as illustrated in Figure 7.8. This allows for the definition of a high-p_ℓ^B control sample, set at $p_\ell^B > 1.4\,\text{GeV}$, resulting in an remarkable purity of 95% for $B \to X\ell\nu$ decays (see Figs. 7.10 and B.17).

Low-momentum $B \to X\ell\nu$ decays and background events are validated using the low-M^2_{miss} and low-q^2 control samples, , resulting in normalization-to-background compositions of 78% vs. 21% and 60% vs. 40%, respectively. These control samples are defined by $M^2_{\text{miss}} < 1.5\,\text{GeV}^2$ and $q^2 < 3.5\,\text{GeV}^2$. The suppression of signal decays is achieved due to their high M^2_{miss} values and their kinematically required minimal momentum transfer of $q^2 > m_\tau^2 \approx 3.2\,\text{GeV}^2$ (see Figs. B.18 and B.19).

Background events can be separated from signal and normalization decays based on the invariant mass of the X system M_X. As illustrated in Figure 7.8, correctly reconstructed $B \to X\tau\nu$ and $B \to X\ell\nu$ decays exhibit M_X values centered around the resonant masses of $D^{(*,**)}$ mesons, ranging from $m_D \approx 1.87\,\text{GeV}$ to $m_{D_2^*} \approx 2.46\,\text{GeV}$ [17], albeit smeared by missed particles and reconstruction effects. In contrast, incorrectly selected signal-lepton candidates from $B\bar{B}$ backgrounds often originate from hadronic B-meson decays, resulting in X-system masses closer to the original B-meson mass of

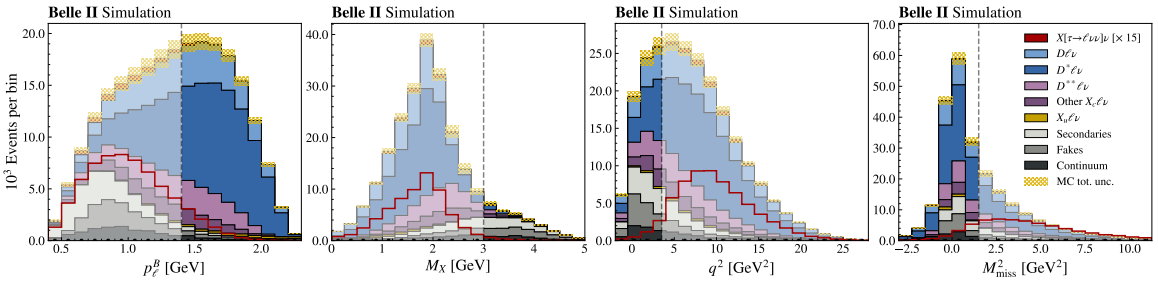

Figure 7.8: The quantities demonstrating the highest potential for separating signal, normalization, and background events are presented in the combined electron and muon channels. They serve as input for defining signal-depleted control samples, as denoted by the shaded areas. The signal distribution in each quantity, enhanced by a factor of 15, is prominently displayed with a red line.

approximately 5.28 GeV. The definition of a high-M_X control sample, set at $M_X > 3$ GeV, yields a background purity of 79% with an additional 21% from normalization decays (see Fig. B.20).

High values of M_X are correlated with lower values of M^2_{miss}. In order to validate background modeling in the signal-enriched high-M^2_{miss} sample, the same-flavor control sample is introduced (as used in the $R(X_{e/\mu})$ measurement, see Sec. 6.1.1). In this sample, the flavor of the B_{sig} candidate, determined by the charge of the signal lepton, is required to match the flavor reconstructed for the B_{tag} candidate. This condition results in a pure composition of 95% backgrounds for charged B_{tag} candidates. Due to $B^0/\overline{B}^0$ mixing, the same-flavor control sample for neutral B_{tag} candidates includes 37% $B \to X\ell\nu$ decays in addition to the 63% backgrounds (see Figs. B.21 and B.22).

Additionally, hadrons misidentified as signal leptons can be validated in control samples defined by lower lepton-identification classifier thresholds as demonstrated in Figure 7.9. For this purpose, a requirement of $\mathcal{P}_e \in [0.5, 0.75]$ or $\mathcal{P}_\mu^{\mathcal{L}/\mathcal{L}} \in [0.5, 0.9(9)]$ is imposed, and the LID-calibration factors are adjusted to the appropriate working point. Signal-lepton candidates originating from pions, kaons, and protons can be distinguished based on $\mathcal{P}^{\mathcal{L}/\mathcal{L}}_{(\pi|K)}$ and $\mathcal{P}^{\mathcal{L}/\mathcal{L}}_p$, as illustrated for $\pi^\pm/K^\pm \xrightarrow{\text{ID}} \ell^\pm$ in the same figure and for $p/\overline{p} \xrightarrow{\text{ID}} e^+/e^-$ in Figure 5.1. To enhance the statistical precision of these backgrounds, the control samples can be merged with the same-flavor control sample.

Finally, control samples enriched with lepton-flavor-specific decays such as $\gamma \to e^+e^-$ or $\pi^-/K^- \to \mu^-\overline{\nu}_\mu$, secondaries from $J/\psi \to \ell^+\ell^-$, or muon fakes can be defined by reversing the requirements introduced in Section 7.1, as depicted in Figures 7.2, 7.4, and 7.7.

7.2.2 Discrepancies in simulation and experimental data

In Figure 7.10, the distributions of p_ℓ^B, M_X, q^2, and M^2_{miss} are compared between experimental data and simulation in the high-p_ℓ^B control sample.

In all quantities related to the X system – M_X, q^2, and M^2_{miss}– significant differences between the distributions in experimental data and simulation are evident, that are not covered by systematic shape uncertainties of the simulation. Particularly, for low M_X values, simulations tend to underestimate the relative number of events compared to experimental data, while events with high M_X values are overestimated. This observation is closely linked to the transferred momentum q^2, which tends to be higher on average in experimental data compared to simulation. Interestingly, a similar q^2 mismodeling is also observed in a recent inclusive analysis by Belle, as illustrated in Figure 3 of

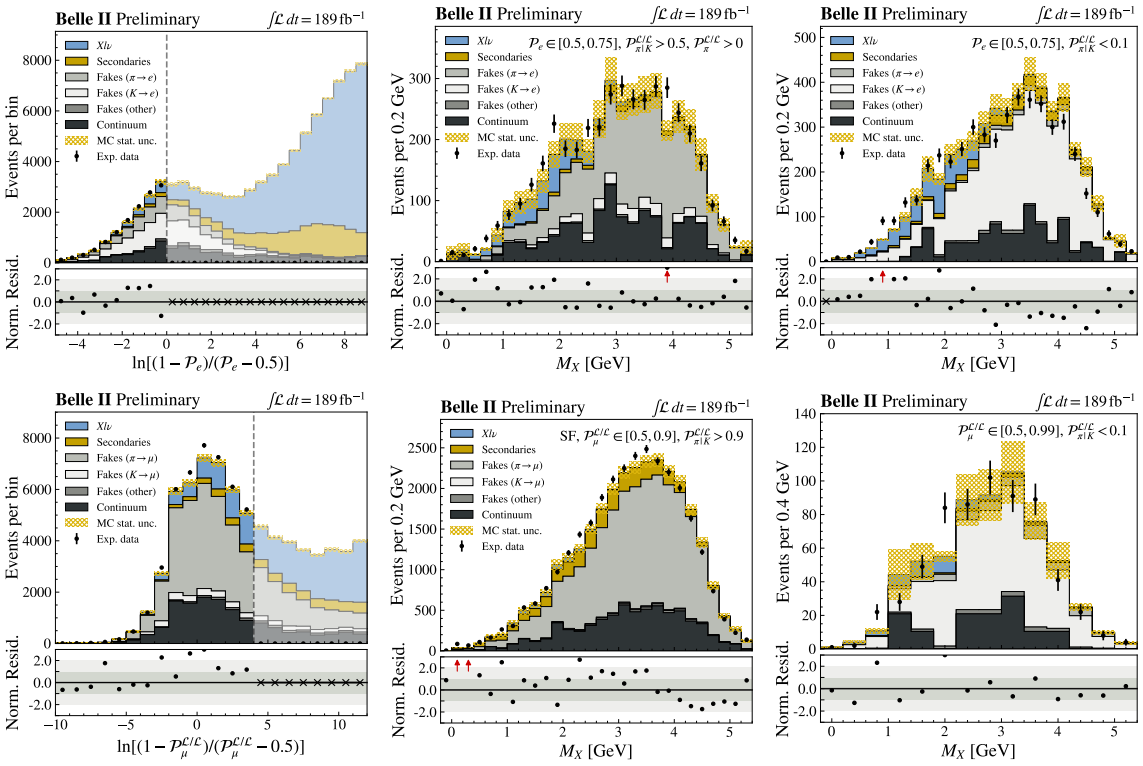

Figure 7.9: The distributions of M_X are presented in fake-enriched control samples for electrons (top row) and muons (bottom row). These samples are characterized by low LID-classifier thresholds, as presented in the leftmost figures. For better visibility, the classifiers are transformed via $\ln[(\mathcal{P}_\ell - 0.9)/(0.5 - \mathcal{P}_\ell)]$. Fake candidates originating from pions (dark gray) and kaons (light gray) are distinguished based on requirements on $\mathcal{P}_{(\pi|K)}^{\mathcal{L}/\mathcal{L}}$. In the electron case, the additional requirement of $\mathcal{P}_\pi^{\mathcal{L}/\mathcal{L}} > 0$ is imposed. For muons, the same-flavor control sample (SF) is illustrated for pion fakes.

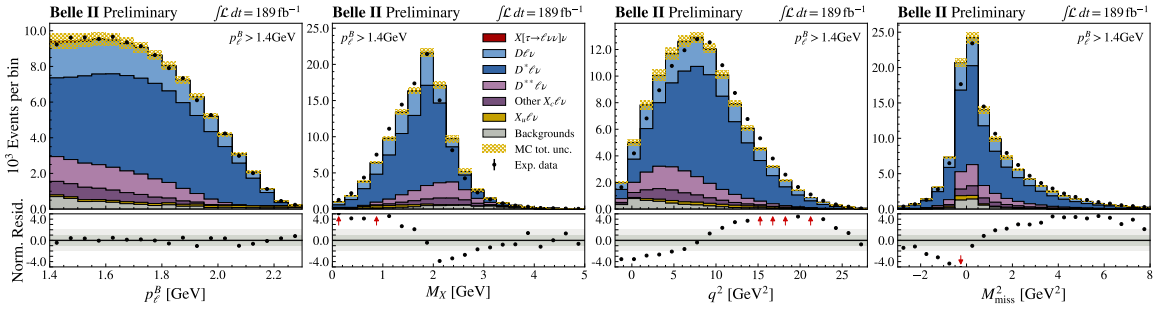

Figure 7.10: Simulation is compared to experimental data in the quantities p_ℓ^B, M_X, q^2, and M_{miss}^2 in the high-p_ℓ^B control sample and combined electron and muon channels. Uncertainty-normalized residuals are presented below.

Reference [155]. Moreover, there is an observed deficit in experimental data at low M^2_{miss} values, while the opposite holds true for high M^2_{miss} values. As highlighted in Section 2.3.2, persistent discrepancies in M^2_{miss} eventually prevented a collaboration-approved publication of Belle's $R(X_{\tau/\ell})$ analysis [136]. Consequently, the identification of the cause of the observed mismodeling and the development of an effective correction method, as discussed in Section 7.3, stand out as key achievements in this analysis.

In general, differences between experimental data and simulation may arise from either inadequacies in the generated physical processes, leading to an inaccurate reflection of nature, or from mismodeling of the interactions of generated particles with the detector. In the context of this thesis, various potential sources of mismodeling are investigated in detail and are briefly presented in the following.

Detector performance mismodeling

A direct interpretation of the observed discrepancies suggests a potential mismodeling of detector performance. To investigate this hypothesis, the multiplicities of tracks and neutral clusters within the X system are compared with data, segmented by energy. Typically, the detector's response to low-energy particles is anticipated to be more challenging to model, leading to accumulating discrepancies for low-momentum tracks or low-energy clusters. However, no such energy-dependent mismodeling is observed. Similarly, an examination of the kinematic properties of individual components of the X system – such as momentum, energy, or polar angle θ of various tracks and clusters within the X system, organized by energy – reveals not to be correlated with observed mismodeling.

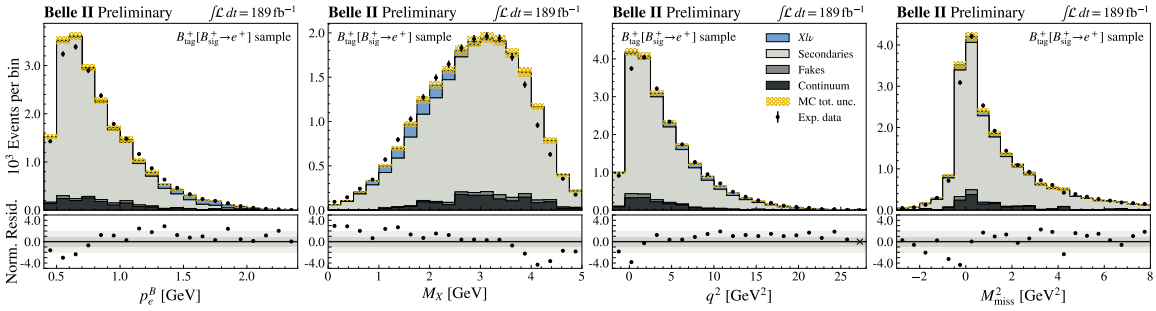

Figure 7.11: Simulation is compared to experimental data in the quantities p^B_ℓ, M_X, q^2, and M^2_{miss} in the same-flavor $B^+_{\text{tag}}[B^+_{\text{sig}} \to e^+]$ sample. Uncertainty-normalized residuals are presented below.

Additionally, in Figure 7.11, the same-flavor control sample is presented for charged B_{tag} candidates in the electron channel, yielding a secondary-enriched sample with high purity (86% secondaries and 7% off-resonance-constrained continuum events). In this control sample, as well as in the tertiary-enriched and fake-enriched samples depicted in Figures 7.2, 7.4, 7.7, and 7.9, the observed mismodeling appears to be less pronounced than in the case of $B \to X\ell\nu$ decays shown in Figure 7.10, irrespective of the reduced statistical precision in these control samples. Mismodeling induced by inaccurately simulated detector responses, however, should be independent of the event type.

Furthermore, the selection criteria for tracks and neutral clusters, as outlined in Section 4.4, are systematically varied in multiple ways, including the imposition of much more stringent requirements. Again, no significant impact on the observed deviations is noted.

As a result, the observed discrepancies cannot be attributed to inaccurately simulated track or cluster reconstruction or mismodeling related to beam-induced backgrounds.

Hadron-identification efficiencies

Although the track-reconstruction efficiency appears to be accurately modeled, inaccuracies in simulating particle-identification efficiencies can lead to variations in candidate multiplicities for charged pions and kaons between simulation and experimental data. Indeed, discrepancies in the multiplicities of charged hadron-candidate, as well as photon-candidates, are observed in Figure 7.12. For leptons, LID-calibration factors deviate significantly from unity, particularly for fake rates (see Figs. B.2 to B.5), further motivating an investigation of the impact of hadron-identification efficiencies.

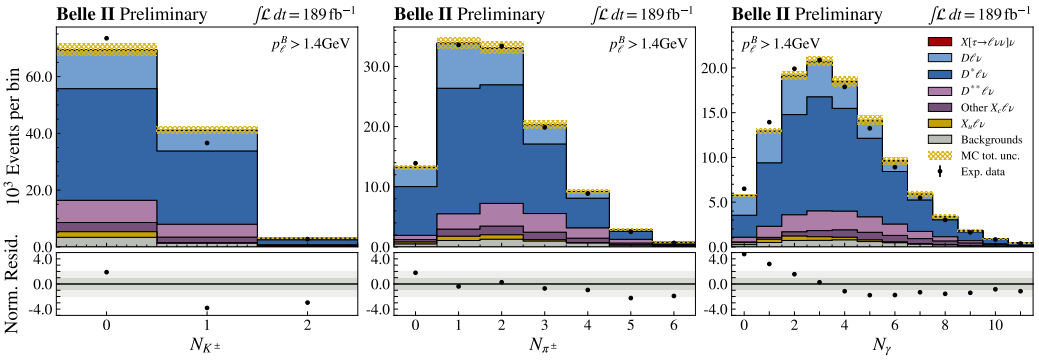

Figure 7.12: Final-state particle multiplicities in the X system are presented in the high-p_ℓ^B control sample.

The Belle II Particle Identification Group provides calibration factors for charged-kaon identification efficiencies and pion-to-kaon fake rates. The calibration factors for kaon efficiencies in $p_K \in [0.5, 1.0]$ GeV range from 0.93 to 0.95, whereas pion-to-kaon fakes in the same momentum range are increased by factors ranging from 1.25 to 1.5. Since the event selection is not particle-specific within the X system, the overall number of events should remain constant, making an efficiency-calibration procedure, as performed for signal-lepton candidates, infeasible.

Instead, averaged calibration factors are applied for each correctly or falsely reconstructed charged kaon. Changes in yields for specific true-and-fake kaon multiplicities are retrieved through a scaling of events with multiplicities corresponding to scenarios in which the kaon was differently identified. In the simplest example, the reduction in yield for events with exactly one correctly identified charged kaon in the X system is accounted for by appropriately increasing the number of events with exactly one true kaon that was not identified as such in the reconstruction.

The observed impact on the M_X, q^2, and M^2_{miss} distributions is extremely small. Additionally, if inaccuracies in hadron-efficiency modeling were relevant, the overestimated number of kaons in simulation, in agreement with efficiency-calibration factors below unity, would need to be accompanied by an underestimation of pion multiplicities. The opposite is true; all particle multiplicities are collectively observed to be higher in simulation than in experimental data. In summary, this suggests that hadron-identification mismodeling can be excluded as a significant source for the observed discrepancies.

This aligns with the findings of Belle's $R(X_{\tau/\ell})$ analysis. In that analysis, detector responses were meticulously examined and the X system was reconstructed with the pion hypotheses assigned to all tracks, making the result independent of particle-identification discrepancies between simulation and experimental data. The impact of all investigated effects were shown to be too small to explain the mismodeling [136].

$B \to D^{**}_{(\text{gap})}\ell\nu$ modeling

Non-resonant D^{**}_{gap} modes, introduced to fill the gap between the sum of exclusive branching fractions and the measured inclusive branching fraction (see Sec. 3.4.3), remain experimentally unexplored. Similarly, $B \to D^{**}\ell\nu$ decays and their subsequent decays exhibit significant uncertainties. However, judging by the relative fraction of such decays, it appears unlikely that the mismodeling can be solely attributed to these decays. This is particularly evident considering their existing large systematic uncertainties, which do not account for the discrepancies observed in experimental data, as illustrated in Figure 7.10.

Furthermore, a substantial deviation of such decays in the $B \to X\ell\nu$ composition would be anticipated to visibly alter the lepton momentum distribution. Yet, as already utilized in the successful extraction of $R(X_{e/\mu})$ in Chapter 6, the lepton-momentum distribution is well modeled. As the remaining $B \to D^{(*)}\ell\nu$ decays are precisely known, the semileptonic $B \to X\ell\nu$ decay itself cannot be the source of the observed mismodeling.

Mismodeling of B_{tag} properties and the center-of-mass energy

As presented in Equations (4.8) and (4.9), both q^2 and M^2_{miss} depend on the three-momentum of the B_{tag} candidate, a quantity observed to be mismodeled due to differences in the c. m. energy between experimental data and simulation (see Secs. 4.1 and A.1). Nevertheless, as depicted in Figure A.1, this only results in a shift of the B_{tag} candidate's three-momentum of approximately 30 MeV. In the laboratory frame, the B_{tag} momentum exhibits only minor deviations between experimental data and simulation within its resolution. Computing q^2 and M^2_{miss} using lab-frame properties (including $E_{B_{\text{tag}}}$ instead of $\sqrt{s}/2$) reveals no discernible changes. Moreover, the mismodeling in M_X remains unaffected by B_{tag} properties. Consequently, the observed mismodeling cannot be attributed to B_{tag} properties and is not induced by discrepancies in c. m. energies between experimental data and simulation.

7.2.3 D-meson decay mismodeling

Building upon the insights presented in Section 7.2.2, the mismodeling can be exclusively attributed to the X system in $B \to X\ell\nu$ decays, explaining the simultaneous observation of discrepancies in M_X, q^2, and M^2_{miss}, while p^B_ℓ and lab-frame $p_{B_{\text{tag}}}$ show good agreement. Moreover, it is highly improbable for the mismodeling to be predominantly caused by detector-response or particle-identification effects. Therefore, mismodeling at the generator level, referring to discrepancies in the underlying physical input of the simulation, emerges as the only plausible explanation.

The fraction of experimentally poorly studied or even unexplored $B \to D^{**}_{(\text{gap})}\ell\nu$ decays is too small to explain of the observed mismodeling. Hence, the modeling of subsequent X_c-meson decays appears as the sole conceivable cause for the observed discrepancy. All $B \to X_c\ell\nu$ decays eventually produce D mesons, featuring a multitude of subsequent D-meson decays. While several D-meson branching fractions, especially those with distinct experimental signatures typically used for reconstruction in exclusive analyses, are well-measured and controlled, a substantial fraction of purely hadronic decays exhibits considerable uncertainties in their exact composition and decay kinematics. Consequently, in Belle II's generic MC simulation, approximately 40% of the D-meson decays are modeled purely based on phase-space assumptions due to a lack of more precise experimental knowledge. A mismodeling

of D-meson decays alters the final multiplicities of decay products, aligning with the simultaneous observation of discrepancies in all final-state particle multiplicities, as evident in Figure 7.12.

$D \to \ldots$	$\mathcal{B}(D^0)$ [%]		$\mathcal{B}(D^+)$ [%]	
+ anything	World average	Simulation	World average	Simulation
K^-	54.7 ± 2.8	56.0	25.7 ± 1.4	**30.5**
K^+	3.4 ± 0.4	3.6	5.9 ± 0.8	6.8
$K^0/\,\overline{K}^0$	47 ± 4	**39.9**	61 ± 5	**57.5**
K^{*-}	15 ± 9	12.6	6 ± 5	4.5
$\overline{K}^{*0}$	9 ± 4	9.1	23 ± 5	19.4
K^{*0}	2.8 ± 1.3		< 6.6	

Table 7.5: The experimental world averages of inclusive D-meson branching fractions into kaons are presented for neutral and charged D mesons (see Ref. [17]). These values are compared to the simulation input.

Aligning the numerous exclusive branching fractions with the inclusive ones presented in Table 7.5 poses a considerable challenge. As a result, the simulations deviate by up to $2\,\sigma$ from the inclusive branching-fraction measurements, overestimating $D \to K^\pm$ decays and underestimating $D \to K^0/\overline{K}^0$ decays. About half of the generated neutral kaons are long-lived K^0_L mesons, that are not reconstructed as discussed in Section 3.2.3. Consequently, events involving $D \to K^0_L$ decays exhibit deficits in reconstructed M_X values of at least $m_{K^0_L} \approx 497\,\text{MeV}$ [17], resulting in substantial missing masses, properties that align well with the excesses observed in experimental data (see Fig. 7.10).

To assess the impact of a potential underestimation of $D \to K^0_L$ decays, the simulation sample is modified using generator-level D-meson decay information. The resulting D-meson decay compositions, presented in Table 7.6, align with the central value of the inclusive world average for $D \to K^0/\overline{K}^0$, or approximately explore its $1\,\sigma$ uncertainty towards higher values.

$D \to \ldots$	Modified simulation ($K^0 \Uparrow\uparrow$)		Modified simulation ($K^\pm \Downarrow\downarrow$)	
+ anything	$\mathcal{B}(D^0)$ [%]	$\mathcal{B}(D^+)$ [%]	$\mathcal{B}(D^0)$ [%]	$\mathcal{B}(D^+)$ [%]
K^-	49.3	22.5	39.2	21.3
K^+	3.6	6.2	2.9	5.9
$K^0/\,\overline{K}^0$	47.9	69.0	53.8	64.8
$K^{*+}/\,K^{*-}$	13.7	5.0	14.3	4.7
$K^{*0}/\,\overline{K}^{*0}$	9.1	17.3	8.9	16.5

Table 7.6: The inclusive D-meson branching fractions are presented for two scenarios based on modified simulation. They are created by either enhancing the relative fraction of $\mathcal{B}(D \to K^0/\overline{K}^0)$ decays (left) or by reducing the relative fraction of $\mathcal{B}(D \to K^\pm)$ decays (right) while adjusting the total yield to its previous value.

In Figure 7.13, the resulting updated distributions of M_X and M^2_{miss} are illustrated and compared to simulated distributions aligned with those from experimental data through a data-driven reweighting technique introduced in the next section. Striking similarities between the modified and reweighted simulation are evident in both M_X and M^2_{miss}, providing strong support for the hypothesis that

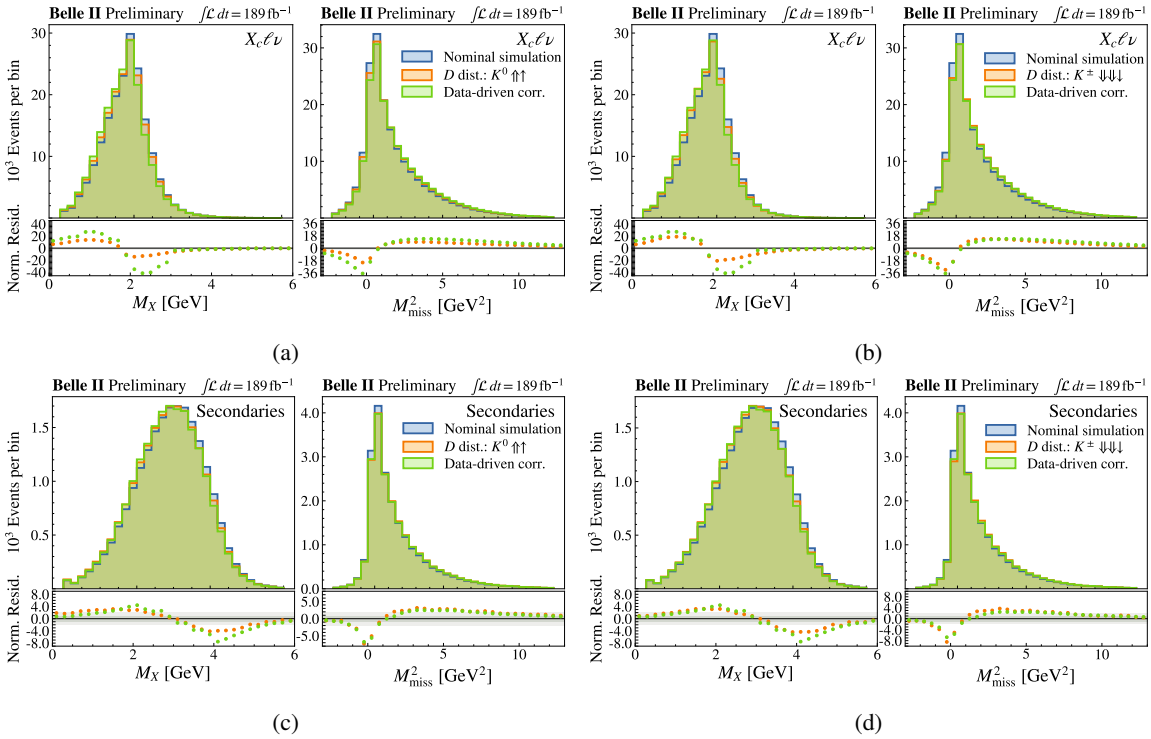

Figure 7.13: The distributions of M_X and M^2_{miss} are compared between the nominal MC simulation (blue), the modified D-meson decay distributions (orange), and distributions aligned with experimental data through a data-driven reweighting technique introduced in Section 7.3 (green). Variations in shape for $B \to X_c\ell\nu$ decays are displayed for enhanced $D \to K^0/\overline{K}^0$ decays (a) or substantially reduced $D \to K^\pm$ decays (b), effectively also resulting in enhanced $D \to K^0/\overline{K}^0$ decays, as presented in Table 7.6. In (c) and (d), the shape differences introduced by the same modifications are illustrated for secondaries, respectively. Uncertainty-normalized residuals compared to the nominal simulation are shown below.

mismodeling in D-meson decays is the primary cause of the observed discrepancies.

This interpretation offers a plausible explanation for the observed event-type dependence, suggesting that the mismodeling is less pronounced in fake and secondary events. In the case of correctly reconstructed $B \to X\ell\nu$ decays, the X system constitutes a clean sample of fully inclusively decaying D mesons with minimal additional particles. However, for $B\overline{B}$ backgrounds, the B_{sig} meson mostly decays hadronically and the signal-lepton candidate often originates from the D-meson decay itself. This introduces additional substantial uncertainties in the modeling of several of these fully hadronic decays and generally results in higher particle multiplicities, thereby diffusing the effect of underestimated $D \to K^0_L$ decays.

Exclusive analyses, which focus on specific D-meson decays that are well-constrained, usually observe smaller discrepancies between simulation and experimental data. Inclusive analyses, however, are sensitive to all D-meson decays, so that the mismodeling becomes apparent as observed in previous Belle analyses [136, 155] and in an early Belle II analysis before introducing kinematic corrections, which effectively assumed $M^2_{\text{miss}} = 0\,\text{GeV}^2$ [222, 223].

In conclusion, compelling evidence is found in support of the hypothesis that the observed

discrepancies in the signal-extraction quantities primarily stem from mismodeling of D-meson decays, with a particular sensitivity to $D \to K_L^0$ decays. In Section 7.3, a reweighting strategy is introduced to correct the mismodeling and to quantify the associated uncertainties.

7.3 Data-driven simulation reweighting

Typically, mismodeling of branching fractions at the generator level is corrected by reweighting the corresponding events in simulation, as discussed in Section 3.4.3. However, addressing the inclusive D-meson decay mismodeling in the current scenario poses two significant challenges that make such reweighting impractical.

Firstly, hundreds of exclusive D-meson decay modes have to be aligned with each other and with the inclusive measurements. Creating a coherent sample of D-meson decays that avoids subtle discrepancies with some measurements is highly challenging as observed in the existing simulation.

Secondly, the branching fraction measurements into neutral and charged kaons are only precise up to 5% – 10%. These uncertainties are propagated to uncertainties of pion and photon multiplicities based on subsequent decays, such as $K^* \to K\pi$, $K_S^0 \to \pi^{\pm,0}\pi^{\mp,0}$, and $\pi^0 \to \gamma\gamma$. As illustrated in Figure 7.13 deviations of this size already introduce significant shape differences in M_X and M^2_{miss}. Therefore, existing inclusive branching-fraction measurements are insufficient to correct the observed discrepancies, necessitating a data-driven correction.

In an ideal scenario, one would identify a manageable set of characteristics within the X-system composition, for instance, by categorizing events based on the presence of a K_L^0 meson, and subsequently conduct a fitting procedure for these distinct components against experimental data within a dedicated control sample. This approach was investigated as part of a Bachelor thesis outlined in Reference [224], yielding promising results. However, such a method is only practical when the mismodeling is reduced to a single source which is perfectly represented within the different fit templates. At the early stage of Belle II's operation, this level of understanding has not yet been sufficiently attained.

For instance, other analyses conducted by Belle II [119, 154] identify a comparable mismodeling in the ECL energy, and propose to attribute this to the mismodeling of fake photons emerging from detector interactions Although this explanation alone cannot fully account for the observed mismodeling in this analysis, it remains a plausible consideration. Additionally, the notion that the overall scaling of $D \to K_L^0$ decays alone adequately addresses the issue seems unlikely. Experimental data suggests a deficit of 30% – 40% in such decays, a value independently derived in this analysis and in Reference [154]. However, such a deficit is in tension with resulting inclusive D-meson decay distributions. It is probable that a significant impact arises from limitations in the kinematic modeling of the 40% of D-meson decays that are solely approximated using phase-space assumptions.

Consequently, an alternative and more cautious approach is adopted. As evident from Figure 7.13, the quantity M_X is very sensitive to the mismodeling and to the X-system properties E_X and $\vec{p}_X$ that serve as input for q^2 and M^2_{miss}. Therefore, $B \to X_c \ell \nu$ and $B \to X_c \tau \nu$ decays are corrected with event weights using the experimental-to-simulated yield ratio in different intervals of M_X in the high-p_ℓ^B sample as described in Section 7.3.2. This corrective process, involving both yield and shape adjustments, is conducted in two successive steps, with the initial step outlined in Section 7.3.1. The validity of the introduced reweighting across the entire lepton-momentum range is examined in Section 7.3.3 and corrections for $B\bar{B}$ backgrounds are derived in Section 7.3.4. In Section B.5 in the appendix, the effect of the reweighting procedure is validated in several control samples.

7.3.1 Yield calibration

The reweighting is introduced to adjust the X-system properties. Since the event selection relies solely on the properties of the signal-lepton candidate, the efficiencies for signal and normalization ($B \to X_c l\nu$) decays are anticipated to be unaffected by D-meson decay mismodeling. Consequently, any deviations in the total yield between experimental data and simulation in $B \to X_c \ell\nu$ are attributed to discrepancies in the B_{tag}-selection efficiency. Notably, the calibration detailed in Section 4.1 relies on an outdated simulation sample.

As depicted in Figure 5.3(a), $B\bar{B}$-background events exhibit a distinct good-to-bad tag composition compared to $Xl\nu$ decays, motivating different calibration factors for the B_{tag}-selection efficiency. Furthermore, the signal-lepton momentum distribution of $B\bar{B}$-background events is influenced by D-meson decay modeling (see Figs. B.9 to B.11). This implies that their efficiencies and, consequently, their total yields may significantly differ in simulation and experimental data. Hence, preliminary global scaling factors are individually determined for backgrounds and $B \to Xl\nu$ decays.

The same-flavor control sample with charged B_{tag} candidates provides an exceptionally clean data sample for secondaries in the electron case (see Fig. 7.11). Hence, this sample is used to derive a global experimental-to-simulated yield ratio for secondaries. As muon secondaries mainly originating from the same D-meson decay modes, the same control sample is used with adjusted lepton-momentum thresholds. Remaining yield ratios in the muon channel are attributed to muon fakes. Subsequently, calibration factors for signal and normalization decays are determined in the high-p_ℓ^B control sample for each lepton flavor.

For neutral B_{tag} candidates, the calibration factors for $B \to Xl\nu$ decays are derived first, based on a very-high-p_ℓ^B control sample $p_\ell^B > 1.6\,\text{GeV}$. These factors are subsequently applied to corresponding events originating from $B^0/\bar{B}^0$ mixing in the same-flavor control sample, before secondary and muon-fake scaling factors are obtained, following the procedure described for charged B_{tag} candidates.

Channel	Initial calibration	$X\ell\nu$, $X\tau\nu$	Secondaries	Fakes
$B^+_{\text{tag}}e^\mp$	0.65	1.013 ± 0.006	1.05 ± 0.01	
$B^0_{\text{tag}}e^\mp$	0.72	0.947 ± 0.009	0.93 ± 0.01	
$B^+_{\text{tag}}\mu^\mp$	0.64	1.027 ± 0.007	1.11 ± 0.02	0.90 ± 0.04
$B^0_{\text{tag}}\mu^\mp$	0.72	0.951 ± 0.009	0.97 ± 0.02	0.79 ± 0.04

Table 7.7: Correction factors to the initial B_{tag} calibration as introduced in Table 4.1 are presented for signal, normalization, and $B\bar{B}$-background events.

All calibration factors are summarized in Table 7.7. Based on the observation that signal and background events share the same B_{tag} properties (see Secs. 5.4.1), the same factor is applied for signal and normalization decays, resulting in a cancellation in $R(X_{\tau/\ell})$. The deviation of calibration factors from unity for $B\bar{B}$-background yields is attributed to the presumably dominant role of D-meson decay mismodeling, causing lepton-momentum-based efficiency discrepancies between simulation and experimental data.

In the signal-extraction fit presented in Chapter 8, the signal, normalization, and $B\bar{B}$-background yields are freely floating parameters, dynamically readjusting the calibration factors introduced earlier.

The relative fraction of events with charged and neutral B_{tag} candidates, however, is not determined in the fit. Therefore, the statistical precision of the calibration factors from Table 7.7 serves as an additional uncertainty associated with the B^+_{tag}-B^0_{tag} composition. Moreover, the relative proportion of secondary to fake events in the muon channel introduces another source of uncertainty. Following the extraction of correction factors, these factors are treated as fully anticorrelated, leading to the maximal $B\bar{B}$-background shape uncertainty in the muon channel. The integration of calibration factors and their associated uncertainties into the signal-extraction fit aligns with the methodology used for branching-fraction uncertainties (see Sec. 5.3.2) for uncorrelated factors and form-factor uncertainties for the anticorrelated ones (see Sec. 5.3.3).

7.3.2 Reweighting of signal and normalization decays

To obtain M_X-based correction weights for $B \to X_c \ell \nu$ decays, the high-p_ℓ^B control sample is used. The M_X distribution is split into 17 intervals with approximately equal experimental-data content. The boundaries of these intervals are

$$\begin{aligned} M_X = \{&-\infty, 0.5, 0.75, 0.95, 1.15, 1.3, 1.45, 1.55, 1.65, \\ &1.75, 1.85, 1.95, 2.05, 2.20, 2.35, 2.60, 3.0, \infty\}\ \text{GeV}. \end{aligned} \tag{7.2}$$

Within each M_X interval m, non-reweightable event types are subtracted from the experimental data. Subsequently, the correction weight for $B \to X_c \ell \nu$ decays, denoted as $\tilde{w}_m^{M_X}$, is determined from the remaining experimental-to-simulated yield ratio. This weight is then applied as an event weight $\tilde{w}_{\text{evt}}^{M_X} = \tilde{w}_m^{M_X}$ if evt $\in m$. The uncertainties of the correction weights, denoted as $\tilde{\sigma}_m^{M_X}$, are defined by the statistical precision of experimental data and simulation in each interval.

As illustrated in Figure 7.14, events with charged and neutral B_{sig} mesons (inferred from the reconstructed B_{tag}-candidate flavor) exhibit distinct sensitivities to D^+- and D^0-meson decays. Consequently, the reweighting procedure is separated by B_{tag}-candidate charge to account for potential dependencies of the mismodeling on the D-meson flavor.

The correction weights obtained from the charged-B_{tag} channel are applied to all $B^\mp_{\text{sig}} \to X_c \ell \nu$ decays. Since neutral D mesons predominantly contribute to this channel, these weights are also applied to events with a neutral B_{sig} candidate featuring a neutral D meson, $\bar{B}^0_{\text{sig}} \to [X_c \to D^0 \ldots] \ell \nu$. The remaining deviations from unity in the experimental-to-simulated yield ratios in the neutral-B_{tag} channel are assigned to mismodeled $\bar{B}^0_{\text{sig}} \to [X_c \to D^+ \ldots] \ell \nu$ decays, and corresponding correction weights are applied.

In Figure 7.15, the correction weights are illustrated. The largest weights are observed at low M_X, a region enriched with $D \to K^0_L$ decays, while events with high M_X values are corrected with weights below unity. As demonstrated in Section B.6 in the appendix, $B \to X_c \tau \nu$ decays are equally influenced by D-meson decay mismodeling as $B \to X_c \ell \nu$ decays; hence, the former are reweighted using the same correction weights.

Subsequently, the yields of all measured exclusive semileptonic B-meson decays are adjusted to their original values in four lepton-momentum intervals (see Sec. 7.3.3) to preserve the branching fractions

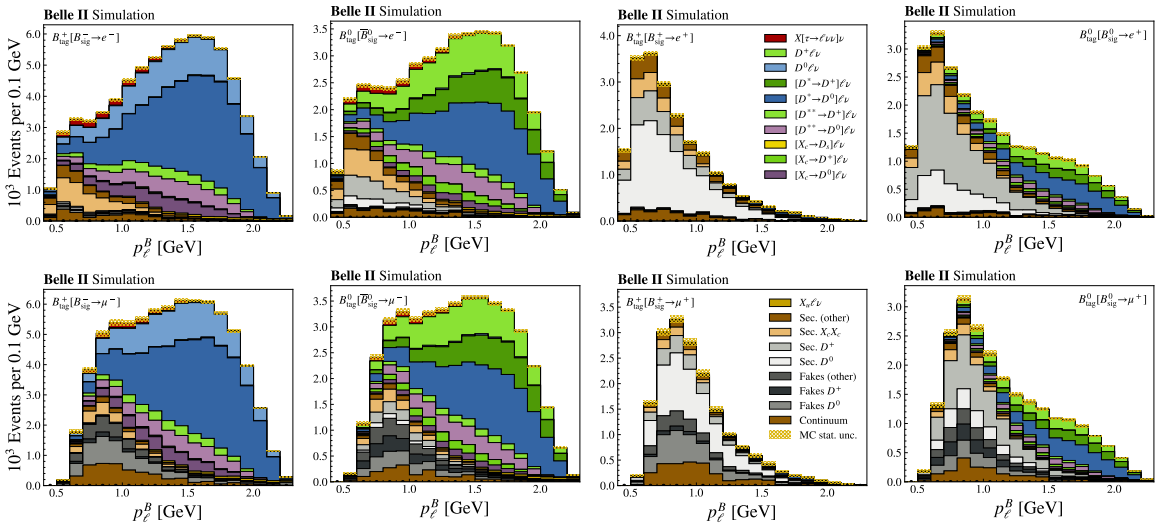

(a) $B^+_{\text{tag}}[B^-_{\text{sig}} \to \ell^-]$ (b) $B^0_{\text{tag}}[\overline{B}^0_{\text{sig}} \to \ell^-]$ (c) $B^+_{\text{tag}}[B^+_{\text{sig}} \to \ell^+]$ (d) $B^0_{\text{tag}}[B^0_{\text{sig}} \to \ell^+]$

Figure 7.14: The p_ℓ^B distribution is illustrated for events featuring charged and neutral B_{tag} candidates in the opposite-flavor signal sample (a) and (b), as well as in the same-flavor control sample (c) and (d), respectively, for signal-electron candidates (top row) and signal-muon candidates (bottom row). The categories introduced in Section 4.5 are further divided into sub-categories based on the presence of charged or neutral D mesons. In the case of a charged B_{tag} candidate, charged D mesons only appear in $B^-_{\text{sig}} \to [D^{**0} \to D^+ \ldots]\ell^-\nu$ decays as neutral D^* mesons exclusively decay into neutral D mesons. In contrast, in approximately half of the $\overline{B}^0_{\text{sig}} \to X\ell^-\nu$ decays, a neutral (blue, purple) or a charged (green) D meson is generated in a subsequent stage of the decay chain. The $B\overline{B}$-background composition is discussed in more detail in Section 7.3.4.

(see Tab. 3.1) and B-meson decay kinematics derived from form-factor models (see Sec. 3.4.3).

$$w_{\text{evt}}^{M_X} = \tilde{w}_{\text{evt}}^{M_X} \cdot \frac{N_k^{\text{sel}}}{\tilde{N}_k^{\text{sel}}} \text{ with } N_k^{\text{sel}} = \sum_{\text{evt}\in k} w_{\text{evt}}, \quad \tilde{N}_k^{\text{sel}} = \sum_{\text{evt}\in k} \left(w_{\text{evt}} \cdot \tilde{w}_{\text{evt}}^{M_X} \right) \quad \left(k = [X_c l\nu \in p_\ell^B \text{ interval}] \right) \tag{7.3}$$

Since $D^{**}_{\text{gap}}\ell\nu$ decays lack experimental observation, they are not subject to rescaling, $w_{\text{evt}}^{M_X} = \tilde{w}_{\text{evt}}^{M_X}$, leading to a reduction of their yield by approximately 10%. The $D^{**}_{\text{gap}}\tau\nu$ yields are appropriately adjusted to restore the $R(X_{\tau/\ell})$ theory prediction (see Eq. (2.31)).

In Figure 7.16, the reweighted distributions in the high-p_ℓ^B control sample are presented. Additional figures, dependent on the B_{tag} charge, are shown in the appendix (see Fig. B.17). A significant improvement of the modeling of the kinematic variables correlated with the X system is observed when compared to Figure 7.10. Such a simultaneous amelioration is highly nontrivial.[2] Therefore, the observations strongly suggest that the reweighting appropriately addresses the mismodeling. The reweighting has negligible effect on the p_ℓ^B shape for $B \to X_c\ell\nu$ decays as the lepton momentum is largely independent of the hadronic X system.

[2] For example, employing event-based adjustments with a constant factor for the four-momentum of the X-system can align the simulated q^2 spectrum with the experimental data. Such an approach, however, is too simplistic to simultaneously correct the M^2_{miss} distribution.

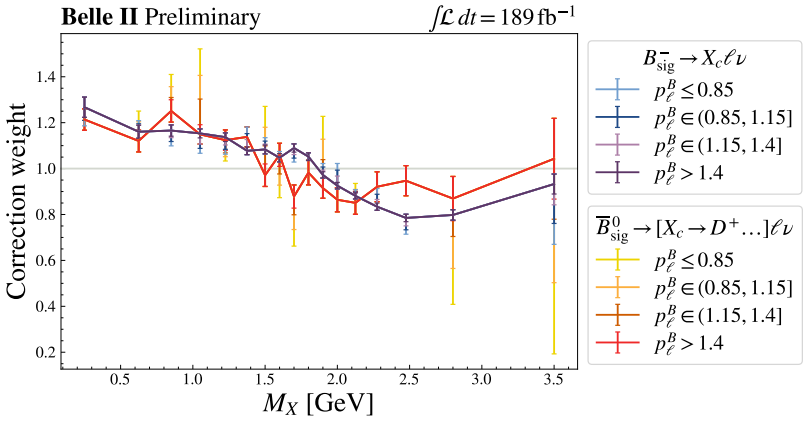

Figure 7.15: The correction weights $\tilde{w}_m^{M_X}$, obtained from experimental-to-simulated yield ratios in M_X intervals m in the high-p_ℓ^B control sample featuring charged and neutral B_{tag} candidates, are illustrated. These weights are applied to $B \to X_c \ell \nu$ and $B \to X_c \tau \nu$ decays. As discussed in Section 7.3.3, additional uncertainties are introduced for signal and normalization decays with low-momentum signal lepton.

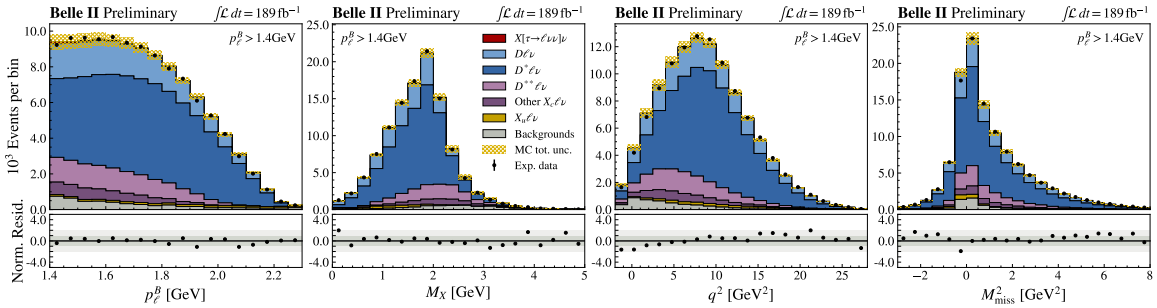

Figure 7.16: The signal-extraction quantities p_ℓ^B and M^2_{miss}, as well as the correlated M_X and q^2 variables are displayed in the high-p_ℓ^B control sample and combined electron and muon channels after simulation reweighting. Below each plot, uncertainty-normalized residuals are presented, demonstrating a significant reduction compared to the pre-reweighting distributions shown in Figure 7.10.

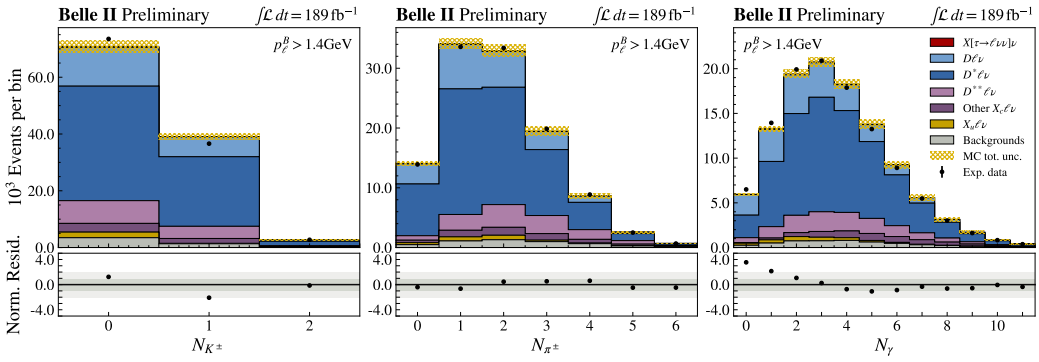

Figure 7.17: Final-state particle multiplicities in the X system are presented in the high-p_ℓ^B control sample after simulation reweighting. Uncertainty-normalized residuals are presented below each plot, revealing a substantial reduction compared to the pre-reweighting distributions in Figure 7.12.

In Figure 7.17, the final-state particle multiplicities, which are not actively adjusted in the reweighting procedure, are presented after the reweighting.[3] Again, the previously observed mismodeling in Figure 7.12 is significantly mitigated, particularly for charged kaons, which have the most substantial impact on M_X. Small discrepancies still persist in the photon-cluster multiplicity. These are likely caused by low-energy cluster split-offs from particle-detector interactions, that have too little impact on M_X to be addressed by the reweighting. For the same reason, however, their effect on the signal-extraction quantity M^2_{miss} is tiny.

7.3.3 Extrapolation towards the low lepton-momentum region

No correlation between the lepton momentum and the D-meson decay distribution is observed for $B \to X_c \ell \nu$ decays, as demonstrated in studies with modified inclusive branching fractions of D mesons in Figures B.9, B.10, and B.11. Nevertheless, low-lepton momenta are loosely associated with a larger boost of the X-system, leading to slightly higher average values of M_X due to misreconstruction effects, as observed in Figure 7.18. In this section, the representativeness of the correction weights derived in the previous Section 7.3.2 is assessed across the entire $B \to X_c \ell \nu$ lepton-momentum spectrum.

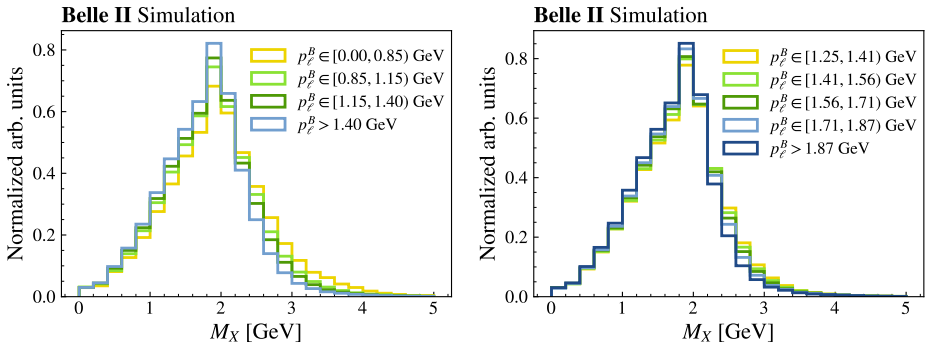

Figure 7.18: The M_X distribution for $B \to X_c \ell \nu$ decays is illustrated in various intervals of p_ℓ^B. The left plot represents the entire momentum range, while the right plot focuses on the intervals defined for the extrapolation discussed in this section.

To address the low-lepton momentum region without box-opening, an extrapolation is performed from an extended high-p_ℓ^B control sample with $p_\ell^B > 1.25\,\text{GeV}$. Five p_ℓ^B intervals are defined with boundaries at $p_\ell^B = \{1.25, 1.41, 1.56, 1.71, 1.87, \infty\}$ GeV, each containing approximately equal amounts of experimental data. As depicted in Figure 7.18, the characteristic correlation towards higher M_X values is evident in these intervals. Subsequently, M_X-based correction weights are extracted for each of the five p_ℓ^B intervals, following the procedure described in Section 7.3.2.[4]

The weights obtained for $B_{\text{sig}} \to X_c \ell \nu$ and $\bar{B}^0_{\text{sig}} \to [X_c \to D^0 \ldots] \ell \nu$ decays, as well as for $\bar{B}^0_{\text{sig}} \to [X_c \to D^+ \ldots] \ell \nu$ decays are presented in Figure 7.19, providing no direct evidence of a p_ℓ^B-dependence.

[3] The reweighting can also be defined based on particle multiplicities. This was successfully tested, yielding similar improvements with sufficient granularity in the three-dimensional (N_K, N_π, N_γ) hyperspace. However, the M_X-based reweighting performs well with 17 intervals only, resulting in superior statistical precision for the correction weights.

[4] $B\bar{B}$-background contributions, especially important in the lowest p_ℓ^B interval, are reweighted first as discussed in the following Section 7.3.4.

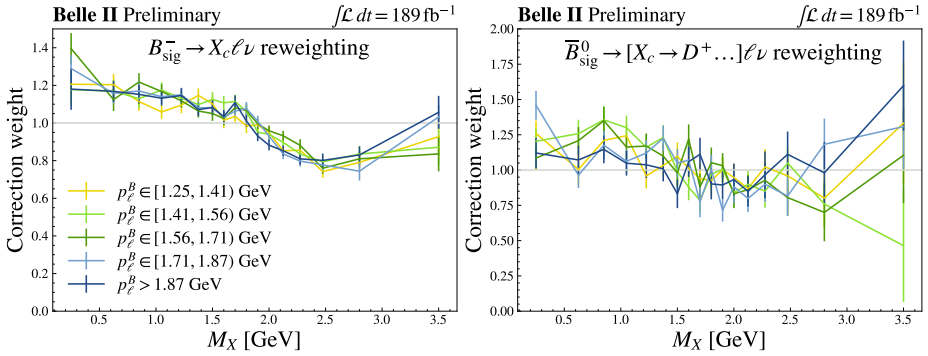

Figure 7.19: The M_X-based correction weights $\tilde{w}_m^{M_X}$ in different p_ℓ^B intervals are depicted for $B^-_{\text{sig}} \to X_c \ell \nu$ and $\overline{B}^0_{\text{sig}} \to [X_c \to D^0 \ldots] \ell \nu$ decays (left) and $\overline{B}^0_{\text{sig}} \to [X_c \to D^+ \ldots] \ell \nu$ events (right).

Consistency of the five individual correction weights with their average is examined in each M_X interval through χ^2 tests. In Figure B.24 and B.25 in the appendix, all χ^2 values and their corresponding p values are presented. Only in one out of the 34 intervals of M_X, a p value below 0.05 is observed (highlighted in light green in Figure B.25), which aligns with the statistically expected abundance of such cases. This supports the assumption that the correction weights are independent of p_ℓ^B, making the weights derived in Section 7.3.2 representative for the entire lepton-momentum range of $B \to X_c \ell \nu$ and $B \to X_c \tau \nu$ decays.

Nonetheless, the possibility of a drift of correction weights with p_ℓ^B values is included as an additional source of systematic uncertainty. For this purpose, a straight line is fitted to the five correction weights in each M_X bin, as illustrated in Figure 7.20 for one example interval (see Figs. B.24 and B.25 for the remaining intervals). Here the p_ℓ^B values of the five weights, serving as x-axis coordinates, are defined by the averaged value in each of the introduced p_ℓ^B intervals.

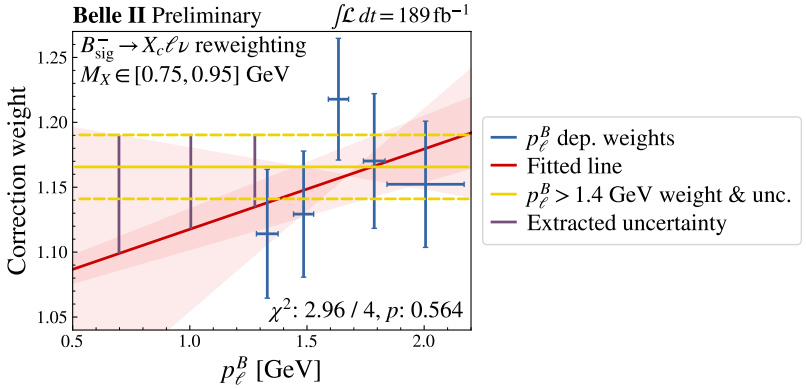

Figure 7.20: The correction weights for $B^-_{\text{sig}} \to X_c \ell \nu$ events in different p_ℓ^B intervals for $M_X \in [0.75, 0.95]$ GeV are shown (blue crosses). The result of the χ^2 test, conducted to assess the hypothesis that these weights align with the nominal one derived in the full high-p_ℓ^B control sample (yellow), is presented. A straight line is fitted to the data points and extrapolated towards lower p_ℓ^B values (red). Additional uncertainties for low-momentum $B_{\text{sig}} \to X_c \ell \nu$ and $B_{\text{sig}} \to X_c \tau \nu$ decays (purple) are introduced in cases when the fitted line exceeds the statistical uncertainty of the nominal weight (dashed yellow lines).

The line is extrapolated to lower p_ℓ^B values, and average p_ℓ^B values are defined for intervals of $p_\ell^B < 0.85\,\text{GeV}$, $p_\ell^B \in [0.85, 1.15]\,\text{GeV}$, and $p_\ell^B \in [1.15, 1.4]\,\text{GeV}$, each containing approximately equal amounts of experimental data. In cases where the central value of the fit (red line) exceeds the statistical uncertainties of the correction weight extracted in the entire high-p_ℓ^B control sample (dashed yellow lines), the entire deviation from the correction weight is taken as additional uncertainty (purple lines). The volatile nature of the sign of the fitted slope provides no evidence for an underlying systematic behavior, supporting the assumption of a p_ℓ^B-independence of the correction weights. Consequently, the inclusion of additional systematic uncertainties is very conservative. The final p_ℓ^B-dependent correction-weight uncertainties are illustrated in Figure 7.15, and all correction weights and uncertainties are summarized in Table B.3 in the appendix.

In Figure 7.21, the impact of simulation reweighting on $B \to X_c \ell \nu$ decays with low momentum is illustrated, requiring $p_\ell^B < 1.3\,\text{GeV}$, $M_{\text{miss}}^2 < 1.5\,\text{GeV}^2$, and $M_X < 3.5\,\text{GeV}$. No evidence of caveats associated with the introduced reweighting is observed.

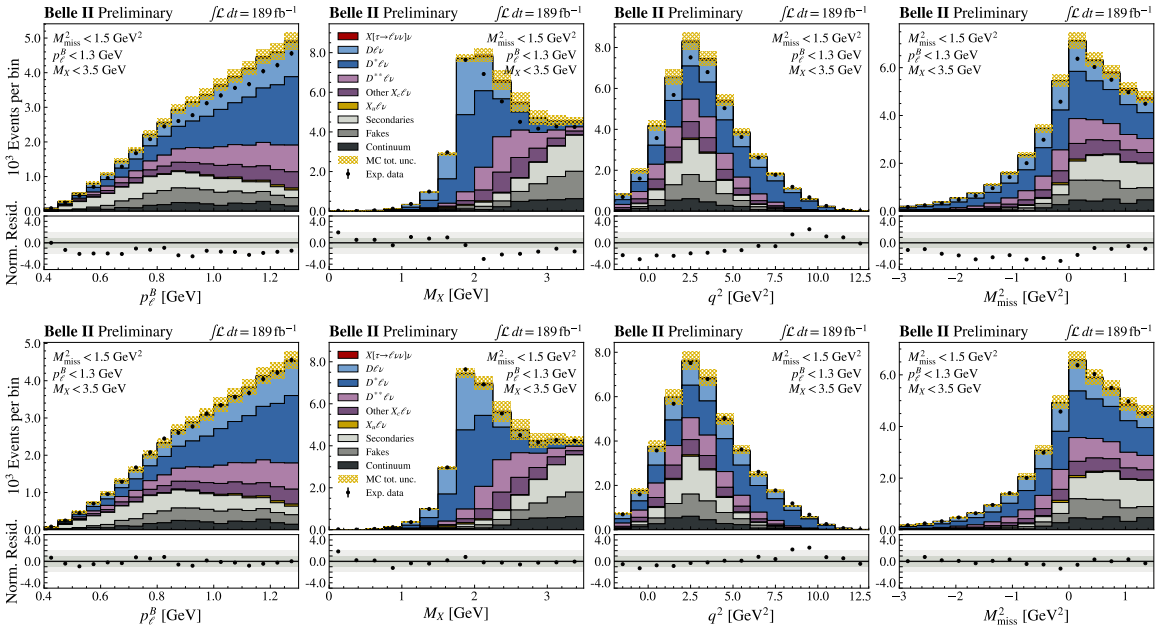

Figure 7.21: The signal-extraction quantities and correlated variables are presented in the low-M_{miss}^2 control sample, both before (top row) and after (bottom row) the simulation reweighting. To specifically assess the modeling of low-momentum $B \to X_c \ell \nu$ decays, additional constraints of $p_\ell^B < 1.3\,\text{GeV}$ and $M_X < 3.5\,\text{GeV}$ are imposed. The uncertainty-normalized residuals, shown below each plot, significantly improve.

The uncertainties of the weights from the same M_X interval are fully correlated across all momentum ranges for both $B \to X_c \ell \nu$ and $B \to X_c \tau \nu$. Due to their statistical nature, weight uncertainties across different M_X intervals are considered uncorrelated, resulting in maximum shape uncertainties for the corrected templates. Nevertheless, as outlined in the previous Sections 7.3.1 and 7.3.2, the total yield of the different $B \to X_c \ell \nu$ and $B \to X_c \tau \nu$ decays is assumed to remain unaffected by D-meson decay mismodeling. To fulfill these requirements, the implementation of uncertainties in the final maximum-likelihood fit (see Sec. 5.2) is carried out in multiple steps.

Similar to the handling of lepton-identification uncertainties outlined in Section 5.3.5, a set of $N_{\text{var}} = 500$ variations, generated through a Gaussian distribution $\vec{\mathcal{G}}$, is assigned to the yield-normalized weight $w_m^{M_X}$ for each M_X interval m:

$$\vec{\hat{w}}_m^{\mathcal{G}} = w_m^{M_X} + \vec{\mathcal{G}}\left(0, \sigma_m^{M_X}\right) \quad \left(m = 1, \ldots, N_{\text{intervals}}^{M_X}\right). \tag{7.4}$$

For asymmetric uncertainties, two distinct Gaussian distributions are generated to represent the upper and lower uncertainties. These distributions are split based on their sign and combined in a manner that ensures their average is zero. Subsequently, the total yield of each exclusive $B \to X_c l\nu$ decay in each p_ℓ^B interval ($k = [X_c l\nu$ in p_ℓ^B interval]) is adjusted to its nominal yield for all variations $j \in \mathcal{G} = 0, \ldots, N_{\text{var}}$:

$$w_{\text{evt}}^{\mathcal{G}_j} = \hat{w}_{\text{evt}}^{\mathcal{G}_j} \cdot \frac{N_k^{\text{sel}}}{\hat{N}_{k,j}^{\text{sel}}} \quad \text{with} \quad N_k^{\text{sel}} = \sum_{\text{evt}\in k}\left(w_{\text{evt}} \cdot w_{\text{evt}}^{M_X}\right), \quad \hat{N}_{k,j}^{\text{sel}} = \sum_{\text{evt}\in k}\left(w_{\text{evt}} \cdot \hat{w}_{\text{evt}}^{\mathcal{G}_j}\right) \tag{7.5}$$

This effectively introduces a subtle anticorrelation among different M_X intervals, stemming from bin migrations. Finally, a set of 500 varied template histograms is generated using the set of weights for each histogram bin i by

$$\vec{h}_i^{\mathcal{G}} = \sum_{\text{evt}\in i}\left(w_{\text{evt}} \cdot \vec{w}_{\text{evt}}^{\mathcal{G}}\right) \quad (i \in \text{bins, templates}), \tag{7.6}$$

and the covariance matrix $C_\theta^{M_X}$ is constructed as described in Equation 5.23:

$$\left(C_\theta^{M_X}\right)_{ij} = \frac{1}{N_{\text{var}} - 1}\sum_{n=1}^{N_{\text{var}}}(h_{in}^{\mathcal{G}} - h_i)(h_{jn}^{\mathcal{G}} - h_j) \quad (i, j \in \text{bins, templates}). \tag{7.7}$$

By design, the reweighting procedure keeps N^{sel} unchanged, ensuring that no efficiency uncertainty is introduced. In Figure 7.22, the 500 varied histograms are shown for M_{miss}^2 to illustrate the introduced shape uncertainty. While asymmetric uncertainties are evident for $\bar{B}_{\text{sig}}^0 \to [X_c \to D^+ \ldots]\ell\nu$ decays in the low-momentum range, the overall shape is predominantly influenced by the substantially higher number of high-p_ℓ^B events with symmetric uncertainties.

7.3.4 Reweighting of $B\bar{B}$-background events

Mismodeled D-meson decays also impact events featuring secondary or fake-lepton candidates. In the context of $B\bar{B}$ backgrounds, the lepton candidate is often associated with the D-meson decay itself, establishing a correlation between lepton momentum and the inclusive D-meson branching fractions, as illustrated in Figures B.9 to B.11. Furthermore, the correlation between p_ℓ and M_X is substantially increased. To address this, the correction weights for $B\bar{B}$ backgrounds are derived in 16 (e) and 11 (μ) two-dimensional intervals of the lab-frame lepton momentum p_ℓ and M_X, as visualized in Figure 7.23. These intervals are designed to approximately contain equal amounts of experimental data, and the background-enriched same-flavor control sample (see Sec. 7.2.1) is utilized for the reweighting.

As visualized in Figures B.21 and B.22, $B\bar{B}$ backgrounds are almost exclusively composed of secondaries in the electron channel, while the muon channel incorporates additional significant

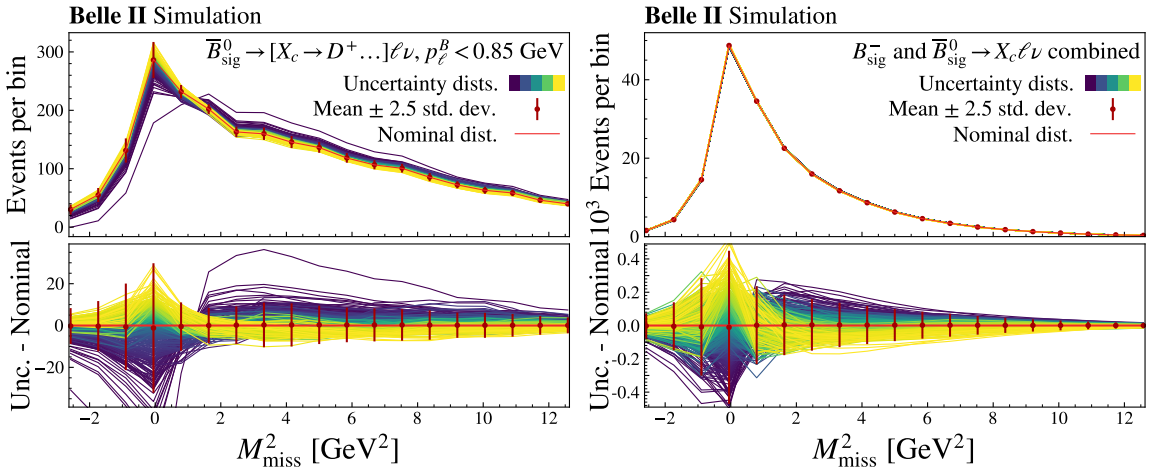

Figure 7.22: The 500 varied histograms, employed to assess the shape uncertainties resulting from the simulation reweighting, are visualized using a blue-to-yellow color map for the M^2_{miss} distribution, with nominal distributions shown in red. In the lower plots, the difference of the nominal distribution from each histogram is highlighted. The left plots exclusively display $\overline{B}^0_{\text{sig}} \to [X_c \to D^+ \ldots]\ell\nu$ decays in the low-momentum range, that feature the most significant asymmetries in their uncertainties. On the right, the distributions are presented for the entire $B_{\text{sig}} \to X_c\ell\nu$ decays.

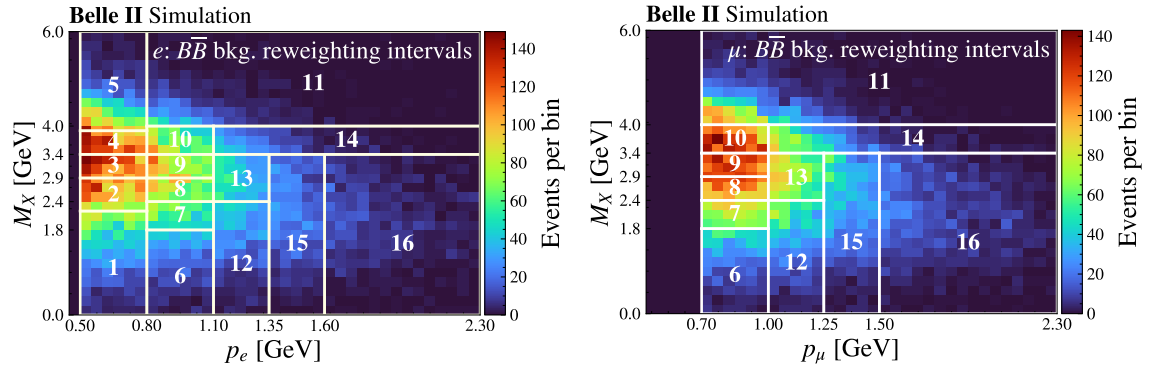

(a) (b)

Figure 7.23: The two-dimensional intervals in p_ℓ and M_X are depicted for the electron (a) and muon channel (b), utilized for extracting $B\overline{B}$-background correction weights. The first five intervals are exclusive to the electron channel due to the lepton-flavor specific p_ℓ thresholds introduced in Section 7.1.4. The abundance of $B\overline{B}$ backgrounds in the same-flavor control sample for each lepton flavor is presented as a heat map.

fake-lepton components. Given the strict suppression of lepton-flavor exclusive *tertiaries* introduced in Section 7.1, the remaining electron and muon secondaries predominantly originate from the same D-meson decay modes. Consequently, correction weights derived from electron secondaries are also applied to muon secondaries. In this context, the p_μ-interval edges are reduced by 100 MeV compared to p_e (see Fig. 7.23), accounting for the lepton-mass difference. The interval definitions reflect the distinct p_ℓ thresholds for electron and muon candidates.

In analogy to the methodology outlined in Section 7.3.2, correction weights are obtained from

experimental-to-simulated yield ratios within each $p_\ell - M_X$ interval. Initially, correction weights for secondaries are extracted in the electron channel and then applied to muon secondaries. The remaining yield ratios in the muon channel are attributed to muon-fake mismodeling, and corresponding correction weights are extracted. The correction weights are visualized in Figure 7.24, and their numerical values are summarized in Table B.4. To assess potential impacts of $B \to X_c \ell \nu$ decays from $B^0/\bar{B}^0$ mixing, correction weights are also obtained in control samples split by B_{tag}-candidate charge. However, no significant deviations in correction weights are observed, so that the statistically more precise control sample with both B_{tag} charges is used.

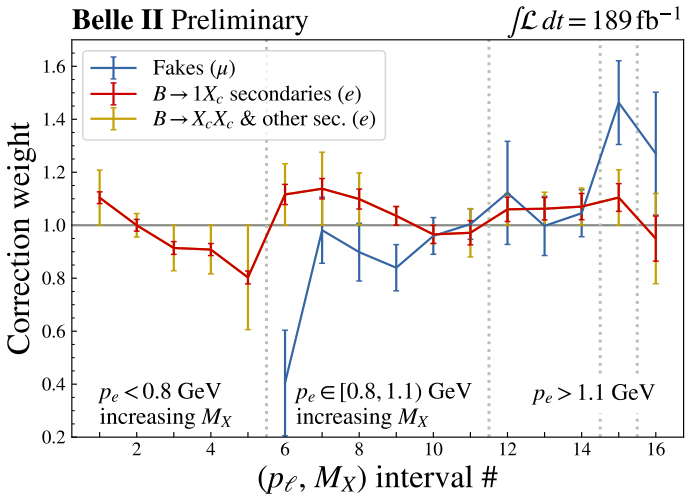

Figure 7.24: The correction weights $\tilde{w}_m^{M_X}$ for $B\bar{B}$-background events, derived from experimental-to-simulated yield ratios in intervals m of p_ℓ and M_X (see Fig. 7.23) in the same-flavor control sample, are illustrated.

As observed for $B \to X_c \ell \nu$ decays (see Fig 7.15), the highest correction weights for secondaries are observed for low-M_X intervals.

As evident in Figure 7.14, secondaries originating from B_{sig} decays into a single X_c meson (light gray components) are significantly more abundant in the same-flavor control sample than in the opposite-flavor signal sample. Analogously, secondary leptons emerging from B_{sig} decays into two charmed mesons (orange), as well as remaining tertiary events (see Sec. 7.1, brown in Fig. 7.14), are not equally well represented in the same-flavor sample. To address this, secondary leptons not arising from D-mesons from B_{sig}-to-single-charm decays are assigned shape and yield uncertainties that cover the initially simulated shape up to twice the correction derived from the same-flavor secondaries (illustrated in gold in Figure 7.24). In Section 8.2.2, it is demonstrated that the resulting uncertainties cover effects of significantly altered relative fractions of $B \to X_c X_c$ events on $R(X_{\tau/\ell})$.

The impact of the $B\bar{B}$-background reweighting is verified in multiple control samples in Section B.5, resulting in significant improvements observed across all phase-space regions (see Figs. B.18 to B.22).

CHAPTER 8

Measurement of the tau-to-light-lepton ratio $R(X_{\tau/\ell})$

In this chapter, the first successful measurement of inclusive $B \to X\tau\nu$ decays, measured in a ratio relative to $B \to X\ell\nu$ decays, $R(X_{\tau/\ell}) = \mathcal{B}(B \to X\tau\nu)/\mathcal{B}(B \to X\ell\nu)$, is presented. This measurement is enabled by two key advancements. Firstly, a comprehensive understanding of the primary sources of data-to-simulation discrepancies, as discussed in Section 7.2, is achieved. Secondly, a robust data-driven correction method is developed, detailed in Section 7.3. As of the current writing, the results are published in Reference [2] and have been submitted to Physical Review Letters.

In Section 8.1, a comprehensive overview of the signal-extraction strategy for $R(X_{\tau/\ell})$ is provided. Additionally, various sources of uncertainty affecting this measurement are quantified and validated. Subsequently, the measured value is presented, validated, and discussed in Section 8.2.

8.1 $R(X_{\tau/\ell})$-extraction strategy and quantification of uncertainties

In Section 8.1.1, the signal-extraction procedure is outlined. Uncertainties are quantified and discussed in Section 8.1.2. Effects of the introduced reweighting procedure (see Sec. 7.3) on $R(X_{\tau/\ell})$ are investigated in Section 8.1.3 for various D-meson decay distribution. Subsequently, in Section 8.1.4, the independence of the result concerning the signal-lepton momentum threshold is confirmed.

In a first box-opening attempt, a significant dependence of the result on the lepton-momentum threshold was observed, necessitating updates in the event selection and uncertainty estimation. This dependence is primarily identified to be caused by a selection criterion applied at an early stage of the data processing, as detailed in Section 8.1.5.

8.1.1 Fit setup

The signal decay, $B \to X[\tau \to \ell\nu\nu]\nu$, is extracted in a two-dimensional maximum-likelihood fit using the observables p_ℓ^B and M^2_{miss}. As illustrated in Figure 8.1, signal decays feature substantial M^2_{miss} values attributed to three neutrinos in the final state, while normalization and background events exhibit a peak around $M^2_{\text{miss}} \approx 0\,\text{GeV}^2$. The separation of normalization and background events is based on the lepton momentum in the B_{sig} frame, p_ℓ^B. As presented in Section 5.2, four templates are fitted per lepton flavor, with the continuum yield constrained by off-resonance data. Both lepton

flavors are simultaneously fitted to leverage their combined constraining power on correlated nuisance parameters.

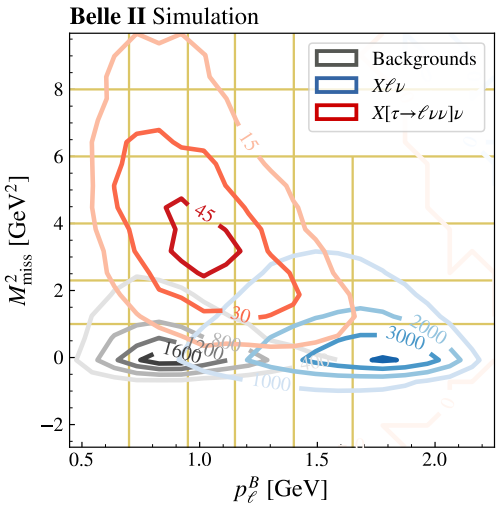

Figure 8.1: The two-dimensional distributions of p^B_ℓ vs. M^2_{miss} for signal, normalization, and background events are illustrated. The p^B_ℓ-M^2_{miss} intervals employed in the signal-extraction fit are highlighted in gold.

The p^B_ℓ-M^2_{miss} intervals are defined to prevent the occurrence of empty intervals or intervals exclusively populated by a single template. The interval edges are defined as

$$p^B_e = \{0.00, 0.70, 0.95, 1.15, 1.40, 1.65, \infty\}\,\text{GeV}, \tag{8.1}$$

$$p^B_\mu = \{0.00, 0.80, 1.00, 1.20, 1.40, 1.65, \infty\}\,\text{GeV, and} \tag{8.2}$$

$$M^2_{\text{miss}} = \{-\infty, 1.0, 2.3, 4.0, 6.0, 8.0, \infty\}\,\text{GeV}^2, \tag{8.3}$$

as visualized in Figure 8.1 for the electron-channel intervals. The first M^2_{miss} interval covers the entire region around $M^2_{\text{miss}} \approx 0\,\text{GeV}^2$ to ensure the fit's insensitivity to hypothetically remaining detector-resolution mismodeling in this region. The last two p^B_ℓ intervals are combined in the highest M^2_{miss} interval, resulting in a total of 34 $p^B_\ell - M^2_{\text{miss}}$ intervals per lepton flavor. In the fit, the two-dimensional histograms are unfolded into one dimension, as demonstrated in Figures 8.8 (pre-fit) and 8.9 (post-fit).

In Section A.4 in the appendix, the fit setup is demonstrated to correctly extract various different values of $R(X_{\tau/\ell})$ within predicted statistical uncertainties in a linearity and a pull test.

8.1.2 Estimation of uncertainties

The impact of various uncertainty sources on both $R(X_{\tau/\ell})$ and the different fit templates is evaluated through fits on Asimov data, as outlined in Section 6.1.2. The resulting uncertainties are documented in Tables 8.1 and 8.2 for the electron and muon channels, respectively. The magnitude of each uncertainty is validated using ensembles of artificially varied data sets (see Sec. A.4 for one example), following a similar approach as in the $R(X_{e/\mu})$ measurement in Section A.3.

Uncertainty source	**Electron channel: Relative uncertainty [%]** Continuum	$B\bar{B}$ bkg.	$Xe\nu$	$X\tau\nu$	$R(X_{\tau/e})$
Total	5.6	4.0	0.8	17.9	18.4
Exp. sample size	5.5	1.9	0.4	8.9	9.0
Sim. sample size	0.6	1.2	0.2	6.6	6.7
Lepton identification	0.4	1.5	0.2	2.7	2.8
Track-reco. eff.	0.1	0.4	0.0	2.9	2.9
$B\bar{B}$-bkg. composition	0.0	0.1	0.0	0.3	0.3
$B\bar{B}$ bkg.: (p_ℓ, M_X) shape	0.2	1.1	0.1	5.8	5.8
$Xl\nu$: B^0_{tag}-B^+_{tag} composition	0.0	0.1	0.0	0.4	0.4
$X_c l\nu$: M_X shape	0.1	0.9	0.0	7.3	7.3
$\mathcal{B}(X\tau\nu)$ total	0.0	0.1	0.0	0.6	1.0
$\mathcal{B}(X\ell\nu)$ total	0.3	1.0	0.3	6.7	7.0
$\mathcal{B}(X_u\ell\nu)$	0.0	0.0	0.0	1.3	1.4
$\mathcal{B}(D\ell\nu)$	0.0	0.0	0.0	1.6	1.7
$\mathcal{B}(D^*\ell\nu)$	0.1	0.4	0.1	1.9	2.1
$\mathcal{B}(D^{**}\ell\nu)$	0.2	0.7	0.2	2.9	3.1
$\mathcal{B}(D^{(*)}\pi\pi\ell\nu)$	0.2	0.6	0.2	2.4	2.5
$\mathcal{B}(D^{(*)}\eta\ell\nu)$	0.3	0.9	0.3	6.4	6.7
$\mathcal{B}(D_s^{(*)}K\ell\nu)$	0.0	0.4	0.1	0.2	0.2
$\mathcal{B}(X_c\ell\nu)$ correlation	-0.4	-1.0	-0.3	-4.3	-4.5
FF $X_c l\nu$ total	0.3	1.0	0.3	7.1	7.4
FF $D^{(*)}l\nu$	0.1	0.3	0.1	1.8	1.9
FF $D\ell\nu$ diff.: [85] vs. [204]	0.0	0.2	0.0	0.6	0.7
FF $D^*\ell\nu$ diff.: [85] vs. [205]	0.3	0.5	0.2	3.8	4.0
FF $D\tau\nu$ diff.: [85] vs. [130]	0.0	0.0	0.0	0.1	0.1
FF $D^*\tau\nu$ diff.: [85] vs. [130]	0.0	0.0	0.0	0.0	0.1
FF $D^{**}l\nu$	0.2	0.4	0.2	3.0	3.1
FF $D^{**}_{\text{gap}}l\nu$	0.2	0.3	0.1	1.8	1.9
FF $X_c l\nu$ correlation	-0.3	0.6	0.2	4.5	4.7
Total correlation	-0.4	2.1	0.4	1.2	2.0

Table 8.1: A detailed breakdown of both relative statistical and systematic uncertainties is provided for each electron-channel template yield N^{meas}. Uncertainties linked to form-factor parameters are denoted by the abbreviation "FF", while composition and shape uncertainties are associated with the simulation reweighting. The uncertainties on the ratio $R(X_{\tau/e})$, extracted from yields and efficiencies of $X[\tau \to e\nu\nu]\nu$ and $Xe\nu$ decays, are also provided.

Uncertainty source	**Muon channel: Relative uncertainty [%]** Continuum	$B\bar{B}$ bkg.	$X\mu\nu$	$X\tau\nu$	$R(X_{\tau/\mu})$
Total	3.9	3.5	0.9	25.1	25.6
Exp. sample size	3.9	1.8	0.4	11.8	12.0
Sim. sample size	0.5	1.2	0.3	10.5	10.6
Lepton identification	0.1	0.9	0.3	5.0	5.2
Track-reco. eff.	0.0	0.4	0.0	3.4	3.3
$B\bar{B}$-bkg. composition	0.0	0.2	0.1	4.2	4.3
$B\bar{B}$ bkg.: (p_ℓ, M_X) shape	0.1	1.8	0.4	10.5	10.7
$Xl\nu$: B^0_{tag}-B^+_{tag} composition	0.0	0.1	0.0	0.5	0.5
$X_c l\nu$: M_X shape	0.1	0.6	0.0	6.8	6.8
$\mathcal{B}(X\tau\nu)$ total	0.0	0.1	0.0	0.5	1.0
$\mathcal{B}(X\ell\nu)$ total	0.1	0.9	0.3	9.7	10.0
$\mathcal{B}(X_u\ell\nu)$	0.0	0.0	0.0	2.2	2.3
$\mathcal{B}(D\ell\nu)$	0.0	0.0	0.1	2.4	2.4
$\mathcal{B}(D^*\ell\nu)$	0.0	0.3	0.1	3.2	3.4
$\mathcal{B}(D^{**}\ell\nu)$	0.0	0.6	0.2	4.8	5.0
$\mathcal{B}(D^{(*)}\pi\pi\ell\nu)$	0.0	0.5	0.2	4.1	4.3
$\mathcal{B}(D^{(*)}\eta\ell\nu)$	0.1	0.8	0.3	9.1	9.4
$\mathcal{B}(D_s^{(*)}K\ell\nu)$	0.0	0.2	0.1	0.3	0.3
$\mathcal{B}(X_c\ell\nu)$ correlation	-0.1	-0.9	-0.3	-7.2	-7.5
FF $X_c l\nu$ total	0.1	0.5	0.3	8.7	8.9
FF $D^{(*)}l\nu$	0.0	0.3	0.1	3.0	3.1
FF $D\ell\nu$ diff.: [85] vs. [204]	0.0	0.1	0.0	0.6	0.6
FF $D^*\ell\nu$ diff.: [85] vs. [205]	0.1	0.4	0.2	5.6	5.8
FF $D\tau\nu$ diff.: [85] vs. [130]	0.0	0.0	0.0	0.0	0.1
FF $D^*\tau\nu$ diff.: [85] vs. [130]	0.0	0.0	0.0	0.0	0.1
FF $D^{**}l\nu$	0.1	0.2	0.1	3.6	3.7
FF $D^{**}_{\text{gap}}l\nu$	0.0	0.2	0.1	1.7	1.8
FF $X_c l\nu$ correlation	-0.1	-0.2	0.1	4.3	4.4
Total correlation	-0.1	1.2	0.3	0.3	1.3

Table 8.2: A detailed breakdown of both relative statistical and systematic uncertainties is provided for each muon-channel template yield N^{meas}. Uncertainties linked to form-factor parameters are denoted by the abbreviation "FF", while composition and shape uncertainties are associated with the simulation reweighting. The uncertainties on the ratio $R(X_{\tau/\mu})$, extracted from yields and efficiencies of $X[\tau \to \mu\nu\nu]\nu$ and $X\mu\nu$ decays, are also provided.

The lepton-flavor specific results are combined in a weighted average of correlated values following Equation (5.4). Table 8.3 provides a concise overview of the uncertainties associated with $R(X_{\tau/\ell})$ for both the electron and muon channels, as well as their combined result. Furthermore, the semitauonic branching-fraction ratio

$$\mathcal{R}(X_{e/\mu}^{\tau\rightarrow}) = \frac{\mathcal{B}(X[\tau \rightarrow e\nu\nu]\nu)}{\mathcal{B}(X[\tau \rightarrow \mu\nu\nu]\nu)} \tag{8.4}$$

is measured as a crosscheck, and its expected uncertainties are presented.

Uncertainty Source	Relative uncertainty [%] $R(X_{\tau/e})$	$R(X_{\tau/\mu})$	$R(X_{\tau/\ell})$	$\mathcal{R}(X_{e/\mu}^{\tau\rightarrow})$
Total	18.4	25.6	17.5	24.0
Exp. sample size	9.0	12.0	7.2	14.8
Sim. sample size	6.7	10.6	5.7	12.4
Lepton identification	2.8	5.2	2.4	5.9
Track-reco. eff.	2.9	3.3	3.0	0.5
$B\bar{B}$-bkg. reweighting	5.8	11.5	5.7	12.1
$X_c l\nu$ reweighting	7.3	6.8	7.1	2.3
$X\tau\nu$ branching fractions	1.0	1.0	1.0	0.2
$X\ell\nu$ branching fractions	7.0	10.0	7.7	3.1
$X_c l\nu$ form factors	7.4	8.9	7.8	2.1

Table 8.3: A concise breakdown of relative statistical and systematic uncertainties on $R(X_{\tau/e})$ and $R(X_{\tau/\mu})$ is provided, as discussed in more detail in the text. The relative uncertainties on the combined result $R(X_{\tau/\ell})$ and on the ratio $\mathcal{R}(X_{e/\mu}^{\tau\rightarrow}) = \mathcal{B}(X[\tau \rightarrow e\nu\nu]\nu)/\mathcal{B}(X[\tau \rightarrow \mu\nu\nu]\nu)$ are also presented.

In total, a relative uncertainty of 17.5% is observed for the combined value of $R(X_{\tau/\ell})$. The electron channel provides a higher precision with a relative uncertainty of 18.4% compared to the muon channel, which has a relative uncertainty of 25.6%. This discrepancy is attributed to the lower efficiency of signal decays in the muon case (see Tab. 8.7), due to more stringent constraints on the lepton-momentum threshold (see Sec. 7.1). Background yields are comparable between the two channels. Consequently, the relative size of background and normalization events is higher in the muon channel, leading to uncertainties associated with these templates having a greater impact on $R(X_{\tau/\mu})$ than on $R(X_{\tau/e})$.

The most significant individual source of uncertainty for $R(X_{\tau/e})$ (9.0%) and $R(X_{\tau/\mu})$ (12.0%) stems from **statistical uncertainties** associated with the experimental sample size, resulting in a relative uncertainty of 7.2% on the combined result $R(X_{\tau/\ell})$. Systematic uncertainties arising from the simulation sample size, the reweighting procedure introduced in Section 7.3, $B \rightarrow Xl\nu$ branching fractions, and $B \rightarrow X_c l\nu$ form-factor parameters all contribute approximately equally, ranging from 5.8% – 7.4% each in the electron channel to 6.8% – 11.5% each in the muon channel. Collectively, their contribution surpasses statistical uncertainties, indicating that this analysis is systematically limited. However, several of the leading systematic uncertainties are directly influenced by the experimental sample size, suggesting that they should decrease in a manner analogous to statistical uncertainties.

Uncertainties associated with the **lepton-identification** correction factors (see Sec. 5.3.5) and **track-reconstruction efficiency** (see Sec. 5.3.4), while non-negligible, do not induce uncertainties of a similar magnitude as other sources.

The uncertainties attributed to the data-driven **simulation reweighting** are limited by the statistical precision of the experimental control sample. They are organized in four components.

Uncertainties related to the relative **composition** of events with charged and neutral B_{tag} candidates, as determined during the initial yield calibration in Section 7.3.1, are labeled as $Xl\nu$*:* B^0_{tag}-B^+_{tag} *composition*. Potential variations in the relative composition of different sources of secondary and fake leptons are denoted $B\bar{B}$*-bkg. composition*. While both contributions are negligible in the electron channel, in the muon channel, where $B\bar{B}$ backgrounds consist almost equally of secondary and fake leptons, uncertainties in their composition contribute to the overall uncertainty.

Uncertainties associated with the template **shapes**, introduced in Sections 7.3.2 to 7.3.4 via event weights, are referred to as $X_c l\nu$*:* M_X *shape* and $B\bar{B}$ *bkg.:* (p_ℓ, M_X) *shape*. They significantly contribute to the overall uncertainty. In Table 8.3, the reweighting-related shape and composition uncertainties are combined for each event type.

Uncertainties arising from $B \to X\ell\nu$ **branching fractions** (see Sec. 5.3.2) are predominantly driven by the 100% uncertainty assigned to the non-resonant $B \to D^{(*)}\eta\ell\nu$ gap-mode decays (see Tab. 3.1). Due to the statistical uncertainty of experimental data being significantly smaller than the uncertainty induced by the gap modes, the latter is notably constrained in the fit. This reduces the impact of the gap-mode uncertainties by a factor of two to three, as observed in post-fit nuisance-parameter pulls presented in Figure 8.10.

The same effect results in a combined $B \to X\ell\nu$ branching-fraction uncertainty that only marginally surpasses the uncertainty induced by these gap modes, as indicated by the negative correlation associated with branching-fraction uncertainties in Tables 8.1 and 8.2. Uncertainties on $R(X_{\tau/\ell})$ attributed to semitauonic branching fractions remain comparatively small, as the $B \to X\tau\nu$ yield uncertainty is driven by uncertainties on the significantly larger $B \to X\ell\nu$, continuum, and $B\bar{B}$-background templates in the fit.

Uncertainties linked to **form-factor parameters** are primarily influenced by discrepancies in the $B \to D^*\ell\nu$ decay kinematics predicted by BLPRXP-model-based parameters from Reference [85] compared to BGL-model-based predictions by parameters from Reference [205] (referred to as **FF $D^*\ell\nu$ diff.** in Tables 8.1 and 8.2). Negligible differences are observed for $B \to D\ell\nu$ decay kinematics between BLPRXP and BGL parameters from Reference [204]. Similar to the findings for branching fractions, the shape uncertainties induced by form factors on the $B \to X\tau\nu$ template have only minor effects on $R(X_{\tau/\ell})$. Consequently, differences between BLPRXP and CLN (from Ref. [130]) for $B \to D^{(*)}\tau\nu$ decays are negligible.

Uncertainties associated with the BLPRXP-model parameters for $B \to D^{(*)}l\nu$ decays and the BLR model parameters for $B \to D^{**}_{(\text{gap})}l\nu$ (see Ref. [89]) are quantified through eigenvariations (see Sec. 5.3.3). In the latter case, additional shape uncertainties in $B \to D^*_0 l\nu$ and $B \to D'_1 l\nu$ decays, arising from the unappreciated broad nature of the charmed meson in the form-factor model (see Sec. 3.4.3), are accounted for in parameter variations corresponding to $\pm 1.5\,\sigma$ instead of $\pm 1\,\sigma$. This approach is motivated by the differences observed in the kinematic distributions of $B \to D^{**}\ell\nu$ decays

reproduced on generator level with EvtGen, both with and without considering the broad width of the D^{**} mesons. Gap modes modeled with intermediate D_0^* or D_1' resonances (see Sec. 3.4.3) are allowed to vary independently from measured $B \to D^{**} l\nu$ decays, resulting in uncorrelated uncertainties.

The simultaneous incorporation of all form-factor-associated uncertainties as nuisance parameters allows for additional flexibility in varying the $B \to X\ell\nu$-template shapes. This results in a noticeably larger uncertainty associated with form factors than a straightforward sum in quadrature of the individual components (denoted as **FF $X_c l\nu$ correlation**). In a future iteration of the measurement, this could likely be mitigated by making small adjustments to the p_ℓ^B-M_{miss}^2 intervals in the final fit.

For **the ratio $\mathcal{R}(X_{e/\mu}^{\tau\to}) = \mathcal{B}(X[\tau \to e\nu\nu]\nu)/\mathcal{B}(X[\tau \to \mu\nu\nu]\nu)$**, a precision of 24% is achieved. In this case, uncertainties that are correlated between lepton flavors, such as the ones on track-reconstruction efficiency, the reweighting of $X_c l\nu$ decays, $Xl\nu$ branching ratios, and $X_c l\nu$ form factors, largely cancel out. However, lepton-identification uncertainties and those related to the lepton-flavor-dependent $B\bar{B}$ backgrounds, as well as statistical uncertainties, do not cancel and predominantly contribute to the overall uncertainties of $\mathcal{R}(X_{e/\mu}^{\tau\to})$.

8.1.3 Effects of modified D-meson decay distributions

In this section, the robustness of the data-driven reweighting concerning modified D-meson decay distributions in simulation is investigated.

For this purpose, several simulation samples with modified D-meson decay distributions are generated, as detailed in Section 6.1.3. The relative fraction of D-meson decays into specific kaon charges and excitations is manipulated, as illustrated in Table 8.4 for two examples. In Tables B.5 and B.6 in the appendix, all 16 utilized distributions are provided. Subsequently, the modified simulation samples are reweighted with experimental data as outlined in Section 7.3. The resulting reweighted sample is then fitted against Asimov data drawn from the reweighted distribution of the nominal simulation, and the extracted value of $R(X_{\tau/\ell})$ is determined.

$D \to \ldots$	Distr. 12: $K^\pm \Uparrow\uparrow$ [%]		Distr. 16: $K^\pm \Downarrow\downarrow$ [%]	
+ anything	$\mathcal{B}(D^0)$ [%]	$\mathcal{B}(D^+)$ [%]	$\mathcal{B}(D^0)$ [%]	$\mathcal{B}(D^+)$ [%]
K^-	67.2	36.6	39.2	21.3
K^+	4.0	7.4	2.9	5.9
$K^0/\,\bar{K}^0$	30.6	52.6	53.8	64.8
$K^{*+}/\,K^{*-}$	11.5	4.4	14.3	4.7
$K^{*0}/\,\bar{K}^{*0}$	9.3	21.3	8.9	16.5

Table 8.4: Two example D-meson decay distributions are presented that are used to validate the reweighting procedure. These distributions are generated by adjusting the inclusive D-meson branching fractions for specific kaon flavors, as specified in each title. For comparison, the nominal D-meson decay distribution in simulation and the experimental world averages are provided in Table 7.5.

With unlimited computing resources, an ideal approach would involve sampling within the uncertainty range of each inclusive D-meson branching fraction, imposing constraints to ensure that the final distribution does not deviate by more than $2-3$ standard deviations from world averages in

any of the probed branching fractions. However, due to limited resources, the validation is constrained to the presented set of 16 variations. In this context, the presented distributions serve as the edge cases of the large hyperparameter space of physical and unphysical D-meson decay distributions, each deviating from the SM distribution by several standard deviations. Consequently, this approach does not aim to quantify uncertainties but serves as a validation of the uncertainties associated with the reweighting outlined in Section 7.3.

Figure 7.13 illustrates the resulting M_X and M^2_{miss} distributions for two scenarios (distributions 9 and 16) characterized by enhanced $D \to K^0/\overline{K}^0$ (and consequently, reduced $D \to K^\pm$) branching fractions. In Figure 8.2, the effects of a scenario with reduced $D \to K^0/\overline{K}^0$ (i.e., enhanced $D \to K^\pm$) contributions (distribution 12) on M_X are presented.

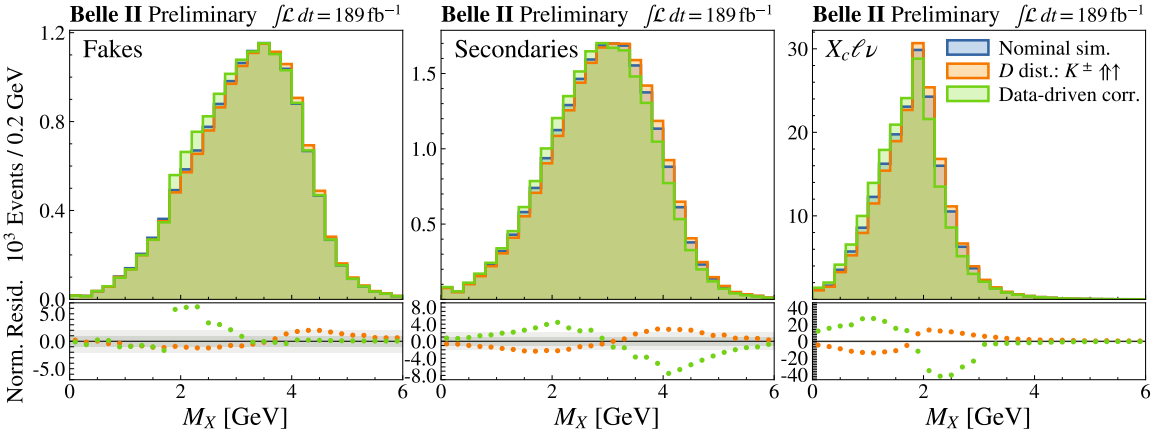

Figure 8.2: The M_X distribution is compared among three scenarios: the nominal MC simulation input (blue), the modified D-meson decay distribution 12 (orange, featuring enhanced $D \to K^\pm$), and the data-driven reweighted nominal simulation (green) considering fakes, secondaries, and $B \to X_c \ell\nu$ decays. Uncertainty-normalized residuals compared to the nominal simulation are shown below.

The associated M_X and (p_ℓ, M_X)-based correction weights are illustrated in Figure 8.3 and are contrasted with the nominal correction weights as presented in Figures 7.15 and 7.24. As anticipated, the correction weights extracted from scenarios with enhanced $D \to K^0/\overline{K}^0$ branching fractions (i.e., reduced $D \to K^\pm$) align more closely with unity.

Figure 8.4 provides a summary of the deviations from the nominal values of $R(X_{\tau/e})$ and $R(X_{\tau/\mu})$, comparing them to the combined predicted uncertainty of 9.3% (e) and 13.4% (μ) caused by the $X_c l\nu$ and $B\overline{B}$-background reweighting procedure (see Tab. 8.3).

The approximate *local* pull, as discussed in Section 6.1.3, on each varied inclusive branching fraction is highlighted in red. The *global* pull, considering the deviation of all inclusive $D \to K$ branching fractions, is presented in blue on top of the plot, extending to values of up to ten standard deviations.

All extracted $R(X_{\tau/\ell})$ values are well within the predicted precision of the reweighting procedure. Deviations larger than half a standard deviation are only observed in the most extreme D-meson decay-distribution scenarios, corresponding to global pulls of six to ten standard deviations. This strongly enhances confidence in the presented reweighting method, suggesting that the statistical precision obtained in the control samples is a reliable estimate of uncertainty. The remarkable

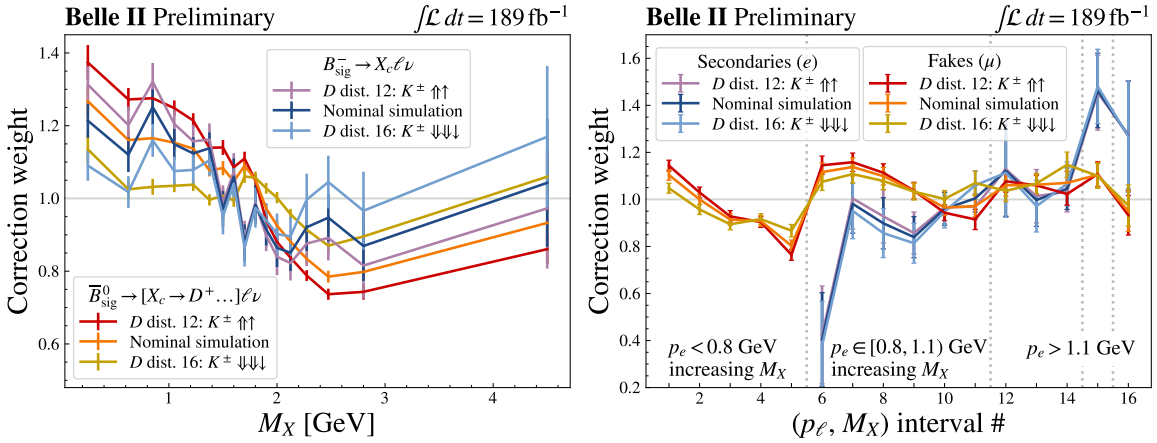

Figure 8.3: The correction weights, obtained as detailed in Section 7.3, are compared among distribution 12 (see Tab. B.6, featuring enhanced $D \to K^\pm$ branching fractions), distribution 16 (with reduced $D \to K^\pm$ branching fractions), and the nominal simulation (see Figs. 7.15 and 7.24) for $B \to X_c \ell \nu$ decays (left) and $B\overline{B}$ backgrounds (right).

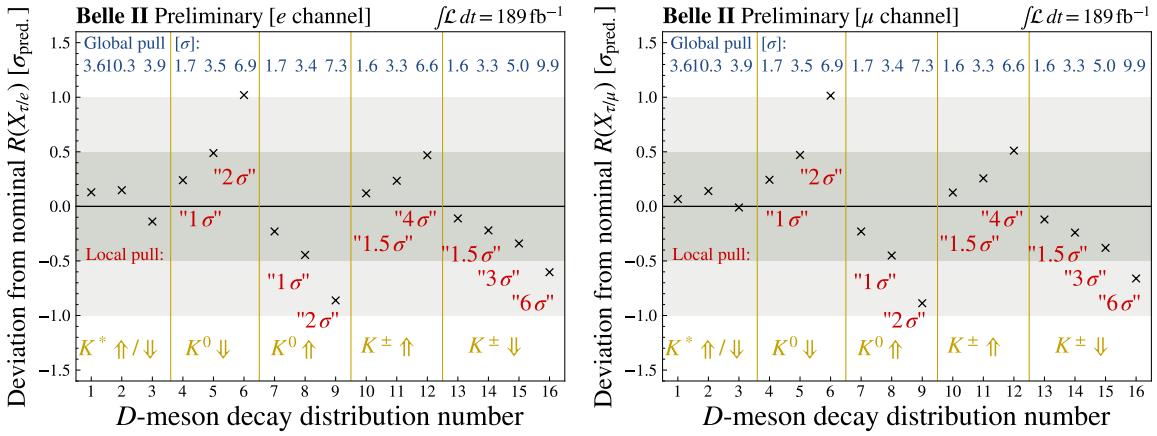

Figure 8.4: The deviations of the extracted $R(X_{\tau/e})$ and $R(X_{\tau/\mu})$ from their nominal values are shown, with the 16 modified D-meson decay distributions (see Tabs. B.5 and B.6, modification highlighted in gold) are fitted against the nominal simulation. These deviations are normalized by the predicted precision of 9.3% (e) and 13.4% (μ) of the reweighting procedure (black crosses). The *global* and *local* pulls that the different D-meson decay distributions correspond to are introduced in the text and are presented in blue and red, respectively.

symmetry in observed deviation strength in both lepton flavors further increases confidence in the reliability of predicted $B\overline{B}$-background uncertainties for both lepton flavors.

Exploration of modified hadronic B-meson decay branching fractions, primarily impactful for $B\overline{B}$ backgrounds, is undertaken by extensively adjusting the $B \to X_c X_c$ branching fractions, as elaborated in Section 8.2.2.

8.1.4 Dependence on the lepton-momentum threshold

Similar to the stability test conducted for the $R(X_{e/\mu})$ measurement in Section 6.2.3, the dependence of $R(X_{\tau/\ell})$ on the lepton-momentum selection requirements is investigated.

In this evaluation, $R(X_{\tau/\ell})$ is derived from experimental data with gradually increased lepton-momentum thresholds. Subsequently, the extracted results are compared to the nominal value obtained at the lowest thresholds. The individual results, along with the direction of their deviation from the nominal value, are kept box-closed by normalizing the absolute deviation by the increasing uncertainty associated with the threshold-dependent outcomes:

$$\frac{\left|R(X)_{\text{indv.}} - R(X)_{\text{nom.}}\right|}{\Delta R(X)_{\text{indv.}}}. \tag{8.5}$$

The resulting pulls for modified lepton-momentum thresholds in different reference frames are summarized in Figure 8.5. The maximal observed pull corresponds to approximately $0.65\,\sigma$, and no continuous growth in the pulls is evident.

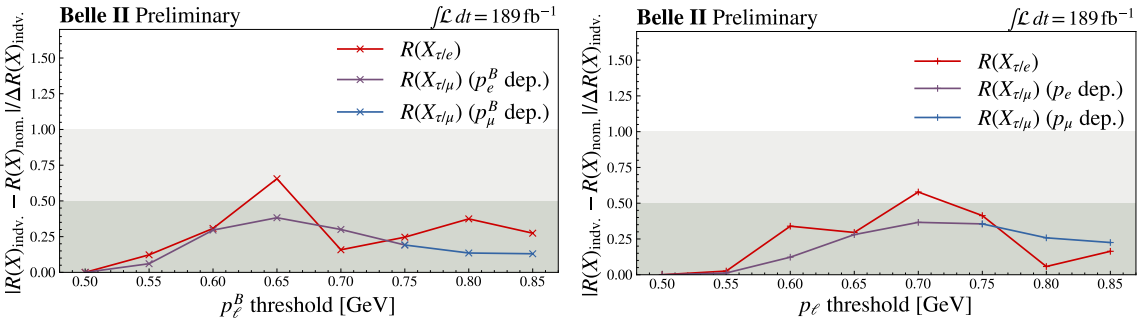

(a) (b)

Figure 8.5: The extracted values of $R(X_{\tau/\ell})$ for gradually increased lepton-momentum thresholds in both the B_{sig} frame (a) and the laboratory frame (b) are depicted. The absolute value of the deviation from the nominal value is normalized by the individual uncertainty of each measurement, ensuring the conduction of this study in a box-closed manner.

To quantify expected fluctuations, the uncertainties on $R(X_{\tau/\ell})$, as detailed in Table 8.3, are separated into two components. All uncertainties associated with $B \to X\ell\nu$ decays, including those related to the reweighting, form factors, $X\ell\nu$ branching fractions, track-reconstruction efficiency, and lepton identification, are assumed to be fully correlated across all results. This conservative assumption is made based on the understanding that these decays are minimally affected by an increased lepton momentum threshold. On the other hand, uncertainties linked to signal and background events, encompassing statistical uncertainties and $B\overline{B}$-background reweighting, exhibit partial decorrelation among the outcomes. The correlation coefficient to the nominal result is estimated using the general equation for statistical correlation between two overlapping samples, denoted as A and B:

$$\rho_{A,B} = N_{AB}/\sqrt{N_A \cdot N_B} \tag{8.6}$$

Here, N_B represents the signal plus background sample size of the nominal sample, while $N_A = N_{AB}$ (100% overlap) denote the remaining signal plus background sample size for the more restrictive

lepton momentum threshold.

The remaining yield fractions per lepton-momentum threshold and the resulting correlation coefficients $\rho_{A,B}$ are summarized in Tables 8.5 and 8.6. These $\rho_{A,B}$ values, in conjunction with the signal-and-background-related uncertainties, are employed to quantify the observed pulls from Figure 8.5, as detailed in the same tables.

	Electron channel							**Muon channel**		
p_ℓ^B thres. [GeV]	0.55	0.6	0.65	0.7	0.75	0.8	0.85	0.75	0.8	0.85
$X\tau\nu$ frac.	93%	87%	82%	76%	70%	64%	58%	90%	85%	78%
Bkg. frac.	85%	75%	67%	59%	52%	46%	40%	85%	77%	69%
$\rho_{A,B}$	0.93	0.88	0.83	0.78	0.74	0.69	0.65	0.92	0.88	0.83
Pull	$0.4\,\sigma$	$0.8\,\sigma$	$1.4\,\sigma$	$0.3\,\sigma$	$0.4\,\sigma$	$0.6\,\sigma$	$0.4\,\sigma$	$0.6\,\sigma$	$0.8\,\sigma$	$0.5\,\sigma$

Table 8.5: The fractions of remaining signal and background events for each lepton-momentum threshold **in the B_{sig} frame** are presented. The resulting correlation coefficient is computed, and the observed pull in $R(X_{\tau/\ell})$ (see Fig. 8.5(a)) is quantified using this correlation.

	Electron channel							**Muon channel**		
p_ℓ thres. [GeV]	0.55	0.6	0.65	0.7	0.75	0.8	0.85	0.75	0.8	0.85
$X\tau\nu$ frac.	95%	90%	85%	80%	75%	69%	64%	95%	89%	82%
Bkg. frac.	91%	82%	73%	66%	60%	54%	48%	92%	83%	75%
$\rho_{A,B}$	0.95	0.91	0.87	0.82	0.78	0.75	0.71	0.96	0.92	0.87
Pull	$0.1\,\sigma$	$1.0\,\sigma$	$0.7\,\sigma$	$1.2\,\sigma$	$0.8\,\sigma$	$0.1\,\sigma$	$0.3\,\sigma$	$0.7\,\sigma$	$1.2\,\sigma$	$0.1\,\sigma$

Table 8.6: The fractions of remaining signal and background events for each lepton-momentum threshold **in the laboratory frame** are presented. The resulting correlation coefficient is computed, and the observed pull in $R(X_{\tau/\ell})$ (see Fig. 8.5(b)) is quantified using this correlation.

Despite the simplicity of the estimation or correlations, no pulls larger than $1.4\,\sigma$ are observed. A consideration of existing decorrelation of $B \to X\ell\nu$ decays and their corresponding uncertainties would further decrease these values, suggesting that observed deviations are adequately accounted for by expected statistical and systematic fluctuations. Hence, the box-opened $R(X_{\tau/\ell})$ values presented in Section 8.2.1 are demonstrated to be stable against varying lepton-momentum thresholds.

8.1.5 First box opening

This analysis is designed as a box-closed analysis (see Sec. 3.4.2). During the first box opening of the signal region, a significant instability in the measured $R(X_{\tau/\ell})$ value with respect to the lepton-momentum threshold was observed in the electron channel in a study as conducted in Section 8.1.4.

While the current setup yields fluctuations within the anticipated uncertainties (see Fig. 8.5), the first box opening revealed a continuously increasing pull, reaching values of up to two standard deviations.

The instability was investigated in a re-blinded analysis and was primarily attributed to a selection criterion applied in an early data-processing step for centrally produced subsets of experimental and simulated data using hadronic tagging (see Sec. 4.1 and Eq. (4.2)). Initially, the total energy deposited in the ECL by tracks and clusters satisfying Equation (4.2) was constrained to values within $E_{\text{ECL}} \in (2, 7)\,\text{GeV}$. In Figure 8.6, this quantity is presented in both the electron and muon channels for $p_\ell^B > 1.3\,\text{GeV}$ in experimental data and simulation.

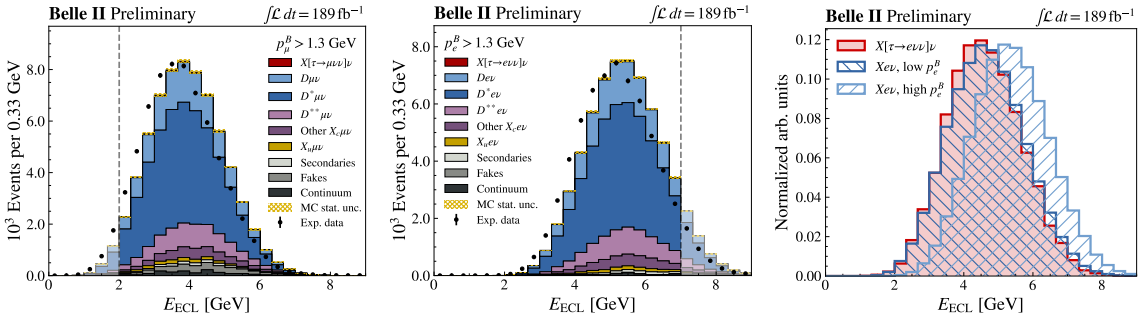

Figure 8.6: The E_{ECL} distribution, representing the total energy deposited in the ECL by cleaned tracks and clusters, is presented in the muon (a) and electron (b) channels for experimental data and simulation for $p_\ell^B > 1.3\,\text{GeV}$. The initial requirement of $E_{\text{ECL}} \in (2, 7)\,\text{GeV}$ is highlighted. In (c), the shapes of E_{ECL} are compared between signal and normalization decays, the latter with low ($p_e^B > 0.9\,\text{GeV}$) and high signal-electron momentum ($p_e^B > 1.2\,\text{GeV}$), illustrating the lepton-momentum dependence of this quantity in the electron channel.

A significant mismodeling is evident, leading to distinct event-rejection patterns between simulation and experimental data and, consequently, inaccurate efficiency and template-shape estimations. Furthermore, this quantity is strongly correlated with the signal-electron momentum, which predominantly deposits its energy in the ECL, as illustrated in Figure 8.6(c). Consequently, the requirement on E_{ECL} affects signal and normalization efficiencies differently. Moreover, $B \to Xe\nu$ and $B \to X\mu\nu$ decays are impacted differently, introducing a bias in the initial measurement of $R(X_{e/\mu})$, as apparent when comparing Equations (6.3) and (6.12).

As a result of these observations, the requirement on E_{ECL} was removed. Additionally, the $B\bar{B}$-background treatment was re-investigated, involving the introduction of more stringent background-rejection criteria and tightened lepton-selection requirements, as presented in Section 7.1. These adjustments significantly reduce the diversity and lepton-flavor dependence of $B\bar{B}$-background events, enabling an independent reweighting for secondaries and fakes in p_ℓ and M_X, as described in Section 7.3.4. In the previous approach, their reweighting was based on the invariant mass of the B_{sig} system:

$$M_{B_{\text{sig}}} = \sqrt{\left(P_X^* + P_\ell^*\right)^2}, \tag{8.7}$$

and the resulting uncertainties were underestimated.

The results presented in Section 8.2.1 are now insensitive to the lepton-momentum threshold as demonstrated in Section 8.1.4. Additionally, the uncertainty induced by $B\bar{B}$-background modeling

is expected to be robustly evaluated. This is evidenced by the lepton-flavor symmetric dependence on modified D-meson decay distributions, as investigated in Section 8.1.3. In the previous $B\bar{B}$-background reweighting approach, relatively higher fluctuations were observed in the muon channel due to insufficiently addressing the distinct behaviors of fakes and secondaries.

In summary, the conducted validation tests have effectively identified an underappreciated selection bias, leading to its successful removal. Given that the affected subsets were used within the entire collaboration, this finding holds significant value for future analyses.

8.2 Measurement and validation studies

The measured values of $R(X_{\tau/\ell})$ are presented in Section 8.2.1. In Section 8.2.2 the stability of the result is validated through various crosschecks and in Section 8.2.3, the implications of this measurement on the $b \to c\tau\nu$ anomaly are discussed.

8.2.1 Measurement of $R(X_{\tau/\ell})$

In Figure 8.7, the signal-extraction quantities p_ℓ^B, M^2_{miss}, and the correlated observables M_X and q^2 are compared between experimental data and simulation in the entire phase space after the simulation reweighting, demonstrating a remarkable agreement also in signal-enhanced regions before the signal-extraction fit.

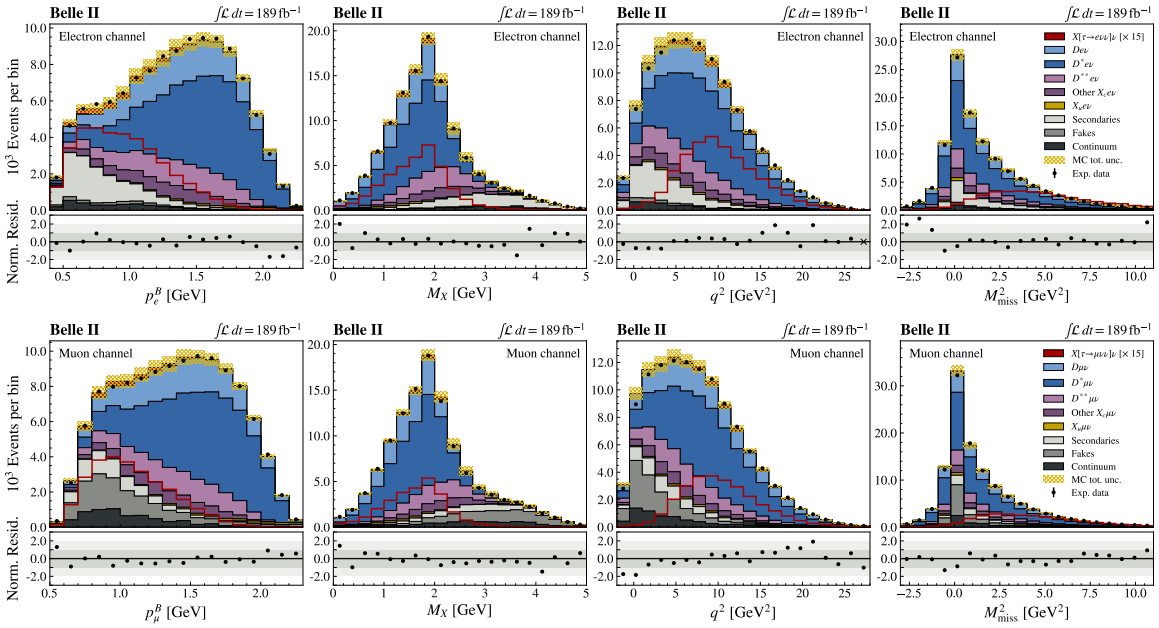

Figure 8.7: The distributions of p_ℓ^B, M_X, q^2, and M^2_{miss} are presented in the electron (top) and muon channel (bottom) before the signal-extraction fit. The signal distribution in each quantity, enhanced by a factor of 15, is prominently displayed with a red line.

In Figure 8.8, the pre-fit distributions are displayed in the signal-extraction intervals of p_ℓ^B and M^2_{miss}. Additional figures, categorized by B_{tag}-candidate and lepton charge, are presented in the

appendix in Figures B.26 and B.27.

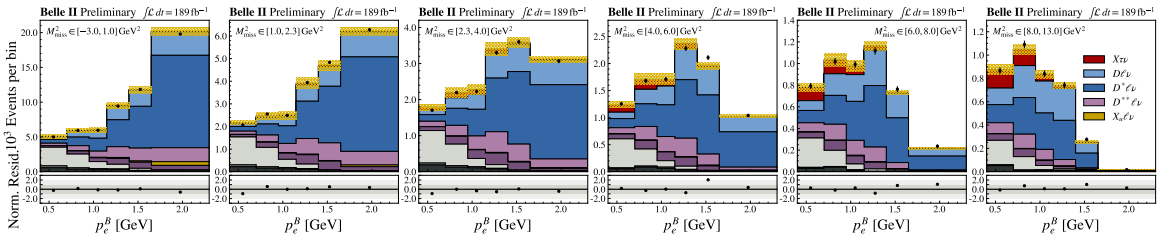

(a) Electron channel

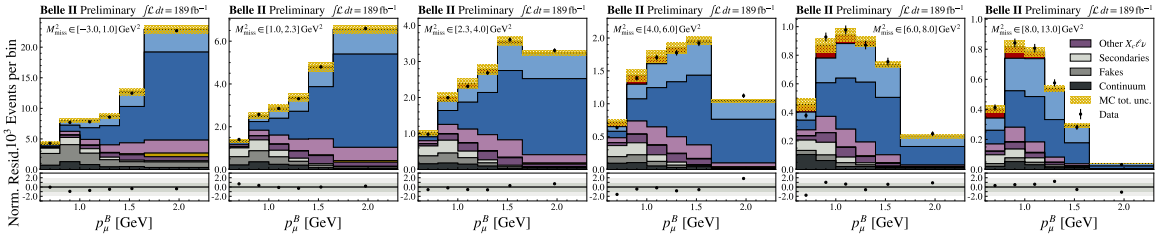

(b) Muon channel

Figure 8.8: Two-dimensional pre-fit distributions of p_ℓ^B vs. M_{miss}^2 are presented flattened to one dimension in intervals as used in the signal-extraction fit. To avoid sparsely populated intervals, the last two displayed p_ℓ^B intervals are merged in the two regions with highest M_{miss}^2 requirements (see Sec. 8.1.1).

The post-fit distributions are depicted in Figure 8.9. Tables 8.7 and 8.8 present the extracted yields N^{meas} of the templates and their correlations, respectively.

The electron-channel efficiencies are determined to be $\epsilon_{\tau\to e} = (1.50 \pm 0.02) \cdot 10^{-3}$ in the signal mode and $\epsilon_e = (2.29 \pm 0.03) \cdot 10^{-3}$ in the normalization mode, with a correlation between the two efficiencies of 0.62 due to shared systematic uncertainties. Correspondingly, the muon-channel efficiencies are $\epsilon_{\tau\to\mu} = (1.12 \pm 0.02) \cdot 10^{-3}$ and $\epsilon_\mu = (2.15 \pm 0.03) \cdot 10^{-3}$, with a correlation of 0.71.

Using Equation (5.3), the $R(X_{\tau/\ell})$ values for electrons and muons are

$$R(X_{\tau/e}) = 0.232 \pm 0.020\ (\text{stat.}) \pm 0.037\ (\text{syst.}), \text{ and} \tag{8.8}$$

$$R(X_{\tau/\mu}) = 0.222 \pm 0.027\ (\text{stat.}) \pm 0.050\ (\text{syst.}), \tag{8.9}$$

respectively. The combination of lepton flavors in a weighted average of correlated values yields

$$R(X_{\tau/\ell}) = 0.228 \pm 0.016\ (\text{stat.}) \pm 0.036\ (\text{syst.}). \tag{8.10}$$

The uncertainties are consistent with their expected values (see Tab. 8.3), when accounting for the slightly elevated $R(X_{\tau/\ell})$ values observed in the electron channel and the combined result. In this context, the statistical uncertainties are obtained from a fit with all nuisance parameters fixed to their post-fit values. Furthermore, the results are in excellent agreement with the average of SM predictions of $R(X_{\tau/\ell})_{\text{SM}} = 0.223 \pm 0.005$ [126, 128, 129] (see Eq. (2.31)).

The pulls on the constrained nuisance parameters are illustrated in Figure 8.10. For the nuisance parameters associated with the $X\ell\nu$ templates, a consistent pull toward lower values is observed, aligning well with the reduction of the D_{gap}^{**} components observed in the $R(X_{e/\mu})$ measurement (see

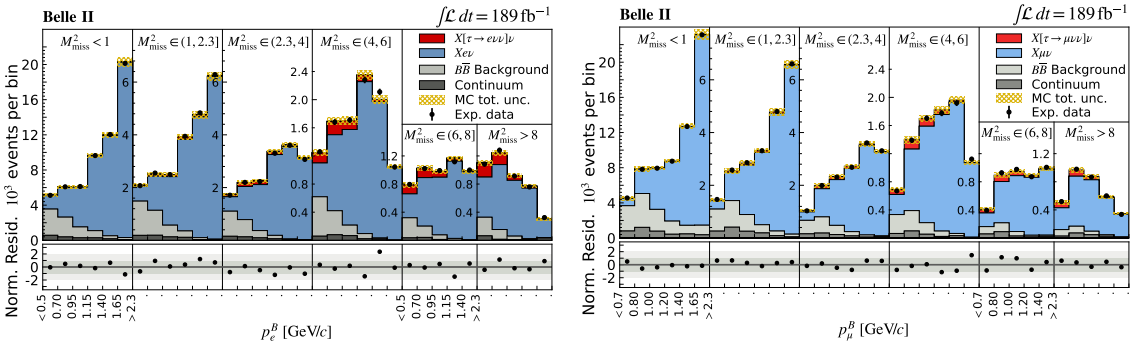

(a) Electron channel

(b) Muon channel

Figure 8.9: Two-dimensional distributions of p_ℓ^B vs. M^2_{miss} are presented for all fit-template results and experimental data, flattened to one dimension in intervals as used in the signal-extraction fit. The residuals are normalized to the statistical uncertainty of the data points and the M^2_{miss} intervals are given in units of GeV^2.

	Electron channel		**Muon channel**	
	N^{sel}	N^{meas}	N^{sel}	N^{meas}
$X[\tau \to \ell\nu\nu]\nu$	2 513 ± 451	2 594 ± 452	1 834 ± 459	1 812 ± 458
$X\ell\nu$	96 065 ± 760	95 686 ± 768	90 264 ± 825	89 974 ± 812
$B\bar{B}$ background	14 848 ± 589	15 129 ± 601	19 856 ± 688	19 058 ± 672
Continuum	3 336 ± 185	3 360 ± 186	6 609 ± 261	6 624 ± 262

Table 8.7: The pre-fit N^{sel} and post-fit N^{meas} yields of the fit templates in the $R(X_{\tau/\ell})$ extraction are summarized. The uncertainties presented for N^{sel} are obtained from fits to Asimov data.

	Electron channel				**Muon channel**			
	$X\tau\nu$	$Xe\nu$	$B\bar{B}$ Bkg.	Cont.	$X\tau\nu$	$X\mu\nu$	$B\bar{B}$ Bkg.	Cont.
$X[\tau \to e\nu\nu]\nu$	1.00	−0.53	−0.06	0.01	0.42	−0.25	0.02	0.00
$Xe\nu$	−0.53	1.00	−0.65	−0.06	−0.41	0.47	−0.29	−0.01
$B\bar{B}$ Bkg. (e)	−0.06	−0.65	1.00	−0.24	0.20	−0.41	0.35	0.01
Cont. (e)	0.01	−0.06	−0.24	1.00	0.01	−0.02	0.02	0.00
$X[\tau \to \mu\nu\nu]\nu$	0.42	−0.41	0.20	0.01	1.00	−0.54	−0.02	−0.02
$X\mu\nu$	−0.25	0.47	−0.41	−0.02	−0.54	1.00	−0.66	−0.03
$B\bar{B}$ Bkg. (μ)	0.02	−0.29	0.35	0.02	−0.02	−0.66	1.00	−0.34
Cont. (μ)	0.00	−0.01	0.01	0.00	−0.02	−0.03	−0.34	1.00

Table 8.8: The correlations of the extracted template yields in the $R(X_{\tau/\ell})$ measurement are presented.

Sec. 6.2.1) and the measurements of the exclusive ratio $R(D^*)$ by Belle II [119, 218]. Additionally, the constraining impact of experimental data on the 100% gap-mode branching-fraction uncertainties is evident, resulting in a reduction of the nuisance-parameter uncertainty by a factor of two to three.

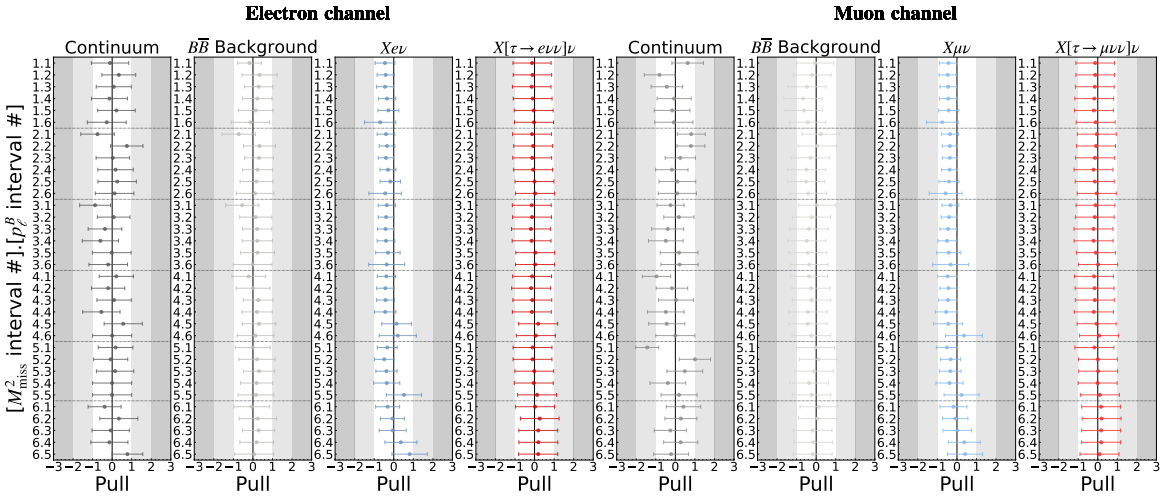

Figure 8.10: The pulls on the nuisance parameters for the electron and muon-channel templates are shown after the signal-extraction fit. The nuisance parameters, each corresponding to a specific interval in $M^2_{\rm miss}$ and p^B_ℓ, are numbered with the first digit indicating the $M^2_{\rm miss}$ interval and the second digit indicating the p^B_ℓ interval.

The global χ^2 can be calculated analogously to Equation (6.4) as

$$\begin{aligned}\chi^2_{\rm global} &= \chi^2_{\text{Data vs. MC}} + \chi^2_{\text{NP pulls}} + \chi^2_{\rm constraints}\\ &= \quad 17.56 \quad + \quad 25.40 \quad + \quad 0.02 \quad = 42.98,\end{aligned} \tag{8.11}$$

resulting in a p value of

$$p \text{ value}\left(\chi^2_{\rm global} = 42.98, \text{dof.} = N_{\rm bins} - N^{\rm fitted}_{\rm yields} = 62\right) = 0.969. \tag{8.12}$$

The unusually high p value might be attributed to the reweighting procedure in the high-p^B_ℓ control sample. The effective reduction of degrees of freedom caused by this procedure is not considered in the presented calculation. Nevertheless, no indications of unusual nuisance-parameter pulls are observed, and the fit does not significantly alter the continuum-template yields.

8.2.2 Result stability and crosschecks

Extraction of $R(X_{\tau/\ell})$ in various subsets

In addition to the validation of uncertainties before box opening (see Secs. 8.1.3 and 8.1.4), the stability of the result is assessed by extracting it in various subsets of the data, that might be sensitive to hypothetical, unacknowledged systematic uncertainties.

For this purpose, the data sample is divided based on the reconstructed $B_{\rm tag}$-candidate charge to probe their different background compositions. In the reweighting procedure, distinct weights are

derived for events with neutral and charged B_{tag} mesons, providing an additional rationale for such a division (see Sec. 7.3.2). Additionally, two subsets based on the signal-lepton charge are investigated, considering the noticeable charge-dependence of the lepton-identification efficiency, especially for electrons. Furthermore, LID-correction factors are charge-dependent, and fake rates, as well as fake compositions, slightly differ. For instance, (anti)proton fakes are almost exclusively identified as negatively charged electron candidates (see Tab. 5.1). The lepton identification also varies with the data production period, as discussed in Section 6.2.4, justifying the same production-period-based subsets as outlined in Table 6.12. Finally, a split based on the event number is implemented, which should only induce statistical fluctuations, and two approximately equal-sized subsets are defined based on the signal-lepton angle $\theta_\ell = 74.5°$.

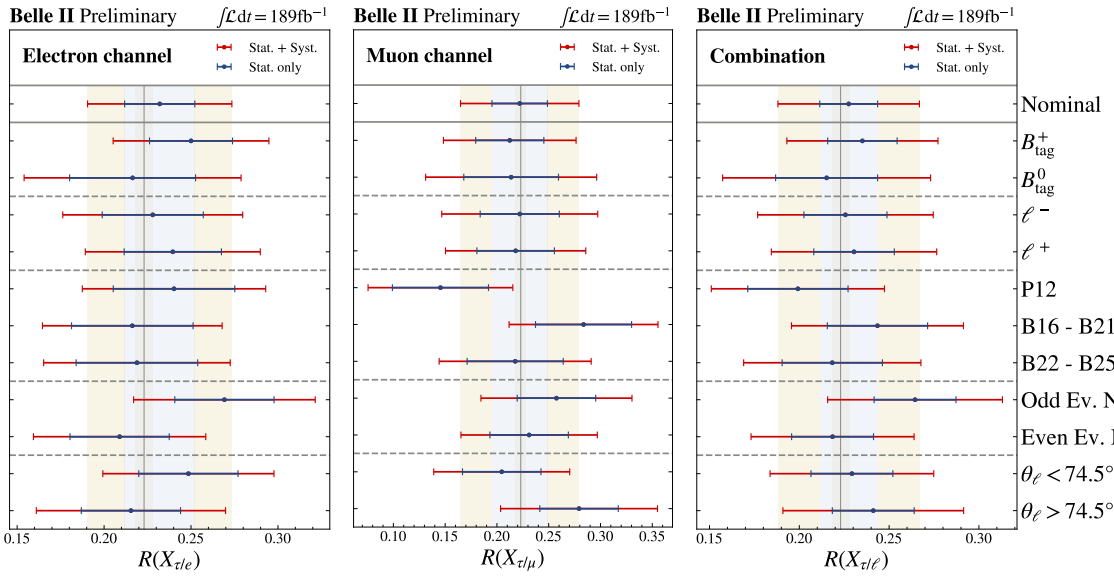

Figure 8.11: The extracted $R(X_{\tau/\ell})$ values for each lepton flavor and their combination are presented when the data sample is split into two or three subsets based on B_{tag} charge, signal-lepton charge, data-production period, event number, and signal-lepton angle θ_ℓ. The subset results are expected to fluctuate within statistical precision, as illustrated by the blue band. Full systematic uncertainties are depicted in gold, and the SM expectation, derived from References [126, 128, 129], is illustrated in gray.

In Figure 8.11, the results for $R(X_{\tau/e})$, $R(X_{\tau/\mu})$, and their combination $R(X_{\tau/\ell})$ are presented. In the B_{tag}-charge dependent signal extraction, both values of the muon-channel result $R(X_{\tau/\mu})$ are determined to be below the nominal value of the full dataset. Meanwhile, both the electron value $R(X_{\tau/e})$ and the combination $R(X_{\tau/\ell})$ fluctuate around their nominal values. This arises from the simultaneous extraction in both lepton flavors, where their shared systematic uncertainties are accounted for. Hence, the individual measurements are not fully independent of each other. Similarly, the combined results exceed their nominal value in both subsets of θ_ℓ due to the non-trivial correlation between the individual lepton-flavor measurements. Nevertheless, overall, the magnitude of the fluctuations aligns with expectations, assuming that they are predominantly caused by limited statistics. Consequently, the stability of the $R(X_{\tau/\ell})$ results is demonstrated.

Measurement of $\mathcal{R}(X_{e/\mu}^{\tau\to})$

A powerful crosscheck is the measurement of the ratio of signal decays by lepton flavor, $\mathcal{R}(X_{e/\mu}^{\tau\to}) = \mathcal{B}(X[\tau \to e\nu\nu]\nu)/\mathcal{B}(X[\tau \to \mu\nu\nu]\nu)$. The extracted value is

$$\mathcal{R}(X_{e/\mu}^{\tau\to}) = 1.05 \pm 0.15\ (\text{stat.}) \pm 0.20\ (\text{syst.}). \tag{8.13}$$

This measurement, along with its extractions in subsets of the full data set as presented in Figure 8.12, was performed prior to the extraction of $R(X_{\tau/\ell})$ as part of the box-opening procedure. The measured $\mathcal{R}(X_{e/\mu}^{\tau\to})$ values align well with unity, reflecting the agreement of the $R(X_{\tau/\ell})$ results for both lepton flavors.

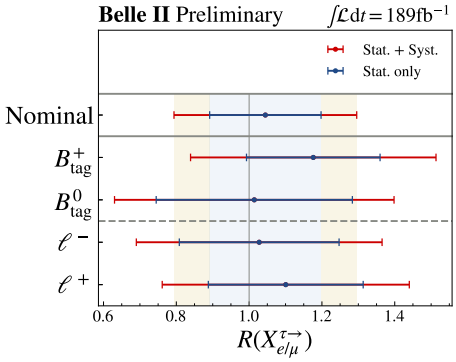

Figure 8.12: The extracted $\mathcal{R}(X_{e/\mu}^{\tau\to})$ values are presented for the full dataset and for subsets based on B_{tag}-candidate and signal-lepton charge. More information is provided in the caption of Figure 8.11.

Measurement of $R(X_{e/\mu})$

Additionally, the ratio of normalization modes $R(X_{e/\mu}) = \mathcal{B}(B \to Xe\nu)/\mathcal{B}(B \to X\mu\nu)$ can be extracted in the same signal-extraction fit and is found to be

$$R(X_{e/\mu})_{\text{Preliminary}} = 0.998 \pm 0.014. \tag{8.14}$$

This value is consistent within uncertainties with the published result for $p_\ell^B > 1.3\,\text{GeV}$, $R(X_{e/\mu}) = 1.007 \pm 0.021$, as presented in Chapter 6. In comparison to the previous result, a larger phase space is explored due to reduced lepton-momentum thresholds of $p_e > 0.5\,\text{GeV}$ and $p_\mu > 0.7\,\text{GeV}$. Furthermore, different signal-lepton identification working points and corresponding LID corrections are employed in the $R(X_{\tau/\ell})$ extraction. As the uncertainties of $R(X_{e/\mu})$ are dominated by LID uncertainties, the result and its uncertainty from Equation (8.14) are largely independent of the value presented in Equation (6.3), explaining the slight deviation within uncertainty.

In contrast to the extraction of $R(X_{e/\mu})$ in the high-momentum range $p_\ell^B > 1.3\,\text{GeV}$ in Chapter 6, the result presented in this section exclusively serves as a validation of the $R(X_{\tau/\ell})$ result. It is not subjected to thorough testing and validation; thus, its uncertainties are regarded as a preliminary estimate. Particularly, the assumption of canceling B_{tag} properties between lepton flavors down to low momenta would need careful re-evaluation. Although the findings for the $R(X_{\tau/\ell})$ extraction in Section 5.4.1 suggest the validity of such an assumption, the necessary cross-checks are not performed

within the scope of this thesis. Therefore, the result of Equation (8.14) remains preliminary and unofficial. Consequently, the $R(X_{e/\mu})$ measurement, presented in Equation (6.3) and published in Reference [1], remains the only official measurement. Nevertheless, the agreement between both extractions is reassuring and enhances confidence in the $R(X_{\tau/\ell})$ measurement presented in this chapter.

Updated $B \to D^{**}\ell\nu$ branching fractions

Recently, a new measurement of $B \to D^{**}\ell\nu$ branching fractions in various decay modes was published by the Belle collaboration in Reference [225], that is not incorporated in the averaged values presented in Table 3.1. Interestingly, the latest results indicate remarkably small values for $\mathcal{B}(B \to D_0^*\ell\nu)$, introducing a tension with previous measurements from Belle [226] and *BABAR* [227] at a significance of four standard deviations. Similarly, the new measurement reports values for $\mathcal{B}(B \to D_2^*\ell\nu)$ in the same decay modes where the deficit in D_0^*-meson decays is observed, surpassing previous measurements by more than two standard deviations. Consequently, a comprehensive scientific discussion is imperative to determine how to incorporate these new results into future world averages, as a straightforward combination is insufficient. Nevertheless, the potential impact of hypothetically shifted new $B \to D^{**}\ell\nu$ branching fractions on the extracted $R(X_{\tau/\ell})$ result is investigated.

A newly calculated world average for $\mathcal{B}(B \to D_1\ell\nu)$ aligns well with the value from Table 3.1 within assigned uncertainty. To include potential new world averages for the branching fractions of D_1', D_2^*, and D_0^*, their uncertainties are scaled by factors of 1.5, 2, and 3, respectively. A subsequent extraction of $R(X_{\tau/\ell})$ results in $R(X_{\tau/e}) = 0.233 \pm 0.042$, $R(X_{\tau/\mu}) = 0.224 \pm 0.057$, and $R(X_{\tau/\ell}) = 0.229 \pm 0.040$, causing only a marginal shift in the third significant digit. An exclusion of the significantly deviating D_0^* measurement leads to $R(X_{\tau/\ell})$ values and uncertainties that precisely match those presented in Equations (8.8), (8.9), and (8.10). Consequently, the effects of potential updates in $\mathcal{B}(B \to D^{**}\ell\nu)$ values are deemed negligible.

Impact of $B \to X_c X_c$ decays

Finally, the same-flavor control sample, used to extract correction weights for the $B\bar{B}$ backgrounds, predominantly represents secondary leptons arising from semileptonic D-meson decays that originate from B-meson decays into a single charmed meson. Events with D mesons resulting from $B \to X_c X_c$ decays are inadequately represented. This limitation is acknowledged through uncertainties that encompass the initially simulated shape up to twice the shape correction derived in the same-flavor control sample, as detailed in Section 7.3.4. As outlined in Table 8.3, $R(X_{\tau/e})$ and $R(X_{\tau/\mu})$ are assigned relative uncertainties of 5.8% and 11.5% due to $B\bar{B}$-background shape uncertainties.

Various control samples, including the low-M_{miss}^2, low-q^2, and high-M_X samples illustrated in Figures B.18, B.19, and B.20, suggest an adequate modeling of secondary events up to a precision of approximately 10%. Nevertheless, the potential impact of a significantly altered fraction of $B \to X_c X_c$ decays is examined by modifying their yield in simulation by factors of 0.5, 0.9, 1.1, 1.5, and 2.0 before re-executing the reweighting procedure and the signal extraction. Table 8.9 provides a summary of the extracted $R(X_{\tau/\ell})$ values and their deviations from the nominal value.

The fluctuations observed in the electron channel are tiny despite significant alterations in the $B\bar{B}$-background composition. This is attributed to the overall limited change in the $B\bar{B}$-background template's shape due to similar properties of different secondary-lepton categories. In contrast, the

$B \to X_c X_c$ scaling factor	$R(X_{\tau/e})$ (relative to nominal)	$R(X_{\tau/\mu})$ (relative to nominal)
0.5	0.2319 (±0.0%)	0.2450 (+10%)
0.9	0.2324 (+0.2%)	0.2264 (+2%)
1.0	**0.2319**	**0.2218**
1.1	0.2325 (+0.2%)	0.2180 (−1.8%)
1.5	0.2314 (−0.2%)	0.2033 (−8.5%)
2.0	0.2287 (−1.4%)	0.1862 (−16%)

Table 8.9: The extracted values of $R(X_{\tau/\ell})$ in the electron and muon channels are presented, considering a substantial modification of the fraction of $B \to X_c X_c$ decays in simulation by scaling their pre-reweighting yield.

muon channel features substantial contributions from fakes in the $B\bar{B}$ background, which significantly deviate in shape from $B \to X_c X_c$ decays. Consequently, discernible deviations in $R(X_{\tau/\mu})$ are observed, surpassing the assigned uncertainty of 11.5% in the extreme scenario of doubling the contribution from $B \to X_c X_c$. Such a scenario, however, can be excluded based on observations in the low-M^2_{miss}, low-q^2, and high-M_X control samples. Additionally, uncertainties are assigned according to the input prediction of $B \to X_c X_c$ decays in simulation. When doubling their initial contribution, the predicted impact of $B\bar{B}$-background shape uncertainties on $R(X_{\tau/\mu})$ increases to 13.7%, so that the observed deviation only corresponds to a deviation of 1.15 σ from the nominal value. Therefore, the fluctuations in the muon channel are considered adequately covered by assigned uncertainties, affirming the robustness of the reweighting procedure against reasonable and extreme deviations from simulated $B\bar{B}$-background compositions.

8.2.3 Implications of $R(X_{\tau/\ell})$ on the $b \to c\tau\nu$ anomaly

In Figure 8.13, the extracted $R(X_{\tau/\ell})$ values are illustrated and compared with the LEP measurements of the inclusive b-hadron admixture $\mathcal{B}(\text{b-admix} \to X\tau\nu)$, Belle's unofficial $R(X_{\tau/\ell})$ result and the exclusive $R(D^{(*)})$ measurements. The B-meson-specific measurements, are additionally normalized to their existing SM prediction, highlighting a potential enhancement of the $b \to c\tau\nu$ decay. Their comparison is presented within the same figure.

Both, a possible enhancement of (12 ± 5)% suggested by the world average of $R(D^*)$ and a (20 ± 10)% enhancement suggested by $R(D)$ is covered by the observed uncertainty on $R(X_{\tau/\ell})$, corresponding to a value higher than its SM prediction of (2 ± 18)%.

Noticeably, an extraction of $R(X_{\tau/\ell})$ without the simulation reweighting (see Sec. 7.3) would result in a significantly higher value of $R(X_{\tau/\ell})$, potentially providing an explanation for the findings in Reference [136]. This reweighting corrects inaccuracies in modeling the D-meson decay distribution. Particularly, inclusive D-meson decays into K^0_L mesons, that share several characteristics with the signal decay such as substantial values of M^2_{miss}, are underestimated in the simulation. It is plausible that such decays may have already been inaccurately modeled in the simulations used by Belle and *BABAR*. While inclusive analyses are maximally sensitive to this mismodeling, accurately estimating its impact on exclusive measurements of $R(D^{(*)})$ poses a considerable challenge.

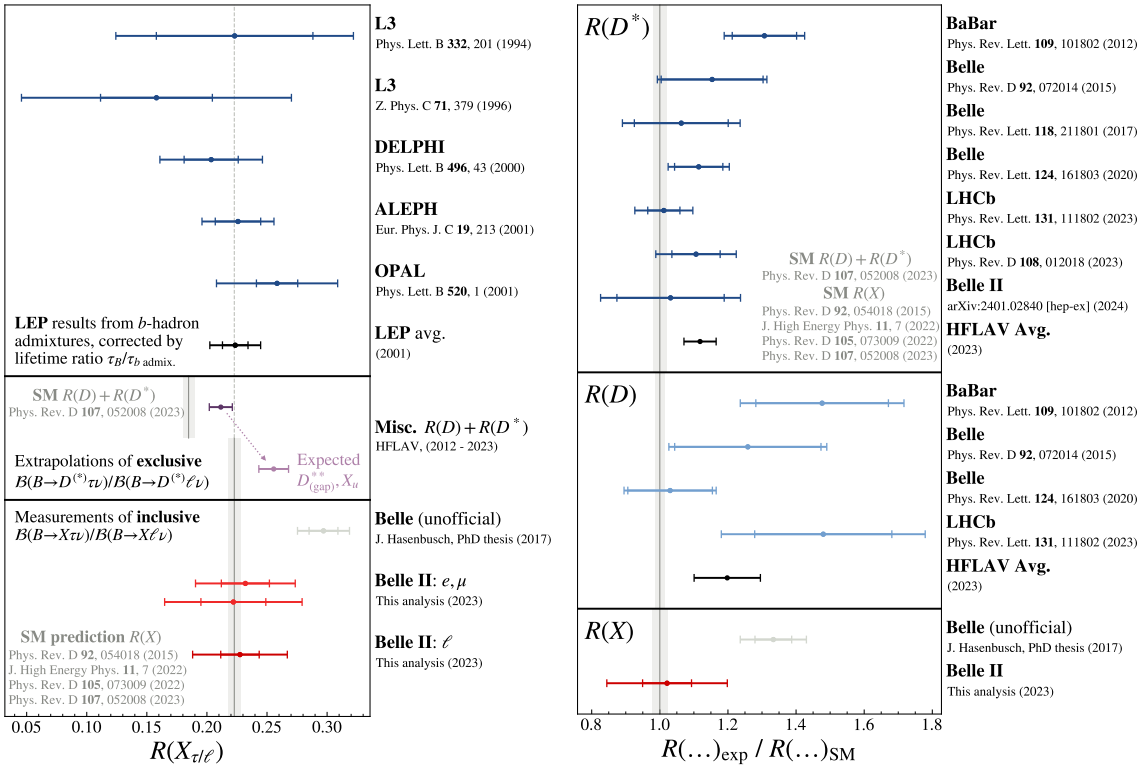

Figure 8.13: In the left plot, the $R(X_{\tau/\ell})$ measurement is depicted for each lepton flavor (light red) and their combination (dark red). It is compared with individual lifetime-corrected LEP results of $\mathcal{B}(\text{b-admix} \to X\tau\nu)$ (blue, [131–135]) and their combined result (in black), normalized by $\mathcal{B}(B \to X\ell\nu) = (10.84 \pm 0.16)\%$ [130]. The sum of suggested $\mathcal{B}(B \to D^{(*)}\tau\nu)$ based on the exclusive $R(D^{(*)})$ findings (dark purple, [113–121, 123]), normalized by $\mathcal{B}(B \to X\ell\nu)$, along with its extrapolation to account for remaining components of the full $B \to X\tau\nu$ branching fraction (light purple), is also presented. Additionally, the unofficial $R(X_{\tau/\ell})$ measurement published only in a PhD thesis is included (light gray, [136]). The SM prediction, if available, is illustrated in gray [126, 128–130].
In the right plot, individual B-meson-based measurements of $R(D^*)$ and $R(D)$ (blue and light blue), along with their average values from Reference [123] (black), are depicted relative to their SM prediction (gray). They are also compared to the corresponding SM-normalized, lepton-flavor combined measurement of $R(X_{\tau/\ell})$ (dark red).

The exclusive measurements, with their reconstruction of certain hadronic decay modes, feature high sensitivities to specific particle multiplicities. Consequently, it is equally plausible that the events underestimated in simulation have negligible impact on $R(D^{(*)})$ or that they result in a small background excess in the signal region, which is hardly observable in signal-depleted control samples. A phase-space dependent calibration of background components originating from misreconstructed charmed hadrons, similar to the approach used in Reference [119], should mitigate effects of the inaccurate modeling. Additionally, it is advisable in future exclusive measurements to quantify potential effects arising from processes like $B \to D^{(*)}[X_c \to [D \to h_\ell K^0_L \ldots] \ldots]$, that may be selected due to hadrons, denoted h_ℓ, mimicking the signal-lepton candidate. However, the impact of $D \to K^0_L X$ decays is expected to vary significantly between the experimental environments of

LHCb and the B factories, rendering their mismodeling as the exclusive explanation for the observed $b \to c\tau\nu$ anomaly unlikely.

The constraints of the measured $R(X_{\tau/\ell})$ value on the $R(D^{(*)})$ anomaly are complex. Using $\mathcal{B}(B \to X\ell\nu) = (10.84 \pm 0.16)\%$ [130], the measured $R(X_{\tau/\ell})_{\text{exp}}$ from Equation (8.10) can be translated into $\mathcal{B}(B \to X\tau\nu)$:

$$\mathcal{B}(B \to X\tau\nu) = (2.47 \pm 0.43)\%. \tag{8.15}$$

This imposes an upper limit on the sum of measured $R(D)$ and $R(D^*)$ values:

$$\begin{aligned} R(X_{\tau/\ell})_{\text{exp}} \cdot \mathcal{B}(B \to X\ell\nu) = & \\ \mathcal{B}(B \to X\tau\nu) &\geq \mathcal{B}(B \to D\tau\nu) + \mathcal{B}(B \to D^*\tau\nu) \\ &= R(D)_{\text{exp}} \cdot \mathcal{B}(B \to D\ell\nu) + R(D^*)_{\text{exp}} \cdot \mathcal{B}(B \to D^*\ell\nu). \end{aligned} \tag{8.16}$$

The difference between $\mathcal{B}(B \to X\tau\nu)$ and the sum of $\mathcal{B}(B \to D\tau\nu)$ and $\mathcal{B}(B \to D^*\tau\nu)$ can be attributed to additional semitauonic contributions arising from D^{**}, D^{**}_{gap}, and X_u:

$$\mathcal{B}(B \to X\tau\nu) = \mathcal{B}(B \to D\tau\nu) + \mathcal{B}(B \to D^*\tau\nu) + \mathcal{B}(B \to D^{**}_{(\text{gap})}, X_u\tau\nu). \tag{8.17}$$

Their combined size can be computed within the SM utilizing the light-lepton branching fractions $\mathcal{B}(B \to D\ell\nu)$, $\mathcal{B}(B \to D^*\ell\nu)$, and $\mathcal{B}(B \to X\ell\nu)$. Using the arithmetic mean of the different B-meson lifetimes along with the values of the B^+ and B^0 measurements summarized in Reference [130], the isospin-averaged exclusive branching fractions are

$$\mathcal{B}(B \to D\ell\nu) = (2.27 \pm 0.06)\% \quad \text{and} \tag{8.18}$$

$$\mathcal{B}(B \to D^*\ell\nu) = (5.23 \pm 0.10)\%. \tag{8.19}$$

This results in an expected branching fraction for additional semitauonic contributions of

$$\begin{aligned} \mathcal{B}(B \to D^{**}_{(\text{gap})}, X_u\tau\nu)_{\text{SM}} = & \\ R(X_{\tau/\ell})_{\text{SM}} \cdot \mathcal{B}(B \to X\ell\nu) - R(D)_{\text{SM}} \cdot \mathcal{B}(B \to D\ell\nu) - R(D^*)_{\text{SM}} \cdot \mathcal{B}(B \to D^*\ell\nu) & \\ = (0.41 \pm 0.08)\%. & \end{aligned} \tag{8.20}$$

Comparing with Equation 2.32, this corresponds to $(17.1 \pm 2.8)\%$ of the total semitauonic branching fraction. The reduced ratio $R(X_{\tau/\ell})^{\dagger}$ can be defined, assuming that all unmeasured semitauonic contributions align with their SM prediction:

$$\begin{aligned} R(X_{\tau/\ell})^{\dagger} &\equiv \frac{\mathcal{B}(B \to X\tau\nu) - \mathcal{B}(B \to D^{**}_{(\text{gap})}, X_u\tau\nu)_{\text{SM}}}{\mathcal{B}(B \to X\ell\nu)} \\ &= R(X_{\tau/\ell})_{\text{exp}} - \frac{\mathcal{B}(B \to D^{**}_{(\text{gap})}, X_u\tau\nu)_{\text{SM}}}{\mathcal{B}(B \to X\ell\nu)}. \end{aligned} \tag{8.21}$$

This allows to visualize the constraining power of $R(X_{\tau/\ell})_{\text{exp}}$ on the iconic $R(D) - R(D^*)$ plane (see Fig. 2.7). For this purpose, Equation (8.17) is rewritten analogously to Equation (8.16), Equation (8.21)

is inserted and the experimental values $R(D)_{\text{exp}}$ and $R(D^*)_{\text{exp}}$ are replaced by running quantities $x_{R(D)}$ and $y_{R(D^*)}$. This results in

$$R(X_{\tau/\ell})^{\dagger} \cdot \mathcal{B}(B \to X\tau\nu) = x_{R(D)} \cdot \mathcal{B}(B \to D\ell\nu) + y_{R(D^*)} \cdot \mathcal{B}(B \to D^*\ell\nu). \tag{8.22}$$

Solving this Equation for $y_{R(D^*)}$ transforms the measured value $R(X_{\tau/\ell})_{\text{exp}}$ into a straight line on the plane, as illustrated in Figure 8.14.

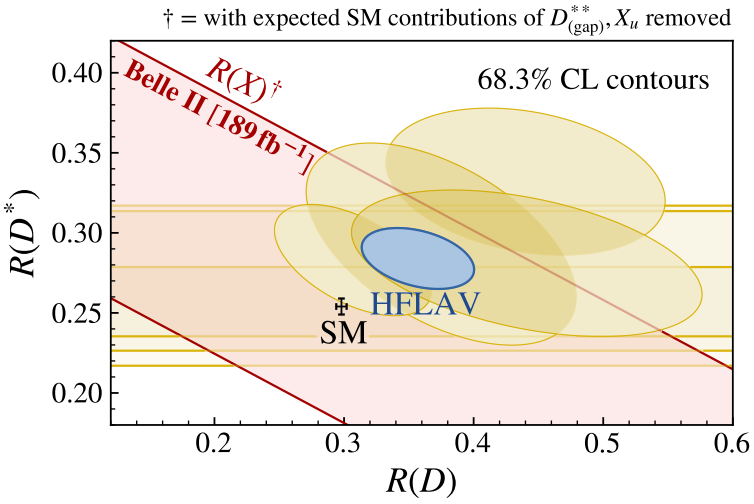

Figure 8.14: Constraints from the measured ratio $R(X_{\tau/\ell})$ (red) on $R(D^{(*)})$ are illustrated and compared to the individual $R(D^{(*)})$ measurements (gold [113–121]), their world average (blue [123]) and the SM expectation (black [123]).

The uniqueness of the red $R(X_{\tau/\ell})^{\dagger}$ band emphasizes the complementarity and novelty of this measurement compared to the exclusive probes of $R(D)$ and $R(D^*)$. However, constraining $R(X_{\tau/\ell})_{\text{exp}}$ on the plane results in significantly larger uncertainties of approximately 30% around expected values of $R(D)$, compared to an extracted precision of 17.3% (see Eq. (8.10)). Nevertheless, the world average of $R(D)$ and $R(D^*)$ values, illustrated by the blue ellipsoid in Figure 8.14, is visibly covered by the uncertainties of $R(X_{\tau/\ell})^{\dagger}$.

Finally, the correlation between the presented value of $R(X_{\tau/\ell})$ and the exclusive measurements of $R(D^{(*)})$ is quantified. Among all exclusive measurements, Belle II's recent result of $R(D^*)$ from Reference [119], which uses the same hadronic tagging approach and data sample, features the strongest correlations with this measurement. Due to the distinct experimental strategies in the exclusive and inclusive analysis approaches, however, the statistical overlap of the signal and normalization events in both measurements is only $\approx 0.4\%$. The estimated statistical-correlation coefficient using Equation (8.6)) is $\rho^{\text{stat.}}_{X,D^*} = 0.02$.

Lepton-identification uncertainties are postulated to be entirely correlated between $R(X_{\tau/\ell})$ and $R(D^*)$. Form-factor-induced uncertainties have minimal effects on $R(D^*)$, meaning that even an implausibly high correlation coefficient of $\rho^{\text{FF}}_{X,D^*} = 1$ hardly affects the overall correlation. In both measurements, the gap-mode branching fractions impose significant uncertainties on the

results, although the impact of modified gap-mode contributions varies substantially. While these events constitute normalization decays for $R(X_{\tau/\ell})$, they serve as background events for $R(D^*)$ and feature distinct properties in the signal-extraction quantities compared to the exclusive normalization mode $B \to D^* \ell \nu$. Therefore, the overall correlation coefficient associated with branching-fraction uncertainties is postulated to be (substantially) less than $\rho^{\mathcal{B}}_{X,D^*} = 0.7$. All remaining systematic uncertainties are unique to one of the two measurements and do not introduce additional correlation.

Based on this reasoning, the total correlation between $R(X_{\tau/\ell})$ and $R(D^*)$ from Reference [119] is calculated to be within $\rho^{\text{total}}_{X,D^*} = 0.04$ for $\rho^{\mathcal{B}}_{X,D^*} = 0$ and $\rho^{\text{total}}_{X,D^*} = 0.1$ for $\rho^{\mathcal{B}}_{X,D^*} = 0.7$, rendering the inclusive measurement of $R(X_{\tau/\ell})$ a largely independent probe of the $b \to c\tau\nu$ anomaly.

CHAPTER 9

Conclusion and outlook

Conclusion

In this thesis, two precision tests of lepton universality are performed.

The **light-lepton branching-fraction ratio** of inclusive semileptonic B-meson decays $\boldsymbol{R(X_{e/\mu})} = \mathcal{B}(B \to Xe\nu)/\mathcal{B}(B \to X\mu\nu)$ is measured for the first time:

$$R(X_{e/\mu}) = 1.007 \pm 0.009\ (\text{stat.}) \pm 0.019\ (\text{syst.}).$$

This result, extracted from events with signal-lepton momenta larger than 1.3 GeV, is in agreement with the SM expectation of $R(X_{e/\mu})_{\text{SM}} = 1.006 \pm 0.001$ [126]. To date, it is the most precise test of lepton universality in semileptonic B-meson decays based on branching fractions, establishing this quantity as an excellent probe of the Standard Model. The high precision is achieved by fitting both lepton flavors simultaneously while incorporating the systematic effects and their correlations in a set of nuisance parameters, resulting in a significant cancellation of correlated systematic uncertainties.

Perhaps the most impactful accomplishment of this thesis is the development of techniques to enable the first successful measurement of the inclusive **tau-to-light-lepton branching-fraction ratio** $\boldsymbol{R(X_{\tau/\ell})} = \mathcal{B}(B \to X\tau\nu)/\mathcal{B}(B \to X\ell\nu)$. The key finding that unlocks the presented measurement is that discrepancies between experimental data and simulation can be attributed to inaccuracies in modeling the D-meson decay distribution. A data-driven simulation-reweighting technique is developed to address this issue, effectively correcting the discrepancy and quantifying the remaining uncertainty on $R(X_{\tau/\ell})$. This correction it essential for the success of the $R(X_{\tau/\ell})$ measurement.

The extracted values for electrons and muons are $R(X_{\tau/e}) = 0.232 \pm 0.020\ (\text{stat.}) \pm 0.037\ (\text{syst.})$, and $R(X_{\tau/\mu}) = 0.222 \pm 0.027\ (\text{stat.}) \pm 0.050\ (\text{syst.})$, respectively. The lepton-flavor combined value

$$R(X_{\tau/\ell}) = 0.228 \pm 0.016\ (\text{stat.}) \pm 0.036\ (\text{syst.})$$

is consistent with its SM expectation of $R(X_{\tau/\ell})_{\text{SM}} = 0.223 \pm 0.005$ [126, 128, 129] but also with a potentially enhanced semitauonic branching fraction, as indicated by the exclusive $R(D^{(*)})$ measurements [113–121, 123] (see Figs. 8.13 and 8.14).

In the following, the projected progress and potential advancements for both measurements are

discussed.

Outlook for the light-lepton ratio $R(X_{e/\mu})$

The precision of the measured value of $R(X_{e/\mu})$ is expected to be significantly improvable in near future for several reasons.

First and foremost, uncertainties associated with lepton-identification efficiencies, currently an order of magnitude larger than other systematic uncertainties, have already been halved since the initial measurement.[1] Further improvements on this source of uncertainty, as well as on the statistical uncertainty, are expected with increasing experimental sample sizes. Secondly, an updated analysis design is likely to amplify the measurement's sensitivity and to enable the measurement of $R(X_{e/\mu})$ with a more comprehensive data sample of $B \to X\ell\nu$ decays, including those with lower signal-lepton momenta.

The current analysis is primarily tailored for optimizing the measurement of $R(X_{\tau/\ell})$ rather than $R(X_{e/\mu})$. A dedicated re-evaluation of the signal-lepton selection is advisable. Specifically, the choice of the identification-classifier working point, along with its associated lepton-identification correction uncertainties, significantly influences the attainable precision. Alternatively, an appealing approach is the simultaneous extraction of both $R(X_{\tau/\ell})$ and $R(X_{e/\mu})$ in the same fit, as presented in Equation 8.14. This strategy allows for a substantial decorrelation of $B \to X\ell\nu$ decays from background events. The primary challenge of such a measurement, however, will be the careful investigation of potential effects arising from mismodeling in the X system and the precise quantification of B_{tag}-related effects, currently indistinguishable from statistical fluctuations, at a precision level of $O(0.1\%)$ for low-momentum signal leptons.

Outlook for the tau-to-light-lepton ratio $R(X_{\tau/\ell})$

Future measurements of $R(X_{\tau/\ell})$, facilitated by the developed reweighting technique in this thesis, are anticipated to substantially enhance their precision.

They will provide essential contributions toward understanding the current $b \to c\tau\nu$ anomaly. Compared to the measurements of the exclusive ratios $R(D^{(*)})$, the distinct sensitivity of $R(X_{\tau/\ell})$ to both statistical and systematic uncertainties positions future measurements as invaluable complementary probes of tau-to-light-lepton universality.

Beyond the anticipated increase in statistical precision, substantial improvements in systematic precision are likely. Several of the leading systematic uncertainties should decrease with larger experimental samples analogously to statistical uncertainties. Refinements in the analysis strategy and updated measurements of external parameters may reduce the systematic uncertainties further.

In the following, strategies to reduce the most significant sources of systematic uncertainty are discussed briefly. Finally, an overview of the expected precision in future measurements of $R(X_{\tau/\ell})$ is provided with respect to the size of the experimental data sample.

[1] The LID-correction uncertainties used in the measurement were dominated by discrepancies among different LID-calibration channels. The Belle II Particle Identification Group has successfully addressed and resolved this challenge subsequently (see Sec. 5.3.5).

Simulation reweighting

The introduced reweighting technique (see Sec. 7.3) quantifies the uncertainties associated with the distributions of $B \to X_c l\nu$ decays and $B\bar{B}$ backgrounds in observables correlated with the signal-extraction variables p_ℓ^B and M^2_{miss}. They are driven by the experimental control-sample sizes and should decrease accordingly.

Furthermore, enhanced statistical precision may open avenues for alternative reweighting techniques, grounded in a deeper understanding of modeling inaccuracies. Presently, correction weights for adjacent M_X intervals are treated independently, representing the most conservative uncertainty assumption. A more holistic approach, such as signal extraction and simulation correction within a simultaneous fit, could be explored. For instance, a strategy based on a $D \to K^0_L X$-enriched $B \to X\ell\nu$ template, as studied in Reference [224] within the context of a Bachelor thesis, could correlate neighboring M_X intervals. This correlation would result in a notable reduction of degrees of freedom in the distribution shapes of $B \to X\ell\nu$ and $B\bar{B}$-background events in the signal-extraction fit.

Nonetheless, adopting such a method is justified only if the remaining modeling inaccuracies are unambiguously attributed to effects that can be accurately represented in fit templates or motivate the use of a specific M_X-based correction function. It is equally plausible that enhanced statistical precision reveals more intricate modeling inaccuracies, necessitating a re-evaluation with more complex correction intervals. Validation methods developed in this thesis, such as the introduced modification of D-meson decay distributions in Section 8.1.3, provide essential tests to assess the adequacy of future reweighting methods.

Ultimately, updated measurements of inclusive D-meson branching fractions by the BESIII [228] and Belle II experiments may pave the way for the development of simulations that require fewer data-driven reweighting adjustments. Particularly the first measurement of $\mathcal{B}(D \to K^0_L X)$ is appealing. In the high-precision era of flavor physics, a collaborative effort towards a thorough re-examination of the entire spectrum of D-meson decays, which serves as a background to any B-meson related measurement, is desirable for the coming decades.

Branching fractions

The impact of $B \to Xl\nu$ branching-fraction uncertainties on $R(X_{\tau/\ell})$ is predominantly driven by the 100% uncertainty assigned to the gap-mode branching fractions. In the fit, this uncertainty is constrained by the statistical precision of experimental data and, consequently, should decrease with larger samples.

Currently, the gap between $\mathcal{B}(B \to X\ell\nu)$ and the sum of exclusive branching fractions relies on a single measurement of $\mathcal{B}(B \to Xe\nu)$ using 140 fb^{-1} of Belle data [229]. This thesis (see Figs. 6.6 and 8.10), along with other semitauonic analyses in Belle II [119, 218], provides evidence suggesting that the gap modes are less abundant than currently assumed. A new measurement of $\mathcal{B}(B \to X\ell\nu)$, potentially including the so-far unmeasured muon channel, will be very interesting and may lead to a substantial reduction in uncertainties associated with gap-mode contributions.

Form factors

The observed high uncertainty associated with form factors is expected to reduce significantly once the existing discrepancies in $B \to D^*\ell\nu$ decays, stemming from the BGL-based parameter extraction in Reference [205] and the BLPRXP-based parameters from Reference [85], are thoroughly understood.

Additionally, employing an optimized binning strategy in the signal-extraction fit could result in considerably tighter constraints from experimental data on associated nuisance parameters compared to the current approach.

For instance, introducing a separation of 3×6 additional signal-depleted intervals in $M_X \times p_\ell^B$, satisfying $M_X > 3\,\text{GeV}$ or $q^2 < 3.5\,\text{GeV}^2$, in the signal-extraction fit effectively disentangles $B\bar{B}$ backgrounds, normalization events, and gap modes from each other. This refinement leads to a reduction in form-factor-associated uncertainties to approximately 5% and in branching-fraction-associated uncertainties to 6%. However, due to limitations in precision with the current reweighting approach for correcting the q^2 distributions, a conservative approach with coarse signal-extraction intervals is chosen in the presented measurement.

Precision vs. experimental sample size

Presently, the data accumulated by the Belle II experiment at the $\Upsilon(4S)$ resonance corresponds to 363 fb^{-1}, representing the available data set during the first long shutdown (LS1), which is approximately twice the amount used in this analysis (189 fb^{-1}). The Belle II experiment just resumed data collection in early 2024, probably leading to significantly larger experimental data samples in the near future.

In Figure 9.1, the achievable relative precision on $R(X_{\tau/\ell})$ is estimated for increasing experimental sample sizes, assuming that most sources of uncertainty decline with $1/\sqrt{N}$, where N represents the multiplicative factor corresponding to the used integrated luminosity of 189 fb^{-1}. The colored areas illustrate the relative contribution of individual sources of uncertainty to the total uncertainty, postulating their accumulation in quadrature.

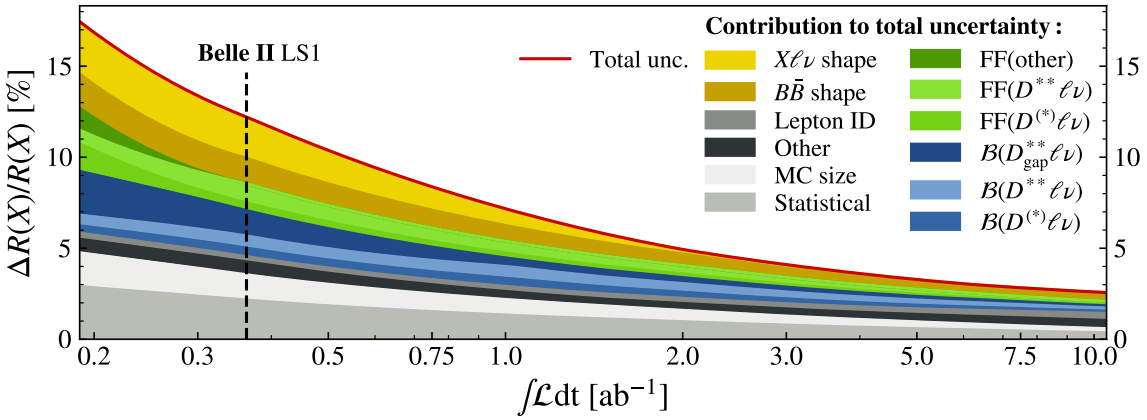

Figure 9.1: The expected precision on $R(X_{\tau/\ell})$ is projected for increasing experimental sample sizes. The total uncertainty (red line) is composed of several individual sources of uncertainty. The contribution of each uncertainty to the total is presented by the colored areas. Since they add up in quadrature, the specific size of each individual uncertainty is not directly reflected on the y-axis. The size of the current data set collected by Belle II is indicated by a black dashed line. The underlying assumptions upon which this figure is based are outlined in the text.

It is assumed that uncertainties caused by differences in $B \to D^{(*)}\ell\nu$ form-factor parameterizations

can already be addressed with the current LS1 Belle II dataset. The relative contribution of uncertainties associated with gap-mode branching fractions is expected to decrease to the size of $\mathcal{B}(B \to D^{(*)}\ell\nu)$ uncertainties at 1 ab^{-1} , and $X\ell\nu$ shape uncertainties are supposed to be reducible to half their naively expected size at 2 ab^{-1} due to a deeper understanding of D-meson decay mismodeling or the application of more sophisticated reweighting methods. Uncertainties associated with the $B\bar{B}$-background shape, lepton identification, and other effects are postulated not to be reducible to values smaller than 1% each.

Based on these assumptions, a relative uncertainty of approximately 7% is predicted when the experimental data sample corresponds to an integrated luminosity of 1 ab^{-1} , further reducing to 2.6% at 10 ab^{-1} . In comparison to the expected relative uncertainties on $R(D^{(*)})$, as estimated based on similar assumptions in Reference [157], future measurements of the inclusive ratio $R(X_{\tau/\ell})$ may offer the most sensitive probes of tau-to-light-lepton universality.

Summary

This work presents the first measurements of two key quantities: the inclusive branching-fraction ratios $R(X_{e/\mu})$ and $R(X_{\tau/\ell})$. Both in their analysis design and their sensitivity to statistical and systematic uncertainties, they are largely independent from exclusive measurements. Particularly, they offer world-leading precision ($R(X_{e/\mu})$) and the potential for world-leading precision ($R(X_{\tau/\ell})$) to probe lepton universality in semileptonic B-meson decays.

This work can serve as guidance for future inclusive measurements, opening promising opportunities with increasing experimental sample sizes.

APPENDIX A

Additional studies

A.1 Suppression of bad B_{tag} candidates

As discussed in Chapter 9, the precision of the $R(X_{\tau/\ell})$ measurement is anticipated to substantially improve with larger datasets. A potential strategy to achieve this is the relaxation of the $\mathcal{P}_{\text{FEI}} > 0.1$ requirement (see Sec. 4.1) by one or two orders of magnitude, as done in other analyses [119, 222]. Such a relaxation leads to a three to ninefold increase in the data sample at the expense of a reduced good-B_{tag} purity. However, the $R(X_{\tau/\ell})$ measurement is exceptionally sensitive to modeling inaccuracies. Events with bad B_{tag} candidates comprise a diverse range of decays, making accurate modeling challenging. Consequently, in this analysis, such events are rigorously controlled by applying a stringent $\mathcal{P}_{\text{FEI}}$ requirement.

This section introduces an alternative approach to mitigate the impact of bad B_{tag} candidates, potentially allowing for the adoption of lower $\mathcal{P}_{\text{FEI}}$ requirements while maintaining a high purity of good B_{tag} candidates.

Similar to the approach for suppressing $e^+e^- \to q\overline{q}$ continuum processes, as discussed in Section 4.2, a BDT is trained to separate *good* B_{tag} candidates, with all decay products correctly reconstructed and assigned, from *wrong charge* candidates (see Sec. 4.1). In the latter case, the B_{tag} charge is incorrectly reconstructed, ensuring a pure set of bad B_{tag} candidates. In this context, the training utilizes not only the *inclusive* set of event-shape quantities used for continuum suppression (see Tab. 4.2) but also incorporates the B_{tag}-candidate momentum in both the c. m. and laboratory frames, as well as the beam-constrained mass M_{bc} and the energy difference ΔE. These quantities are transformations of the B_{tag} kinematics in the c. m. frame (see Eq. (4.3)). In Figure A.1, the momentum distribution of B_{tag} candidates is illustrated in different reference frames. In the c. m. frame, the distinct shapes of good (light gray) to bad (black, red) B_{tag}-candidate momenta are significant, making $p^*_{B_{\text{tag}}}$, along with the quantities M_{bc} and ΔE, the most significant features for the BDT.

However, a significant discrepancy in simulated shapes is observed when compared to experimental data, attributable to the inaccurate modeling of c. m. energies (see Fig. 4.4). Consequently, following the approach outlined in Section 4.2, a *selective* BDT is introduced. This selective BDT only utilizes accurately modeled quantities, effectively narrowing down the options to well-modeled event shape quantities as summarized in Table 4.2. As demonstrated in Figure A.2, this restriction renders the additional separation potential of such a selective multivariate classifier negligible, so that it is not used in this thesis.

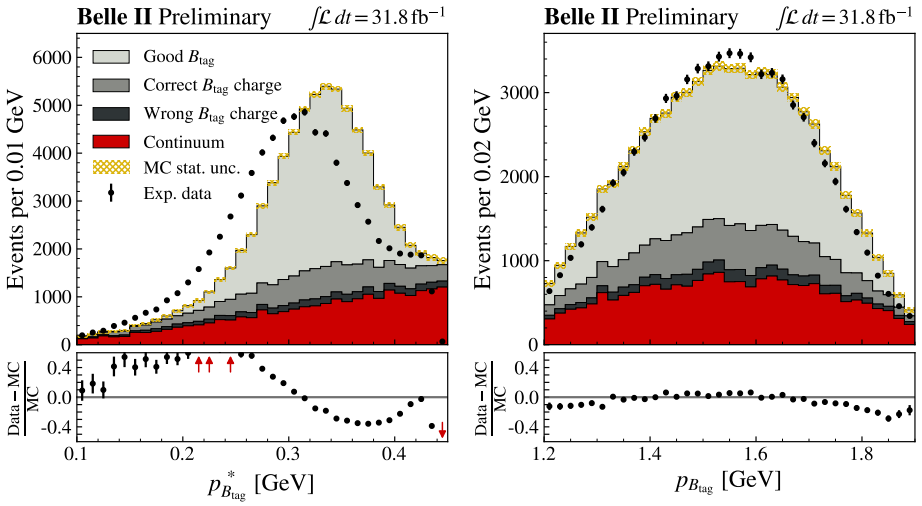

Figure A.1: The distributions of the B_{tag}-candidate momentum are presented in both the c. m. frame (left) and in the laboratory frame (right).

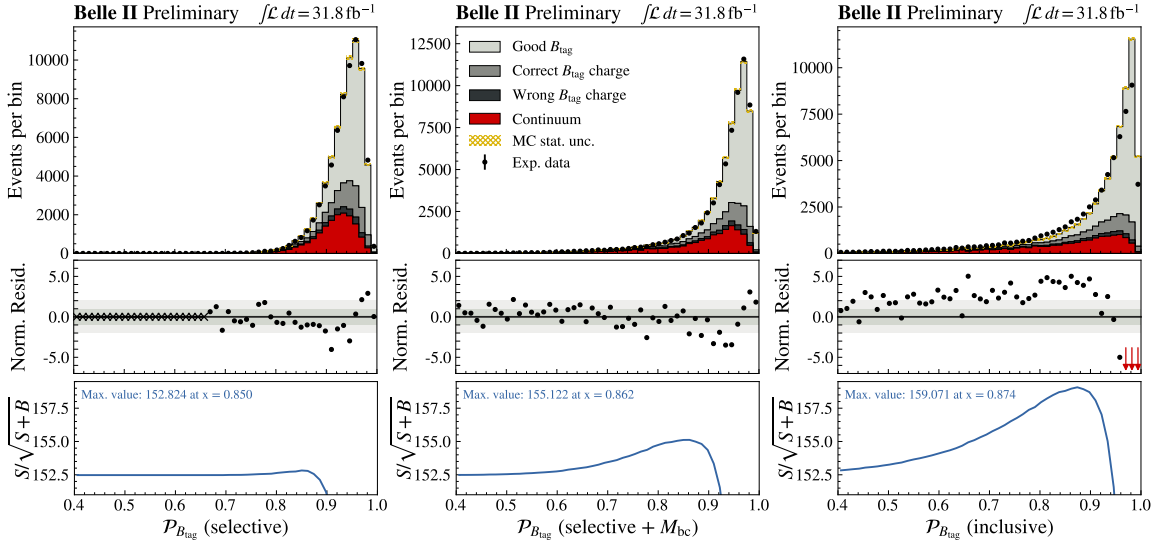

Figure A.2: Experimental data is compared to simulation for various classifiers to suppress bad B_{tag} candidates. In this comparison, the *selective* classifier (left) is confined to only well-modeled quantities, whereas the *inclusive* quantifier (right) illustrates the potential separation achievable when all quantities are utilized. The assessment of their separation potential is conducted through a significance scan, where the classifier threshold is progressively raised along the x-axis. The remaining number of events with good B_{tag} candidates S is then compared to the number of all other events B using $S/\sqrt{S+B}$. The achievable significance of the inclusive classifier surpasses that of the selective classifier, as well as that of a classifier employing only well-modeled quantities and M_{bc} (center).

Nevertheless, the theoretical separation potential presented by the *inclusive* classifier, depicted in the same figure, indicates that reconsidering such an additional strategy for suppressing bad B_{tag}

candidates is promising, once the accurate modeling of c. m. energies in simulation is achieved. Such improvements are expected with the introduction of run-dependent simulations, a current initiative by the Belle II collaboration to replace the previous run-independent ones. Notably, the inclusive classifier's separation potential surpasses the information derived from M_{bc} alone, as evidenced by the comparison between the inclusive classifier and the selective one, where only M_{bc} was additionally included as an input variable.

A.2 Optimization of bremsstrahlung corrections

As outlined in Section 4.3, electrons are susceptible to the radiation of bremsstrahlung photons due to their small mass. To restore the energy lost to the photon, the four-momenta of signal-electron candidates are corrected by incorporating energies from detected photon candidates within a cone centered on the electron's track.

The optimization process for selecting photon candidates is presented in this section. Electron and photon candidates are identified based on the criteria summarized in Table 4.4, with the exception that the criterion on $\Delta R^{\mathrm{track}}_{\mathrm{cluster}}$ is omitted for photon candidates. Accurately selected photons improve the alignment between reconstructed and generated electron momenta. Conversely, falsely selected photons result in a degradation of the electron-momentum resolution. Therefore, the root mean square (RMS) of the differences between reconstructed and generated electron momenta,

$$\mathrm{RMS}(p_e) = \sqrt{\frac{1}{N_{\mathrm{events}}} \sum_{i}^{\mathrm{events}} \left(p^{\mathrm{reco}}_{e,i} - p^{\mathrm{gen}}_{e,i} \right)^2} \tag{A.1}$$

is utilized to quantify the bremsstrahlung-photon selection requirements.

The angle between the photon and electron directions in the laboratory frame depends on the boost of the combined system. Moreover, the impact of the bremsstrahlung correction is significantly influenced by the relative energies of the photon candidate compared to the electron candidate. To account for these dependencies, the electron candidates are categorized into three momentum regions: $p_e < 0.6\,\mathrm{GeV}$, $p_e \in [0.6, 1.0]\,\mathrm{GeV}$, and $p_e > 1.0\,\mathrm{GeV}$. Subsequently, the opening angles of the cone around the electron direction and the upper energy thresholds of photon candidates are successively varied, and the RMS is calculated for each electron-momentum region independently.

In Figure A.3, the two-dimensional distributions of $\mathrm{RMS}(p_e)$ are depicted. The requirements on photon energies, $E^{\mathrm{max}}_{\gamma}$, and cone opening angles are selected that yield minimal values of $\mathrm{RMS}(p_e)$, highlighted in white in the figure. For the different momentum regions, namely $p_e < 0.6\,\mathrm{GeV}$, $p_e \in [0.6, 1.0]\,\mathrm{GeV}$, and $p_e > 1.0\,\mathrm{GeV}$, the energies of photon candidates with $E_{\gamma} < 90\,\mathrm{MeV}$, 0.9 GeV, and 1.2 GeV are added to the electron-candidate momenta if their angle to the track lies in a cone with opening angle of 7.8°, 4.2°, and 3.6°, respectively. In cases where more than one photon candidate is detected in the cone, the one closest to the track is selected. Due to the small number of such events, however, these cases are found to be negligible. The more sophisticated bremsstrahlung-recovery algorithm, as described in Reference [230], is not employed due to revealed ambiguities in some internal parameters during studies of $e^+e^- \to \tau^+\tau^-$ decays by the Belle II Tau Working Group.

This bremsstrahlung-correction procedure results in a notable improvement of 19% in the RMS of electron momenta. If the optimization was conducted without the separation of electrons into three

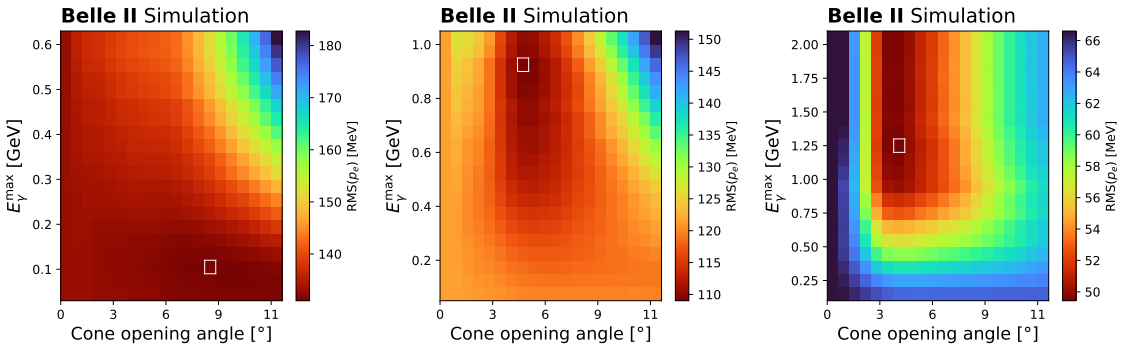

(a) $p_e < 0.6\,\text{GeV}$ (b) $p_e \in [0.6, 1.0]\,\text{GeV}$ (c) $p_e > 1.0\,\text{GeV}$

Figure A.3: The RMS of electron momenta is illustrated for varied upper energy-threshold and cone-opening-angle requirements for bremsstrahlung-photon candidates within three electron-momentum regions. The criteria leading to the lowest RMS(p_e) values, highlighted in white, are selected.

momentum regions, the achievable improvement in RMS would be 11%.

As highlighted in Section 4.3, the measurements of $R(X_{e/\mu})$ and $R(X_{\tau/\ell})$ are not sensitive to bremsstrahlung correction techniques, as long as they do not introduce bias in experimental data compared to simulation. However, the presented approach is solely validated on experimental data with $J/\psi \to e^+e^-$ decays, which primarily test high-momentum electrons. Consequently, this approach is only used in the measurement of $R(X_{e/\mu})$, which is confined to signal-lepton momenta of $p_\ell^B > 1.3\,\text{GeV}$.

Despite the excellent agreement found between data and simulation in all relevant bremsstrahlung properties, a data-MC bias cannot be conclusively ruled out in the low-momentum range. Consequently, for the $R(X_{\tau/\ell})$ measurement, the same bremsstrahlung correction approach employed in the lepton-identification efficiency calibration is utilized (see Sec. 7.1, cone opening angle of 2.9°, and photon energies of $E_\gamma < 1.0\,\text{GeV}$). Considering that low-momentum electrons are expected to benefit the most from the approach presented in this section, a dedicated validation with low-momentum electrons, for example with processes like $e^+e^- \to e^+e^-e^+e^-$, is considered desirable for future investigations.

A.3 Validation of uncertainties on $R(X_{e/\mu})$ with toy data samples

The uncertainties on $R(X_{e/\mu})$ obtained in Section 6.1.2 are validated using ensembles of artificially generated data sets, commonly referred to as toy data. For each source of uncertainty, an ensemble of toy data sets is generated through the bin-by-bin covariance matrix $C_\theta^{\text{indv.}}$, which represents uncertainty-induced variations of the histogram templates. Fits of the nominal data set against toy data are expected to yield variations of a similar magnitude as the predicted uncertainties in fits to Asimov data. In this study, only the template yields are optimized in the fit, meaning that no nuisance parameters are introduced to the likelihood function.

This validation is conducted on data before the removal of the biasing E_{ECL} selection (see Sec. 8.1.5). The removal of this requirement increases the data set by approximately 5%, leading to minor updates in the uncertainty predictions. Additionally, a previous set of LID corrections is used, that is updated in the final measurement of $R(X_{e/\mu})$ in Chapter 6. Table A.1 summarizes the Asimov-data-based

uncertainty predictions in the setup tested in this section.

Uncertainty source	**Relative uncertainty [%]** $R(X_{e/\mu})$
Exp. sample size	0.9
MC sample size	0.3
Lepton ID	1.8
$\mathcal{B}(X\ell\nu)$ total	0.2
FF $X_c\ell\nu$ total	0.1
Total	2.1

Table A.1: Relative statistical and systematic uncertainties on $R(X_{e/\mu})$ predicted in fits to Asimov data (see Sec. 6.1.2) in the outdated setup tested in this section. In comparison to Table 6.3, uncertainties associated with the experimental sample size are slightly enhanced, and LID uncertainties are slightly reduced.

Equation (5.1) can be expressed as an uncorrelated product of the yield ratio $N_{e/\mu} = N_e^{\text{meas}}/N_\mu^{\text{meas}}$ times the efficiency ratio $\epsilon_{\mu/e} = \epsilon_\mu/\epsilon_e$, with trivial error propagation:

$$R(X_{e/\mu}) = N_{e/\mu} \cdot \epsilon_{\mu/e}, \quad \Delta R(X_{e/\mu}) = \sqrt{\left(\Delta N_{e/\mu} \cdot \epsilon_{\mu/e}\right)^2 + \left(N_{e/\mu} \cdot \Delta\epsilon_{\mu/e}\right)^2}. \tag{A.2}$$

In the fitting procedure, the toy ensembles can be used to either vary the input or target data, each having a different impact on $N_{e/\mu}$ and $\epsilon_{\mu/e}$. Figure A.4 visualizes both options for toy ensembles that reflect the LID uncertainty.

Efficiencies are derived from input data, specifically from simulations. As a result, the efficiency ratio $\epsilon_{\mu/e}$ is influenced only when there are variations of the input data. In the case of variations of the target data, the efficiency uncertainty is effectively translated into variations of the template yields. This is because the template yields are determined by scaling the normalized input templates to match the total event yields defined by target data. Similarly, variations in $N_{e/\mu}$ are observed to decrease when the target data is unchanged. Both approaches are interchangeable, resulting in consistent uncertainties on $R(X_{e/\mu})$.

The examination of varied input data reveals a correlation between $N_{e/\mu}$ and $\epsilon_{\mu/e}$, as their individual uncertainties, when added in quadrature, do not align with the observed fluctuation of $R(X_{e/\mu})$. However, as outlined in Section 5.1, the efficiencies, derived from simulation, are assumed to be uncorrelated with the yields, extracted from experimental data. When $N_{e/\mu}$ and $\epsilon_{\mu/e}$ are enforced to be uncorrelated, the uncertainty prediction of 1.8% is restored:

$$\Delta R(X_{e/\mu})_{\text{LID}} = \sqrt{(0.0068 \cdot 0.8276)^2 + (0.0136 \cdot 1.2088)^2} = 0.0174 \approx 0.018. \tag{A.3}$$

This supports the Asimov-data-based uncertainty predictions from the Table A.1, revealing that toy studies can introduce unwanted correlations between yields and efficiencies, leading to a potential underestimation of the overall $R(X_{e/\mu})$ uncertainty. All other sources of uncertainty are tested in a similar manner. Since it is computationally significantly less expensive to probe variations of target data, only these cases are tested. The results for uncertainties attributed to experimental and simulation

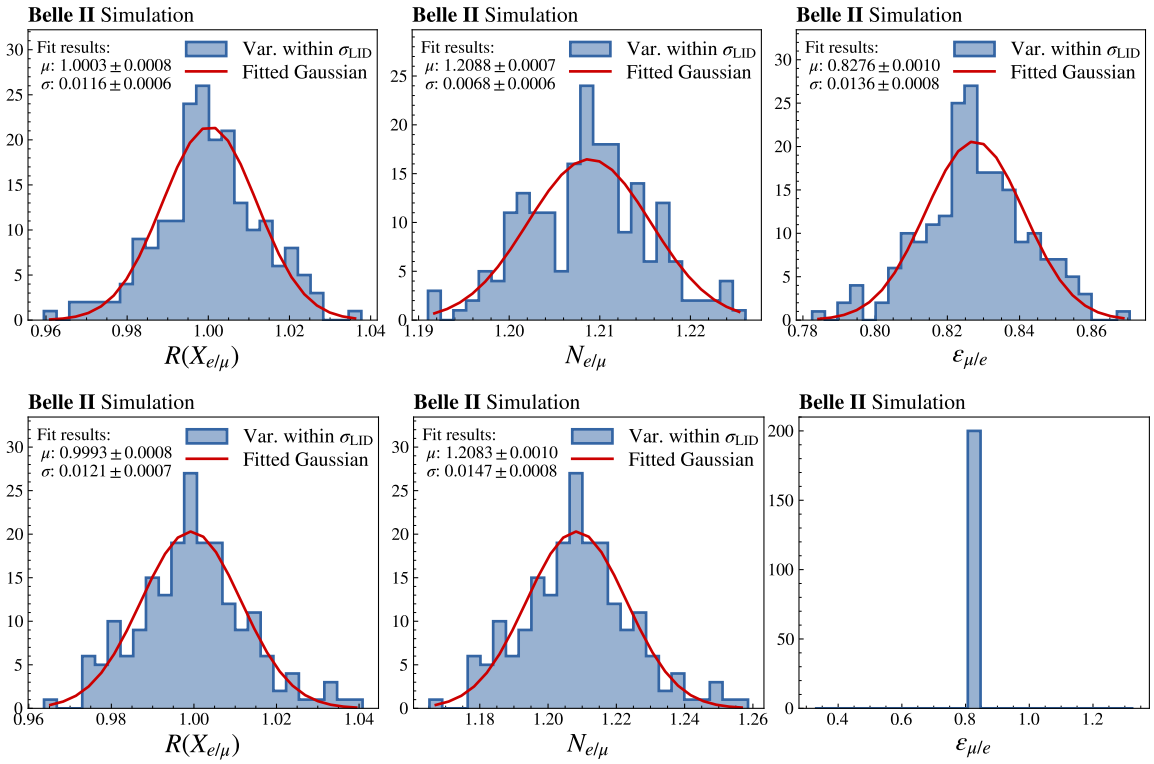

Figure A.4: The extracted values of $R(X_{e/\mu})$, $N_{e/\mu}$, and $\epsilon_{\mu/e}$ from fits using an ensemble of 200 toy data sets that reflect the uncertainty associated with lepton identification are presented in blue. The top row shows the results when toy data replaces the input data of the fit with fixed target data, while in the bottom row, fixed input data but toy target data is used. Gaussian distributions are fitted to each distribution (presented in red), and their mean values (μ) and standard deviations (σ) are provided.

sample sizes are presented in Figure A.5.

The variations in extracted $R(X_{e/\mu})$ caused by changes in experimental data size (0.77%) agree well with the predicted value of 0.86%, as do the values for simulation sample size (0.38% vs. 0.33%). Small underestimations may be attributed to artificially introduced correlations between $N_{e/\mu}$ and $\epsilon_{\mu/e}$. In summary, the uncertainty predictions from Section 6.1.2 are independently validated, and no evidence of deviations is found.

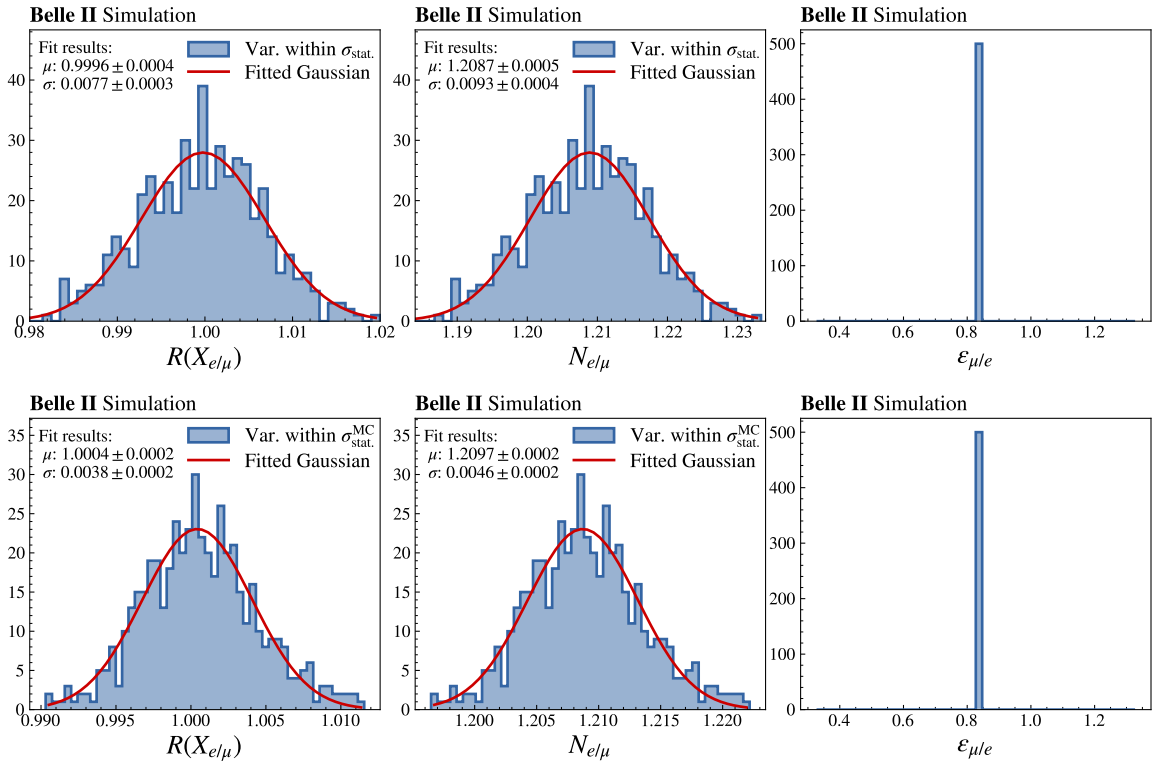

Figure A.5: The extracted values of $R(X_{e/\mu})$, $N_{e/\mu}$, and $\epsilon_{\mu/e}$ from fits using an ensemble of 500 toy data sets are presented in blue. The toy data sets reflect the uncertainty associated with experimental (top) and simulation sample size (bottom). The input data is fixed while the target data is varied. Gaussian distributions are fitted to each distribution (presented in red), and their mean values (μ) and standard deviations (σ) are provided.

A.4 Validation of the fit setup and uncertainties to extract $R(X_{\tau/\ell})$

To validate the uncertainties on $R(X_{\tau/\ell})$ obtained in Section 8.1.2, ensembles of artificially generated data sets are employed, as described in Section A.3. In Figure A.6, the extracted values of $R(X_{\tau/\ell})$ are presented for an ensemble representing the statistical uncertainties associated with the limited experimental-data sample size. The observed relative fluctuations of $(8.96 \pm 0.19)\%$, $(12.20 \pm 0.28)\%$, and $(7.08 \pm 0.19)\%$ in the electron and muon channels, as well as their combination, precisely match the predicted values of 9.0%, 12.0%, and 7.2% (see Tab. 8.3).

In two additional studies conducted by Paolo Rocchetti from Melbourne, the fit setup introduced in Section 8.1.1 is validated. These studies are performed on simulated samples without semitauonic gap modes (see Sec. 3.4.3), yielding a generator-level value of $R(X_{\tau/\ell}) = 0.209$. The findings from these studies are anticipated to be equally applicable when semitauonic gap modes are included.

In a linearity test analogous to the one detailed in Section 6.1.4, the nominal templates are fitted on Asimov data with various multipliers applied to the $X\tau\nu$ signal template. In an unbiased fit, the multiplier should be directly reflected in the extracted value of $R(X_{\tau/\ell})$. As depicted in Figure A.7(a), the results consistently align with a straight line with an offset of zero and a slope of one, thereby validating the fit setup's capability to accurately extract varying values of $R(X_{\tau/\ell})$.

In a second study, commonly referred to as a pull test, the simulated $X\tau\nu$ signal template, used to

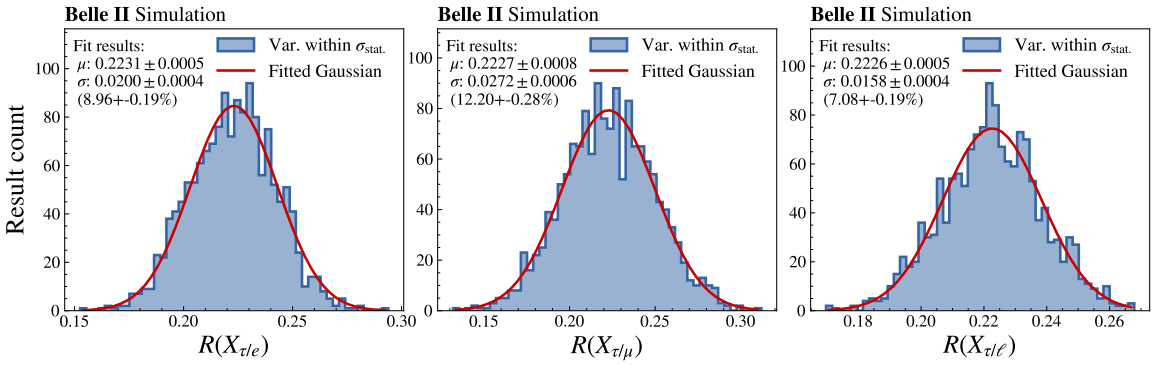

Figure A.6: The extracted values of $R(X_{\tau/e})$, $R(X_{\tau/\mu})$, and their combination $R(X_{\tau/\ell})$ from fits using an ensemble of 1500 toy data sets are presented in blue. The toy data sets reflect the uncertainty associated with experimental sample size. The input data is fixed while the target data is varied. Gaussian distributions are fitted to each distribution (presented in red), and their mean values (μ) and standard deviations (σ) are provided.

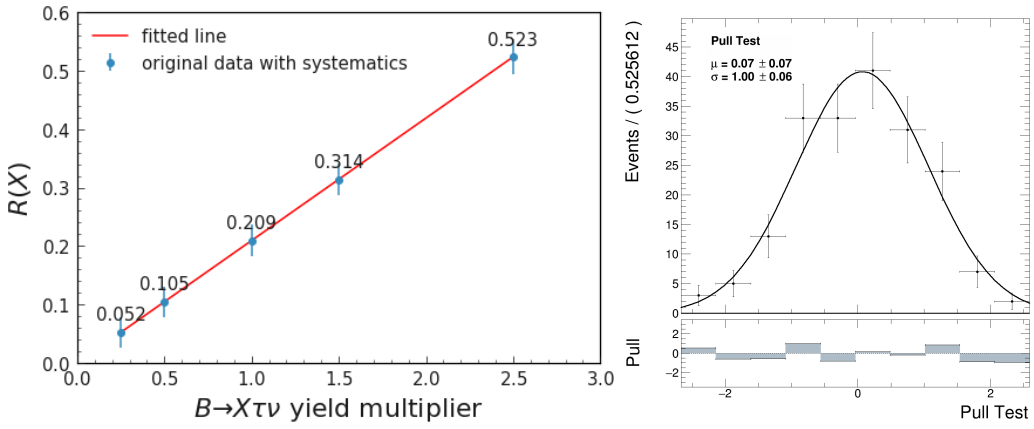

(a) (b)

Figure A.7: In (a), the outcome of a linearity test is displayed. The $B \to X\tau\nu$ yield multiplier is shown on the x-axis, while the extracted values of $R(X_{\tau/\ell})$ are presented on the y-axis (in blue) and are compared to a straight line (in red). In (b), the findings of a pull test are illustrated. The distribution of discrepancies between the nominal and extracted yields of $X\tau\nu$, divided by the predicted statistical uncertainty, is presented. The figure includes the mean (μ) and the standard deviation (σ) of a Gaussian fitted to this distribution.
Both figures are provided by Paolo Rocchetti.

define the Asimov data, is resampled 200 times with replacement, allowing for variation in its total yield within statistical uncertainties. An estimator is defined as the difference between the nominal and extracted yields of $X\tau\nu$, divided by the predicted statistical uncertainty (see Sec. 8.1.2). Ideally, a Gaussian distribution of the estimator with a mean (μ) consistent with zero and a standard deviation (σ) consistent with one is expected. A mean diverging from zero indicates a biased estimator, while a standard deviation diverging from one is in tension with predicted uncertainties. The results of the extracted estimator are presented in Figure A.7(b). The test is found to be successful, with a fitted Gaussian showing $\mu = 0$ and $\sigma = 1$ within uncertainties, providing additional support for the fit setup and the predicted uncertainties.

APPENDIX B

Additional tables and figures

B.1 Lepton-identification correction tables

This section offers additional insights into lepton-identification classifier thresholds and correction factors, as discussed in Sections 3.4.4, 4.3, 5.3.5, and 7.1.

For the $R(X_{e/\mu})$ extraction, the electron-identification working point is tailored to ensure uniform efficiencies of $\epsilon_e = 80\%$ in each interval of (p_ℓ, θ_ℓ, q). This uniformity is achieved by adjusting $\mathcal{P}_e$ classifier thresholds in each interval, as illustrated in Figure B.1.

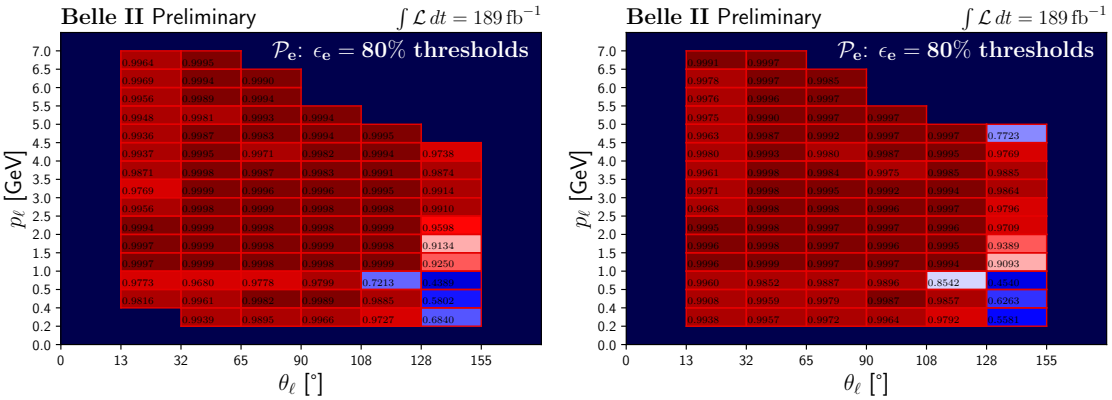

(a) Electrons

(b) Positrons

Figure B.1: The $\mathcal{P}_e$ classifier thresholds are displayed, adjusted to ensure a uniform 80% electron-identification efficiency in each interval of p_ℓ, θ_ℓ, and q.

Furthermore, correction factors applied to correct lepton-identification efficiencies and the probabilities of misidentifying charged hadrons as leptons are depicted in a grid of (p_ℓ, θ_ℓ) per lepton charge. For electron candidates, the factors for the $\mathcal{P}_e : \epsilon_e = 80\%$ working point, utilized in the $R(X_{e/\mu})$ extraction, are presented in Figure B.2. In the $R(X_{\tau/\ell})$ measurement, the working point is adjusted to $\mathcal{P}_e > 0.99$, and the corresponding corrections are displayed in Figure B.3. For muon candidates, a working point of $\mathcal{P}_\mu^{\mathcal{L}/\mathcal{L}} > 0.95$ is employed to measure $R(X_{e/\mu})$, while a more stringent threshold

of $\mathcal{P}_{\mu}^{\ell/\mathcal{L}} > 0.99$ is chosen for the $R(X_{\tau/\ell})$ measurement. The correction factors are summarized in Figures B.4 and B.5, respectively.

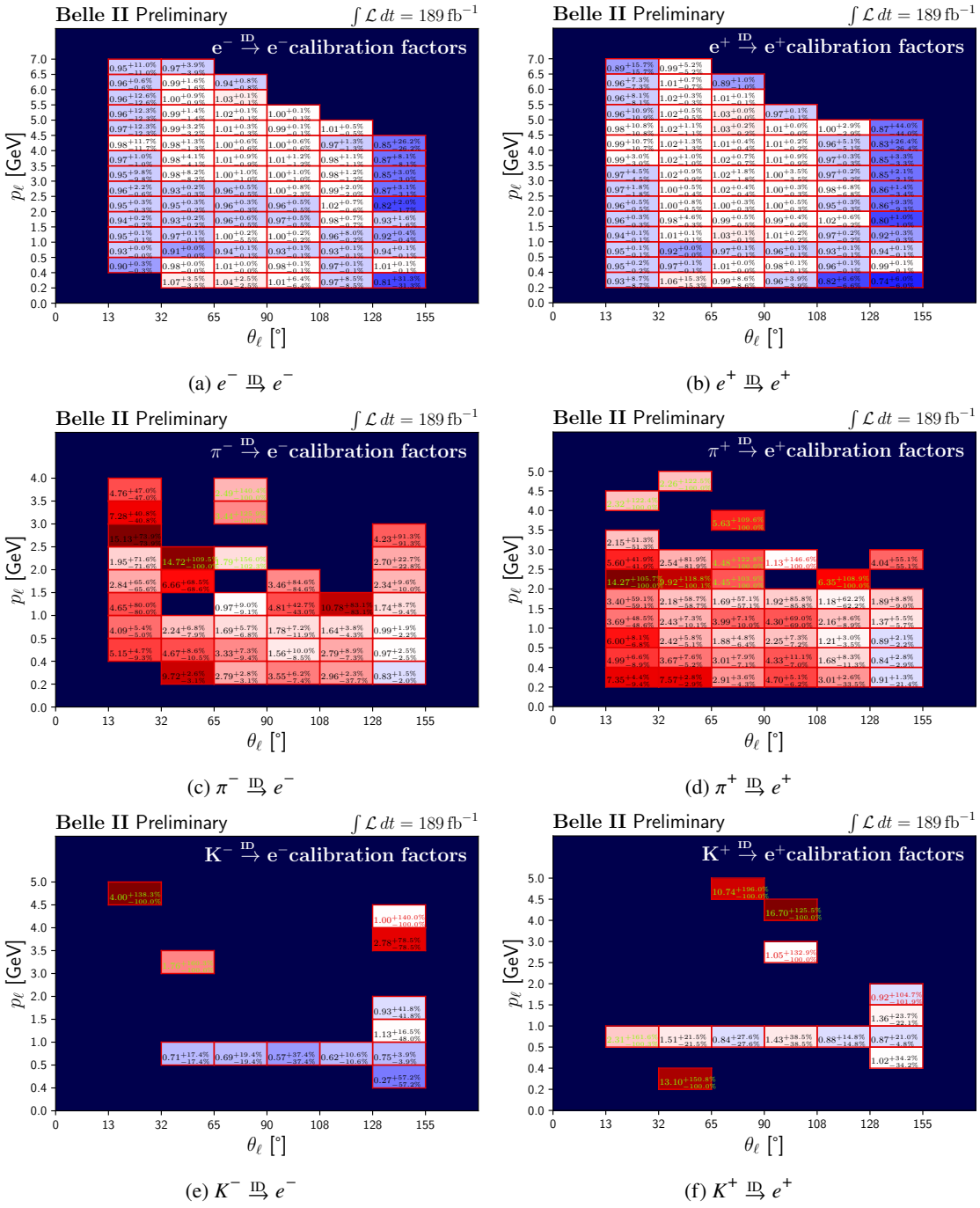

(a) $e^- \xrightarrow{\text{ID}} e^-$ (b) $e^+ \xrightarrow{\text{ID}} e^+$

(c) $\pi^- \xrightarrow{\text{ID}} e^-$ (d) $\pi^+ \xrightarrow{\text{ID}} e^+$

(e) $K^- \xrightarrow{\text{ID}} e^-$ (f) $K^+ \xrightarrow{\text{ID}} e^+$

Figure B.2: Correction factors for efficiencies and fake rates are presented, applicable to electron candidates identified using the $\mathcal{P}_e : \epsilon_e = 80\%$ working point.

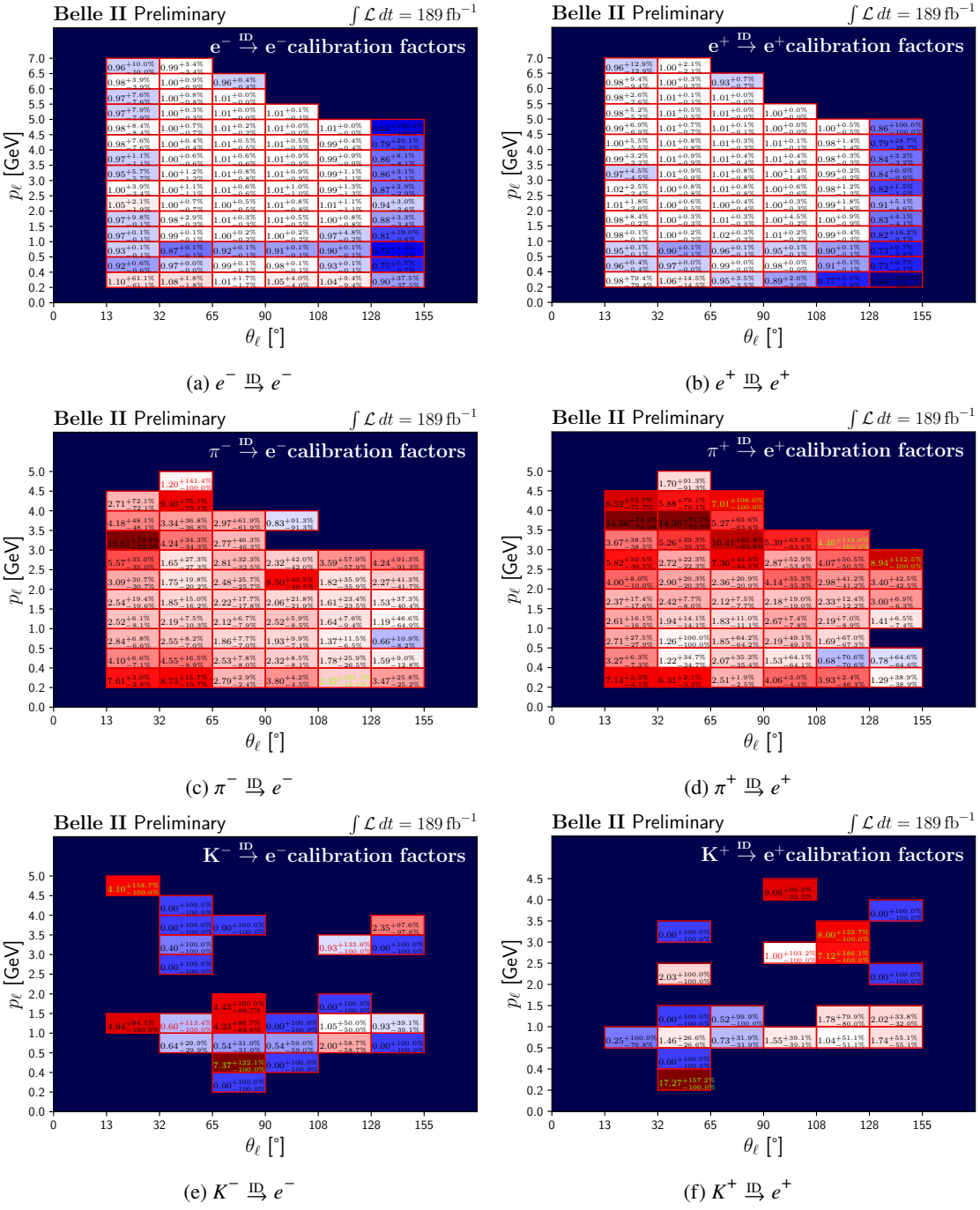

(a) $e^- \xrightarrow{\text{ID}} e^-$ (b) $e^+ \xrightarrow{\text{ID}} e^+$

(c) $\pi^- \xrightarrow{\text{ID}} e^-$ (d) $\pi^+ \xrightarrow{\text{ID}} e^+$

(e) $K^- \xrightarrow{\text{ID}} e^-$ (f) $K^+ \xrightarrow{\text{ID}} e^+$

Figure B.3: Correction factors for efficiencies and fake rates are presented, applicable to electron candidates identified using $\mathcal{P}_e > 0.99$.

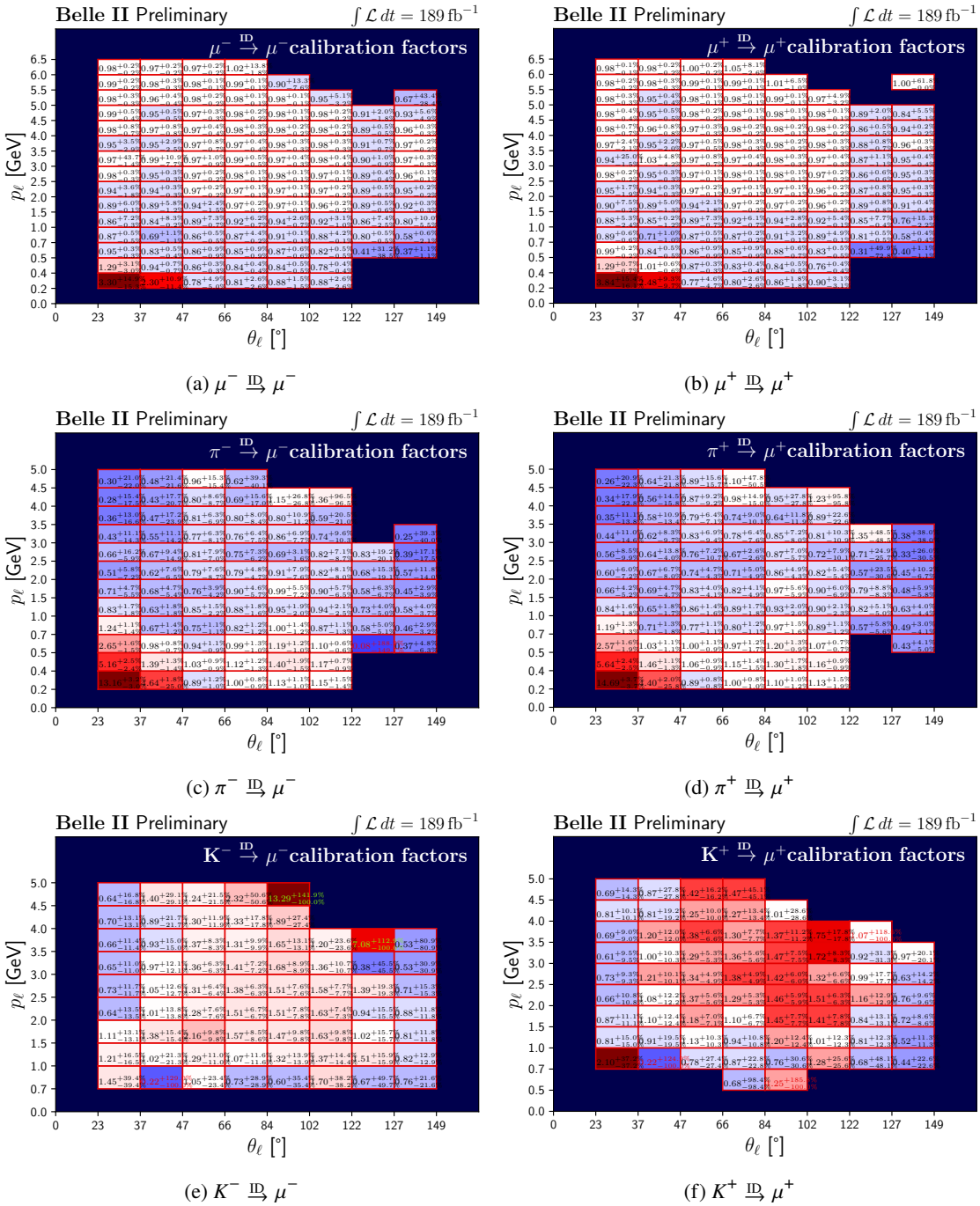

(a) $\mu^- \xrightarrow{\text{ID}} \mu^-$ (b) $\mu^+ \xrightarrow{\text{ID}} \mu^+$

(c) $\pi^- \xrightarrow{\text{ID}} \mu^-$ (d) $\pi^+ \xrightarrow{\text{ID}} \mu^+$

(e) $K^- \xrightarrow{\text{ID}} \mu^-$ (f) $K^+ \xrightarrow{\text{ID}} \mu^+$

Figure B.4: Correction factors for efficiencies and fake rates are presented, applicable to muon candidates identified using $\mathcal{P}_\mu^{\mathcal{L}/\mathcal{L}} > 0.95$.

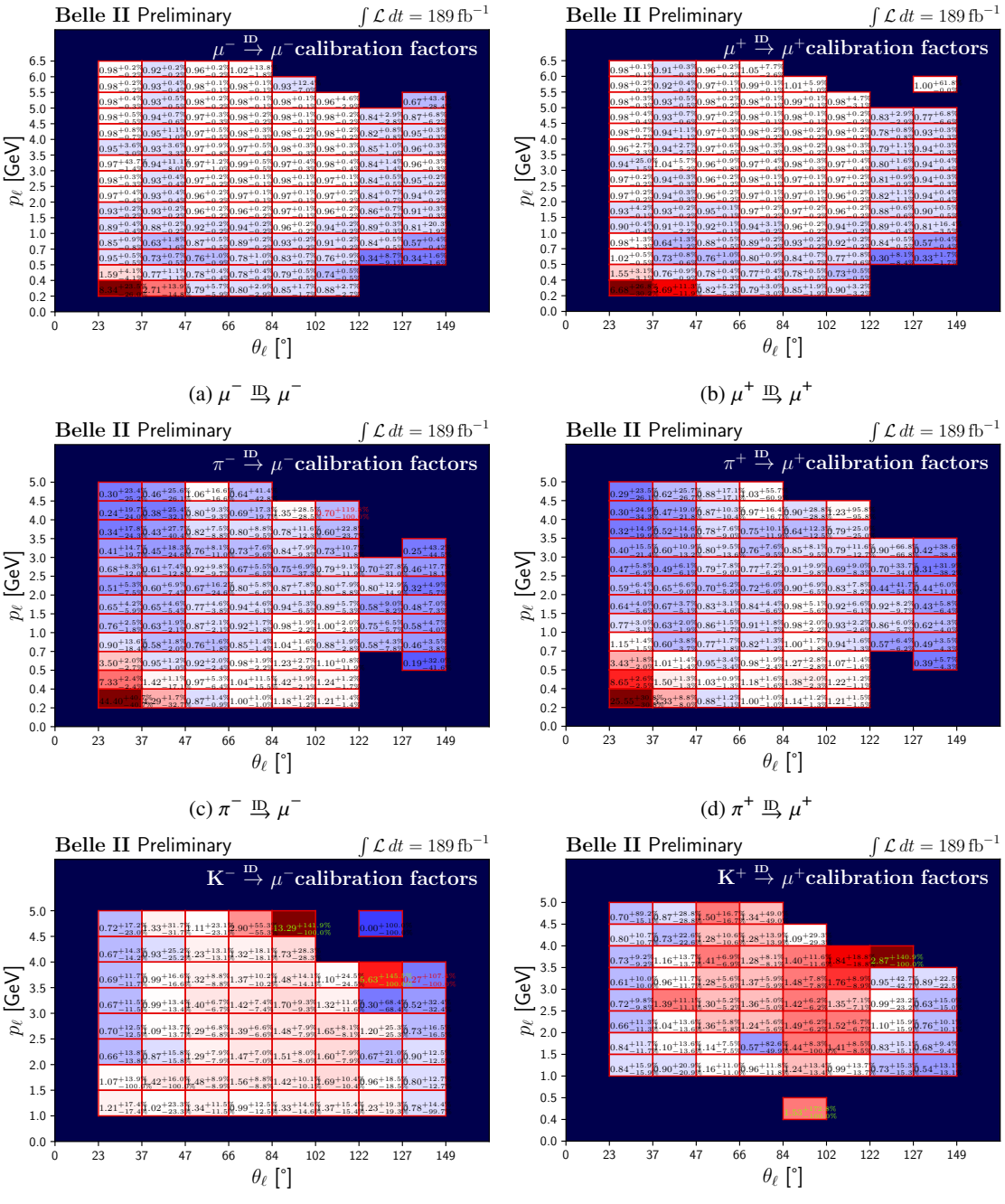

(a) $\mu^- \overset{\mathrm{ID}}{\to} \mu^-$ (b) $\mu^+ \overset{\mathrm{ID}}{\to} \mu^+$

(c) $\pi^- \overset{\mathrm{ID}}{\to} \mu^-$ (d) $\pi^+ \overset{\mathrm{ID}}{\to} \mu^+$

(e) $K^- \overset{\mathrm{ID}}{\to} \mu^-$ (f) $K^+ \overset{\mathrm{ID}}{\to} \mu^+$

Figure B.5: Correction factors for efficiencies and fake rates are presented, applicable to muon candidates identified using $\mathcal{P}_\mu^{\mathcal{L}/\mathcal{L}} > 0.99$.

B.2 Reconstructed B-meson decay modes by the FEI algorithm

Tables B.1 and B.2 provide a list of all B_{tag} decay modes reconstructed by the FEI algorithm.

#	FEI reconstruction mode
0	$B^0 \to D^- \pi^+$
1	$B^0 \to D^- \pi^+ \pi^0$
2	$B^0 \to D^- \pi^+ \pi^0 \pi^0$
3	$B^0 \to D^- \pi^+ \pi^+ \pi^-$
4	$B^0 \to D^- \pi^+ \pi^+ \pi^- \pi^0$
5	$B^0 \to \overline{D}^0 \pi^+ \pi^-$
6	$B^0 \to D^- D^0 K^+$
7	$B^0 \to D^- D^{*0} K^+$
8	$B^0 \to D^{*-} D^0 K^+$
9	$B^0 \to D^{*-} D^{*0} K^+$
10	$B^0 \to D^- D^+ K^0_S$
11	$B^0 \to D^{*-} D^+ K^0_S$
12	$B^0 \to D^- D^{*+} K^0_S$
13	$B^0 \to D^{*-} D^{*+} K^0_S$
14	$B^0 \to D^- D_s$
15	$B^0 \to D^{*-} \pi^+$
16	$B^0 \to D^{*-} \pi^+ \pi^0$
17	$B^0 \to D^{*-} \pi^+ \pi^0 \pi^0$
18	$B^0 \to D^{*-} \pi^+ \pi^+ \pi^-$
19	$B^0 \to D^{*-} \pi^+ \pi^+ \pi^- \pi^0$
20	$B^0 \to D^- D^*_s$
21	$B^0 \to D^{*-} D_s$
22	$B^0 \to D^{*-} D^*_s$
23	$B^0 \to J/\psi\, K^0_S$
24	$B^0 \to J/\psi\, K^+ \pi^-$
25	$B^0 \to J/\psi\, K^0_S \pi^+ \pi^-$
26	$B^0 \to \Lambda_c^- p \pi^+ \pi^-$
27	$B^0 \to \overline{D}^0 p \bar{p}$
28	$B^0 \to D^- p \bar{p} \pi^+$
29	$B^0 \to D^{*-} p \bar{p} \pi^+$
30	$B^0 \to \overline{D}^0 p \bar{p} \pi^+ \pi^-$
31	$B^0 \to \overline{D}^{*0} p \bar{p} \pi^+ \pi^-$

Table B.1: The decay modes of neutral B mesons that are reconstructed by the FEI tagging algorithm.

#	FEI reconstruction mode
0	$B^+ \to \overline{D}^0 \pi^+$
1	$B^+ \to \overline{D}^0 \pi^+ \pi^0$
2	$B^+ \to \overline{D}^0 \pi^+ \pi^0 \pi^0$
3	$B^+ \to \overline{D}^0 \pi^+ \pi^+ \pi^-$
4	$B^+ \to \overline{D}^0 \pi^+ \pi^+ \pi^- \pi^0$
5	$B^+ \to \overline{D}^0 D^+$
6	$B^+ \to \overline{D}^0 D^+ K_S^0$
7	$B^+ \to \overline{D}^{*0} D^+ K_S^0$
8	$B^+ \to \overline{D}^0 D^{*+} K_S^0$
9	$B^+ \to \overline{D}^{*0} D^{*+} K_S^0$
10	$B^+ \to \overline{D}^0 D^0 K^+$
11	$B^+ \to \overline{D}^{*0} D^0 K^+$
12	$B^+ \to \overline{D}^0 D^{*0} K^+$
13	$B^+ \to \overline{D}^{*0} D^{*0} K^+$
14	$B^+ \to \overline{D}^0 D_s$
15	$B^+ \to \overline{D}^{*0} \pi^+$
16	$B^+ \to \overline{D}^{*0} \pi^+ \pi^0$
17	$B^+ \to \overline{D}^{*0} \pi^+ \pi^0 \pi^0$
18	$B^+ \to \overline{D}^{*0} \pi^+ \pi^+ \pi^-$
19	$B^+ \to \overline{D}^{*0} \pi^+ \pi^+ \pi^- \pi^0$
20	$B^+ \to \overline{D}^0 D_s^*$
21	$B^+ \to \overline{D}^{*0} D_s$
22	$B^+ \to \overline{D}^0 K^+$
23	$B^+ \to D^- \pi^+ \pi^+$
24	$B^+ \to D^- \pi^+ \pi^+ \pi^0$
25	$B^+ \to J/\psi\, K^+$
26	$B^+ \to J/\psi\, K^+ \pi^+ \pi^-$
27	$B^+ \to J/\psi\, K^+ \pi^0$
28	$B^+ \to J/\psi\, K_S^0 \pi^+$
29	$B^+ \to \Lambda_c^- p \pi^+ \pi^0$
30	$B^+ \to \Lambda_c^- p \pi^+ \pi^+ \pi^-$
31	$B^+ \to \overline{D}^0 p \bar{p} \pi^+$
32	$B^+ \to \overline{D}^{*0} p \bar{p} \pi^+$
33	$B^+ \to D^+ p \bar{p} \pi^+ \pi^-$
34	$B^+ \to D^{*+} p \bar{p} \pi^+ \pi^-$
35	$B^+ \to \Lambda_c^- p \pi^+$

Table B.2: The decay modes of charged B mesons that are reconstructed by the FEI tagging algorithm.

B.3 Impact of modified D-meson decay distributions on M_X and p_ℓ^B

In this section, the impacts of various modified D-meson decay distributions on M_X (see Figs. B.6, B.7, and B.8) and p_ℓ^B (see Figs. B.9, B.10, and B.11) are presented. These effects are discussed in more detail in Sections 6.1.3, 7.2.3, 7.3, and 8.1.3.

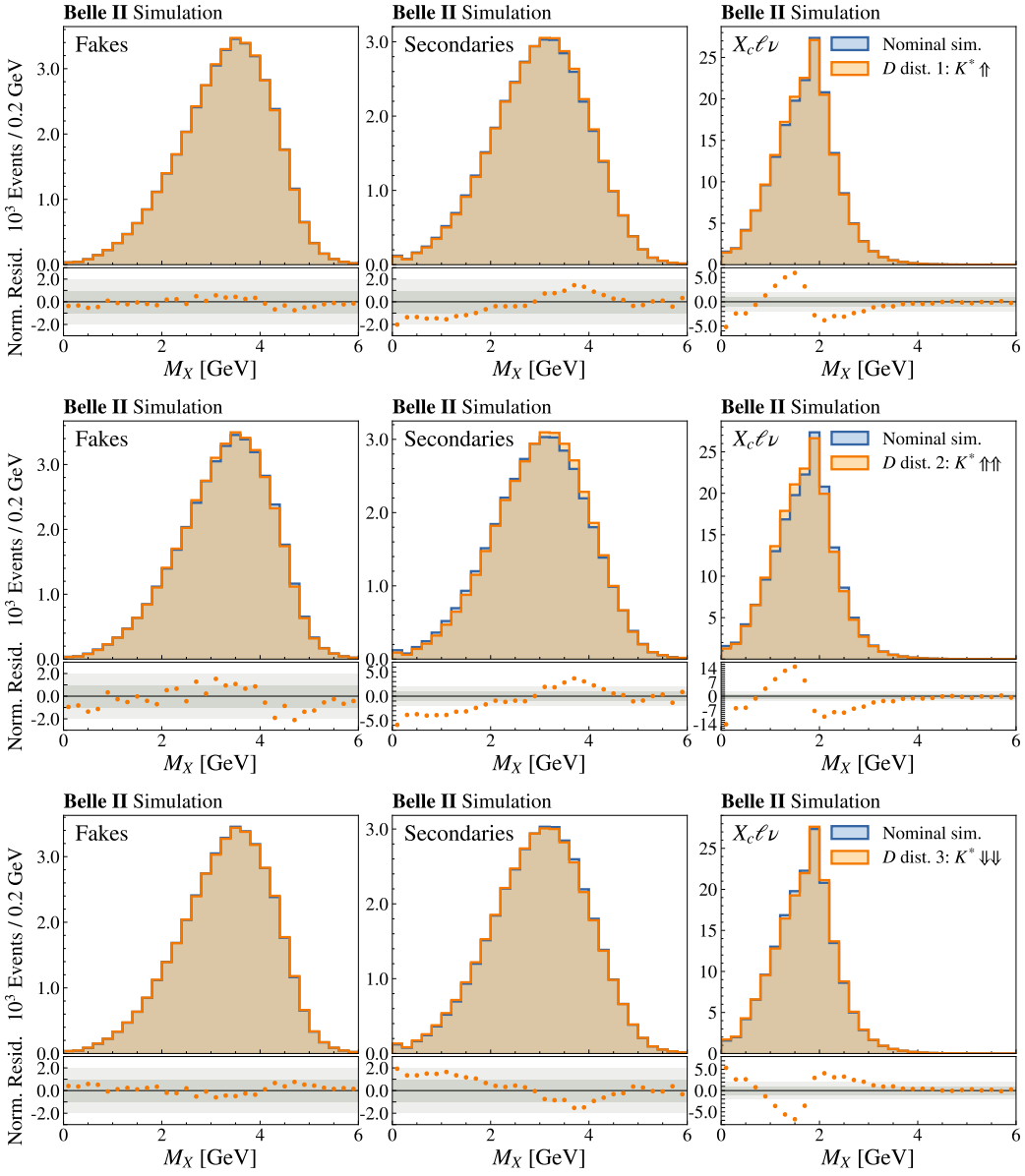

Figure B.6: The impacts of modified D-meson decay distributions on the invariant mass of the X system, M_X, are depicted. The nominal simulation is represented in blue, and the modified sample, specified in Table 6.4, is shown in orange. Their residuals, normalized by the statistical uncertainty of the simulated samples, are presented below.

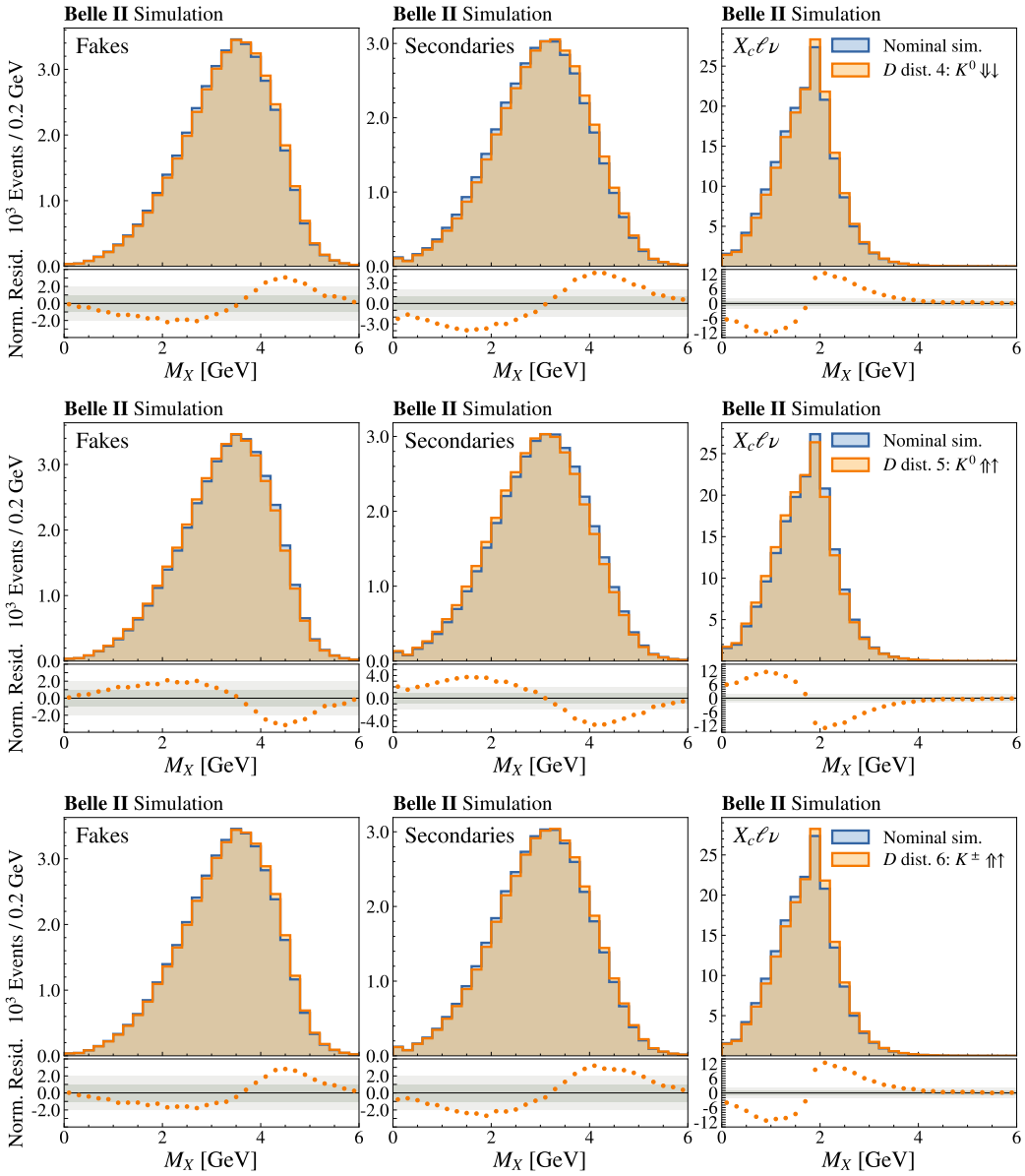

Figure B.7: The impacts of modified D-meson decay distributions on the invariant mass of the X system, M_X, are depicted. The nominal simulation is represented in blue, and the modified sample, specified in Table 6.4, is shown in orange. Their residuals, normalized by the statistical uncertainty of the simulated samples, are presented below.

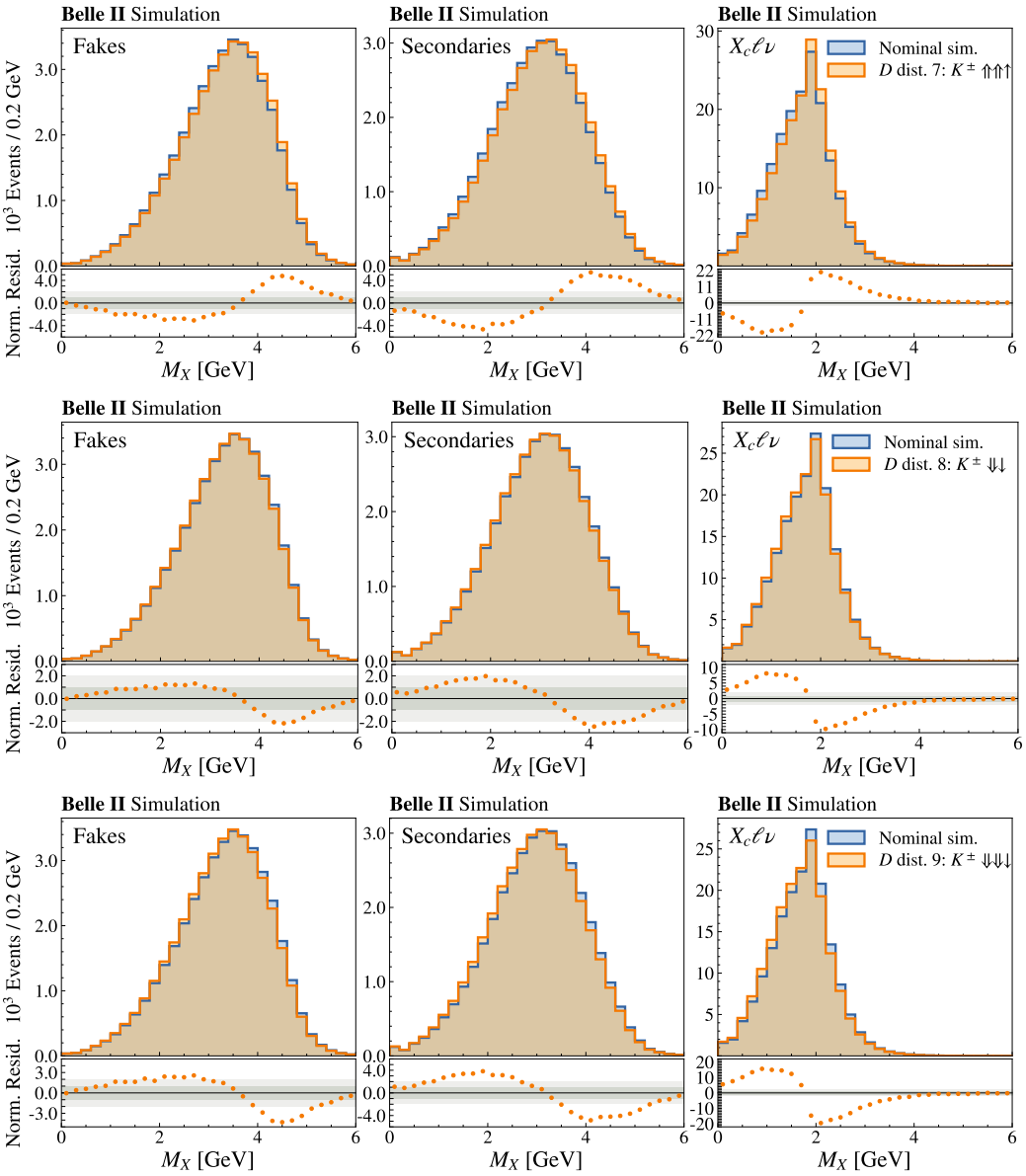

Figure B.8: The impacts of modified D-meson decay distributions on the invariant mass of the X system, M_X, are depicted. The nominal simulation is represented in blue, and the modified sample, specified in Table 6.4, is shown in orange. Their residuals, normalized by the statistical uncertainty of the simulated samples, are presented below.

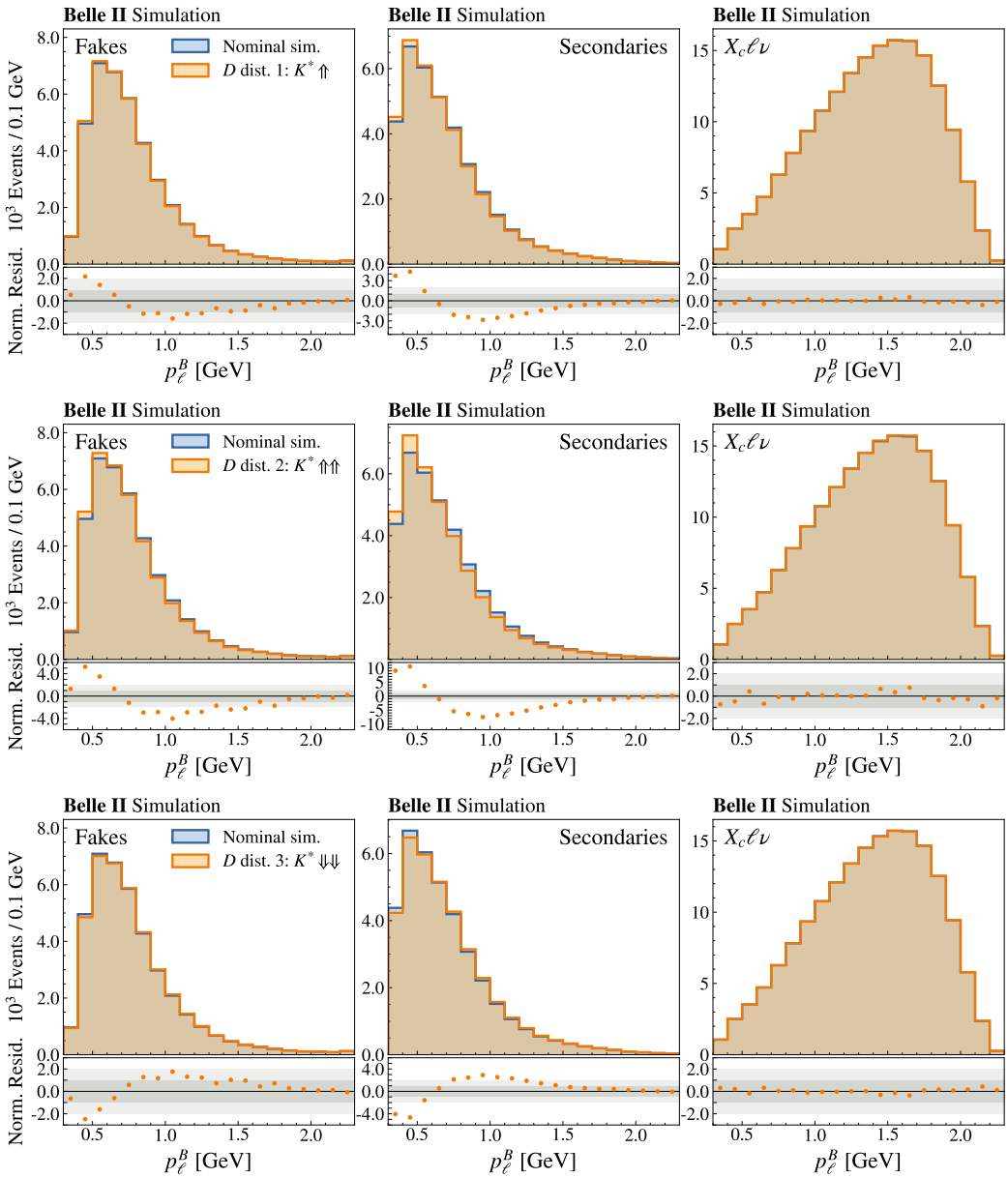

Figure B.9: The impacts of modified D-meson decay distributions on the signal-lepton momentum in the B_{sig} frame, p_ℓ^B, are depicted. The nominal simulation is represented in blue, and the modified sample, specified in Table 6.4, is shown in orange. Their residuals, normalized by the statistical uncertainty of the simulated samples, are presented below.

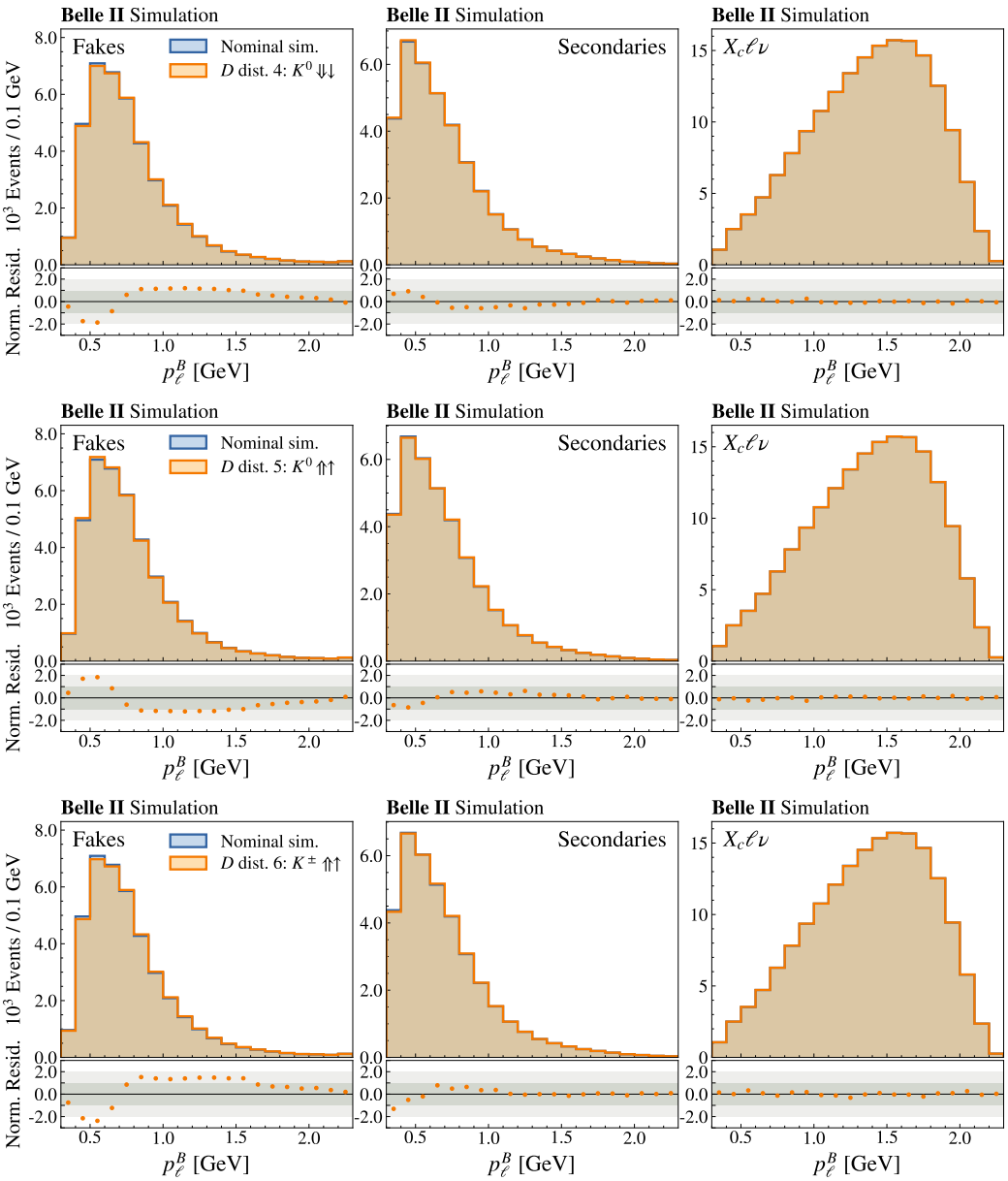

Figure B.10: The impacts of modified D-meson decay distributions on the signal-lepton momentum in the B_{sig} frame, p_ℓ^B, are depicted. The nominal simulation is represented in blue, and the modified sample, specified in Table 6.4, is shown in orange. Their residuals, normalized by the statistical uncertainty of the simulated samples, are presented below.

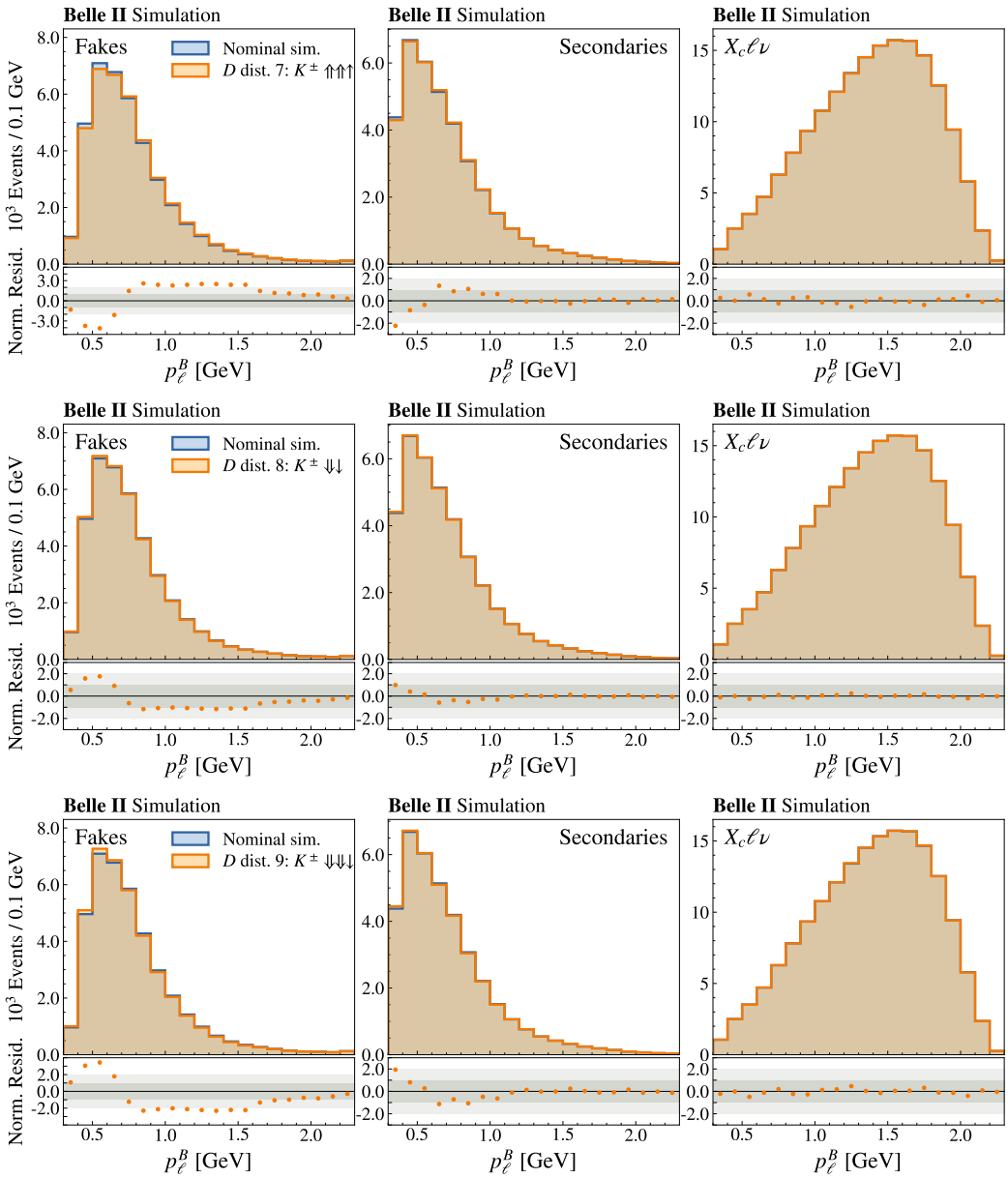

Figure B.11: The impacts of modified D-meson decay distributions on the signal-lepton momentum in the B_{sig} frame, p_ℓ^B, are depicted. The nominal simulation is represented in blue, and the modified sample, specified in Table 6.4, is shown in orange. Their residuals, normalized by the statistical uncertainty of the simulated samples, are presented below.

B.4 Additional information on the resonance-based muon-fake rejection

In this section, the invariant masses and p values resulting from the vertex fit are presented for the intermediate resonances investigated in Section 7.1.5. Figures B.12 and B.13 present these quantities for the resonances incorporated into the event selection for $B\bar{B}$-background suppression. In Figures B.14, B.15, and B.16, resonances are displayed that are evaluated to not provide sufficiently pure background suppression, hence they are not used in the event selection.

The distributions of experimental data and simulation align well. Any remaining discrepancies are expected to be solely attributable to the inadequate statistical precision in the off-resonance data sample utilized to characterize continuum processes.

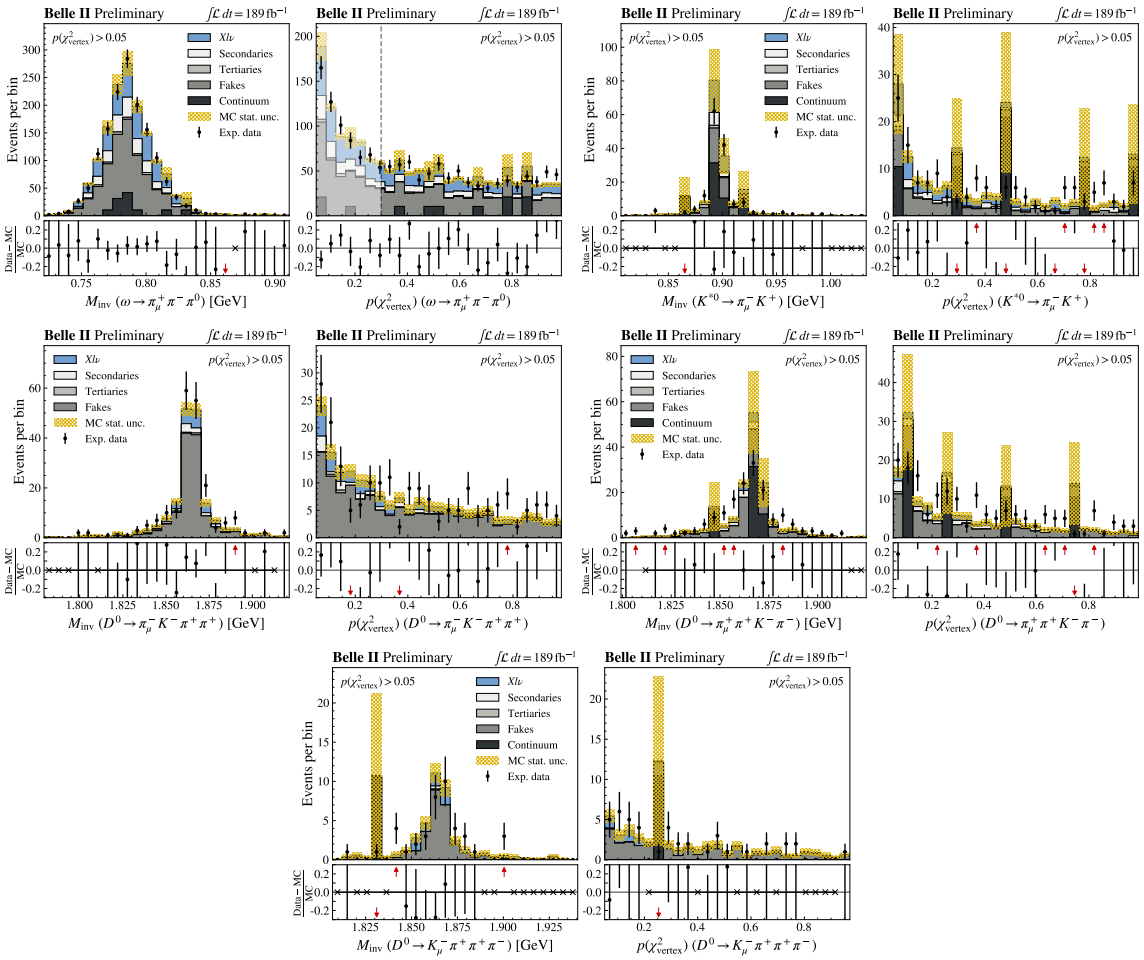

Figure B.12: The invariant mass is depicted for candidates of intermediate resonances that are incorporated into the event selection (see Tab. 7.4). Additionally, the p-value of the vertex fit, denoted as $p(\chi^2_{\text{vertex}})$, is presented. In each figure, the requirement of $p(\chi^2_{\text{vertex}}) > 0.05$ is imposed. For $\omega \to \pi^+_\mu \pi^- \pi^0$ decays, this requirement is tightened to $p(\chi^2_{\text{vertex}}) > 0.3$ in the event selection, as indicated in the figure.

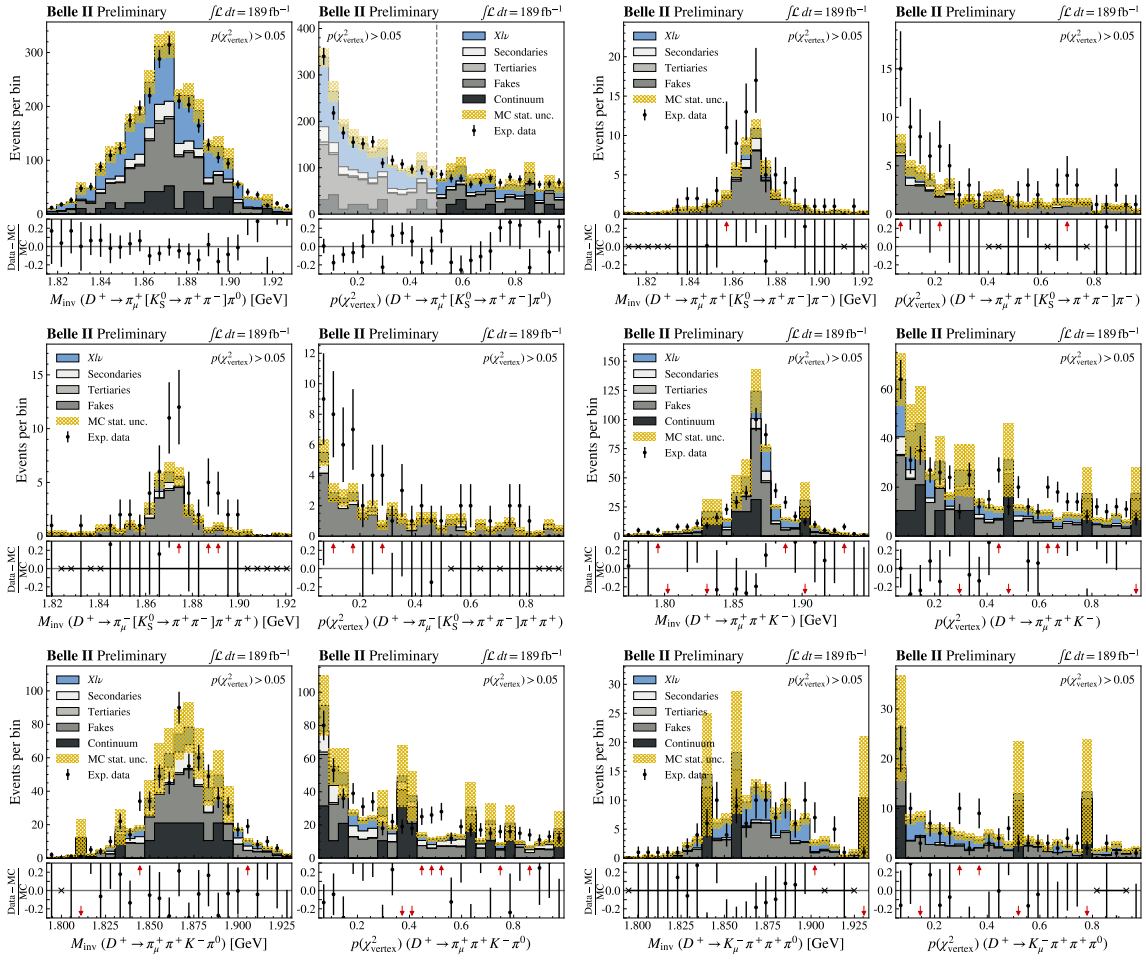

Figure B.13: The invariant mass is depicted for candidates of intermediate resonances that are incorporated into the event selection (see Tab. 7.4). Additionally, the p-value of the vertex fit, denoted as $p(\chi^2_{\mathrm{vertex}})$, is presented. In each figure, the requirement of $p(\chi^2_{\mathrm{vertex}}) > 0.05$ is imposed. For $D^+ \to \pi^+_\mu [K^0_S \to \pi^+\pi^-]\pi^0$ decays, this requirement is tightened to $p(\chi^2_{\mathrm{vertex}}) > 0.5$ in the event selection, as indicated in the figure.

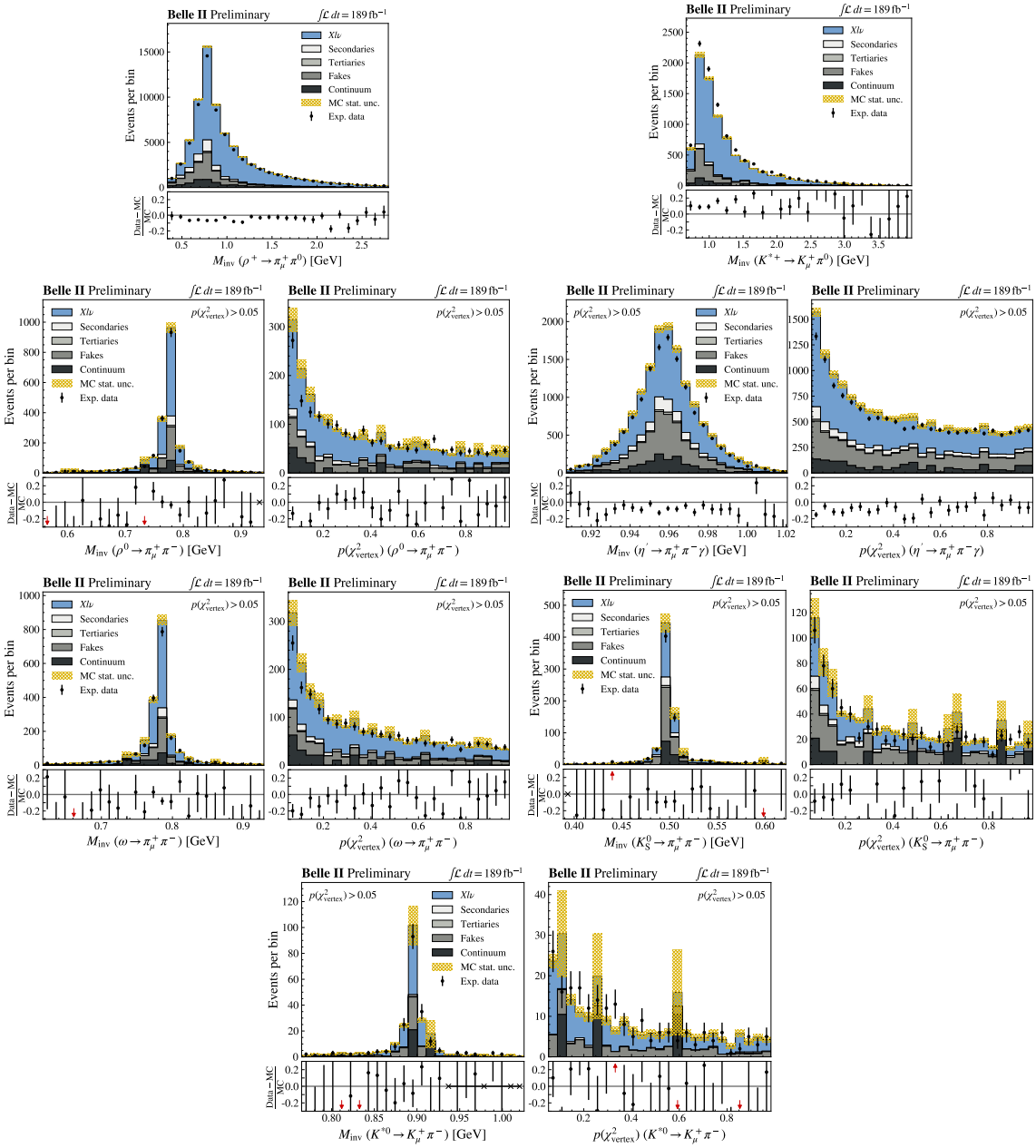

Figure B.14: The invariant mass is depicted for candidates of intermediate resonances that are evaluated to not provide a sufficiently pure $B\bar{B}$-background suppression (see Tab. 7.4). Additionally, the p-value of the vertex fit, denoted as $p(\chi^2_{\mathrm{vertex}})$, is presented. In each figure, the requirement of $p(\chi^2_{\mathrm{vertex}}) > 0.05$ is imposed.

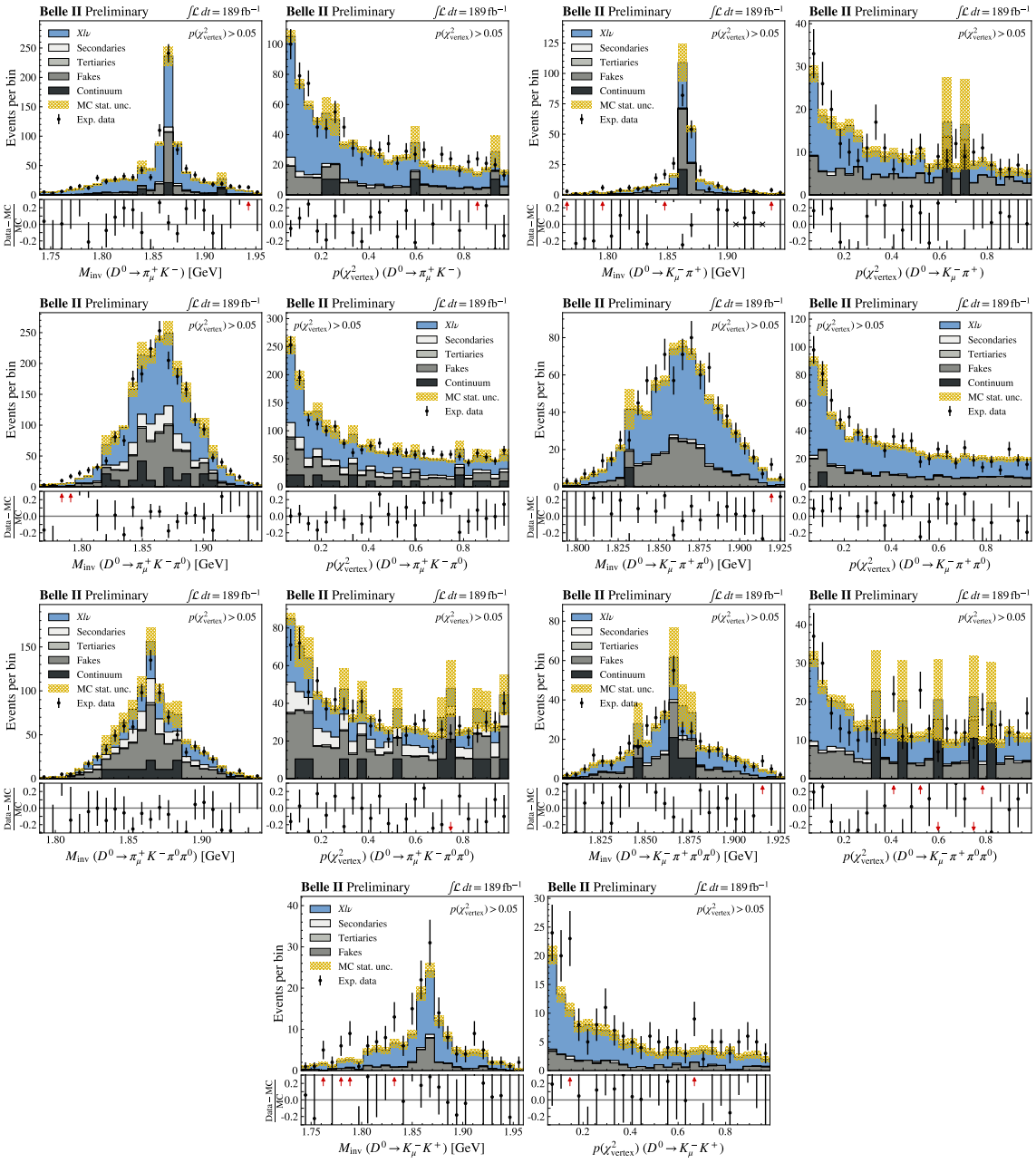

Figure B.15: The invariant mass is depicted for candidates of intermediate resonances that are evaluated to not provide a sufficiently pure $B\bar{B}$-background suppression (see Tab. 7.4). Additionally, the p-value of the vertex fit, denoted as $p(\chi^2_{\mathrm{vertex}})$, is presented. In each figure, the requirement of $p(\chi^2_{\mathrm{vertex}}) > 0.05$ is imposed.

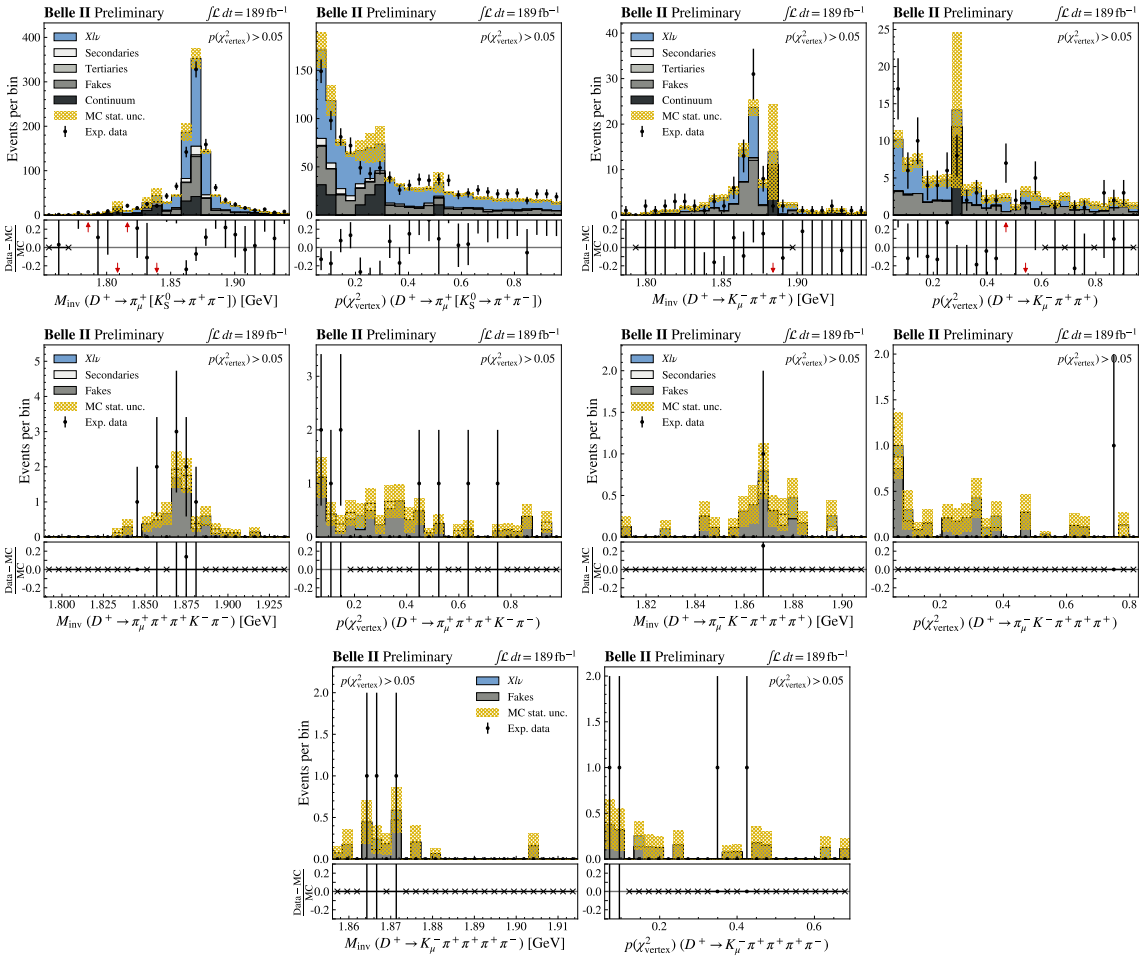

Figure B.16: The invariant mass is depicted for candidates of intermediate resonances that are evaluated to not provide a sufficiently pure $B\bar{B}$-background suppression (see Tab. 7.4). Additionally, the p-value of the vertex fit, denoted as $p(\chi^2_{\mathrm{vertex}})$, is presented. In each figure, the requirement of $p(\chi^2_{\mathrm{vertex}}) > 0.05$ is imposed.
The high-multiplicity decay $D^+ \to K^-\pi^-\pi^+\pi^+\pi^+$, illustrated in the lower three figures with various options of hadrons mimicking the signal lepton, is excluded from the event selection solely based on the observed limited statistical impact.

B.5 Validation of the simulation reweighting in various control samples

In this section, the impact of the simulation reweighting, introduced in Section 7.3, is validated in various control samples defined in Section 7.2.1.

The high-p_ℓ^B control sample, primarily comprising $B \to X\ell\nu$ decays, is individually presented for events with charged and neutral B_{tag} candidates in Figure B.17. Low lepton-momentum $B \to X\ell\nu$ decays are examined in the low-M_{miss}^2 and low-q^2 control samples, presented in Figures B.18 and B.19, respectively.

Validation of the $B\bar{B}$-background reweighting is performed using the high-M_X control sample illustrated in Figure B.20. The examination of background events with low M_X values is carried out in the same-flavor control sample, separately presented for charged and neutral B_{tag} candidates in Figures B.21 and B.22, respectively.

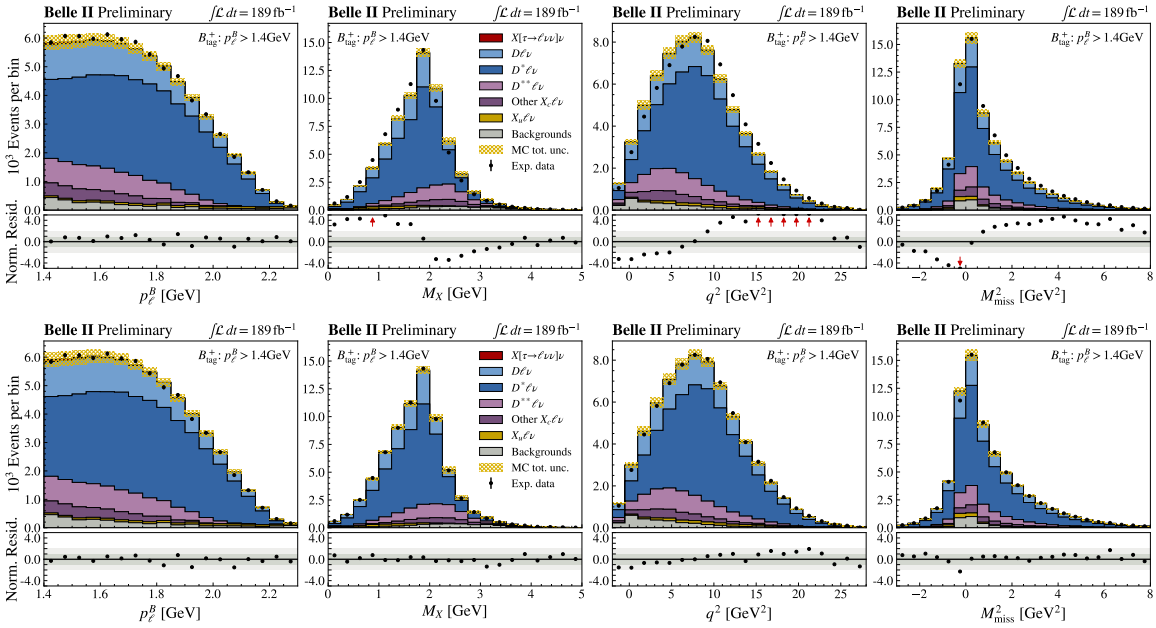

(a) B^+_{tag} channel before (top) and after (bottom) the simulation reweighting

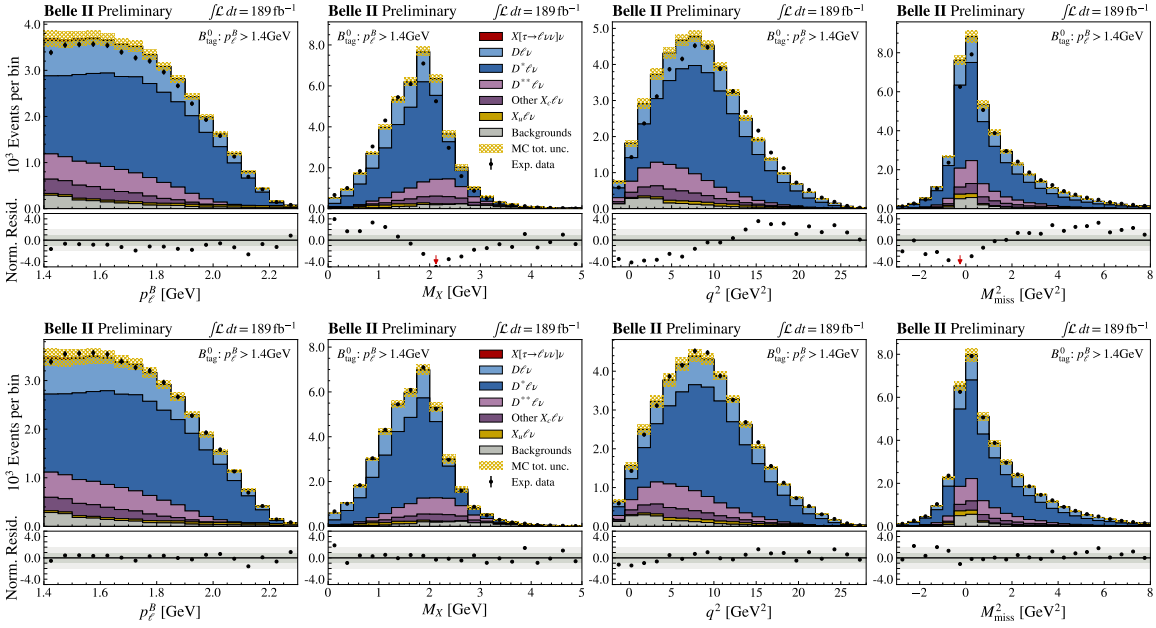

(b) B^0_{tag} channel before (top) and after (bottom) the simulation reweighting

Figure B.17: The impact of the simulation reweighting (see Sec. 7.3) on the kinematic quantities p^B_ℓ, M_X, q^2, and M^2_{miss} is presented for events with charged (a) and neutral (b) B_{tag} candidates in the high-p^B_ℓ control sample. The top rows display the distributions before reweighting, along with the uncertainty-normalized residuals between the distributions of experimental data and simulation. In the bottom row of figures, the reweighted distributions are presented, revealing significantly reduced residuals.

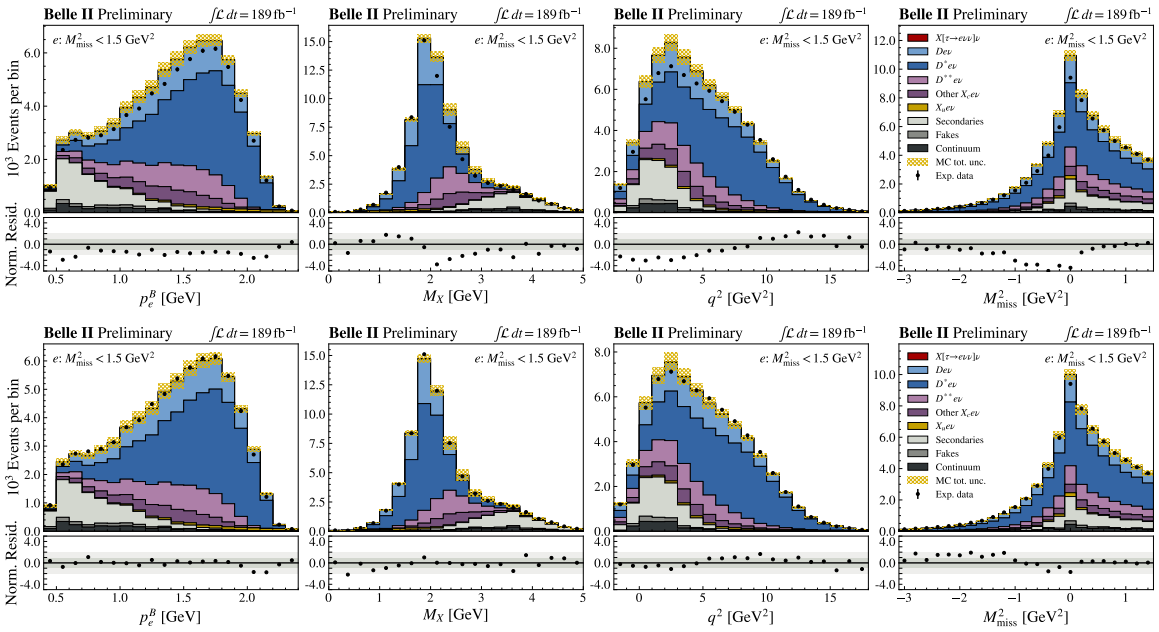

(a) Electron channel before (top) and after (bottom) the simulation reweighting

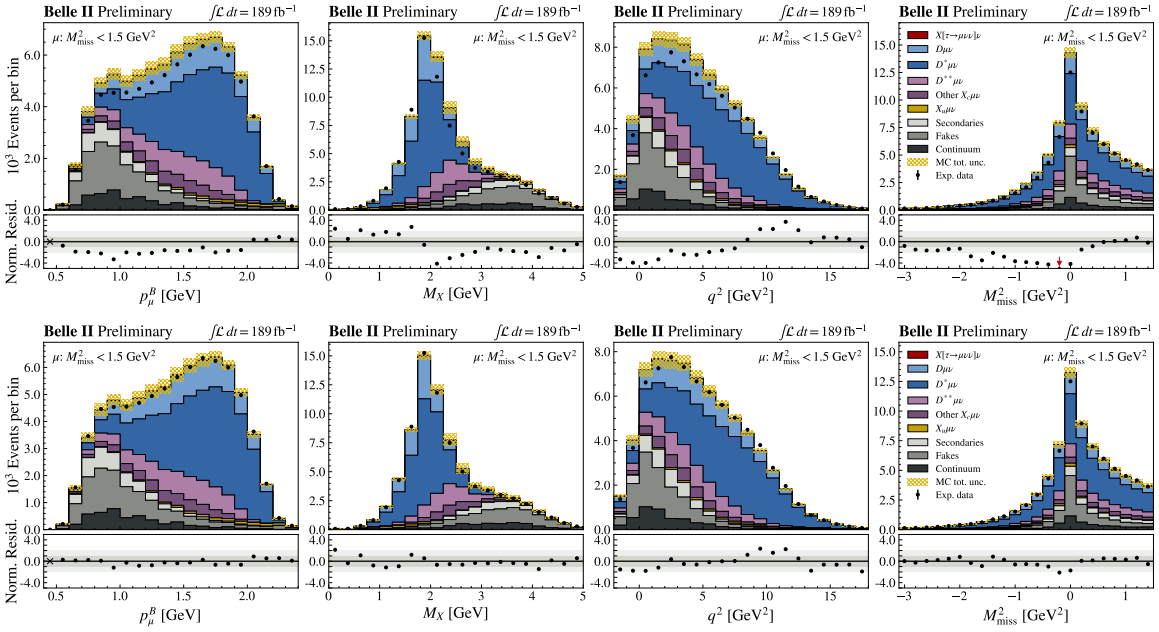

(b) Muon channel before (top) and after (bottom) the simulation reweighting

Figure B.18: The impact of the simulation reweighting (see Sec. 7.3) on the kinematic quantities p^B_ℓ, M_X, q^2, and M^2_{miss} is presented for the electron (a) and muon (b) channel in the low-M^2_{miss} control sample. The top rows display the distributions before reweighting, along with the uncertainty-normalized residuals between the distributions of experimental data and simulation. In the bottom row of figures, the reweighted distributions are presented, revealing significantly reduced residuals.

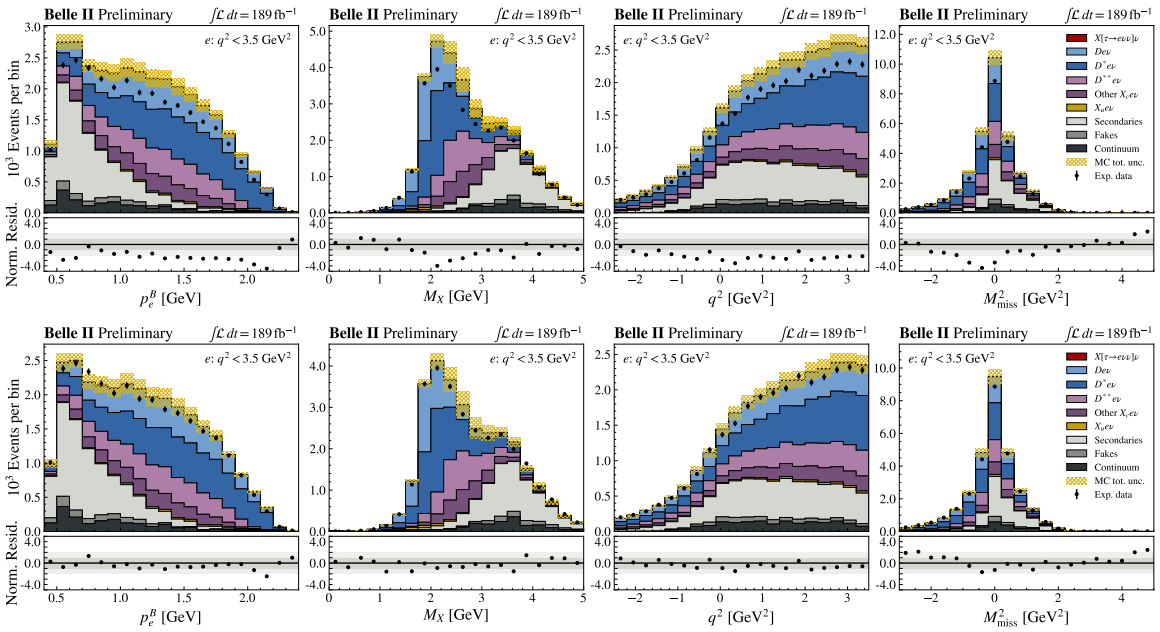

(a) Electron channel before (top) and after (bottom) the simulation reweighting

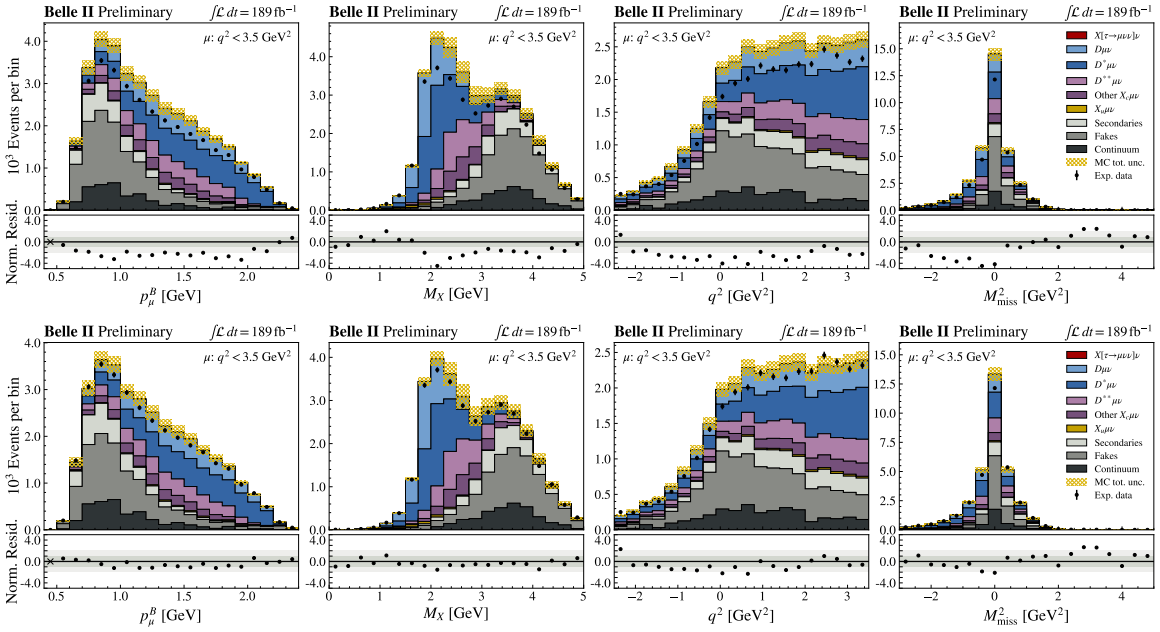

(b) Muon channel before (top) and after (bottom) the simulation reweighting

Figure B.19: The impact of the simulation reweighting (see Sec. 7.3) on the kinematic quantities p_ℓ^B, M_X, q^2, and M^2_{miss} is presented for the electron (a) and muon (b) channel in the low-q^2 control sample. The top rows display the distributions before reweighting, along with the uncertainty-normalized residuals between the distributions of experimental data and simulation. In the bottom row of figures, the reweighted distributions are presented, revealing significantly reduced residuals.

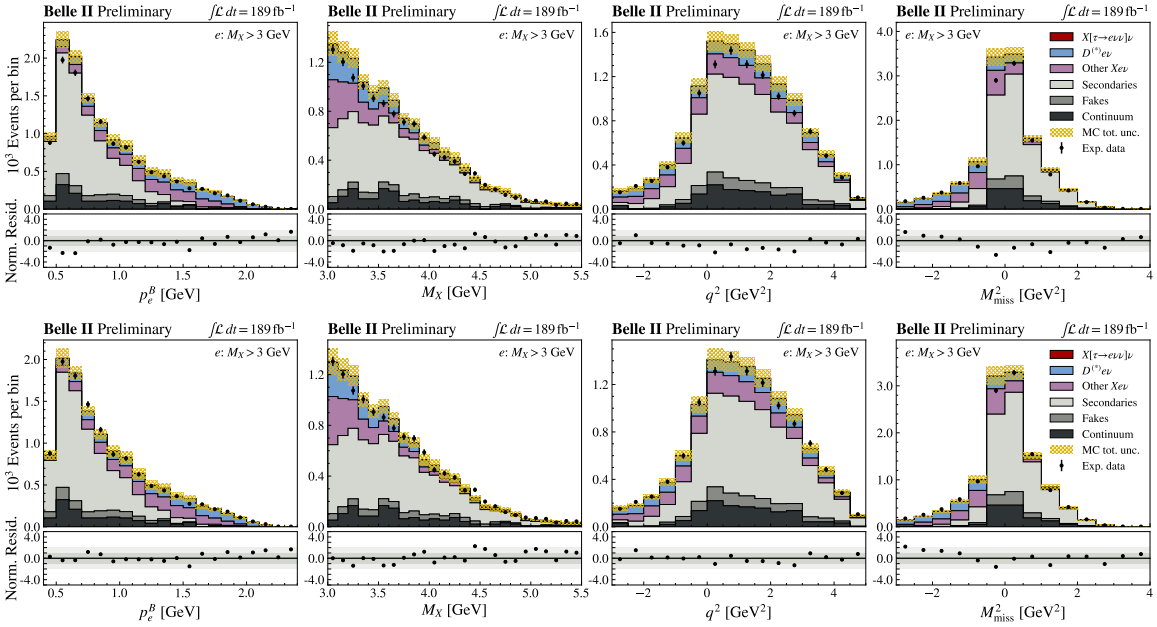

(a) Electron channel before (top) and after (bottom) the simulation reweighting

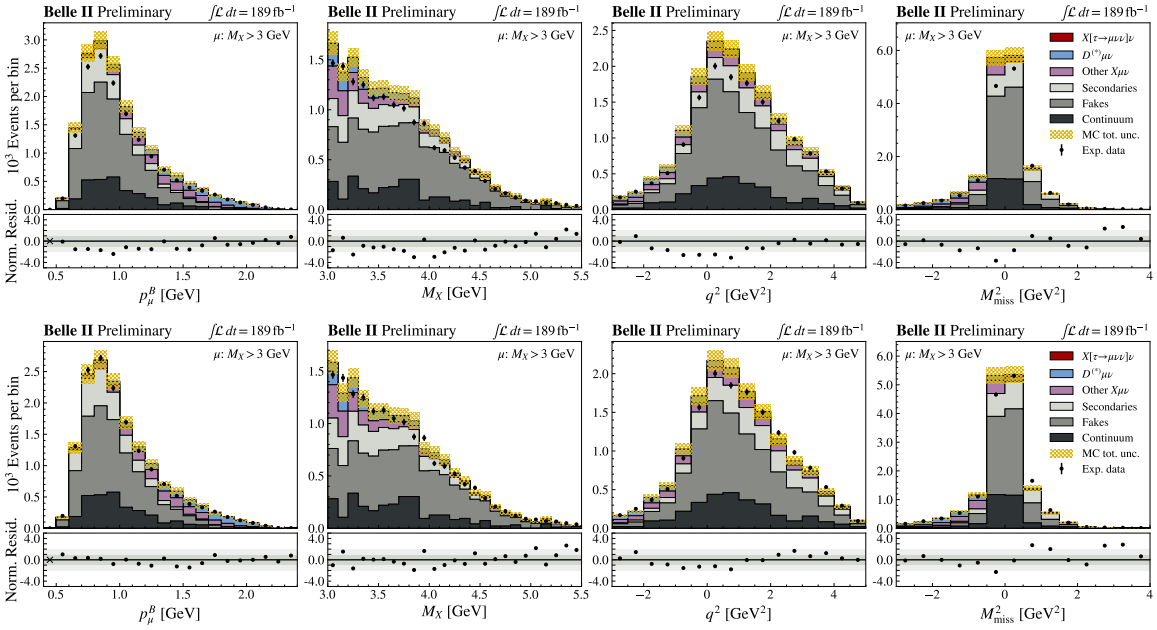

(b) Muon channel before (top) and after (bottom) the simulation reweighting

Figure B.20: The impact of the simulation reweighting (see Sec. 7.3) on the kinematic quantities p_ℓ^B, M_X, q^2, and M^2_{miss} is presented for the electron (a) and muon (b) channel in the high-M_X control sample. The top rows display the distributions before reweighting, along with the uncertainty-normalized residuals between the distributions of experimental data and simulation. In the bottom row of figures, the reweighted distributions are presented, revealing significantly reduced residuals.

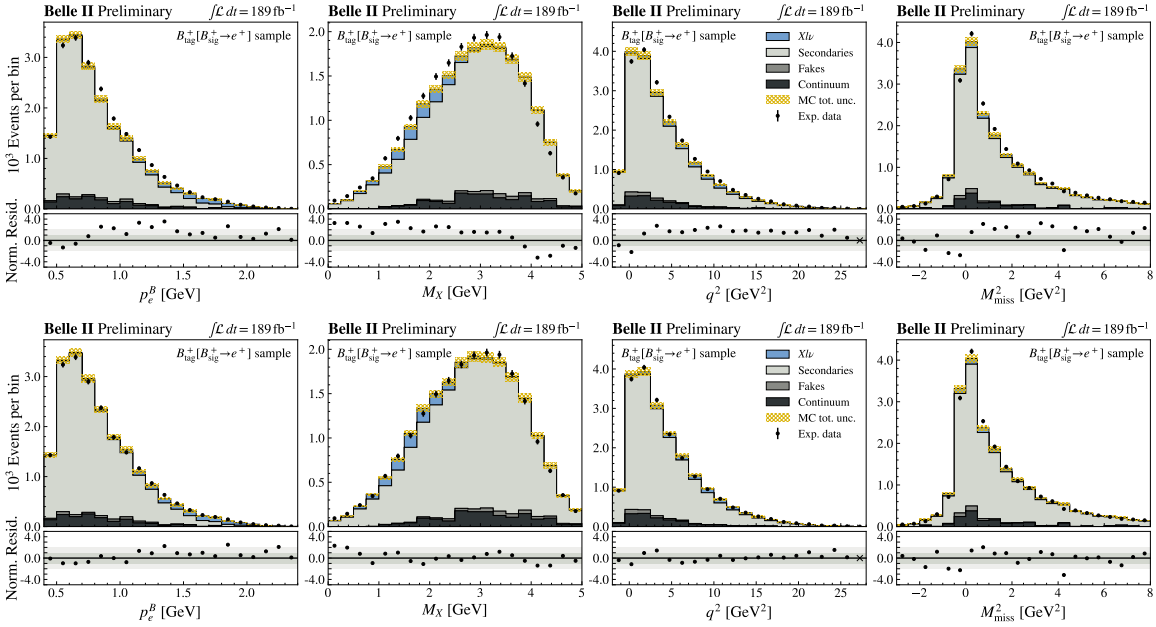

(a) Electron channel before (top) and after (bottom) the simulation reweighting

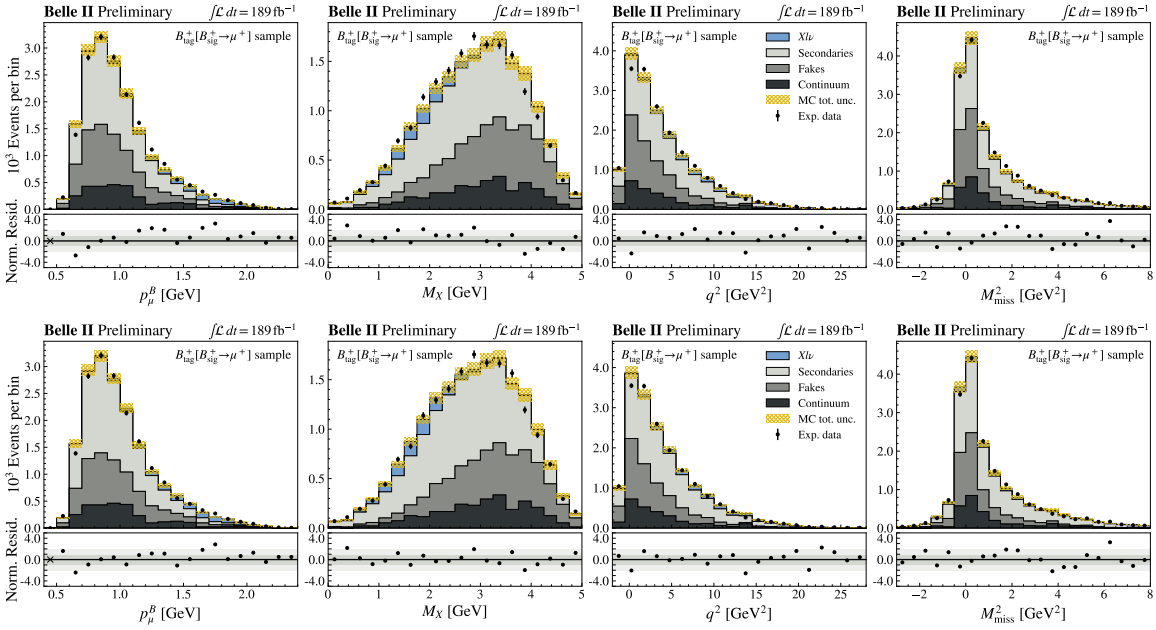

(b) Muon channel before (top) and after (bottom) the simulation reweighting

Figure B.21: The impact of the simulation reweighting (see Sec. 7.3) on the kinematic quantities p^B_ℓ, M_X, q^2, and M^2_{miss} is presented for the electron (a) and muon (b) channel in the same-flavor control sample with charged B_{tag} candidates. The top rows display the distributions before reweighting, along with the uncertainty-normalized residuals between the distributions of experimental data and simulation. In the bottom row of figures, the reweighted distributions are presented, revealing significantly reduced residuals.

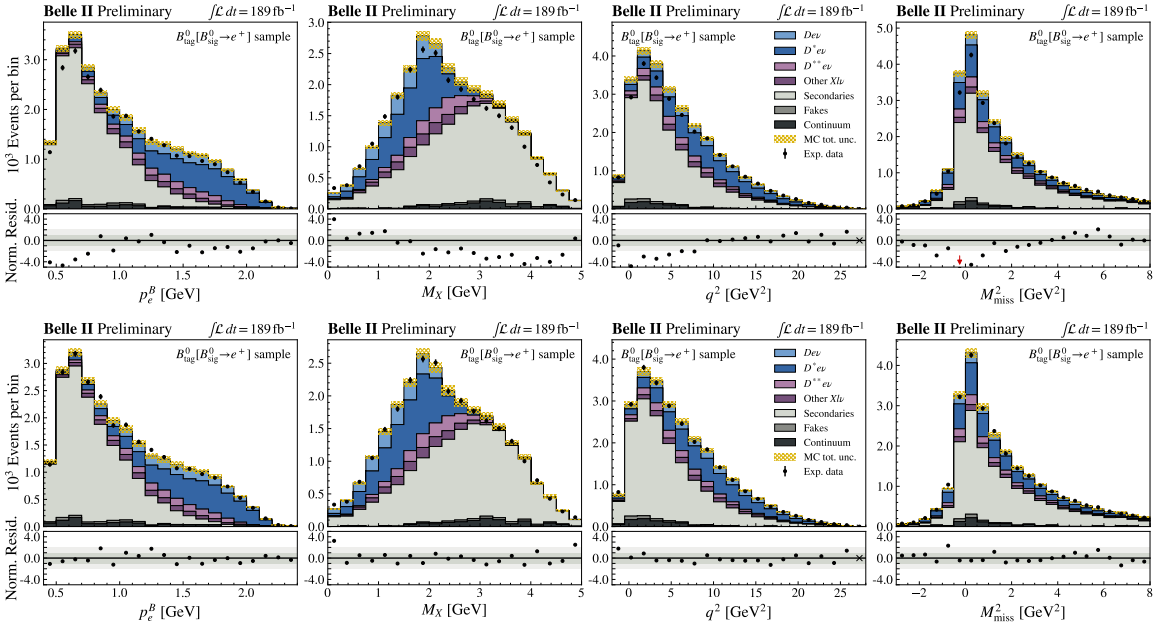

(a) Electron channel before (top) and after (bottom) the simulation reweighting

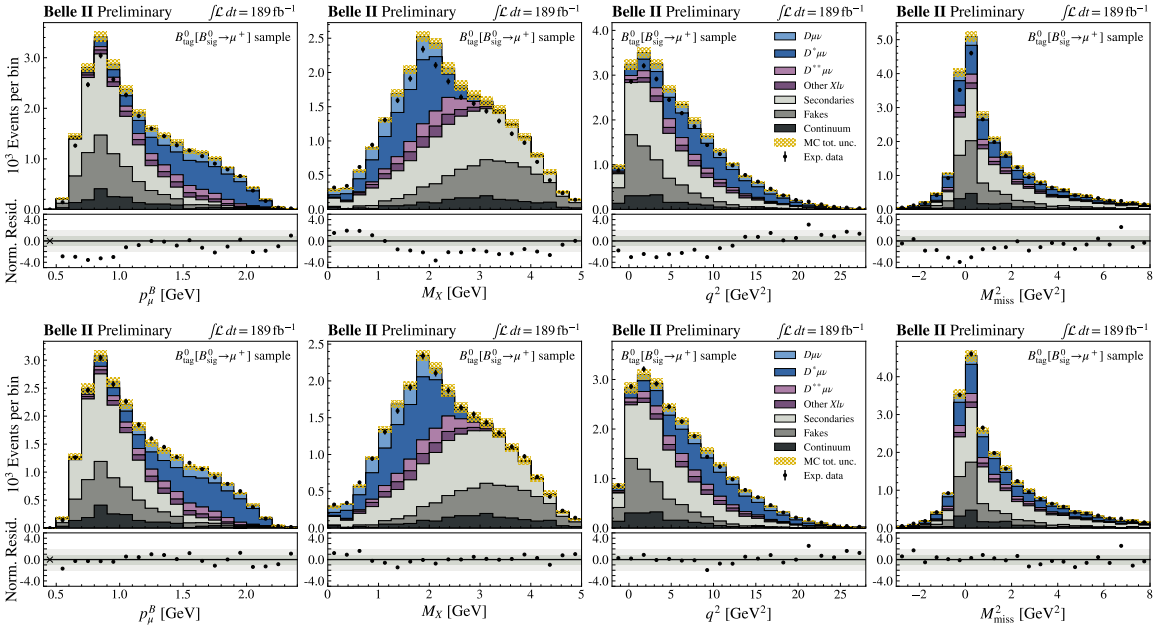

(b) Muon channel before (top) and after (bottom) the simulation reweighting

Figure B.22: The impact of the simulation reweighting (see Sec. 7.3) on the kinematic quantities p_ℓ^B, M_X, q^2, and M^2_{miss} is presented for the electron (a) and muon (b) channel in the same-flavor control sample with neutral B_{tag} candidates. The top rows display the distributions before reweighting, along with the uncertainty-normalized residuals between the distributions of experimental data and simulation. In the bottom row of figures, the reweighted distributions are presented, revealing significantly reduced residuals.

B.6 Impact of modified D-meson decay distributions on signal decays

In Section 7.2.3, compelling evidence is found, pointing to inaccuracies in the modeling of inclusive D-meson decays as the source of discrepancies between experimental data and simulation. These decays are unaffected by the signal-lepton flavor and the lepton momentum (see Sec. 7.3.3). Therefore, it is expected that the correction weights, obtained with $B \to X_c \ell \nu$ events in Section 7.3.2, should be equally applicable to signal decays, $B \to X_c[\tau \to \ell\nu\nu]\nu$. This section aims to validate this assumption.

For this purpose, the impacts of modified D-meson decays on the distributions of signal decays in p_ℓ^B, M_X, and M_{miss}^2 are examined, in analogy to Section B.3. As depicted in Figure B.23 for three example cases, the variation in the M_X distribution induced by the modified D-meson decays (yellow vs. green distributions in the figure) indeed replicates the observed pattern for $B \to X_c \ell \nu$ decays in Figures B.7 and B.8.

Moreover, a comparison is made between the blue distribution, which results from the application of $B \to X_c \ell \nu$-decay-based correction weights to the nominal signal decays, and the reweighted signal-decay distribution originating from the modified D-meson decays. In the latter case, the reweighting procedure outlined in Section 7.3 is repeated with the modified simulation samples, resulting in new correction weights similar to the ones depicted in Figure 8.3. The application of these new weights, derived once again from $B \to X_c \ell \nu$ decays, transforms the yellow distribution into the red one.

All presented quantities, p_ℓ^B, M_X, and M_{miss}^2, show almost perfect alignment between the red and blue distributions, as demonstrated by the normalized residuals. This alignment highlights that the modification of D-meson decays has an identical impact on $B \to X_c \ell \nu$ decays (used for deriving correction weights) as it does on signal decays. Therefore, the M_X-based reweighting is effective in correcting both signal and normalization decays equally.

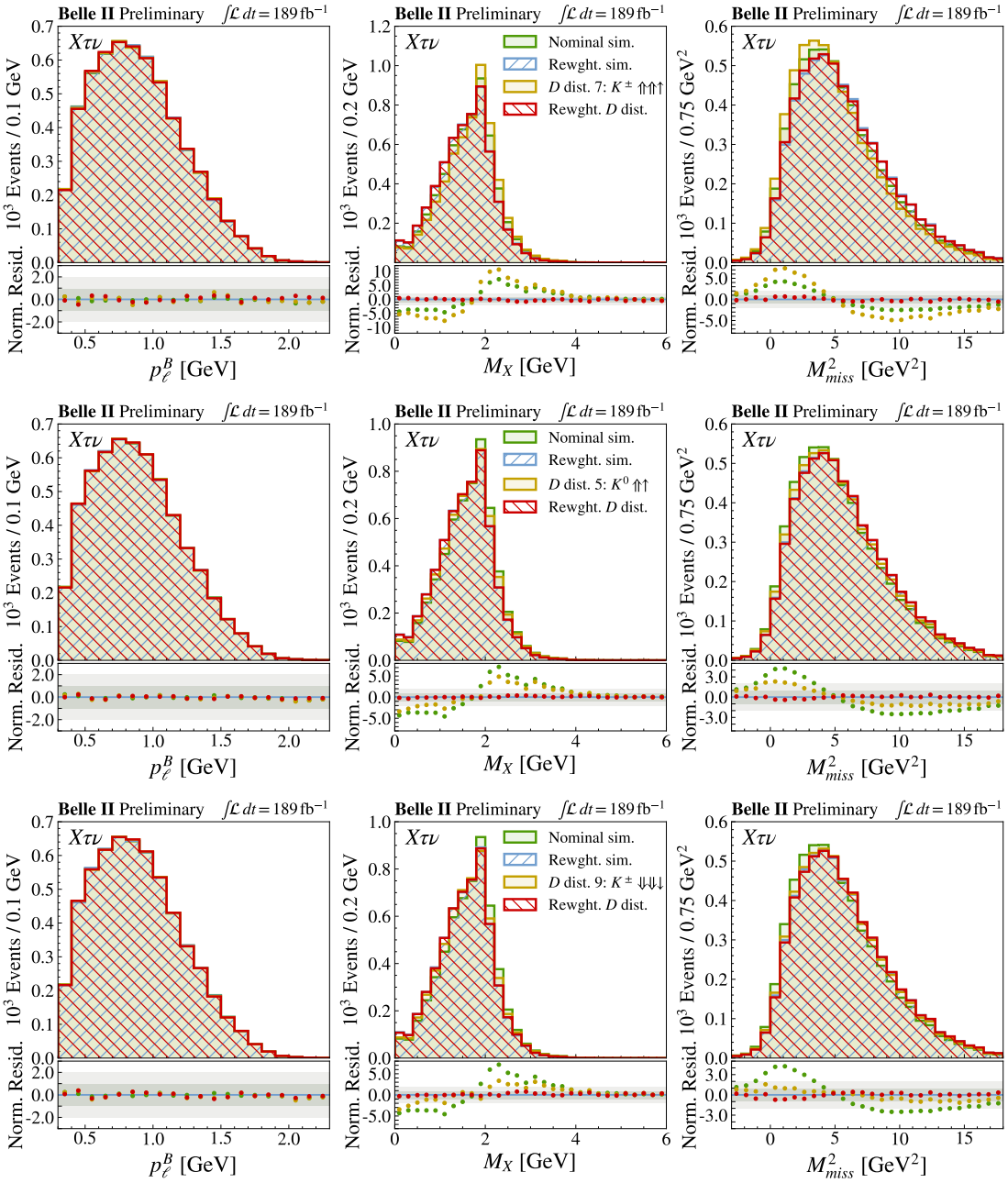

Figure B.23: The impacts of modified D-meson decays on signal-decay distributions are illustrated for p_ℓ^B, M_X, and M^2_{miss}. The nominal simulation is depicted in green, and the modified sample, specified in Table 6.4, is presented in yellow.
In addition, the reweighted nominal distribution, utilizing M_X-based correction weights derived with $B \to X_c \ell \nu$ decays, is shown in blue. A comparable reweighting based on simulations with the modified D-meson decays results in the red distribution. Residuals of each distribution to the blue one, normalized by the statistical uncertainty of the simulated samples, are displayed below.

B.7 Correction weights introduced in the reweighting

This section offers supplementary details regarding the simulation reweighting, as introduced in Section 7.3.

Figures B.24 and B.25 present analogs to Figure 7.20 for each M_X interval for charged B_{tag} candidates, used to reweight events featuring a neutral D-meson decay, and for neutral B_{tag} candidates used to reweight $\overline{B}^0_{\text{sig}} \to [X_c \to D^+ \dots] l\nu$ decays, respectively. These figures serve as the basis for deriving additional uncertainties for $B_{\text{sig}} \to X_c l\nu$ decays with low lepton momenta, as described in Section 7.3.3. Tables B.3 and B.4 summarize the numerical values of the correction weights for signal and normalization events, as well as $B\overline{B}$-background events, respectively.

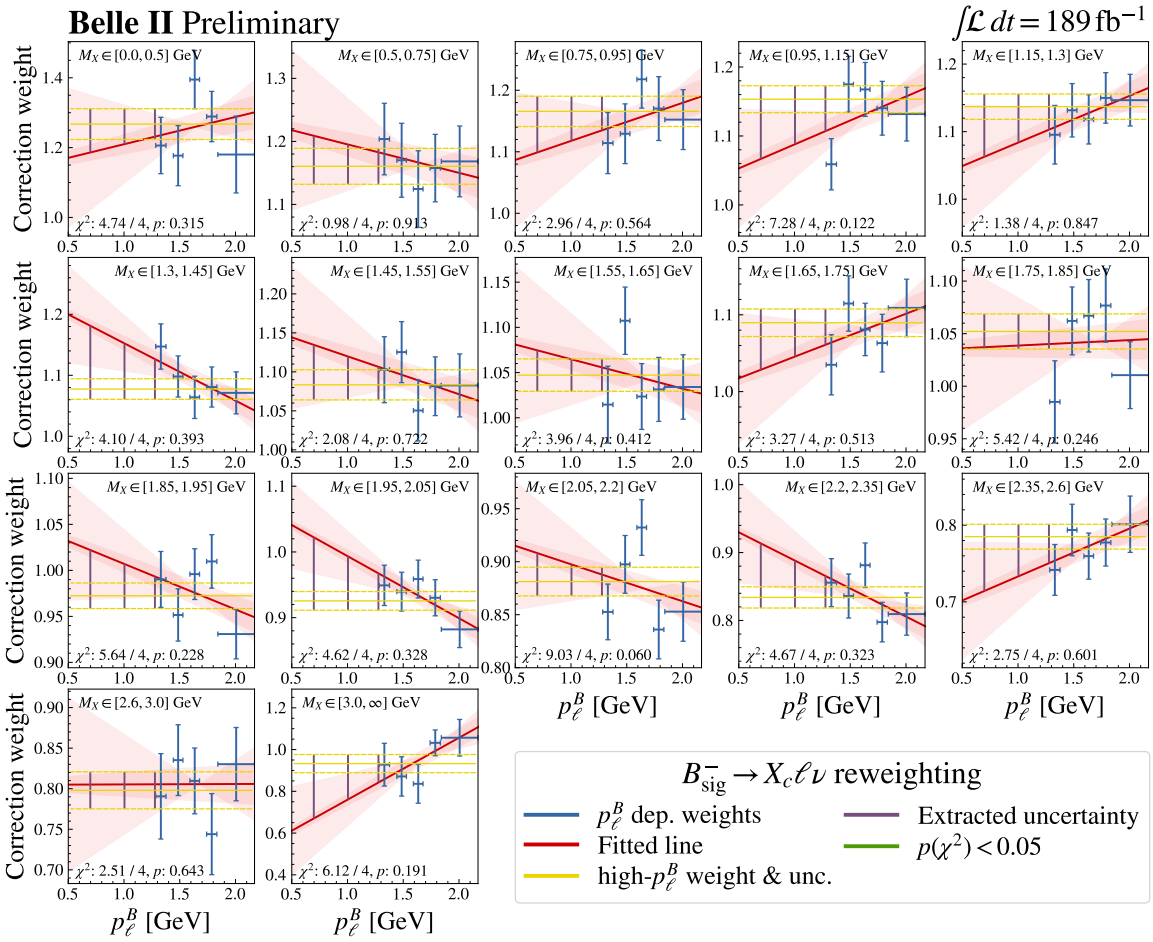

Figure B.24: The experimental-to-simulated yield ratios **for $B^-_{\text{sig}} \to X_c \ell \nu$ decays** in each M_X interval for different p_ℓ^B intervals are presented (blue data points). Their p_ℓ^B value corresponds to the averaged value in experimental data in each of the intervals. The χ^2 test results, performed in each M_X interval individually to quantify the hypothesis that they all agree with the nominal weight derived in the full high-p_ℓ^B control sample (yellow), is presented in each plot. A straight line is fitted to the data points and is extrapolated towards lower values of p_ℓ^B (red). In case of deviations larger than the statistical uncertainty of the nominal weight, additional uncertainties are introduced for low-momentum $B_{\text{sig}} \to X_c \ell \nu$ and $B_{\text{sig}} \to X_c \tau \nu$ decays (purple).

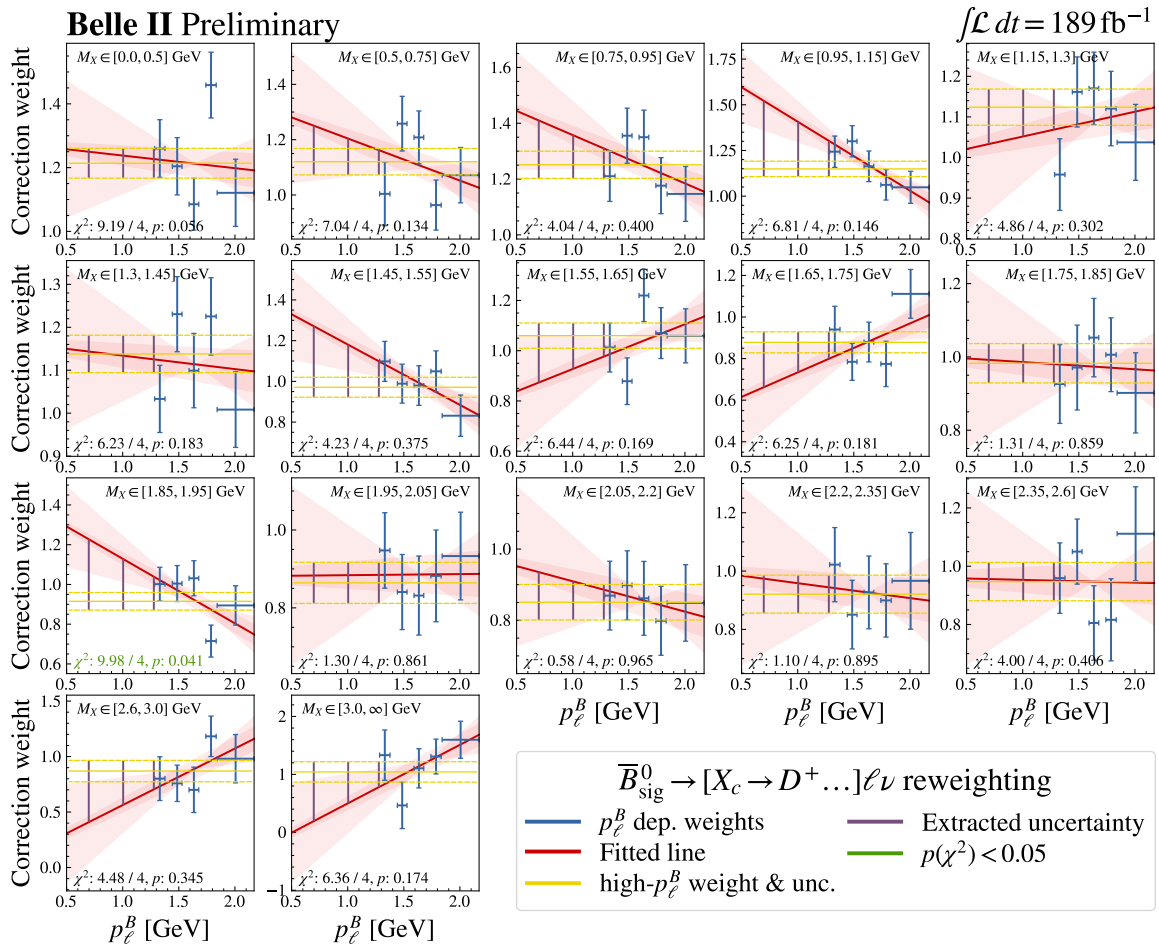

Figure B.25: The experimental-to-simulated yield ratios **for $\overline{B}^0_{\mathrm{sig}} \to [X_c \to D^+ \ldots]\ell\nu$ processes** in each M_X interval for different p_ℓ^B intervals are presented (blue data points). Their p_ℓ^B value corresponds to the averaged value in experimental data in each of the intervals. The χ^2 test results, performed in each M_X interval individually to quantify the hypothesis that they all agree with the nominal weight derived in the full high-p_ℓ^B control sample (yellow), is presented in each plot. A straight line is fitted to the data points and is extrapolated towards lower values of p_ℓ^B (red). In case of deviations larger than the statistical uncertainty of the nominal weight, additional uncertainties are introduced for low-momentum $B_{\mathrm{sig}} \to X_c \ell\nu$ and $B_{\mathrm{sig}} \to X_c \tau\nu$ decays (purple).

M_X interval	$B^-_{\text{sig}} \to X_c l\nu$ Correction weight	$\bar{B}^0_{\text{sig}} \to [X_c \to D^+ \ldots] l\nu$ Correction weight
$[-\infty, 0.5]$	$1.27\ ^{+0.04}_{-0.04}\ ^{+0.04}_{-0.04}\ ^{+0.04}_{-0.06}\ ^{+0.04}_{-0.08}$	$1.21\ ^{+0.05}_{-0.05}\ ^{+0.05}_{-0.05}\ ^{+0.05}_{-0.05}\ ^{+0.05}_{-0.05}$
$[0.5, 0.75]$	$1.16\ ^{+0.03}_{-0.03}\ ^{+0.03}_{-0.03}\ ^{+0.03}_{-0.03}\ ^{+0.05}_{-0.03}$	$1.12\ ^{+0.05}_{-0.05}\ ^{+0.05}_{-0.05}\ ^{+0.08}_{-0.05}\ ^{+0.13}_{-0.05}$
$[0.75, 0.95]$	$1.17\ ^{+0.02}_{-0.02}\ ^{+0.02}_{-0.03}\ ^{+0.02}_{-0.05}\ ^{+0.02}_{-0.07}$	$1.25\ ^{+0.05}_{-0.05}\ ^{+0.06}_{-0.05}\ ^{+0.11}_{-0.05}\ ^{+0.16}_{-0.05}$
$[0.95, 1.15]$	$1.15\ ^{+0.02}_{-0.02}\ ^{+0.02}_{-0.05}\ ^{+0.02}_{-0.07}\ ^{+0.02}_{-0.09}$	$1.15\ ^{+0.04}_{-0.04}\ ^{+0.15}_{-0.04}\ ^{+0.26}_{-0.04}\ ^{+0.37}_{-0.04}$
$[1.15, 1.3]$	$1.14\ ^{+0.02}_{-0.02}\ ^{+0.02}_{-0.03}\ ^{+0.02}_{-0.05}\ ^{+0.02}_{-0.07}$	$1.12\ ^{+0.04}_{-0.04}\ ^{+0.04}_{-0.06}\ ^{+0.04}_{-0.07}\ ^{+0.04}_{-0.09}$
$[1.3, 1.45]$	$1.08\ ^{+0.02}_{-0.02}\ ^{+0.05}_{-0.02}\ ^{+0.07}_{-0.02}\ ^{+0.10}_{-0.02}$	$1.14\ ^{+0.04}_{-0.04}\ ^{+0.04}_{-0.04}\ ^{+0.04}_{-0.04}\ ^{+0.04}_{-0.04}$
$[1.45, 1.55]$	$1.08\ ^{+0.02}_{-0.02}\ ^{+0.02}_{-0.02}\ ^{+0.04}_{-0.02}\ ^{+0.05}_{-0.02}$	$0.97\ ^{+0.05}_{-0.05}\ ^{+0.13}_{-0.05}\ ^{+0.21}_{-0.05}\ ^{+0.30}_{-0.05}$
$[1.55, 1.65]$	$1.05\ ^{+0.02}_{-0.02}\ ^{+0.02}_{-0.02}\ ^{+0.02}_{-0.02}\ ^{+0.03}_{-0.02}$	$1.06\ ^{+0.05}_{-0.05}\ ^{+0.05}_{-0.08}\ ^{+0.05}_{-0.13}\ ^{+0.05}_{-0.19}$
$[1.65, 1.75]$	$1.09\ ^{+0.02}_{-0.02}\ ^{+0.02}_{-0.03}\ ^{+0.02}_{-0.04}\ ^{+0.02}_{-0.06}$	$0.88\ ^{+0.05}_{-0.05}\ ^{+0.05}_{-0.08}\ ^{+0.05}_{-0.14}\ ^{+0.05}_{-0.22}$
$[1.75, 1.85]$	$1.05\ ^{+0.02}_{-0.02}\ ^{+0.02}_{-0.02}\ ^{+0.02}_{-0.02}\ ^{+0.02}_{-0.02}$	$0.98\ ^{+0.05}_{-0.05}\ ^{+0.05}_{-0.05}\ ^{+0.05}_{-0.05}\ ^{+0.05}_{-0.05}$
$[1.85, 1.95]$	$0.97\ ^{+0.01}_{-0.01}\ ^{+0.02}_{-0.01}\ ^{+0.03}_{-0.01}\ ^{+0.05}_{-0.01}$	$0.92\ ^{+0.04}_{-0.04}\ ^{+0.12}_{-0.04}\ ^{+0.21}_{-0.04}\ ^{+0.31}_{-0.04}$
$[1.95, 2.05]$	$0.93\ ^{+0.01}_{-0.01}\ ^{+0.04}_{-0.01}\ ^{+0.07}_{-0.01}\ ^{+0.10}_{-0.01}$	$0.86\ ^{+0.05}_{-0.05}\ ^{+0.05}_{-0.05}\ ^{+0.05}_{-0.05}\ ^{+0.05}_{-0.05}$
$[2.05, 2.2]$	$0.88\ ^{+0.01}_{-0.01}\ ^{+0.01}_{-0.01}\ ^{+0.02}_{-0.01}\ ^{+0.03}_{-0.01}$	$0.85\ ^{+0.05}_{-0.05}\ ^{+0.05}_{-0.05}\ ^{+0.06}_{-0.05}\ ^{+0.08}_{-0.05}$
$[2.2, 2.35]$	$0.83\ ^{+0.02}_{-0.02}\ ^{+0.03}_{-0.02}\ ^{+0.05}_{-0.02}\ ^{+0.08}_{-0.02}$	$0.92\ ^{+0.07}_{-0.07}\ ^{+0.07}_{-0.07}\ ^{+0.07}_{-0.07}\ ^{+0.07}_{-0.07}$
$[2.35, 2.6]$	$0.78\ ^{+0.02}_{-0.02}\ ^{+0.02}_{-0.03}\ ^{+0.02}_{-0.05}\ ^{+0.02}_{-0.07}$	$0.95\ ^{+0.07}_{-0.07}\ ^{+0.07}_{-0.07}\ ^{+0.07}_{-0.07}\ ^{+0.07}_{-0.07}$
$[2.6, 3.0]$	$0.80\ ^{+0.02}_{-0.02}\ ^{+0.02}_{-0.02}\ ^{+0.02}_{-0.02}\ ^{+0.02}_{-0.02}$	$0.87\ ^{+0.10}_{-0.10}\ ^{+0.10}_{-0.17}\ ^{+0.10}_{-0.30}\ ^{+0.10}_{-0.46}$
$[3.0, \infty]$	$0.93\ ^{+0.04}_{-0.04}\ ^{+0.04}_{-0.09}\ ^{+0.04}_{-0.17}\ ^{+0.04}_{-0.26}$	$1.04\ ^{+0.18}_{-0.18}\ ^{+0.18}_{-0.26}\ ^{+0.18}_{-0.54}\ ^{+0.18}_{-0.85}$

Table B.3: The correction weights, obtained in Section 7.3.2, for $B \to X_c \ell\nu$ and $B \to X_c \tau\nu$ decays are summarized for each M_X interval. The first set of uncertainties is applied to events satisfying $p_\ell^B > 1.4\,\text{GeV}$ and is derived based on the statistical precision of experimental data and simulation in the corresponding M_X interval. As described in Section 7.3.3, additional uncertainties are applied to $B \to X_c l\nu$ decays outside of the high-p_ℓ^B control sample. They are summarized subsequently. The second set of uncertainties refers to processes with $p_\ell^B \in [1.15\,\text{GeV}, 1.4\,\text{GeV}]$, followed by uncertainties for $p_\ell^B \in (0.85\,\text{GeV}, 1.15\,\text{GeV}]$ and $p_\ell^B \leq 0.85\,\text{GeV}$.

(p_ℓ, M_X) interval number	**Secondaries** Correction weight	**Muon fakes** Correction weight
1	$1.10(\pm0.02)(\pm0.10)$	–
2	$1.00(\pm0.02)(\pm0.04)$	–
3	$0.91(\pm0.02)(\pm0.09)$	–
4	$0.91(\pm0.02)(\pm0.09)$	–
5	$0.80(\pm0.02)(\pm0.20)$	–
6	$1.12(\pm0.04)(\pm0.12)$	0.40 ± 0.20
7	$1.14(\pm0.04)(\pm0.14)$	0.98 ± 0.12
8	$1.10(\pm0.04)(\pm0.10)$	0.90 ± 0.11
9	$1.04(\pm0.04)(\pm0.04)$	0.84 ± 0.09
10	$0.97(\pm0.03)(\pm0.03)$	0.96 ± 0.07
11	$0.97(\pm0.05)(\pm0.09)$	1.00 ± 0.06
12	$1.06(\pm0.05)(\pm0.06)$	1.12 ± 0.19
13	$1.06(\pm0.04)(\pm0.06)$	1.00 ± 0.11
14	$1.07(\pm0.05)(\pm0.07)$	1.05 ± 0.09
15	$1.10(\pm0.05)(\pm0.10)$	1.46 ± 0.16
16	$0.95(\pm0.09)(\pm0.17)$	1.27 ± 0.23

Table B.4: The correction weights, obtained in Section 7.3.4, for $B\bar{B}$-background events are summarized for each (p_ℓ, M_X) interval (numbered in Fig. 7.23). For secondaries, the first set of uncertainties is applied to all events featuring a B_{sig} decay into a single X_c meson. The second set of uncertainties is applied to all remaining secondaries, including these originating from $B \to X_c X_c$ decays, as well as from events referred to as tertiaries in Section 7.1.

B.8 D-meson decay distributions to validate uncertainties on $R(X_{\tau/\ell})$

In Section 8.1.3, the uncertainties on $R(X_{\tau/\ell})$ associated with the simulation reweighting are validated using various D-meson decay distributions, detailed in Tables B.5 and B.6. Most distributions are reused and relabeled[1] from the prior study that investigated the effects on $R(X_{e/\mu})$ in Section 6.1.3, as highlighted by equal arrow symbols representing varied decays into kaon types. Minor variations in kaon fractions in comparison to Table 6.4 are due to an updated data set.

Additionally, distributions 4, 5, 7, 8, 10, 11, 13, and 14 are introduced in this study to capture more reasonable changes corresponding to one to two standard deviations. Previous distribution 7 from Table 6.4, associated with a global pull of twelve standard deviations, is considered too unrealistic and is excluded from this investigation.

$D \to \ldots$	Distr. 1: $K^*\Uparrow$ [%]		Distr. 2: $K^*\Uparrow\Uparrow$ [%]		Distr. 3: $K^*\Downarrow\Downarrow$ [%]	
+ anything	$\mathcal{B}(D^0)$	$\mathcal{B}(D^+)$	$\mathcal{B}(D^0)$	$\mathcal{B}(D^+)$	$\mathcal{B}(D^0)$	$\mathcal{B}(D^+)$
K^-	54.9	34.4	52.8	41.6	57.3	26.4
K^+	3.4	6.4	3.1	5.5	3.8	7.2
$K^0/\,\bar{K}^0$	41.7	55.3	44.9	51.1	37.9	59.7
$K^{*+}/\,K^{*-}$	18.0	6.0	27.9	7.6	6.6	2.6
$K^{*0}/\,\bar{K}^{*0}$	12.7	28.4	17.9	45.0	4.9	9.9
$D \to \ldots$	Distr. 4: $K^0\downarrow$ [%]		Distr. 5: $K^0\Downarrow$ [%]		Distr. 6: $K^0\Downarrow\downarrow$ [%]	
+ anything	$\mathcal{B}(D^0)$	$\mathcal{B}(D^+)$	$\mathcal{B}(D^0)$	$\mathcal{B}(D^+)$	$\mathcal{B}(D^0)$	$\mathcal{B}(D^+)$
K^-	57.7	32.5	59.4	34.5	62.8	38.4
K^+	3.6	6.9	3.5	7.1	3.5	7.4
$K^0/\,\bar{K}^0$	37.9	54.6	35.9	51.7	31.9	46.0
$K^{*+}/\,K^{*-}$	12.3	4.4	12.1	4.3	11.5	4.1
$K^{*0}/\,\bar{K}^{*0}$	9.1	19.9	9.1	20.4	9.1	21.4
$D \to \ldots$	Distr. 7: $K^0\uparrow$ [%]		Distr. 8: $K^0\Uparrow$ [%]		Distr. 9: $K^0\Uparrow\uparrow$ [%]	
+ anything	$\mathcal{B}(D^0)$	$\mathcal{B}(D^+)$	$\mathcal{B}(D^0)$	$\mathcal{B}(D^+)$	$\mathcal{B}(D^0)$	$\mathcal{B}(D^+)$
K^-	54.3	28.5	53.3	26.5	49.3	22.5
K^+	3.6	6.7	3.6	6.5	3.6	6.2
$K^0/\,\bar{K}^0$	41.9	60.3	43.9	63.2	47.9	69.0
$K^{*+}/\,K^{*-}$	12.9	4.7	13.2	4.8	13.7	5.0
$K^{*0}/\,\bar{K}^{*0}$	9.1	18.9	9.1	18.4	9.1	17.3

Table B.5: The probed D-meson decay distributions are presented. They are created by up- and downweighting of certain inclusive D-meson branching fractions to specific kaon flavors, as indicated in each title. The nominal D-meson decay distribution in simulation and the experimental world average is presented in Table 7.5.

[1] The numbering of distributions 1, 2, and 3 remains unchanged. Previous distributions 4, 5, 6, 8, and 9 are now labeled as distribution numbers 6, 9, 12, 15, and 16, respectively.

$D \to \ldots$ + anything	Distr. 10: $K^{\pm} \uparrow$ [%] $\mathcal{B}(D^0)$	$\mathcal{B}(D^+)$	Distr. 11: $K^{\pm} \Uparrow$ [%] $\mathcal{B}(D^0)$	$\mathcal{B}(D^+)$	Distr. 12: $K^{\pm} \Uparrow\uparrow$ [%] $\mathcal{B}(D^0)$	$\mathcal{B}(D^+)$
K^-	58.8	32.0	61.6	33.5	67.2	36.6
K^+	3.7	6.9	3.8	7.1	4.0	7.4
$K^0/\,\overline{K}^0$	37.6	56.3	35.3	55.0	30.6	52.6
$K^{*+}/\,K^{*-}$	12.3	4.5	12.0	4.5	11.5	4.4
$K^{*0}/\,\overline{K}^{*0}$	9.2	19.9	9.2	20.4	9.3	21.3

$D \to \ldots$ + anything	Distr. 13: $K^{\pm} \downarrow$ [%] $\mathcal{B}(D^0)$	$\mathcal{B}(D^+)$	Distr. 14: $K^{\pm} \Downarrow$ [%] $\mathcal{B}(D^0)$	$\mathcal{B}(D^+)$	Distr. 15: $K^{\pm} \Downarrow\downarrow$ [%] $\mathcal{B}(D^0)$	$\mathcal{B}(D^+)$
K^-	53.2	29.0	50.4	27.4	47.6	25.9
K^+	3.5	6.7	3.4	6.5	3.2	6.4
$K^0/\,\overline{K}^0$	42.2	58.7	44.5	59.9	46.8	61.1
$K^{*+}/\,K^{*-}$	12.9	4.6	13.2	4.6	13.5	4.6
$K^{*0}/\,\overline{K}^{*0}$	9.1	18.9	9.0	18.4	9.0	17.9

$D \to \ldots$ + anything	Distr. 16: $K^{\pm} \Downarrow\Downarrow\downarrow$ [%] $\mathcal{B}(D^0)$	$\mathcal{B}(D^+)$
K^-	39.2	21.3
K^+	2.9	5.9
$K^0/\,\overline{K}^0$	53.8	64.8
$K^{*+}/\,K^{*-}$	14.3	4.7
$K^{*0}/\,\overline{K}^{*0}$	8.9	16.5

Table B.6: The probed D-meson decay distributions are presented. They are created by up- and downweighting of certain inclusive D-meson branching fractions to specific kaon flavors, as indicated in each title. The nominal D-meson decay distribution in simulation and the experimental world average is presented in Table 7.5.

B.9 Pre-fit distributions of p_ℓ^B and M_{miss}^2 in various subsets of data

Figures B.26 and B.27 present the two-dimensional pre-fit distributions of p_ℓ^B and M_{miss}^2, segmented into intervals used in the signal extraction, for subsets in the electron and muon channels, respectively. The subsets are based on the B_{tag}-candidate and signal-lepton charge. Excellent agreement between experimental data and simulation is observed. The full spectra are depicted in Figure 8.8.

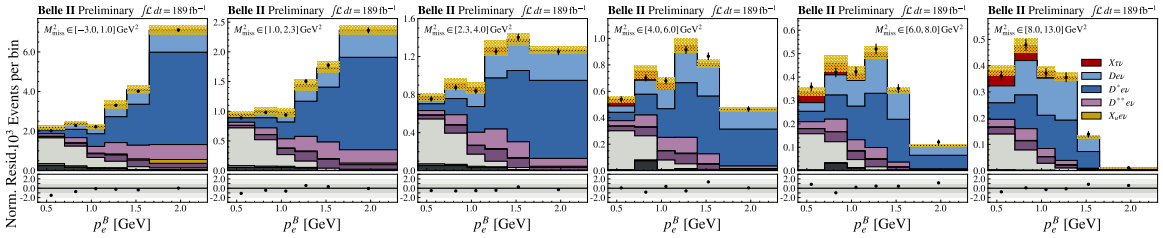

(a) B^0_{tag} channel

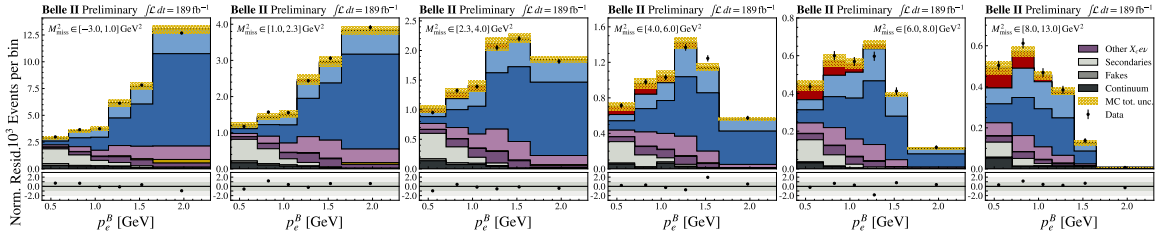

(b) B^+_{tag} channel

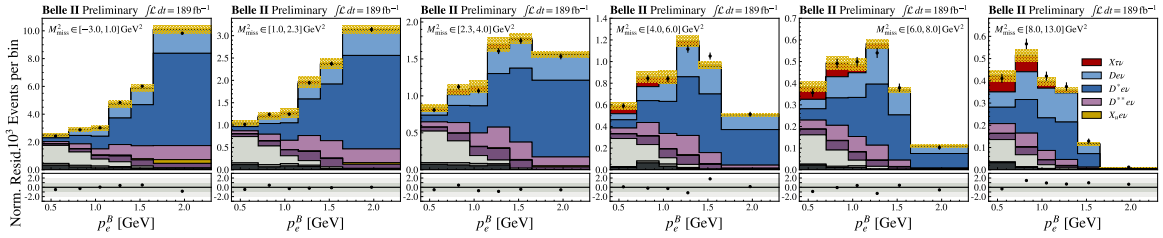

(c) e^- channel

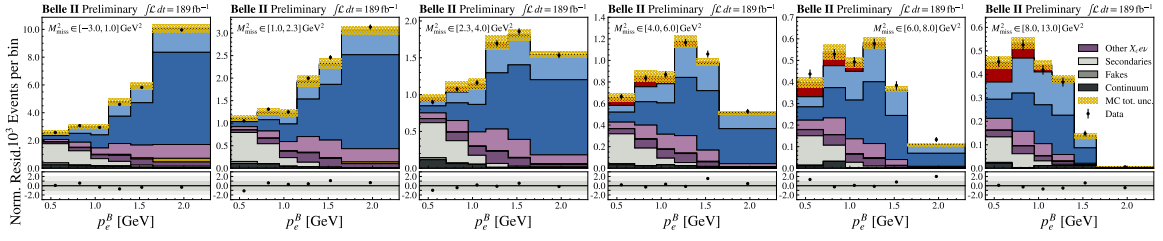

(d) e^+ channel

Figure B.26: The two-dimensional pre-fit distributions of p_ℓ^B and M_{miss}^2, segmented into intervals used in the signal extraction, for subsets **in the electron channel** are shown. The subsets are based on the B_{tag}-candidate and signal-lepton charge.

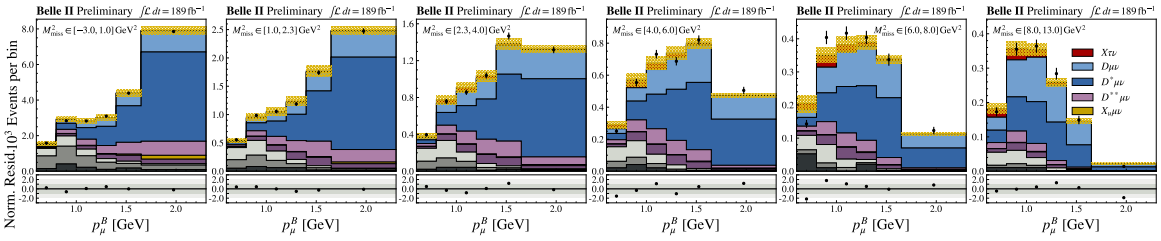

(a) B^0_{tag} channel

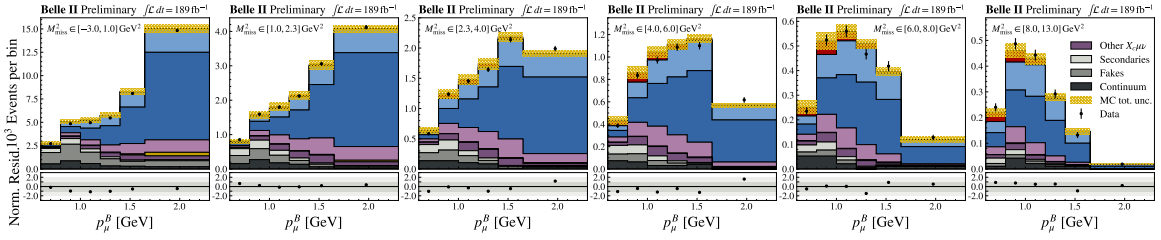

(b) B^+_{tag} channel

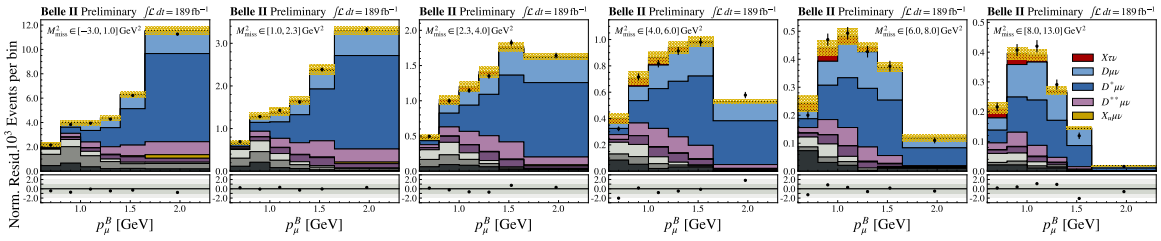

(c) μ^- channel

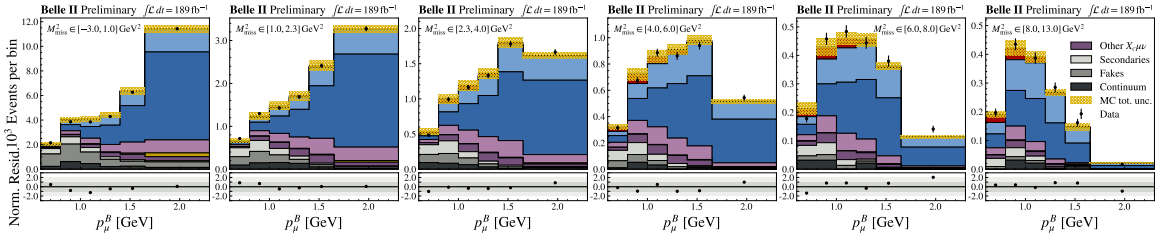

(d) μ^+ channel

Figure B.27: The two-dimensional pre-fit distributions of p_ℓ^B and M^2_{miss}, segmented into intervals used in the signal extraction, for subsets **in the muon channel** are shown. The subsets are based on the B_{tag}-candidate and signal-lepton charge.

Bibliography

[1] L. Aggarwal et al. (Belle II Collaboration), *Test of Light-Lepton Universality in the Rates of Inclusive Semileptonic B-Meson Decays at Belle II*, Phys. Rev. Lett. **131** (2023) 051804 (cit. on pp. 2, 23, 24, 79, 147).

[2] I. Adachi et al. (Belle II Collaboration), *First measurement of $R(X_{\tau/\ell})$ as an inclusive test of the $b \to c\tau\nu$ anomaly*, (2023), arXiv: 2311.07248 [hep-ex] (cit. on pp. 2, 23, 129).

[3] G. 't Hooft and M. J. G. Veltman, *Regularization and Renormalization of Gauge Fields*, Nucl. Phys. B **44** (1972) 189 (cit. on pp. 3, 9).

[4] S. Weinberg, *Elementary particle theory of composite particles*, Phys. Rev. **130** (1963) 776 (cit. on p. 3).

[5] S. L. Glashow, *Partial Symmetries of Weak Interactions*, Nucl. Phys. **22** (1961) 579 (cit. on pp. 3, 8).

[6] A. Salam and J. Ward, *Electromagnetic and weak interactions*, Phys. Lett. **13** (1964) 168 (cit. on pp. 3, 8).

[7] S. Weinberg, *A Model of Leptons*, Phys. Rev. Lett. **19** (1967) 1264 (cit. on pp. 3, 8).

[8] H. Fritzsch, M. Gell-Mann and H. Leutwyler, *Advantages of the Color Octet Gluon Picture*, Phys. Lett. B **47** (1973) 365 (cit. on pp. 3, 6).

[9] T. Aoyama, M. Hayakawa, T. Kinoshita and M. Nio, *Tenth-Order QED Contribution to the Electron $g-2$ and an Improved Value of the Fine Structure Constant*, Phys. Rev. Lett. **109** (2012) 111807 (cit. on p. 3).

[10] T. Aoyama, M. Hayakawa, T. Kinoshita and M. Nio, *Tenth-order electron anomalous magnetic moment: Contribution of diagrams without closed lepton loops*, Phys. Rev. D **91** (2015) 033006, [Erratum Phys. Rev. D **96** (2017) 019901] (cit. on p. 3).

[11] X. Fan, T. G. Myers, B. A. D. Sukra and G. Gabrielse, *Measurement of the Electron Magnetic Moment*, Phys. Rev. Lett. **130** (2023) 071801 (cit. on p. 3).

[12] B. Povh, K. Rith, C. Scholz, F. Zersche and W. Rodejohann, *Particles and nuclei: An Introduction to the physical concepts*, Graduate Texts in Physics, Springer, 1995, ISBN: 978-3-662-46320-8, URL: https://link.springer.com/book/10.1007/978-3-662-46321-5 (cit. on p. 3).

[13] G. Aad et al. (ATLAS Collaboration), *Observation of a new particle in the search for the Standard Model Higgs boson with the ATLAS detector at the LHC*, Phys. Lett. B **716** (2012) 1 (cit. on p. 3).

[14] S. Chatrchyan et al. (CMS Collaboration), *Observation of a new boson at a mass of 125 GeV with the CMS experiment at the LHC*, Phys. Lett. B **716** (2012) 30 (cit. on p. 3).

[15] G. Aad et al. (ATLAS Collaboration and CMS Collaboration), *Combined Measurement of the Higgs Boson Mass in pp Collisions at $\sqrt{s} = 7$ and 8 TeV with the ATLAS and CMS Experiments*, Phys. Rev. Lett. **114** (2015) 191803 (cit. on p. 3).

[16] Cush, *Standard Model of Elementary Particles*, visited on 25/09/2023, URL: https://en.wikipedia.org/wiki/File:Standard_Model_of_Elementary_Particles.svg (cit. on p. 4).

[17] R. L. Workman et al. (Particle Data Group), *Review of Particle Physics*, Prog. Theor. Exp. Phys. **2022** (2022) 083C01 (cit. on pp. 5, 7, 8, 11, 14, 36, 38, 40, 41, 47, 84, 109, 115).

[18] C. N. Yang and R. L. Mills, *Conservation of Isotopic Spin and Isotopic Gauge Invariance*, Phys. Rev. **96** (1954) 191 (cit. on p. 5).

[19] R. P. Feynman, *Mathematical Formulation of the Quantum Theory of Electromagnetic Interaction*, Phys. Rev. **80** (1950) 440 (cit. on p. 6).

[20] M. E. Peskin and D. V. Schroeder, *An Introduction to quantum field theory*, Reading, USA: Addison-Wesley, 1995, ISBN: 978-0-201-50397-5, URL: http://www.slac.stanford.edu/~mpeskin/QFT.html (cit. on pp. 6–11).

[21] M. D. Schwartz, *Quantum Field Theory and the Standard Model*, Cambridge University Press, 2014, ISBN: 978-1-107-03473-0, URL: http://www.cambridge.org/us/academic/subjects/physics/theoretical-physics-and-mathematical-physics/quantum-field-theory-and-standard-model (cit. on p. 6).

[22] C. G. Callan, *Broken Scale Invariance in Scalar Field Theory*, Phys. Rev. D **2** (1970) 1541 (cit. on p. 6).

[23] K. Symanzik, *Small distance behaviour in field theory and power counting*, Commun. Math. Phys. **18** (1970) 227 (cit. on p. 6).

[24] M. Thomson, *Modern particle physics*, New York: Cambridge University Press, 2013, ISBN: 978-1-107-03426-6, URL: https://doi.org/10.1017/CBO9781139525367 (cit. on pp. 7–11).

[25] M. Ablikim et al. (BESIII Collaboration), *Observation of a Near-Threshold Structure in the K^+ Recoil-Mass Spectra in $e^+e^- \to K^+(D_s^- D^{*0} + D_s^{*-} D^0)$*, Phys. Rev. Lett. **126** (2021) 102001 (cit. on p. 8).

[26] R. Aaij et al. (LHCb Collaboration), *Observation of an exotic narrow doubly charmed tetraquark*, Nature Phys. **18** (2022) 751 (cit. on p. 8).

[27] R. Aaij et al. (LHCb Collaboration), *Observation of $J/\psi p$ Resonances Consistent with Pentaquark States in $\Lambda_b^0 \to J/\psi K^- p$ Decays*, Phys. Rev. Lett. **115** (2015) 072001 (cit. on p. 8).

[28] R. Aaij et al. (LHCb Collaboration), *Observation of a narrow pentaquark state, $P_c(4312)^+$, and of two-peak structure of the $P_c(4450)^+$*, Phys. Rev. Lett. **122** (2019) 222001 (cit. on p. 8).

[29] C. S. Wu, E. Ambler, R. W. Hayward, D. D. Hoppes and R. P. Hudson, *Experimental Test of Parity Conservation in Beta Decay*, Phys. Rev. **105** (1957) 1413 (cit. on p. 8).

[30] M. Goldhaber, L. Grodzins and A. W. Sunyar, *Helicity of Neutrinos*, Phys. Rev. **109** (1958) 1015 (cit. on p. 8).

[31] G. 't Hooft, *Renormalization of Massless Yang-Mills Fields*, Nucl. Phys. B **33** (1971) 173 (cit. on p. 9).

[32] G. 't Hooft, *Renormalizable Lagrangians for Massive Yang-Mills Fields*, Nucl. Phys. B **35** (1971) 167 (cit. on p. 9).

[33] P. W. Higgs, *Broken Symmetries and the Masses of Gauge Bosons*, Phys. Rev. Lett. **13** (1964) 508 (cit. on p. 9).

[34] F. Englert and R. Brout, *Broken Symmetry and the Mass of Gauge Vector Mesons*, Phys. Rev. Lett. **13** (1964) 321 (cit. on p. 9).

[35] G. Aad et al. (ATLAS Collaboration), *Measurement of the Higgs boson mass in the $H \to ZZ^* \to 4\ell$ decay channel using 139 fb^{-1} of $\sqrt{s} = 13$ TeV pp collisions recorded by the ATLAS detector at the LHC*, Phys. Lett. B **843** (2023) 137880 (cit. on p. 10).

[36] A. Sirunyan et al. (CMS Collaboration), *A measurement of the Higgs boson mass in the diphoton decay channel*, Phys. Lett. B **805** (2020) 135425 (cit. on p. 10).

[37] H. Junkerkalefeld, *Study Towards Analysing the Higgs Self-Coupling in the $hh \to 4\tau$ Channel at the ATLAS Detector*, Master thesis: Universität Bonn, 2019, URL: https://cds.cern.ch/record/2724038 (cit. on p. 10).

[38] G. Aad et al. (ATLAS Collaboration), *Constraints on the Higgs boson self-coupling from single- and double-Higgs production with the ATLAS detector using pp collisions at $\sqrt{s} = 13$ TeV*, Phys. Lett. B **843** (2023) 137745 (cit. on p. 10).

[39] A. Tumasyan et al. (CMS Collaboration), *A portrait of the Higgs boson by the CMS experiment ten years after the discovery*, Nature **607** (2022) 60 (cit. on p. 10).

[40] N. Cabibbo, *Unitary Symmetry and Leptonic Decays*, Phys. Rev. Lett. **10** (1963) 531 (cit. on p. 11).

[41] M. Kobayashi and T. Maskawa, *CP-Violation in the Renormalizable Theory of Weak Interaction*, Prog. Theor. Phys. **49** (1973) 652 (cit. on p. 11).

[42] L. Wolfenstein, *Parametrization of the Kobayashi-Maskawa Matrix*, Phys. Rev. Lett. **51** (1983) 1945 (cit. on p. 11).

[43] J. Charles et al. (CKMfitter Group), *Current status of the standard model CKM fit and constraints on $\Delta F = 2$ new physics*, Phys. Rev. D **91** (2015) 073007 (cit. on p. 11).

[44] M. Bona et al. (UTfit Collaboration), *New UTfit Analysis of the Unitarity Triangle in the Cabibbo-Kobayashi-Maskawa scheme*, Rend. Lincei Sci. Fis. Nat. **34** (2023) 37 (cit. on p. 11).

[45] J. Charles et al. (CKMfitter Group), *The global CKM fit in the large $(\bar{\rho}, \bar{\eta})$ plane*, visited on 02/10/2023, 2021, URL: http://ckmfitter.in2p3.fr/www/results/plots_spring21/ckm_res_spring21.html (cit. on p. 12).

[46] A. Einstein, *Die Feldgleichungen der Gravitation*, Sitzungsberichte der Königlich Preußischen Akademie der Wissenschaften (Berlin), Seite 844-847. (1915), URL: http://adsabs.harvard.edu/abs/1915SPAW.....844E (cit. on p. 12).

[47] S. M. Carroll, *Spacetime and Geometry: An Introduction to General Relativity*, Cambridge University Press, 2019, ISBN: 978-1-108-48839-6, URL: https://doi.org/10.1017/9781108770385 (cit. on p. 12).

[48] N. Aghanim et al. (Planck Collaboration), *Planck 2018 results. VI. Cosmological parameters*, Astron. Astrophys. **641** (2020) A6, [Erratum: Astron. Astrophys. **652** (2021) C4] (cit. on pp. 12, 13).

[49] E. Aprile et al. (XENON Collaboration), *First Dark Matter Search with Nuclear Recoils from the XENONnT Experiment*, Phys. Rev. Lett. **131** (2023) 041003 (cit. on p. 13).

[50] J. Aalbers et al. (LUX-ZEPLIN Collaboration), *First Dark Matter Search Results from the LUX-ZEPLIN (LZ) Experiment*, Phys. Rev. Lett. **131** (2023) 041002 (cit. on p. 13).

[51] J. E. Kim, *Weak-Interaction Singlet and Strong* CP *Invariance*, Phys. Rev. Lett. **43** (1979) 103 (cit. on p. 13).

[52] M. Shifman, A. Vainshtein and V. Zakharov, *Can confinement ensure natural CP invariance of strong interactions?*, Nucl. Phys. B **166** (1980) 493 (cit. on p. 13).

[53] M. Dine, W. Fischler and M. Srednicki, *A simple solution to the strong CP problem with a harmless axion*, Phys. Lett. B **104** (1981) 199 (cit. on p. 13).

[54] A. R. Zhitnitsky., *On possible suppression of the axion hadron interactions. (in russian)*, Sov. J. Nucl. Phys. **31** (1980) 260 (cit. on p. 13).

[55] S. Dodelson and L. M. Widrow, *Sterile neutrinos as dark matter*, Phys. Rev. Lett. **72** (1994) 17 (cit. on p. 13).

[56] X. Shi and G. M. Fuller, *New Dark Matter Candidate: Nonthermal Sterile Neutrinos*, Phys. Rev. Lett. **82** (1999) 2832 (cit. on p. 13).

[57] R. Adhikari et al., *A White Paper on keV sterile neutrino Dark Matter*, JCAP **2017** (2017) 025 (cit. on p. 13).

[58] B. Carr, F. Kühnel and M. Sandstad, *Primordial black holes as dark matter*, Phys. Rev. D **94** (2016) 083504 (cit. on p. 13).

[59] M. Milgrom, *A modification of the Newtonian dynamics as a possible alternative to the hidden mass hypothesis*, Astrophys. J. **270** (1983) 365 (cit. on p. 13).

[60] V. Mossa et al., *The baryon density of the Universe from an improved rate of deuterium burning*, Nature **587** (2020) 210 (cit. on p. 13).

[61] A. G. Cohen, D. B. Kaplan and A. E. Nelson, *Progress in Electroweak Baryogenesis*, Ann. Rev. Nucl. Part. Sci. **43** (1993) 27 (cit. on p. 13).

[62] D. E. Morrissey and M. J. Ramsey-Musolf, *Electroweak baryogenesis*, New J. Phys. **14** (2012) 125003 (cit. on p. 13).

[63] F. R. Klinkhamer and N. S. Manton, *A Saddle Point Solution in the Weinberg-Salam Theory*, Phys. Rev. D **30** (1984) 2212 (cit. on p. 13).

[64] A. D. Sakharov, *Violation of CP Invariance, C asymmetry, and baryon asymmetry of the universe*, Pisma Zh. Eksp. Teor. Fiz. **5** (1967) 32 (cit. on p. 13).

[65] M. B. Gavela, P. Hernandez, J. Orloff and O. Pene, *Standard model CP violation and baryon asymmetry*, Mod. Phys. Lett. A **9** (1994) 795 (cit. on p. 13).

[66] M. Gavela, P. Hernandez, J. Orloff, O. Pene and C. Quimbay, *Standard model CP-violation and baryon asymmetry (II). Finite temperature*, Nucl. Phys. B **430** (1994) 382 (cit. on p. 13).

[67] Y. Fukuda et al. (Super-Kamiokande Collaboration), *Evidence for Oscillation of Atmospheric Neutrinos*, Phys. Rev. Lett. **81** (1998) 1562 (cit. on p. 13).

[68] Q. R. Ahmad et al. (SNO Collaboration), *Measurement of the Rate of* $\nu_e + d \rightarrow p + p + e^-$ *Interactions Produced by* ^8B *Solar Neutrinos at the Sudbury Neutrino Observatory*, Phys. Rev. Lett. **87** (2001) 071301 (cit. on p. 13).

[69] Q. R. Ahmad et al. (SNO Collaboration), *Direct Evidence for Neutrino Flavor Transformation from Neutral-Current Interactions in the Sudbury Neutrino Observatory*, Phys. Rev. Lett. **89** (2002) 011301 (cit. on p. 13).

[70] P. Minkowski, $\mu \rightarrow e\gamma$ *at a Rate of One Out of* 10^9 *Muon Decays?*, Phys. Lett. B **67** (1977) 421 (cit. on p. 13).

[71] T. Yanagida, *Horizontal Symmetry and Masses of Neutrinos*, Prog. Theor. Phys. **64** (1980) 1103 (cit. on p. 13).

[72] H. Fritzsch and P. Minkowski, *Unified interactions of leptons and hadrons*, Annals Phys. **93** (1975) 193 (cit. on p. 13).

[73] S. Weinberg, *Implications of dynamical symmetry breaking*, Phys. Rev. D **13** (1976) 974 (cit. on p. 14).

[74] L. Susskind, *Dynamics of Spontaneous Symmetry Breaking in the Weinberg-Salam Theory*, Phys. Rev. D **20** (1979) 2619 (cit. on p. 14).

[75] S. P. Martin, *A Supersymmetry primer*, Adv. Ser. Direct. High Energy Phys. **18** (1998) 1, ed. by G. L. Kane (cit. on p. 14).

[76] G. C. Branco et al., *Theory and phenomenology of two-Higgs-doublet models*, Phys. Rept. **516** (2012) 1 (cit. on p. 14).

[77] T. E. Browder, T. Gershon, D. Pirjol, A. Soni and J. Zupan, *New physics at a Super Flavor Factory*, Rev. Mod. Phys. **81** (2009) 1887 (cit. on p. 14).

[78] M. Neubert, *B decays and the heavy quark expansion*, Adv. Ser. Direct. High Energy Phys. **15** (1998) 239, ed. by A. J. Buras and M. Lindner (cit. on p. 15).

[79] I. Caprini, L. Lellouch and M. Neubert, *Dispersive bounds on the shape of $B \to D^{(*)} \ell\nu$ form factors*, Nucl. Phys. B **530** (1998) 153 (cit. on p. 16).

[80] J. A. Bailey et al. (Fermilab Lattice and MILC Collaborations), *$B \to D\ell\nu$ form factors at nonzero recoil and $|V_{cb}|$ from 2 + 1-flavor lattice QCD*, Phys. Rev. D **92** (2015) 034506 (cit. on p. 16).

[81] A. Bazavov et al. (Fermilab Lattice and MILC Collaboration), *Semileptonic form factors for $B \to D^* \ell\nu$ at nonzero recoil from 2 + 1-flavor lattice QCD*, Eur. Phys. J. C **82** (2022) 1141 (cit. on p. 16).

[82] J. Harrison and C. T. H. Davies, *$B \to D^*$ vector, axial-vector and tensor form factors for the full q^2 range from lattice QCD*, (2023), arXiv: 2304.03137 [hep-lat] (cit. on p. 16).

[83] C. G. Boyd, B. Grinstein and R. F. Lebed, *Constraints on form-factors for exclusive semileptonic heavy to light meson decays*, Phys. Rev. Lett. **74** (1995) 4603 (cit. on pp. 17, 38).

[84] F. U. Bernlochner, Z. Ligeti and D. J. Robinson, *$N = 5, 6, 7, 8$: Nested hypothesis tests and truncation dependence of $|V_{cb}|$*, Phys. Rev. D **100** (2019) 013005 (cit. on p. 17).

[85] F. U. Bernlochner et al., *Constrained second-order power corrections in HQET: $R(D^{(*)})$, $|V_{cb}|$, and new physics*, Phys. Rev. D **106** (2022) 096015 (cit. on pp. 17, 38, 65, 131, 132, 134, 155).

[86] A. K. Leibovich, Z. Ligeti, I. W. Stewart and M. B. Wise, *Predictions for $B \to D_1(2420)\ell\overline{\nu}$ and $B \to D_2^*(2460)\ell\overline{\nu}$ at Order $\Lambda_{QCD}/m_{c,b}$*, Phys. Rev. Lett. **78** (1997) 3995 (cit. on p. 17).

[87] A. K. Leibovich, Z. Ligeti, I. W. Stewart and M. B. Wise, *Semileptonic B decays to excited charmed mesons*, Phys. Rev. D **57** (1998) 308 (cit. on p. 17).

[88] F. U. Bernlochner and Z. Ligeti, *Semileptonic $B_{(s)}$ decays to excited charmed mesons with e, μ, τ and searching for new physics with $R(D^{**})$*, Phys. Rev. D **95** (2017) 014022 (cit. on pp. 17, 38).

[89] F. U. Bernlochner, Z. Ligeti and D. J. Robinson, *Model-independent analysis of semileptonic B decays to D^{**} for arbitrary new physics*, Phys. Rev. D **97** (2018) 075011 (cit. on pp. 17, 38, 41, 65, 134).

[90] F. D. Fazio and M. Neubert, *$B \to X_u \ell \overline{\nu}_\ell$ decay distributions to order α_s*, JHEP **1999** (1999) 017 (cit. on p. 18).

[91] S. Bosch, B. Lange, M. Neubert and G. Paz, *Factorization and shape-function effects in inclusive B-meson decays*, Nucl. Phys. B **699** (2004) 335 (cit. on p. 18).

[92] J. R. Andersen and E. Gardi, *Inclusive spectra in charmless semileptonic B decays by dressed gluon exponentiation*, JHEP **2006** (2006) 097 (cit. on p. 18).

[93] P. Gambino, P. Giordano, G. Ossola and N. Uraltsev, *Inclusive semileptonic B decays and the determination of $|V_{ub}|$*, JHEP **2007** (2007) 058 (cit. on p. 18).

[94] U. Aglietti, F. Di Lodovico, G. Ferrera and G. Ricciardi, *Inclusive measure of $|V_{ub}|$ with the analytic coupling model*, Eur. Phys. J. C **59** (2009) 831 (cit. on p. 18).

[95] C. Bourrely, L. Lellouch and I. Caprini, *Model-independent description of $B \to \pi l \nu$ decays and a determination of $|V_{ub}|$*, Phys. Rev. D **79** (2009) 013008, [Erratum: Phys. Rev. D **82** (2010) 099902] (cit. on p. 18).

[96] A. Bharucha, D. M. Straub and R. Zwicky, *$B \to V \ell^+ \ell^-$ in the Standard Model from light-cone sum rules*, JHEP **08** (2016) 098 (cit. on p. 18).

[97] C. Ramirez, J. F. Donoghue and G. Burdman, *Semileptonic $b \to u$ decay*, Phys. Rev. D **41** (1990) 1496 (cit. on pp. 18, 38).

[98] C. Albajar et al. (UA1 Collaboration), *Studies of intermediate vector boson production and decay in UA1 at the CERN proton-antiproton collider*, Zeitschrift für Physik C Particles and Fields **44** (1989) 15 (cit. on p. 18).

[99] F. Abe et al. (CDF Collaboration), *Measurement of the ratio $B(W \to \tau\nu)/B(W \to e\nu)$ in $p\overline{p}$ collisions at $\sqrt{s} = 1.8$ TeV*, Phys. Rev. Lett. **68** (1992) 3398 (cit. on p. 18).

[100] J. Alitti et al. (UA2 Collaboration), *A search for charged Higgs from top quark decay at the CERN $p\overline{p}$ collider*, Phys. Lett. B **280** (1992) 137 (cit. on p. 18).

[101] F. Abe et al. (CDF Collaboration), *Measurement of the production and muonic decay rate of W and Z bosons in $p\overline{p}$-collisions at $\sqrt{s} = 1.8$ TeV*, Phys. Rev. Lett. **69** (1992) 28 (cit. on p. 18).

[102] S. Abachi et al. (D0 Collaboration),
W and Z Boson Production in $p\overline{p}$ Collisions at $\sqrt{s} = 1.8$ TeV, Phys. Rev. Lett. **75** (1995) 1456 (cit. on p. 18).

[103] B. Abbott et al. (D0 Collaboration),
Measurement of the $W \to \tau\nu$ Production Cross Section in $p\bar{p}$ Collisions at $\sqrt{s} = 1.8$ TeV, Phys. Rev. Lett. **84** (2000) 5710 (cit. on p. 18).

[104] ALEPH, DELPHI, L3, OPAL, SLD Collaborations, LEP Electroweak Working Group, SLD Electroweak and Heavy Flavors Group,
Precision electroweak measurements on the Z resonance, Phys. Rept. **427** (2006) 257 (cit. on p. 18).

[105] ALEPH, DELPHI, L3, OPAL, SLD Collaborations, LEP Electroweak Working Group,
Electroweak measurements in electron–positron collisions at W-boson-pair energies at LEP, Phys. Rept. **532** (2013) 119 (cit. on p. 18).

[106] M. Aaboud et al. (ATLAS Collaboration), *Precision measurement and interpretation of inclusive W^+ , W^- and Z/γ^* production cross sections with the ATLAS detector*, Eur. Phys. J. C **77** (2017) 367 (cit. on p. 18).

[107] G. Aad et al. (ATLAS Collaboration), *Test of the universality of τ and μ lepton couplings in W-boson decays with the ATLAS detector*, Nature Phys. **17** (2021) 813 (cit. on p. 18).

[108] A. Tumasyan et al. (CMS Collaboration), *Precision measurement of the W boson decay branching fractions in proton-proton collisions at $\sqrt{s} = 13$ TeV*, Phys. Rev. D **105** (2022) 072008 (cit. on p. 18).

[109] R. Aaij et al. (LHCb Collaboration),
Measurement of forward $W \to e\nu$ production in pp collisions at $\sqrt{s} = 8$ TeV, JHEP **10** (2016) 030 (cit. on p. 18).

[110] R. Aaij et al. (LHCb Collaboration),
Measurement of $Z \to \tau^+\tau^-$ production in proton-proton collisions at $\sqrt{s} = 8$ TeV, JHEP **09** (2018) 159 (cit. on p. 18).

[111] Y. Grossman and Z. Ligeti, *The Inclusive $\bar{B} \to \tau\bar{\nu}X$ decay in two Higgs doublet models*, Phys. Lett. B **332** (1994) 373 (cit. on p. 18).

[112] D. Bečirević et al.,
Scalar leptoquarks from grand unified theories to accommodate the B-physics anomalies, Phys. Rev. D **98** (2018) 055003 (cit. on p. 18).

[113] J. P. Lees et al. (BaBar Collaboration), *Evidence for an excess of $\bar{B} \to D^{(*)}\tau^-\bar{\nu}_\tau$ decays*, Phys. Rev. Lett. **109** (2012) 101802 (cit. on pp. 19–21, 23, 149, 151, 153).

[114] J. P. Lees et al. (BaBar Collaboration), *Measurement of an Excess of $\bar{B} \to D^{(*)}\tau^-\bar{\nu}_\tau$ Decays and Implications for Charged Higgs Bosons*, Phys. Rev. D **88** (2013) 072012 (cit. on pp. 19–21, 23, 149, 151, 153).

[115] M. Huschle et al. (Belle Collaboration), *Measurement of the branching ratio of $\bar{B} \to D^{(*)}\tau^-\bar{\nu}_\tau$ relative to $\bar{B} \to D^{(*)}\ell^-\bar{\nu}_\ell$ decays with hadronic tagging at Belle*, Phys. Rev. D **92** (2015) 072014 (cit. on pp. 19–21, 23, 149, 151, 153).

[116] S. Hirose et al. (Belle Collaboration),
Measurement of the τ lepton polarization and $R(D^*)$ in the decay $\bar{B} \to D^* \tau^- \bar{\nu}_\tau$,
Phys. Rev. Lett. **118** (2017) 211801 (cit. on pp. 19–21, 23, 149, 151, 153).

[117] S. Hirose et al. (Belle Collaboration), *Measurement of the τ lepton polarization and $R(D^*)$ in the decay $\overline{B} \to D^* \tau^- \overline{\nu}_\tau$ with one-prong hadronic τ decays at Belle*,
Phys. Rev. D **97** (2018) 012004 (cit. on pp. 19–21, 23, 149, 151, 153).

[118] G. Caria et al. (Belle Collaboration),
Measurement of $\mathcal{R}(D)$ and $\mathcal{R}(D^*)$ with a Semileptonic Tagging Method,
Phys. Rev. Lett. **124** (2020) 161803 (cit. on pp. 19–21, 23, 149, 151, 153).

[119] I. Adachi et al. (Belle II Collaboration), *A test of lepton flavor universality with a measurement of $R(D^*)$ using hadronic B tagging at the Belle II experiment*, (2024),
arXiv: 2401.02840 [hep-ex]
(cit. on pp. 19–21, 23, 89, 107, 117, 144, 149, 151–153, 155, 159).

[120] R. Aaij et al. (LHCb Collaboration),
Test of lepton flavour universality using $B^0 \to D^{*-} \tau^+ \nu_\tau$ decays with hadronic τ channels,
Phys. Rev. D **108** (2023) 012018 (cit. on pp. 19, 20, 23, 149, 151, 153).

[121] R. Aaij et al. (LHCb Collaboration),
Measurement of the ratios of branching fractions $\mathcal{R}(D^*)$ and $\mathcal{R}(D^0)$,
Phys. Rev. Lett. **131** (2023) 111802 (cit. on pp. 19, 20, 23, 149, 151, 153).

[122] A. J. Bevan et al., *The Physics of the B Factories*, Eur. Phys. J. C **74** (2014) 3026
(cit. on pp. 19, 47, 48).

[123] Y. Amhis et al. (Heavy Flavor Averaging Group (HFLAV)),
Preliminary average of $R(D)$ and $R(D^*)$ for Summer 2023, visited on 02/10/2023,
URL: https://hflav-eos.web.cern.ch/hflav-eos/semi/summer23/html/RDsDsstar/RDRDs.html (cit. on pp. 20, 23, 149, 151, 153).

[124] A. Hayrapetyan et al. (CMS Collaboration),
Search for a third-generation leptoquark coupled to a τ lepton and a b quark through single, pair, and nonresonant production in proton-proton collisions at $\sqrt{s} = 13$ TeV, (2023),
arXiv: 2308.07826 [hep-ex] (cit. on p. 20).

[125] A. Tumasyan et al. (CMS Collaboration), *Searches for additional Higgs bosons and for vector leptoquarks in $\tau\tau$ final states in proton-proton collisions at $\sqrt{s} = 13$ TeV*, JHEP **07** (2023) 073
(cit. on p. 20).

[126] M. Rahimi and K. K. Vos, *Standard Model predictions for lepton flavour universality ratios of inclusive semileptonic B decays*, J. High Energ. Phys. **2022** (2022) 7
(cit. on pp. 21, 23, 24, 38, 88, 142, 145, 149, 153).

[127] T. Mannel, A. V. Rusov and F. Shahriaran,
Inclusive semitauonic B decays to order $O(\Lambda_{\rm QCD}^3/m_b^3)$, Nucl. Phys. B **921** (2017) 211
(cit. on p. 21).

[128] M. Freytsis, Z. Ligeti and J. T. Ruderman, *Flavor models for $\overline{B} \to D^{(*)} \tau \overline{\nu}$*,
Phys. Rev. D **92** (2015) 054018 (cit. on pp. 21, 23, 38, 142, 145, 149, 153).

[129] Z. Ligeti, M. Luke and F. J. Tackmann,
Theoretical predictions for inclusive $B \to X_u \tau \bar{\nu}$ decay, Phys. Rev. D **105** (2022) 073009
(cit. on pp. 21, 23, 38, 142, 145, 149, 153).

[130] Y. S. Amhis et al. (Heavy Flavor Averaging Group, HFLAV),
Averages of b-hadron, c-hadron, and τ-lepton properties as of 2021,
Phys. Rev. D **107** (2023) 052008 (cit. on pp. 21–23, 38, 131, 132, 134, 149, 150).

[131] M. Acciarri et al. (L3 Collaboration),
Measurement of the inclusive $B \to \tau \nu X$ branching ratio, Phys. Lett. B **332** (1994) 201
(cit. on pp. 22, 23, 149).

[132] M. Acciarri et al. (L3 Collaboration),
Measurement of the branching ratios $b \to e\nu X, \mu\nu X, \tau\nu X$ and νX, Z. Phys. C **71** (1996) 379
(cit. on pp. 22, 23, 149).

[133] P. Abreu et al. (DELPHI Collaboration),
Upper limit for the decay $B^- \to \tau^- \bar{\nu}_\tau$ and measurement of the $b \to \tau \bar{\nu}_\tau X$ branching ratio,
Phys. Lett. B **496** (2000) 43 (cit. on pp. 22, 23, 149).

[134] R. Barate et al. (ALEPH Collaboration), *Measurements of BR ($b \to \tau^- \bar{\nu}_\tau X$) and BR ($b \to \tau^- \bar{\nu}_\tau D^{*\pm} X$) and upper limits on $\mathcal{B}$ ($B^- \to \tau^- \bar{\nu}_\tau$) and $\mathcal{B}$ ($b \to s\nu\bar{\nu}$)*,
Eur. Phys. J. C **19** (2001) 213 (cit. on pp. 22, 23, 149).

[135] G. Abbiendi et al. (OPAL Collaboration),
Measurement of the branching ratio for the process $b \to \tau^- \bar{\nu}_\tau X$, Phys. Lett. B **520** (2001) 1
(cit. on pp. 22, 23, 149).

[136] J. Hasenbusch, *Analysis of inclusive semileptonic B meson decays with τ lepton final states at the Belle experiment*, PhD thesis: Rheinische Friedrich-Wilhelms-Universität Bonn, 2018,
URL: https://hdl.handle.net/20.500.11811/7578
(cit. on pp. 22, 23, 112, 113, 116, 148, 149).

[137] C. Bobeth et al., *Lepton-flavour non-universality of $\bar{B} \to D^* \ell \bar{\nu}$ angular distributions in and beyond the Standard Model*, Eur. Phys. J. C **81** (2021) 984 (cit. on p. 23).

[138] E. Waheed et al. (Belle Collaboration),
Measurement of the CKM matrix element $|V_{cb}|$ from $B^0 \to D^{*-} \ell^+ \nu_\ell$ at Belle,
Phys. Rev. D **100** (2019) 052007 (cit. on pp. 23, 24, 88).

[139] M. T. Prim et al. (Belle Collaboration),
Measurement of differential distributions of $B \to D^* \ell \bar{\nu}_\ell$ and implications on $|V_{cb}|$,
Phys. Rev. D **108** (2023) 012002 (cit. on pp. 23, 88).

[140] I. Adachi et al. (Belle II Collaboration),
Tests of Light-Lepton Universality in Angular Asymmetries of $B^0 \to D^{*-} \ell \nu$ Decays,
Phys. Rev. Lett. **131** (2023) 181801 (cit. on p. 23).

[141] I. Adachi et al. (Belle II Collaboration),
Determination of $|V_{cb}|$ using $\overline{B}^0 \to D^{*+} \ell^- \bar{\nu}_\ell$ decays with Belle II,
Phys. Rev. D **108** (2023) 092013 (cit. on pp. 23, 88).

[142] M. T. Prim et al. (Belle Collaboration), *Measurement of Angular Coefficients of $\bar{B} \to D^* \ell \bar{\nu}_\ell$: Implications for $|V_{cb}|$ and Tests of Lepton Flavor Universality*, (2023), arXiv: 2310.20286 [hep-ex] (cit. on p. 23).

[143] R. Aaij et al. (LHCb Collaboration), *Test of lepton universality in beauty-quark decays*, Nature Phys. **18** (2022) 277, [Addendum: Nature Phys. **19** (2023) 1517] (cit. on p. 24).

[144] R. Aaij et al. (LHCb Collaboration), *Test of Lepton Universality in $b \to s\ell^+\ell^-$ Decays*, Phys. Rev. Lett. **131** (2023) 051803 (cit. on p. 24).

[145] R. Aaij et al. (LHCb Collaboration), *Measurement of lepton universality parameters in $B^+ \to K^+\ell^+\ell^-$ and $B^0 \to K^{*0}\ell^+\ell^-$ decays*, Phys. Rev. D **108** (2023) 032002 (cit. on p. 24).

[146] K. Wright, *Standard Model Stays Strong for Leptons*, Physics Magazine (2023), visited on 06/10/2023, URL: https://physics.aps.org/articles/v16/s91 (cit. on p. 24).

[147] V. Khachatryan et al. (CMS Collaboration), *Angular analysis of the decay $B^0 \to K^{*0}\mu^+\mu^-$ from pp collisions at $\sqrt{s} = 8$ TeV*, Phys. Lett. B **753** (2016) 424 (cit. on p. 24).

[148] R. Aaij et al. (LHCb Collaboration), *Angular analysis of the $B^0 \to K^{*0}\mu^+\mu^-$ decay using 3 fb^{-1} of integrated luminosity*, JHEP **02** (2016) 104 (cit. on p. 24).

[149] A. Sirunyan et al. (CMS Collaboration), *Measurement of angular parameters from the decay $B^0 \to K^{*0}\mu^+\mu^-$ in proton–proton collisions at $\sqrt{s} = 8$ TeV*, Phys. Lett. B **781** (2018) 517 (cit. on p. 24).

[150] M. Aaboud et al. (ATLAS Collaboration), *Angular analysis of $B_d^0 \to K^*\mu^+\mu^-$ decays in pp collisions at $\sqrt{s} = 8$ TeV with the ATLAS detector*, JHEP **10** (2018) 047 (cit. on p. 24).

[151] R. Aaij et al. (LHCb Collaboration), *Angular Analysis of the $B^+ \to K^{*+}\mu^+\mu^-$ Decay*, Phys. Rev. Lett. **126** (2021) 161802 (cit. on p. 24).

[152] R. Aaij et al. (LHCb Collaboration), *Angular analysis of the rare decay $B_s^0 \to \phi\mu^+\mu^-$*, JHEP **11** (2021) 043 (cit. on p. 24).

[153] R. Aaij et al. (LHCb Collaboration), *Differential branching fraction and angular analysis of $\Lambda_b^0 \to \Lambda\mu^+\mu^-$ decays*, JHEP **06** (2015) 115, [Erratum: JHEP **09** (2018) 145] (cit. on p. 24).

[154] I. Adachi et al. (Belle II Collaboration), *Evidence for $B^+ \to K^+\nu\bar{\nu}$ Decays*, (2023), arXiv: 2311.14647 [hep-ex] (cit. on pp. 24, 117).

[155] R. van Tonder et al. (Belle Collaboration), *Measurements of q^2 Moments of Inclusive $B \to X_c\ell^+\nu_\ell$ Decays with Hadronic Tagging*, Phys. Rev. D **104** (2021) 112011 (cit. on pp. 24, 112, 116).

[156] W. Altmannshofer et al., *The Belle II Physics Book*, Prog. Theor. Exp. Phys. **2019** (2019) 123C01, ed. by E. Kou et al., [Erratum: Prog. Theor. Exp. Phys. **2020** (2020) 029201] (cit. on pp. 25, 26, 48).

[157] L. Aggarwal et al.,
Snowmass White Paper: Belle II physics reach and plans for the next decade and beyond,
(2022), arXiv: 2207.06307 [hep-ex] (cit. on pp. 25, 157).

[158] D. Andrews et al. (CLEO Collaboration), *The CLEO detector*,
Nucl. Instrum. Meth. **211** (1983) 47 (cit. on p. 25).

[159] H. Albrecht et al. (ARGUS Collaboration), *Argus: A universal detector at DORIS II*,
Nucl. Instrum. Meth. A **275** (1989) 1 (cit. on p. 25).

[160] D. Boutigny et al. (BaBar Collaboration), *BaBar technical design report*,
(1995), SLAC Report: SLAC-R-457, URL: https://www-public.slac.stanford.edu/sciDoc/docMeta.aspx?slacPubNumber=slac-r-457
(cit. on p. 25).

[161] A. Abashian et al. (Belle Collaboration), *The Belle detector*,
Nucl. Instrum. Meth. A **479** (2002) 117 (cit. on pp. 25, 27).

[162] A. Augusto Alves Jr. et al. (LHCb Collaboration), *The LHCb Detector at the LHC*,
JINST **3** (2008) S08005 (cit. on p. 25).

[163] K. Akai et al. (SuperKEKB accelerator team), *SuperKEKB Collider*,
Nucl. Instrum. Meth. A **907** (2018) 188 (cit. on pp. 25, 26).

[164] T. Abe et al. (Belle II Collaboration), *Belle II Technical Design Report*, (2010),
arXiv: 1011.0352 [physics.ins-det] (cit. on pp. 25, 27).

[165] *KEKB B factory design report*, (1995), KEK-REPORT-95-7,
URL: https://inspirehep.net/files/8306509502dba26d6a2d84aeae56e435
(cit. on p. 25).

[166] S. Kurokawa and E. Kikutani, *Overview of the KEKB accelerators*,
Nucl. Instrum. Meth. A **499** (2003) 1 (cit. on p. 25).

[167] M. Bona et al. (SuperB Collaboration), *SuperB: A High-Luminosity Asymmetric e+ e- Super Flavor Factory. Conceptual Design Report*, (2007), arXiv: 0709.0451 [hep-ex]
(cit. on p. 26).

[168] D. Zhou, K. O. Y. Funakoshi and Y. Ohnishi, *Luminosity performance of SuperKEKB*, (2023),
arXiv: 2306.02692 [physics.acc-ph] (cit. on p. 27).

[169] Belle II Collaboration, *The Belle II Experiment – The Detector*, visited on 09/10/2023,
URL: https://belle2.jp/detector/ (cit. on p. 27).

[170] H. Kolanoski and N. Wermes, *Teilchendetektoren: Grundlagen und Anwendungen*,
Springer, 2016, ISBN: 978-3-662-45349-0,
URL: https://link.springer.com/book/10.1007/978-3-662-45350-6
(cit. on pp. 28, 33).

[171] B. Wang et al. (Belle-II DEPFET and PXD Collaboration),
Operational experience of the Belle II pixel detector,
Nucl. Instrum. Meth. A **1032** (2022) 166631 (cit. on pp. 28, 29).

[172] MPP, *Belle II: Das Auge für die Antimaterie*, visited on 11/10/2023, URL: https://www.mpp.mpg.de/forschung/aufbau-der-materie/belle-ii-dem-antimaterie-raetsel-auf-der-spur/belle-ii-das-auge-fuer-antimaterie (cit. on p. 28).

[173] Belle II Italian Collaboration, *Silicon Vertex Detector*, visited on 11/10/2023, URL: https://web.infn.it/Belle-II/index.php/detector/svd/20-silicon-vertex-detector (cit. on p. 28).

[174] V. Bertacchi et al. (Belle II Tracking Group), *Track finding at Belle II*, Comput. Phys. Commun. **259** (2021) 107610 (cit. on pp. 28, 29, 33).

[175] C. Irmler et al. (Belle-II SVD Collaboration), *The silicon vertex detector of the Belle II experiment*, Nucl. Instrum. Meth. A **1045** (2023) 167578 (cit. on p. 29).

[176] G. Rizzo et al. (Belle-II SVD Collaboration), *The Belle II Silicon Vertex Detector: Performance and Operational Experience in the First Year of Data Taking*, JPS Conf. Proc. **34** (2021) 010003 (cit. on p. 29).

[177] N. Taniguchi (Belle II Collaboration), *Central Drift Chamber for Belle-II*, J. Instrum. **12** (2017) C06014 (cit. on p. 29).

[178] J. Fast (Belle II Barrel Particle Identification Group), *The Belle II imaging Time-of-Propagation (iTOP) detector*, Nucl. Instrum. Meth. A **876** (2017) 145 (cit. on p. 30).

[179] M. Yonenaga et al., *Performance evaluation of the aerogel RICH counter for the Belle II spectrometer using early beam collision data*, Prog. Theor. Exp. Phys. **2020** (2020) 093H01 (cit. on pp. 30, 31).

[180] K. Kojima (Belle II TOP Group), *The operation and performance of the TOP detector at the Belle II experiment*, PoS **EPS-HEP2021** (2022) 803 (cit. on p. 30).

[181] S. Nishida et al., *Aerogel RICH for the Belle II forward PID*, Nucl. Instrum. Meth. A **766** (2014) 28 (cit. on p. 30).

[182] V. Aulchenko et al. (Belle-II ECL Collaboration), *Electromagnetic calorimeter for Belle II*, J. Phys. Conf. Ser. **587** (2015) 012045 (cit. on p. 31).

[183] T. Aushev et al., *A scintillator based endcap K_L and muon detector for the Belle II experiment*, Nucl. Instrum. Meth. A **789** (2015) 134 (cit. on p. 31).

[184] T. Alexopoulos, M. Bachtis, E. Gazis and G. Tsipolitis, *Implementation of the Legendre Transform for track segment reconstruction in drift tube chambers*, Nucl. Instrum. Meth. A **592** (2008) 456 (cit. on p. 33).

[185] R. Frühwirth, R. Glattauer, J. Lettenbichler, W. Mitaroff and M. Nadler, *Track finding in silicon trackers with a small number of layers*, Nucl. Instrum. Meth. A **732** (2013) 95 (cit. on p. 33).

[186] T. Bilka et al.,
Implementation of GENFIT2 as an experiment independent track-fitting framework, (2019), arXiv: 1902.04405 [physics.data-an] (cit. on pp. 33, 34).

[187] T. Keck, *FastBDT: A Speed-Optimized Multivariate Classification Algorithm for the Belle II Experiment*, Comput. Softw. Big Sci. **1** (2017) 2 (cit. on pp. 33, 50).

[188] M. Eliachevitch, *Tracking Performance Studies on Cosmic Rays and a Track Quality Estimation for the Central Drift Chamber of the Belle II-Experiment*,
Master thesis: Karlsruher Institut für Technologie (KIT), 2018,
URL: https://publish.etp.kit.edu/record/21558 (cit. on p. 33).

[189] P. Billoir, *Progressive track recognition with a Kalman-like fitting procedure*,
Comput. Phys. Commun. **57** (1989) 390 (cit. on p. 33).

[190] N. Braun, *Combinatorial Kalman Filter and High Level Trigger Reconstruction for the Belle II Experiment*, PhD thesis: Karlsuher Institut für Technologie (KIT), 2019,
URL: https://doi.org/10.1007/978-3-030-24997-7 (cit. on p. 33).

[191] J. Lettenbichler,
Real-time pattern recognition in the central tracking detector of the Belle II Experiment,
PhD thesis: Technische Universität Wien, 2016,
URL: http://hdl.handle.net/20.500.12708/6439 (cit. on p. 33).

[192] M. Milesi, J. Tan and P. Urquijo, *Lepton identification in Belle II using observables from the electromagnetic calorimeter and precision trackers*, EPJ Web Conf. **245** (2020) 06023
(cit. on p. 34).

[193] T. Kuhr et al. (Belle II Framework Software Group), *The Belle II Core Software*,
Comput. Softw. Big Sci. **3** (2019) 1 (cit. on p. 35).

[194] Belle II Collaboration, *Belle II Analysis Software Framework (basf2)*, (2022),
URL: https://doi.org/10.5281/zenodo.5574115 (cit. on p. 35).

[195] Belle II Collaboration, *Belle II Luminosity*, visited on 06/10/2023,
URL: https://confluence.desy.de/display/BI/Belle+II+Luminosity
(cit. on p. 35).

[196] D. J. Lange, *The EvtGen particle decay simulation package*,
Nucl. Instrum. Meth. A **462** (2001) 152 (cit. on p. 36).

[197] T. Sjöstrand et al., *An introduction to PYTHIA 8.2*, Comput. Phys. Commun. **191** (2015) 159
(cit. on p. 36).

[198] S. Jadach et al.,
The Precision Monte Carlo event generator KK for two fermion final states in e^+e^- collisions,
Comput. Phys. Commun. **130** (2000) 260 (cit. on p. 36).

[199] E. Barberio, B. van Eijk and Z. Was,
Photos - a universal Monte Carlo for QED radiative corrections in decays,
Comput. Phys. Commun. **66** (1991) 115 (cit. on p. 36).

[200] S. Agostinelli et al. (GEANT4 Collaboration), *GEANT4 – a simulation toolkit*,
Nucl. Instrum. Meth. A **506** (2003) 250 (cit. on p. 36).

[201] A. Natochii et al., *Beam background expectations for Belle II at SuperKEKB*, (2022), arXiv: 2203.05731 [hep-ex] (cit. on p. 36).

[202] J. P. Lees et al. (BaBar Collaboration), *Observation of $\overline{B} \to D^{(*)}\,\pi^+\pi^-\ell^-\overline{\nu}$ Decays in e^+e^- Collisions at the $\Upsilon(4S)$ Resonance*, Phys. Rev. Lett. **116** (2016) 041801 (cit. on p. 38).

[203] F. U. Bernlochner et al., *Combined analysis of semileptonic B decays to D and D^*: $R(D^{(*)})$, $|V_{cb}|$, and new physics*, Phys. Rev. D **95** (2017) 115008 (cit. on p. 38).

[204] R. Glattauer et al. (Belle Collaboration), *Measurement of the decay $B \to D\ell\nu_\ell$ in fully reconstructed events and determination of the Cabibbo-Kobayashi-Maskawa matrix element $|V_{cb}|$*, Phys. Rev. D **93** (2016) 032006 (cit. on pp. 38, 65, 131, 132, 134).

[205] D. Ferlewicz, P. Urquijo and E. Waheed, *Revisiting fits to $B^0 \to D^*\ell\nu$ to measure $|V_{cb}|$ with novel methods and preliminary LQCD data at nonzero recoil*, Phys. Rev. D **103** (2021) 073005 (cit. on pp. 38, 65, 131, 132, 134, 155).

[206] T. Keck et al., *The Full Event Interpretation: An Exclusive Tagging Algorithm for the Belle II Experiment*, Comput. Softw. Big Sci. **3** (2019) 6 (cit. on pp. 44, 45).

[207] F. Abudinén et al. (Belle II Collaboration), *A calibration of the Belle II hadronic tag-side reconstruction algorithm with $B \to X\ell\nu$ decays*, 2020, arXiv: 2008.06096 [hep-ex] (cit. on p. 46).

[208] P. Koppenburg, *Statistical biases in measurements with multiple candidates*, (2017), arXiv: 1703.01128 [hep-ex] (cit. on p. 46).

[209] H. Albrecht et al. (ARGUS Collaboration), *Search for hadronic $b \to u$ decays*, Phys. Lett. B **241** (1990) 278 (cit. on p. 47).

[210] M. Röhrken, *Time-Dependent CP Violation Measurements in Neutral B Meson to Double-Charm Decays at the Japanese Belle Experiment*, PhD thesis: Karlsruher Institut für Technologie (KIT), 2012, URL: https://publikationen.bibliothek.kit.edu/1000028856 (cit. on p. 49).

[211] D. M. Asner et al. (CLEO Collaboration), *Search for exclusive charmless hadronic B decays*, Phys. Rev. D **53** (1996) 1039 (cit. on p. 49).

[212] G. C. Fox and S. Wolfram, *Observables for the Analysis of Event Shapes in e^+e^- Annihilation and Other Processes*, Phys. Rev. Lett. **41** (1978) 1581 (cit. on p. 49).

[213] M. Milesi (Belle II PID Working Group), personal communication, 2023 (cit. on pp. 53, 54, 97).

[214] F. Zernike, *Beugungstheorie des Schneidenverfahrens und seiner verbesserten Form, der Phasenkontrastmethode*, Physica **1** (1934) 689 (cit. on p. 57).

[215] G. Cowan, *Statistical data analysis*, Oxford University Press, USA, 1998, ISBN: 978-0-19-850156-5 (cit. on p. 62).

[216] F. James and M. Roos, *Minuit - a system for function minimization and analysis of the parameter errors and correlations*, Comput. Phys. Commun. **10** (1975) 343 (cit. on p. 63).

[217] F. U. Bernlochner et al.,
Das ist der HAMMER: consistent new physics interpretations of semileptonic decays,
Eur. Phys. J. C **80** (2020) (cit. on p. 65).

[218] Belle II Collaboration, *Measurement of $R(D)$ and $R(D^*)$ at Belle II using semileptonic tagging and leptonic τ decays*, (2024), (unpublished) (cit. on pp. 89, 144, 155).

[219] K. G. Hayes, M. L. Perl and B. Efron,
Application of the bootstrap statistical method to the tau-decay-mode problem,
Phys. Rev. D **39** (1989) 274 (cit. on p. 92).

[220] K. Uno (Belle II PID Working Group), personal communication, 2023 (cit. on p. 100).

[221] Belle II Collaboration, `basf2: $V^0$ Finding`, visited on 10/12/2023, URL: `https://software.belle2.org/development/sphinx/tracking/doc/v0Finding.html` (cit. on p. 101).

[222] F. Abudinén et al. (Belle II Collaboration), *Measurement of lepton mass squared moments in $B \to X_c \ell \overline{\nu}_\ell$ decays with the Belle II experiment*, Phys. Rev. D **107** (2023) 072002
(cit. on pp. 116, 159).

[223] M. Welsch, personal communication, 2021 (cit. on p. 116).

[224] F. Strohkirch, *Entwicklung einer datengestützten Formanpassung von inklusiven hadronischen Zerfallskaskaden in semileptonischen B-meson Zerfällen bei Belle II*,
Bachelor thesis: Rheinische Friedrich-Wilhelms-Universität Bonn, 2023
(cit. on pp. 117, 155).

[225] F. Meier et al. (Belle Collaboration),
First observation of $B \to \overline{D}_1(\to \overline{D}\pi^+\pi^-)\ell^+\nu_\ell$ and measurement of the $B \to \overline{D}^{(*)}\pi\ell^+\nu_\ell$ and $B \to \overline{D}^{(*)}\pi^+\pi^-\ell^+\nu_\ell$ branching fractions with hadronic tagging at Belle,
Phys. Rev. D **107** (2023) 092003 (cit. on p. 147).

[226] D. Liventsev et al. (Belle Collaboration),
Study of $B \to D^{**}\ell\nu$ with full reconstruction tagging, Phys. Rev. D **77** (2008) 091503
(cit. on p. 147).

[227] B. Aubert et al. (BaBar Collaboration), *Measurement of the Branching Fractions of $\overline{B} \to D^{**}\ell^-\overline{\nu}_\ell$ Decays in Events Tagged by a Fully Reconstructed B Meson*,
Phys. Rev. Lett. **101** (2008) 261802 (cit. on p. 147).

[228] M. Ablikim et al. (BESIII Collaboration), *Design and construction of the BESIII detector*,
Nucl. Instrum. Meth. A **614** (2010) 345 (cit. on p. 155).

[229] P. Urquijo et al. (Belle Collaboration), *Moments of the electron energy spectrum and partial branching fraction of $B \to X_c e\nu$ decays at Belle*, Phys. Rev. D **75** (2007) 032001
(cit. on p. 155).

[230] P. Ecker, *Study of Bremsstrahlung Finding at the Belle II Experiment*,
Bachelor thesis: Karlsruher Institut für Technologie (KIT), 2018,
URL: `https://publish.etp.kit.edu/record/21390` (cit. on p. 161).

List of Figures

2.1 Elementary particles of the Standard Model . . . 4
2.2 QCD interaction vertices . . . 7
2.3 Running of the strong coupling α_s . . . 8
2.4 The unitary triangle . . . 12
2.5 $B \to X l \nu$ decay as described in the SM . . . 15
2.6 $B \to X l \nu$ decays with LUV . . . 19
2.7 Experimental measurements of $R(D)$ and $R(D^*)$ compared to theory predictions . . . 20
2.8 Fraction of $B \to X \ell \nu$ events that is selected in the $R(D^{(*)})$ measurements . . . 21
2.9 Experimental results related to $\mathcal{B}(B \to X \tau \nu)$ . . . 23

3.1 Schematic view of SuperKEKB . . . 26
3.2 Schematic view of the Belle II detector . . . 27
3.3 Schematic view of the PXD, SVD, and CDC . . . 28
3.4 Operating principles of the TOP and ARICH detectors . . . 30
3.5 Track reconstruction at Belle II . . . 33
3.6 Kinematic distributions for different $B \to D^{**}_{\text{gap}} \ell \nu$ decay models . . . 40
3.7 Mass distributions of D^{**} mesons . . . 40
3.8 w, q^2 and p^B_ℓ distributions for $B \to D^{**} \ell \nu$ decays . . . 41

4.1 Schematic view of an $\Upsilon(4S) \to [B_{\text{tag}} \to \text{had.}][B_{\text{sig}} \to X[\tau \to \ell \nu \nu]\nu]$ event . . . 43
4.2 Schematic overview of the FEI algorithm . . . 45
4.3 Modeling of ΔE and M_{bc} . . . 47
4.4 Variation of the achieved $\sqrt{s}$ in experimental data . . . 48
4.5 Event topology of $q\bar{q}$ vs $B\bar{B}$ . . . 49
4.6 Modeling of R_2 and $|\cos\theta_T|$ . . . 50
4.7 Modeling and separation potential for different continuum-suppression classifiers . . . 52
4.8 Distributions of ECL clusters in the polar angle θ . . . 55
4.9 Energy distributions of ECL clusters in different detector regions . . . 56
4.10 E_γ and θ distributions of ECL clusters for different data-taking periods . . . 56
4.11 Modeling and background separation potential of $\Delta R^{\text{track}}_{\text{cluster}}$, $\mathcal{P}_{\text{Zernike}}$, and $\mathcal{P}_{\text{BKG}}$ . . . 57
4.12 p^B_ℓ distributions after the event selection . . . 59

5.1 p_ℓ and M_X distributions in the proton-fake enriched control sample . . . 70
5.2 B_{tag} properties for signal and normalization decays . . . 71
5.3 M_{bc} distributions for different event types and momentum ranges . . . 72

5.4 M_{bc} distributions for different event types in experimental data . . . 73
5.5 M_{bc} distributions in the signal-enriched sample . . . 73
5.6 B_{tag} reconstruction-mode distributions for $X\tau\nu$ vs. $X\ell\nu$ in experimental data . . . 74
5.7 B_{tag} properties for $B \to Xe\nu$ and $B \to X\mu\nu$ decays . . . 75
5.8 Lepton-flavor dependent B_{tag} selection in experimental data vs. simulation . . . 76
5.9 B_{tag} reconstruction-mode modeling for $Xe\nu$ vs. $X\mu\nu$ . . . 77

6.1 Template fit in the same-flavor control sample for the $R(X_{e/\mu})$ measurement . . . 81
6.2 p_ℓ^B distributions of $X\ell\nu$ and $B\overline{B}$ backgrounds in the same-flavor control region . . . 81
6.3 $R(X_{e/\mu})$ values for modified D-meson decay distributions . . . 86
6.4 Result of the linearity test for $R(X_{e/\mu})$ . . . 87
6.5 Template fit in the signal sample for the $R(X_{e/\mu})$ measurement . . . 88
6.6 Post-fit nuisance-parameter pulls for the $R(X_{e/\mu})$ measurement . . . 89
6.7 Extracted $R(X_{e/\mu})$ values for various p_ℓ^B thresholds . . . 92
6.8 Scatter plots of p_ℓ^B-threshold-dependent $R(X_{e/\mu})$ values . . . 93
6.9 LID efficiencies for different data-production periods . . . 97

7.1 Quantities employed to suppress electron tertiaries . . . 103
7.2 Distributions of p_ℓ^B, M_X, q^2, and M_{miss}^2 for rejected electron tertiaries . . . 104
7.3 Muon-tertiary suppression quantity $|D_\mu|$ . . . 104
7.4 Distributions of p_ℓ^B, M_X, q^2, and M_{miss}^2 for rejected muon tertiaries . . . 105
7.5 Invariant masses of $J/\psi \to \ell^+\ell^-$ candidates . . . 105
7.6 Lepton-momentum based significance scans . . . 106
7.7 Distributions of p_ℓ^B, M_X, q^2, and M_{miss}^2 for events rejected based on resonances . . . 107
7.8 Quantities to define control samples . . . 110
7.9 Fake-enriched control samples . . . 111
7.10 p_ℓ^B, M_X, q^2, and M_{miss}^2 in the high-p_ℓ^B control sample . . . 111
7.11 p_ℓ^B, M_X, q^2, and M_{miss}^2 in the same-flavor $B_{\mathrm{tag}}^+[B_{\mathrm{sig}}^+ \to e^+]$ control sample . . . 112
7.12 Final-state particle multiplicities in the high-p_ℓ^B control sample . . . 113
7.13 Effects of different D-meson decay distributions on M_X and M_{miss}^2 . . . 116
7.14 Detailed composition of events in each combination of B_{tag} and B_{sig} flavor . . . 120
7.15 M_X-based correction weights for signal and normalization decays . . . 121
7.16 Reweighted p_ℓ^B, M_X, q^2, and M_{miss}^2 in the high-p_ℓ^B control sample . . . 121
7.17 Reweighted final-state particle multiplicities in the high-p_ℓ^B control sample . . . 121
7.18 M_X distributions for $B \to X_c\ell\nu$ decays in different intervals of p_ℓ^B . . . 122
7.19 M_X-based correction weights for $B \to X_c\ell\nu$ decays in different intervals of p_ℓ^B . . . 123
7.20 Correction weights for $B_{\mathrm{sig}}^- \to X_c\ell\nu$ events in different p_ℓ^B intervals for $M_X \in (0.75, 0.95]$ GeV . . . 123
7.21 Effects of the simulation reweighting on low-momentum $B \to X_c\ell\nu$ decays . . . 124
7.22 Uncertainties on M_{miss}^2 caused by the simulation reweighting of $B \to X_c\ell\nu$ decays . . . 126
7.23 Intervals in p_ℓ and M_X used to extract $B\overline{B}$-background correction weights . . . 126
7.24 p_ℓ-M_X-based correction weights for $B\overline{B}$-background events . . . 127

8.1 Two-dimensional distributions of p_ℓ^B vs. M_{miss}^2 . . . 130

8.2 Effects of an enhanced $D \to K^{\pm}$ branching fraction on M_X . . . 136
8.3 Correction weights for different D-meson decay distributions . . . 137
8.4 Extracted values of $R(X_{\tau/\ell})$ for modified D-meson decay distributions . . . 137
8.5 Extracted values of $R(X_{\tau/\ell})$ for gradually increased lepton-momentum thresholds . . . 138
8.6 E_{ECL} distributions in the electron and muon channels . . . 140
8.7 Box-opened distributions of p_ℓ^B, M_X, q^2, and M^2_{miss} . . . 141
8.8 Pre-fit distributions of p_ℓ^B vs. M^2_{miss} in intervals as used in the signal-extraction fit . . . 142
8.9 Post-fit distributions of p_ℓ^B vs. M^2_{miss} in intervals as used in the signal-extraction fit . . . 143
8.10 Post-fit nuisance parameter pulls for the $R(X_{\tau/\ell})$ measurement . . . 144
8.11 Extracted $R(X_{\tau/\ell})$ values in various subsets . . . 145
8.12 Extracted $\mathcal{R}(X_{e/\mu}^{\tau\to})$ values in various subsets . . . 146
8.13 $R(X_{\tau/\ell})$ compared to related experimental results . . . 149
8.14 Constrains from $R(X_{\tau/\ell})$ on $R(D^{(*)})$ . . . 151

9.1 Expected precision on $R(X_{\tau/\ell})$ for increasing experimental sample sizes . . . 156

A.1 B_{tag}-candidate momentum in different reference frames . . . 160
A.2 Modeling and separation potential for various classifiers to suppress bad B_{tag} candidates 160
A.3 Results of the bremsstrahlung-optimization study . . . 162
A.4 Varied $R(X_{e/\mu})$ and related values for toy data sets representing LID uncertainties . . . 164
A.5 Varied $R(X_{e/\mu})$ and related values for toy data sets representing statistical uncertainties 165
A.6 Varied $R(X_{\tau/\ell})$ values for toy data sets representing statistical uncertainties . . . 166
A.7 Linearity and pull test to validate the $R(X_{\tau/\ell})$ signal-extraction setup . . . 166

B.1 Classifier thresholds for $\mathcal{P}_e : \epsilon_e = 80\%$ . . . 167
B.2 LID correction factors for $\mathcal{P}_e : \epsilon_e = 80\%$ . . . 168
B.3 LID correction factors for $\mathcal{P}_e > 0.99$ . . . 169
B.4 LID correction factors for $\mathcal{P}_\mu^{\ell/\ell} > 0.95$ . . . 170
B.5 LID correction factors for $\mathcal{P}_\mu^{\ell/\ell} > 0.99$ . . . 171
B.6 Impact of modified D-meson decay distributions on M_X (1) . . . 174
B.7 Impact of modified D-meson decay distributions on M_X (2) . . . 175
B.8 Impact of modified D-meson decay distributions on M_X (3) . . . 176
B.9 Impact of modified D-meson decay distributions on p_ℓ^B (1) . . . 177
B.10 Impact of modified D-meson decay distributions on p_ℓ^B (2) . . . 178
B.11 Impact of modified D-meson decay distributions on p_ℓ^B (3) . . . 179
B.12 Invariant masses and $p(\chi^2_{\mathrm{vertex}})$ for utilized resonances (1) . . . 180
B.13 Invariant masses and $p(\chi^2_{\mathrm{vertex}})$ for utilized resonances (2) . . . 181
B.14 Invariant masses and $p(\chi^2_{\mathrm{vertex}})$ for unused resonances (1) . . . 182
B.15 Invariant masses and $p(\chi^2_{\mathrm{vertex}})$ for unused resonances (2) . . . 183
B.16 Invariant masses and $p(\chi^2_{\mathrm{vertex}})$ for unused resonances (3) . . . 184
B.17 Impact of the simulation reweighting in the high-p_ℓ^B control sample . . . 186
B.18 Impact of the simulation reweighting in the low-M^2_{miss} control sample . . . 187
B.19 Impact of the simulation reweighting in the low-q^2 control sample . . . 188
B.20 Impact of the simulation reweighting in the high-M_X control sample . . . 189
B.21 Impact of the simulation reweighting in the same-flavor $B^+_{\mathrm{tag}}[B^+_{\mathrm{sig}} \to \ell^+]$ control sample 190

B.22 Impact of the simulation reweighting in the same-flavor $B^0_{\text{tag}}[B^0_{\text{sig}} \to \ell^+]$ control sample 191
B.23 Impact of modified D-meson decay distributions on signal decays 193
B.24 Correction weights for $B^-_{\text{sig}} \to X_c \ell \nu$ decays in different p^B_ℓ intervals for each M_X interval 194
B.25 Correction weights for $\overline{B}^0_{\text{sig}} \to [X_c \to D^+ \ldots]\ell\nu$ decays in different p^B_ℓ intervals for each M_X interval 195
B.26 Pre-fit p^B_ℓ vs. M^2_{miss} distributions for subsets of data in the electron channel 200
B.27 Pre-fit p^B_ℓ vs. M^2_{miss} distributions for subsets of data in the muon channel 201

List of Tables

3.1 Branching fractions of $B \to X\ell\nu$ and $B \to X\tau\nu$ decays . . . 37
3.2 Sample sizes of simulated $B \to D^{**}_{\text{gap}} l\nu$ decays . . . 39
3.3 Masses and widths of D^{**} mesons . . . 40
3.4 Average LID-correction weights and uncertainties . . . 42

4.1 Baseline FEI-calibration factors . . . 46
4.2 Continuum-suppression quantities and their separation potential . . . 51
4.3 Signal-lepton selection requirements in the $R(X_{e/\mu})$ measurement . . . 53
4.4 Identification requirements for particles within the X system . . . 54

5.1 Fake composition and LID coverage for the $R(X_{e/\mu})$ and $R(X_{\tau/\ell})$ measurement . . . 69

6.1 N^{sel} and N^{meas} in the background-calibration fit . . . 81
6.2 Template-yield correlations in the background-calibration fit . . . 82
6.3 Relative uncertainties on $R(X_{e/\mu})$ . . . 83
6.4 Modified D-meson decay distributions used to probe $R(X_{e/\mu})$ stability . . . 85
6.5 $B\bar{B}$-background yield and calibration-factor changes for modified D-decay distributions 86
6.6 N^{sel} and N^{meas} in the $R(X_{e/\mu})$-extraction fit . . . 88
6.7 Template-yield correlations in the $R(X_{e/\mu})$-extraction fit . . . 89
6.8 Background-calibration factors for different p^B_ℓ thresholds . . . 91
6.9 Extracted $R(X_{e/\mu})$ values for alternative fit setups or subsets of experimental data . . . 94
6.10 Extracted $R(X_{e/\mu})$ values for different subsets of experimental data . . . 95
6.11 Relative deviations of $R(X_{e/\mu})$ values based on subsets of M_X . . . 96
6.12 Relative deviations of $R(X_{e/\mu})$ values based on subsets of data-production periods . . . 96

7.1 Composition of secondary events, categorized by signal-lepton origin . . . 100
7.2 Signal-lepton selection requirements in the $R(X_{\tau/\ell})$ measurement . . . 101
7.3 Impact of the $B\bar{B}$-background suppression requirements on each event type . . . 102
7.4 Intermediate resonances studied to suppress fakes . . . 108
7.5 Inclusive D-meson branching fractions in measurements and simulation . . . 115
7.6 D-meson decay distributions used to probe mismodeling effects on M_X and M^2_{miss} . . . 115
7.7 Correction factors to the initial B_{tag} calibration . . . 118

8.1 Relative uncertainties on $R(X_{\tau/e})$ . . . 131
8.2 Relative uncertainties on $R(X_{\tau/\mu})$ . . . 132

8.3 Summary of uncertainties on $R(X_{\tau/\ell})$ for e, μ, and their combination 133
8.4 Example D-meson decay distributions used to probe the $R(X_{\tau/\ell})$ stability 135
8.5 Dependence of $R(X_{\tau/\ell})$ on the B_{sig}-frame momentum p_ℓ^B 139
8.6 Dependence of $R(X_{\tau/\ell})$ on the lab-frame momentum p_ℓ 139
8.7 N^{sel} and N^{meas} in the $R(X_{\tau/\ell})$-extraction fit 143
8.8 Template-yield correlations in the $R(X_{\tau/\ell})$-extraction fit 143
8.9 Dependence of $R(X_{\tau/\ell})$ on significantly modified $B \to X_c X_c$ yields 148

A.1 Relative uncertainties on $R(X_{e/\mu})$ in toy-study setup 163

B.1 FEI reconstruction modes for B^0_{tag} 172
B.2 FEI reconstruction modes for B^+_{tag} 173
B.3 Numerical values of correction weights applied to $B \to X_c \ell \nu$ and $B \to X_c \tau \nu$ decays 196
B.4 Numerical values of correction weights applied to $B\bar{B}$-background events 197
B.5 Modified D-meson decay distributions used to probe $R(X_{\tau/\ell})$ stability (1) 198
B.6 Modified D-meson decay distributions used to probe $R(X_{\tau/\ell})$ stability (2) 199

List of Abbreviations

2HDM	**Two**-**H**iggs-**D**oublet **M**odel
basf2	**B**elle **II** **A**nalysi**S** **F**ramework
ARICH	**A**erogel **R**ing-**I**maging **CH**erenkov counter
BDT	**B**oosted **D**ecision **T**ree
BLR	**B**ernlochner-**L**igeti-**R**obinson
BLPRXP	**B**ernlochner-**L**igeti-**P**apucci-**R**obinson-**X**iong-**P**rim
BGL	**B**oyd-**G**rinstein-**L**ebed
Chap.	**Chap**ter
CDC	**C**entral **D**rift **C**hamber
CLN	**C**aprini-**L**ellouch-**N**eubert
CERN	**C**onseil **E**uropéen pour la **R**echerche **N**ucléaire
CKF	**C**ombinatorial **K**alman **F**ilter
CKM	**C**abbibo-**K**obayashi-**M**askawa
c. m.	**c**enter-of-**m**ass
DAF	**D**eterministic **A**nnealing **F**ilter
DEPFET	**DEP**leted-**F**ield-**E**ffect **T**ransistor
dof.	**d**egrees **o**f **f**reedom
ECL	**E**lectromagnetic **C**a**L**orimeter
Eq.	**Eq**uation
Fig.	**Fig**ure
FF	**F**orm **F**actors
HQE	**H**eavy **Q**uark **E**xpansion
HQET	**H**eavy **Q**uark **E**ffective **T**heory
IP	**I**nteraction **P**oint
KEK	High Energy Accelerator Research Organization (in Japanese)
KLM	K_L^0 and **M**yon detector

LEP	**L**arge **E**lectron-**P**ositron collider
LFV	**L**epton-**F**lavor **V**iolation
LHC	**L**arge **H**adron **C**ollider
LID	**L**epton **ID**entification
LLSW	**L**eibovich-**L**igeti-**S**tewart-**W**ise
LQ	**L**epto**Q**uark
LU	**L**epton **U**niversality
LUV	**L**epton-**U**niversality **V**iolation
LS1	**L**ong **S**hutdown **1**
MC	**M**onte **C**arlo
PID	**P**article **ID**entification
POCA	**P**oint **O**f **C**losest **A**pproach
PXD	**P**i**X**el **D**etector
QCD	**Q**uantum **C**hromo**D**ynamics
QED	**Q**uantum **E**lectro**D**ynamics
QFT	**Q**uantum **F**ield **T**heory
Ref.	**Ref**erence
RMS	**R**oot **M**ean **S**quare
Sec.	**Sec**tion
SM	**S**tandard **M**odel of particle physics
SVD	**S**ilicon **V**ertex **D**etector
Tab.	**Tab**le
TOP	**T**ime-**O**f-**P**ropagation counter
WIMP	**W**eakly **I**nteracting **M**assive **P**article

Acknowledgements

The research presented in this thesis owes its realization to invaluable discussions, suggestions, and the unwavering support of various groups and individuals.

Foremost among them, I would like to thank my doctoral advisor, Prof. Jochen Dingfelder, for granting me the opportunity to delve deep into this research project. I appreciate the excellent scientific environment provided at the University of Bonn, his scientific guidance and feedback, and his consistent support that allowed me to participate in numerous conferences, collaboration meetings, research visits, and summer schools worldwide. In this context, I am also grateful to the Studienstiftung des deutschen Volkes for both financial and non-monetary support throughout my thesis, and to the Bonn-Melbourne Research Excellence Fund for facilitating my travels to Australia.

In addition, I extend my sincere gratitude to my primary supervisor, Prof. Peter Lewis, for countless constructive discussions, ideas, and insightful suggestions that enriched every stage of this thesis. I am also thankful to Prof. Florian Bernlochner for graciously sharing his invaluable expertise whenever it was required.

I wish to express my acknowledgment to Dr. Mirco Dorigo, Prof. Yoshihide Sakai, Dr. Raynette van Tonder, Prof. Ariane Frey, Dr. Christoph Schwanda, and Dr. Diego Tonelli for their significant contributions to the rigorous and constructive internal reviews of my analyses within the Belle II collaboration. Additionally, I express my thanks to Dr. Marco Milesi, Paolo Rocchetti, and Prof. Phillip Urquijo from the University of Melbourne for valuable scientific discussions but also for the enjoyable non-work-related experiences during our mutual research visits. Thanks go to Dr. Simon Kurz for his role in facilitating my entry into Belle II's software through his comprehensive supervision during my qualification task, despite the challenges imposed by the pandemic.

To my colleagues, office mates, and friends from the University of Bonn, I express my heartfelt gratitude for creating a cooperative, engaging, and humorous atmosphere that consistently added to the enjoyment of this endeavor. A special acknowledgment goes to Stephan Duell and Svenja Granderath for patiently and profoundly introducing me to all the technicalities of Belle II. I also extend my thanks to Gerrit Bickendorf, Munira Khan, Martin Angelsmark, Dr. Felix Metzner, Dr. Chaoyi Lyu, Ilias Tsaklidis, and Tobias Böckh for their proofreading of chapters of my thesis.

I thank Prof. Klaus Desch for agreeing to serve as the second reviewer of this work, as well as Prof. Herbi Dreiner and Prof. Elena Demidova for their willingness to participate in the dissertation committee. Special thanks go to Andrea Fürstenberg for her continuous support with all the administrative paperwork related to the business travels.

Last but certainly not least, I want to express my gratitude to Rebekka for her unwavering encouragement throughout my academic journey. Not only has she been the best source of motivation for me to maintain a healthy work-life balance with sufficient vacation periods, but she has also provided invaluable support during the challenging periods of my thesis. Thank you for all our shared adventures and experiences, and for many more to come.